Università degli Studi di Ferrara

DOTTORATO DI RICERCA IN
SCIEZE CHIMICHE

CICLO XXVIII

COORDINATORE Prof. Carlo Alberto Bignozzi

ADSORPTION OF ORGANIC COMPOUNDS ON MICROPOROUS AND NANOSTRUCTURED MATERIALS

Settore Scientifico Disciplinare CHIM/01

Dottorando
Dott. Bosi Valentina

Tutore
Prof. Pasti Luisa

Cotutore
Prof. Cavazzini Alberto

Anni 2013/2016

INDEX

INTRODUCTION

Nanoscience and nanotechnology have aroused considerable interest in the scientific community not only because of the expectation of the impact nanomaterials may have on improving the quality of life, but also for the preservation of the environment. Many of the current problems involving, for example, the development of drug delivery systems and the removal of pollutants from water could be resolved using the nano-scale adsorbents, called nanoadsorbent.

In recent years nanotechnology has provided different types of nanometrials that are being evaluated as possible nanoadsorbent materials [Savage et al. 2005, 2009; Khajeh et al. 2013]. These materials have a range of physical and chemical properties that make them fascinating for the development of adsorption devices with high sensitivity, selectivity and efficiency. Of particular interest is the fact that nanostructures have higher surface areas than do conventional materials (it means that these materials exhibit a very large number of atoms, or chemical species in general, likely to reduce the free energy of the system that is inserted through chemical bonds or physical interactions with other chemical species present in their vicinity). For this reason, the study of the adsorption on nanostructured materials is an area of increasing importance to understand, create and improve materials for applications in different fields.

There are indeed many areas of current academic and industrial activity where the use of these materials have significant impact:

- microporous materials for separations technologies and energy storage;
- biochemical and pharmaceutical separations;
- incorporation into construction industry materials for improved strength or for fault diagnostics;
- battery or capacitor elements for new or improved operation;
- product-specific catalysts for almost every petrochemical process.

The nanoadsorbent materials belonging to the most general class of the nanostructrured materials (NMs). A classification of NMs with respect to the synthetic route and possible applications is given in the figure 1 below.

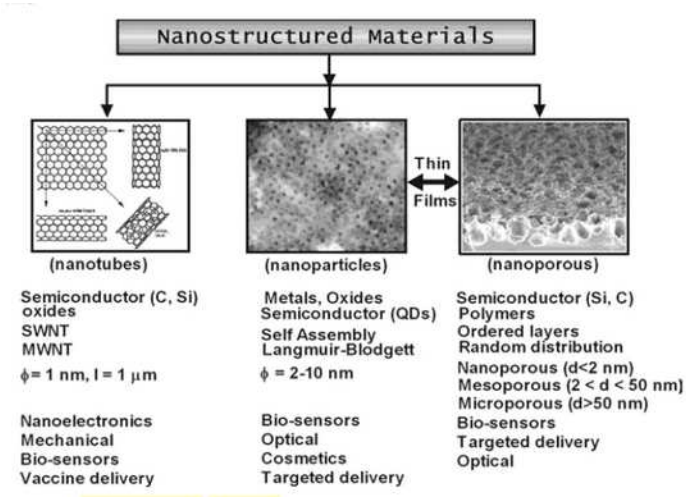

Figure 1: classification of NMs [Kassing et al. 2005]

In particular, during my thesis I studied the adsorption behaviour of different nanostructured materials and in particular, my work has been mainly devoted to the investigation of the adsorption process of particles belonging to the classes of both nanoparticles and nanoporous materials. Both types of NMs (i.e. nanoparticles and nanoporous) present high surface areas which are attained by fabricating small particles or clusters where the surface-to-volume ratio of each particle is high (nanoparticles) or by creating materials where the void surface area (pores) is high compared to the amount of bulk support material (nanoporous). In particular, highly dispersed metal nanoparticles (such as gold nanoparticles) fall into the first category and zeolites (nanometer-pored) materials fall into the latter category.

The phenomenon of adsorption of various types of molecule (in particular compounds which present biological activity and organic pollutants) on nanostructured materials has the purpose of evaluating performances of these nano-adsorbents for their applicability in remediation technologies of natural waters and as medium for enrichment step of analytical procedures.

In the first part of the PhD the adsorption/desorption of gold nanoparticles towards molecules which present biological activity (such as labelled nucleosides and oligonucleotides) in order to examine the applicability of these nanoparticles in pre-concentration and/or clean-up step for the analysis of biological samples (i.e. urine) has been investigated. Additionally, the diffusion process of nanoparticles-drug adducts has been studied due to its importance in drug transport and controlled release for the development of new drug delivery systems. In the second part, we focused our attention

on the adsorption of nanoporous zeolites (ZSM-5 and zeolite Y) towards organic pollutants for investigating their applicability in water remediation technologies.

To better understand what are nanostructured materials, in the 1st chapter a short overview of their classification and properties has been done.

The results on the applicability of gold nanoparticles for the enrichment of analytes in biological samples are presented in chapter 2. In this work the sensitivity of the micellar electrokinetic chromatography (MEKC) method was increased by using two preconcentration techniques: micro solid phase extraction (μSPE) with gold nanoparticles followed by reversed electrode polarity stacking mode (REPSM). By using the proposed methodology and under the optimum conditions, high enrichment factors (in the range from 360 to 400) were obtained and therefore the developed method may have great potential for biochemical applications.

Nucleoside analogues are potential anticancer and/or antiviral agents, the solubility and transport of which could be improved by inclusion inside the cyclodextrin cavity. In view of such kind of applications we investigated the ability of cyclodextrin-capped gold nanoparticles (Au-CDSH) to include the deoxycytidine (DC). Complexation phenomena were detected by measuring the diffusion coefficients of DC in the presence and in the absence of the cyclodextrin-capped gold nanoparticles. The diffusion coefficients was estimated from the enlargement bandwidth of solutes in capillary systems (Taylor Dispersion Analysis). With this method the value of diffusion coefficient of the single components and of the mixtures were determined. Moreover, with this method, it was possible to evaluate the ligand fraction of the biological molecule inserted in the cyclodextrine cavity and the hydrodynamic radius of the nanoparticles. This data are presented in chapter 3.

For that which concerns nanoporous materials, the adsorption isotherms of single component pollutants onto two different zeolites which differ from each other in framework topology and pore window apertures have been determined. The isotherms were obtained at different temperature in order to describe the thermodynamics of the process. The adsorption /desorption process as well as framework structural modifications and the localization of the pollutant molecules were investigated. Finally we evaluated also the adsorption efficiency of the regenerated material after the thermal treatment. Since multiple sorbates often coexist in the environment, quantifying sorbent-sorbate interactions is paramount to predicting the adsorption capability of materials. At low concentrations, comparable to those usually found in surface waters,

competitive interactions are not expected to play a significant role in the adsorption process. However, in the case of a highly concentrated accidental release, or during the life time of the adsorbent a full understanding of the competitive interactions among adsorbates would be necessary to predict adsorbent performances. To evaluate the adsorption performances of nanoporous materials, competitive adsorption isotherms were determined. This data obtained in collaboration with different research units including the diffractometric group of the Department of Physics and Earth Sciences and the groups of analytical chemistry and physical chemistry of the Department of Chemical and Pharmaceutical Sciences are reported in chapter 4 for the single component and in chapter 5 for the binary mixtures.

Finally, during the PhD, I contributed in writing a review about the microscopic models of liquid chromatography which originates in the publication of an article [Pasti L., Marchetti N., Guzzinati R., Catani M., Bosi V., Dondi F., Sepsey A., Felinger A., Cavazzini A., Trends in Analytical Chemistry (2015) (see Appendix I). The models considered have been defined as random or stochastic models. In particular, this study focuses on a unified description of stochastic models through the so-called Levy process representation or formalism, which has allowed for the establishment of a conceptual bridge between single-molecule dynamics observation and chromatographic (i.e. adsorption/desorption) experiments. The Levy process was revised in this work, with particular attention to its basic principles and physical meaning, its applications and future possibilities of development.

CHAPTER 1: NANOADSORBENT MATERIALS

The term nanomaterial comes from the combination of two words: the Greek numerical prefix “nano” and the word “material”. A nanosized structures has at least one or more dimensions (length, width or thickness) in the nanometer size range (approximately 1 to 100 nm) as reported in table 1.1 [European commission nanotechnologies 2013]:

Nanomaterial dimension	Example
All three dimensions < 100 nm	Nanoparticles, quantum dots, nanoshells, nanorings, microcapsules
Two dimensions < 100 nm	Nanotubes, fibres, nanowires
One dimension < 100 nm	Thin films, layers, coatings

Table 1.1: Nanomaterials categorised according to their dimensions

The use of nanomaterials is not a recently discovered area. It dates back at the fourth century AD when Romans used nanosized metals to decorate glasses and cups. In 1857, Faraday published a paper which explained how metal nanoparticles affect the colour of church windows and in 1959, Feynman (awarded Nobel prize in Physics in 1965) gave a lecture titled “There's Plenty of Room at the Bottom” (which is generally considered to be the foreseeing of nanotechnology), suggesting the possibility of manipulating things at atomic level. However, the real burst of nanotechnology did not come until the early 1990s; in fact it is considered an emerging technology due to the possibility to create new products with totally new characteristics [Zhai et al. 2006; Kalfa et al. 2009] and functions with enormous potential in a wide range of applications [Klabunde 2001]. It is also a dynamic field where over 50000 articles have been published annually worldwide in recent years and more than 2500 patents are filed at major patent offices such as the European Patent Office [Huang et al. 2011].

In the follow parts we present the two classes of nanoadsorbent material considered with a particular attention on the materials used in this work.

1.1 NANOPARTICLES

As described above nanoparticles (NPs) have all three dimension in the range of nanometres. NPs are of great scientific interest as they are, in effect, a bridge between bulk materials and atomic or molecular structures. A bulk material should have constant physical properties regardless of its size, but at the nano-scale size-dependent properties are often observed. Thus, the properties of materials change as their size approaches the nanoscale and as the percentage of atoms at the surface of a material becomes significant. Some properties of great importance are:

- Innate surface properties: the physical, material, and chemical properties of NPs are directly related to their intrinsic compositions, apparent sizes and extrinsic surface structures [Mirkin et al. 1996]. As mentioned earlier, it is widely recognized that as particle size decreases to the nanometer scale, there are a variety of reasons, including quantum confinement effects, that cause their physical and chemical properties to differ from those associated with their bulk form. Equally important and widely acknowledged is recognition that a large portion of the atoms in NPs are at or near the surface of the particles [Baer et al. 2010]. Determining the nature and distribution of active sites on nanostructured surfaces is an important challenge. The following are the basic factors which influence the function as adsorbent of NPs in solution or substrate: location of the most atoms in the surface, high surface area, high chemical activity, high adsorptive capacity, lack of internal diffusional resistance and high surface binding energy;
- External functionalization: using the various functional groups, a number of changes emerge in the surface properties of NPs. Coupling the wide variety of NPs with different external functionalization methods will result in excellent adsorption properties. Further functionalization of the surface prevents NPs from aggregating and provides their selectivity. Intended coatings may have a significant impact on a variety of NPs properties. Functionalized groups induce important characteristics to the adsorbents such as high absorption capacity and rapid desorption [Jimenez-Soto et al. 2010];
- Volume effects: which are due to: a lower wavelength (higher frequency and higher energy), a blue shift of atoms for optical absorption spectra, superparamagnetism that occurs when the particle is smaller than the magnetic

domain in a material and the fact that, in a free electron model, average energy spacing increases as the number of atoms is reduced and this enhances the catalytic properties of nanoparticles [Wigginton et al. 2007].

These factors may affect some properties of the NPs such as:

- electrical properties: which can vary between metallic to semiconducting materials. It depends on the diameter of the materials. NPs present a very high electrical conductivity which is due to minimum defects in their structure;
- thermal conductivity: NPs have a very high thermal conductivity (generally 10 times greater than the metal). This is due to the vibration of covalent bonds. The high thermal conductivity is also due to minimum defects in the structure;
- mechanical properties: these materials are very strong and withstand extreme strain. Most of the materials fracture on bending depends on the presence of more defects, but NPs possess only few defects in the structure;
- size dependence: when the dimensions of a material approaches the electron wavelength in one or more dimensions, quantum mechanical characteristics of the electrons that are not manifest in the bulk material can start to contribute to or even dominate the physical properties of the material [Davies et al. 2007]. Besides quantum size effects, the NPs behaviour is different due to surface effects which dominate as nanocrystal size decreases.

NPs are abundant in nature, as they are produced in many natural processes, including photochemical reactions, volcanic eruptions, forest fires, erosion and by plants and animals; but they can also have an anthropogenic origin. In fact humans have created nanomaterials for millennia, as they are by-products of simple combustion and food cooking and, more recently, chemical manufacturing, ore refining and smelting, combustion in vehicle and airplane engines [Rogers et al. 2005] and of coal and fuel oil for power generation [Linak et al. 2000]. There are also engineered NPs (ENPs) which have been on the market for some time and are commonly used in cosmetics, sporting goods, tires, stain-resistant clothing, sunscreens, toothpaste, food additives, etc. Moreover, in recent years, nanotechnology has been embraced by industrial sectors due to its applications in the field of electronic storage systems [Kang et al. 1996], biotechnology [Pankhurst et al. 2003], magnetic separation and preconcentration of target analytes, targeted drug delivery [Dobson 2006; Rudge et al. 2001] and vehicles

for gene and drug delivery [Appenzeller 1991]. In any case the ENPs and the new more deliberately fabricated NPs constitute a small minority of environmental NPs.

Currently, the cost of these type of nanomaterials is highlighted as a major obstacle impeding its large-scale application. However, efficient and continuous production using low-cost resources will reduce, probably, the cost of production in coming years.

Nanoparticles play a remarkable role in toxicity especially in respiratory diseases. Their size is an important factor in the occurrence of disease. Some studies on the different sizes of carbon and titanium oxide showed that reduction in nanoparticle size increases its toxicity in the lungs. Also notable is that combining some metals with each other causes complex toxicity, which does not occur with single metals. In 1975, a study showed the effect of oxidative stress caused by asbestos as the main factor in asbestosis and also in disturbing cell structure. In 1998, Zhang presented his findings on the effects of nanoparticles on respiratory toxicity and inflammation [Zhang et al. 1998]. Some of the particle features such as size, surface chemistry and oxidative stress functions play important roles in nanotoxicity. Other features such as crystallinity, coating and the longevity of particles have also been studied as important parameters [Schlesinger 1995]. Some researchers have shown that most of the nanoparticles can release active oxygen and cause oxidative stress and inflammation by the reticoendothelial system (RES). Acute toxicity resulting from nanoparticles has been investigated in rats. The results indicate that toxicity depends on the size, coating and chemical component of the nanoparticles. The effects on inflammatory and immunological systems may include oxidative stress or pre-inflammatory cytotoxin activity in the lungs, liver, heart and brain. The effects on the circulatory system can include prethrombosis effects and paradox effects on heart function. Genotoxicity, carcinogenicity and teratogenicity may occur as a result of the effects of nanoparticles. Some nanoparticles could pass the blood–brain barrier and cause brain toxicity as represented in figure 1.1 [Mühlfeld et al. 2008; Rutishauser et al. 2007; Yacobi et al. 2007].

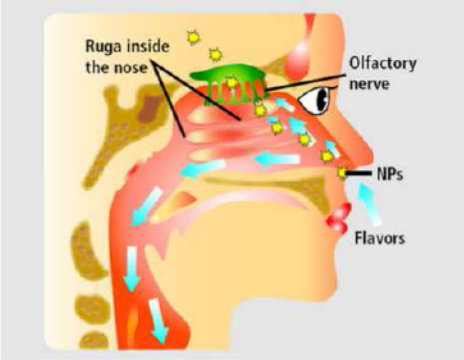

Figure 1.1: The passage of NPs from the nose to the cerebral system

By gaining control over dangerous particles, we can increase the use of nanoparticles by reducing their harmful effects and thus allowing them to be used in the curing of diseases [Holsapple et al. 2005; Hyuk et al. 2009].

1.2 GOLD NANOPARTICLES

In antiquity, colloidal gold was used to make ruby glass and for colouring ceramics and these applications are still continuing nowadays. The reputation of soluble gold until the Middle Ages was to have curative powers for various diseases. This is well detailed in what is considered the first book on colloidal gold, published by the philosopher and medical doctor Antonii in 1618. In 1676, the German chemist Kunckels published another book, whose chapter 7 concerned "Drinkable gold that contains metallic gold in a neutral, slightly pink solution that exert curative properties for several diseases". In 1857, Faraday reported the formation of deep-red solutions of colloidal gold by reduction of an aqueous solution of chloroaurate ($AuCl_4^-$) using phosphorus in CS_2 (a two-phase system) in a well-known work. He investigated the optical properties of thin films prepared from dried colloidal solutions and observed reversible colour changes of the films upon mechanical compression. In the 20th century gold colloids have been the subject of a considerably increased number of books and reviews. The subject is now so intensively investigated, due in particular to fundamental and applied aspects relevant to the quantum size effect.

There are various synthesis methods for gold nanoparticles (AuNPs). The two most important are:

- citrate reduction: it is reduction of $HAuCl_4$ in the presence of citrate (which acts as reduce and stabilize agent) in water, which leads to AuNPs of ca. 20 nm [Turkevich et al. 1951; Frens et al. 1973]. It is also possible to obtain AuNPs of

prechosen size (between 16 and 147 nm) via their controlled formation varying the ratio between the reducing/stabilizing agents and the $HAuCl_4$;

- Brust-Schiffrin method: is the synthesis of thermally stable AuNPs of reduced dispersity and controlled size (ranging in diameter between 1.5 and 5.2 nm).

About the properties of AuNPs the most relevant are:

- surface plasmon resonance band: the deep-red color of AuNPs in water and glasses reflects the surface plasmon band (SPB), a broad absorption band in the visible region around 520 nm. The SPB is due to the collective oscillations of the electron gas at the surface of nanoparticles (electrons of the conduction band for AuNPs) that is correlated with the electromagnetic field of the incoming light, i.e., the excitation of the coherent oscillation of the conduction band. The SPB band has some particular characteristics: its position around 520 nm; a sharp decrease with decreasing core size for AuNPs with 1.4-3.2 nm core diameters due to the onset of quantum size effects that become important for particles with core sizes < 3 nm in diameter and also cause a slight blue shift;
- large surface area-to-volume ratio as compared to the bulk material: it means that AuNPs can interact with column surface and analyte. It is important to notice that very little research has been devoted to understanding their impact on separation science;
- high electrocatalytic activity [Katz et al. 2004]
- reactions of thiolate-stabilized AuNPs: some of the thiolate ligands in alkanethiolate stabilized AuNPs can be substituted by reaction with other thiols at rates depending on the chain length and steric bulk of the leaving thiolate and incoming thiols and on the charge of the AuNPs;
- supramolecular chemistry: this is a strategy for surface modification of AuNPs which brings to the formation of self assembled monolayers (SAMs). The chemical species are adsorbed on the surface of AuNPs and originates a covering in which the adsorbate is distributed in a single crystalline layer. Biomolecules containing thiol (SH) or amino (NH_2) groups can be adsorbed spontaneously onto gold surfaces to generate well-organized SAMs [Niemeyer 2001];
- gold is inert and non-toxic [Connor et al. 2005]. However, the toxicity of AuNPs is still a controversial matter.

AuNPs can be applied in various field[Gunduz et al. 2011; Leopold et al. 2009]. For example their use in colorimetric assay of DNA samples is one of the most widely application. In electrochemistry AuNPs were introduced onto the electrochemical interfaces infusing new vigor into this field [Daniel et al. 2004; Kohli et al. 2004] and also AuNPs modified electrode surfaces, generating functional electrochemical sensing interfaces, have been reported in great quantity. In the field of catalysis gold is very popular for being chemically inert. It is indeed one of the most stable metals in its group and it is also resistant to oxidation. Co_3O_4, Fe_2O_3, or TiO_2 supported on AuNPs are highly active catalysts for CO and H_2 oxidation, NO reduction, water-gas shift reaction, CO_2 hydrogenation, and catalytic combustion of methanol. So nowadays catalysis with AuNPs is now an expanding area and a large number of new catalytic systems for various reactions are now being explored. About biological applications of AuNPs they started in 1971 as labels in immunostaining [Faulk et al. 1971] and recently they have also emerged as an attractive candidate for delivery of various molecules (small drug molecules or large biomolecules, like proteins, DNA or RNA) into their targets [Paciotti et al. 2004; 2006] and also their photophysical properties could trigger drug release at remote place [Skirtach et al. 2006]. Several reviews describing nanoparticle-biomacromolecule interactions have recently been published, generally focusing on biosensing [Cheng et al. 2006] and diagnostic [Rosi et al. 2005] applications and drug, gene and protein delivery [Gosch et al. 2008], tumor-detector [Qian et al. 2008] and photothermal agent or radiotherapy dose enhancer as reported in figure 1.2.

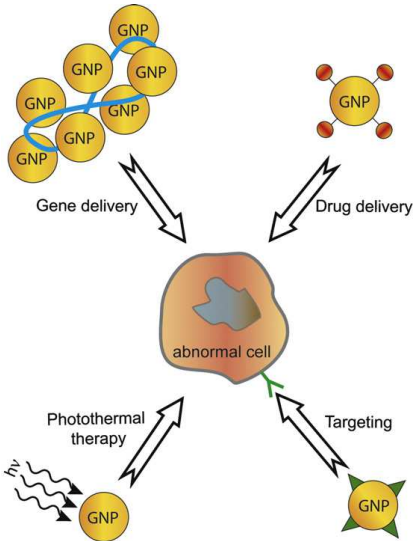

Figure 1.2: Common medical applications of gold nanoparticles

Despite these numerous uses of AuNPs in medicine it is important to underline that this material presents possible medical hazards as the high surface to volume ratio causes catalytic properties and can make particles very reactive [Slocik et al. 2013]. Furthermore, AuNPs easily pass cell membranes and can interact with intracellular metabolism [Hanley et al. 2009]. In recent studies, Conde et al. [Conde et al. 2014] assessed AuNPs aspects of genotoxicity and cell toxicity, Kim et al. [Kim et al. 2013] examined the role of surface charge and size on AuNPs in in-vivo toxicity and Balasubramanian et al. [Balasubramanian et al. 2010] reported on smaller AuNPs found in the brain so it can be speculate that the penetration of nanoparticles through the blood brain barrier (BBB). All this aspects are resumed in figure 1.3.

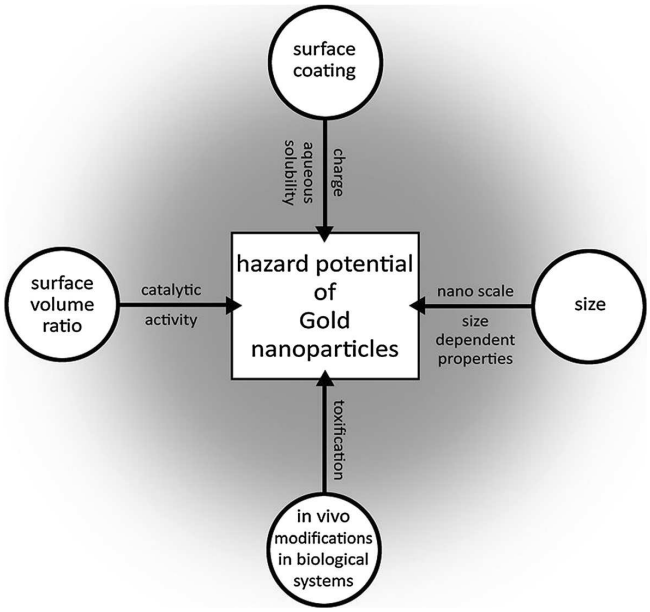

Figure 1.3: Aspects that contribute to the hazard potential of AuNPs

A screening of the literature data conducted by Khlebtsov and Dykmana in 2011 showed that in the past years, there had been a sharp explosion of research activity in the biodistribution and toxicity of AuNPs (as reported in figure 1.4).

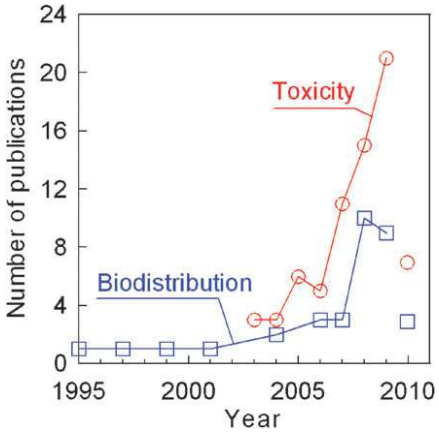

Figure 1.4: Number of publications on the biodistribution and toxicity of GNPs. Data for 2010 are limited to April

This recent published literature shows that the potential toxic impact of AuNPs may be multisided and also hard to predict.

In conclusion the ultimate goal is to characterize the biological action of AuNPs and to evaluate the risks involved by integrating all cellular level information and at the whole organism level.

1.3 HEPTAKIS(6-DEOXY-6-THIO)CYCLOMALTOHEPTAOSE CAPPED GOLD NANOPARTICLES

As reported above AuNPs can be superficially functionalized. In this work AuNPs derivatized with β-cyclodextrines functionalized -SH (β-CDSH) provided by Professor Gloria Uccello-Barretta from University of Pisa were employed.

The supramolecular aggregation of AuNPs to host compounds such as the cyclodextrins gives the opportunity to conjugate their biosensing properties to drug transport and controlled release for developing new strategies of specific drug targeting. In view of such a kind of attractive application, the affinity of sulphur to gold has been already exploited by using chemical reduction methods [Liu et al. 2000, Park et al. 2009] in order to obtain heptakis(6-deoxy-6-thio)cyclomaltoheptaose (figure 1.5) (AuNPs β-CDSH) capped gold nanoparticles, which are water soluble.

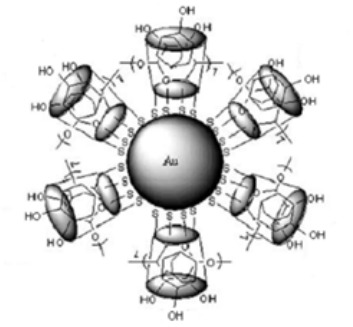

Figure 1.5: heptakis(6-deoxy-6-thio)cyclomaltoheptaose capped gold nanoparticles

The three-dimensional structure of cyclodextrines forces the hydroxyl groups on the outer edges and then, inside the cavity, only hydrogen atoms and oxygen bridges are present. This suggests, therefore, that the central cavity is hydrophobic while the outer wall is hydrophilic. This means that inside the cavity of the cyclodextrin can be hosted hydrophobic molecules remaining at the same time water soluble and thus making the hydrophobic molecule equally soluble in water forming a so-called inclusion complex which may also involve the formation or breaking of non-covalent bonds.

Cyclodextrins are used in various fields such as food, pharmaceutical, textile, cosmetic, for environmental protection and for bioconversion. In fact, the molecules that can be hosted inside their cavity are numerous and include: aliphatic linear or branched chains, aldehydes, ketones, alcohols, organic acids, fatty acids, aromatic compounds, gas and polar compounds such as halogens, oxo acids and amines. Another important use is in the separation of optical isomers in chromatographic separations and in capillary electrophoresis and it is due to the ability of cyclodextrins of specifically recognize molecules. Finally cyclodextrins can also be modified by replacing the functional groups in the primary and\or secondary ring.

1.4 NANOPORUS MATERIALS

Another type of nanoadsorbent materials employed in this work are the nanoporous materials. The presence of pores (holes) in a material can render itself all sorts of useful properties that the corresponding bulk material would not have. Generally porous materials have porosity (i.e. volume ratio of pore space to the total volume of the material) between 0.2-0.95.

If pore diameter have nanometric dimensions, we can speak of nanoporous materials (NPMs). There is a large variety of NPMs, with many different properties, structures

and applications. To classify these systems we can make a distinction about pore diameter dimension, the type and the structure of pores, the nature of material that form pore walls or their macrometric aspect. Focusing on the pore dimension (d) we can distinguish, according to IUPAC definition [Sing et al. 1985], three main groups:

- microporous materials ($d < 2$ nm): these materials have very narrow pores. They can host only small molecules, such as gases or linear molecules and generally show slow diffusion kinetics and high interaction properties. They are used as gas purification systems, filtering membranes or gas-storage materials;
- mesoporous materials ($2 < d < 50$ nm): these materials have pores with diameter enough large to host some big molecules, for example aromatic systems or large polymeric monomers. Diffusion kinetic of adsorbed molecules is often due to capillarity, with a initial interaction with pore walls followed by pore filling. These systems can be used as nano-reactors for polymerization or adsorbing systems for liquids or vapours;
- macroporous systems ($d > 50$ nm): pores of these materials could host very large molecules, such as polyaromatic systems or small biological molecules and interactions with pore walls are often secondary respect to interactions with other molecules, overall in case of very small guest molecules. These material are principally used as matrices to store functional molecules, as scaffolds to graft functional groups, such as catalytic centres and as sensing materials thanks to the quick diffusion of chemical species in the pore system.

NPMs have specifically a high surface to volume ratio, with a high surface area and large porosity and a very ordered, uniform pore structure. They have very versatile and rich surface composition, surface properties, they are often non-toxic, inert and chemically and thermally stable. These properties can influence other characteristics such as [Lu et al. 2004]:

- high adsorption capacity: the very regular structure, high surface area and pore volume properties consent to nanoporous materials to be excellent adsorptive media for gases or vapors;
- high selectivity: the narrow pore size distribution and specific interaction with pore walls make these systems ideal devices for mixture separation or ideal nanoreactors for confined chemical reactions;

- favourable adsorption kinetics: the large number of pore openings at the surface and regular pore structure consent a quick diffusion of guest species, that completely fill the material in relatively short time;
- good mechanical properties: once formed, nanoporous materials are resistant to hurts and mechanical stresses, so they could be handled without fear to break porous structure;
- stability and durability in use: nanoporous materials are stable in ambient condition and adsorption and desorption process are completely reversible. These materials can be used and re-used for long time without lost their properties.

Because of their vast ability to adsorb and interact with atoms, ions and molecules on their large interior surfaces and in the nanometer sized pore space, NPMs are of scientific and technological importance. They offer new opportunities in areas of inclusion chemistry, guest-host synthesis and molecular manipulations and reaction in the nanoscale for making different materials such as nanoparticles, nanowires and other quantum nanostructures. Besides the traditional areas of adsorption and separation processes other expanding applications for NPMs are in the field of catalysis, environmental separations (for example to remove contaminants and pollutants from waste gas and water streams), clean energy production and storage, sensors and actuator and biological application [Lu et al. 2004].

1.5 ZEOLITES

Zeolites are crystalline, microporous materials consisting of AlO_4 and SiO_4 tetrahedra connected via oxygen atom bridges. The AlO_4 tetrahedra induce the negative charge of the lattice while extraframework cation (usually proton, NH_4^+ and metal cations) compensates the negative charge, so the overall framework is kept neutral. The general formula of a zeolite is:

$$M_{x/n}[(AlO_2)_x(SiO_2)_y].mH_2O$$

Where M indicates the cations and n the valence. An example of zeolite general structure is reported in figure 1.6.

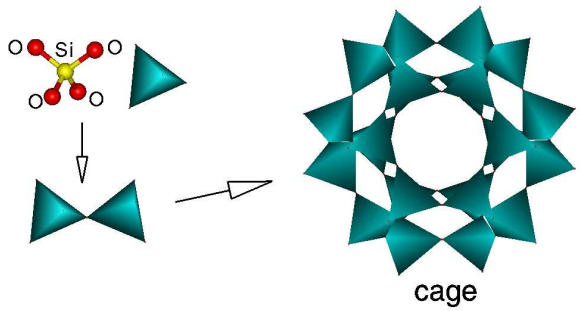

Figure 1.6: structure of a zeolite

Generally, the structure of zeolites can be one, two or three dimensional and may comprise channels (interconnected or separated) or cages. Some of the structures can have two sets of cages, the largest one named as supercage. The micropore of zeolites is typically constructed from 12-, 10- and 8- rings and pore sizes are roughly 0.7 nm (large), 0.55 nm (medium) and 0.4 nm (small) respectively [Niwa et al. 2010].

The amount of Al within the framework can vary over a wide range, with SAR (Si/Al ratio) ranging from = 1 to ∞. As the Si/Al ratio of the framework increases, the hydrothermal stability as well as the hydrophobicity of zeolites increases.

In all silica zeolites the overall charge of the surface is zero and the formula unit of the material is SiO_2. Introduction of aluminum or another element with valence less than 4 creates a deficiency of positive charge, which needs to be compensated. In this way ion-exchange sites are created on the surface of the zeolite and can be exchanged by a variety of different cations to modify the zeolite properties . Replacing an alkali cation by a proton is one of the most important modifications and it creates Brønsted acidic sites on the zeolite surface. On the other hand thermal dehydration of zeolites results in release of water and creation of Lewis acid site. The two types of acidic sites are represented in figure 1.7.

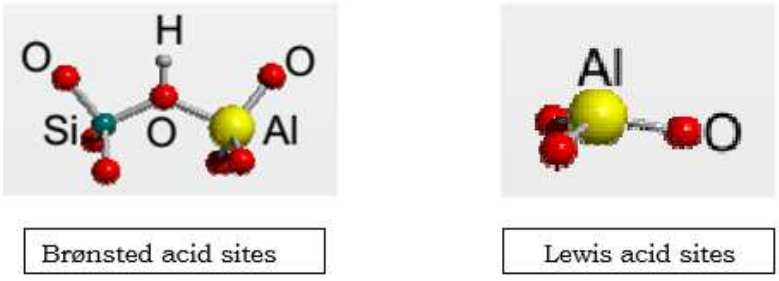

Figure 1.7: Brønsted and Lewis acidic sites

The well defined pore structures and topologies and the presence of uniform cavities and channels, give at these materials the properties of high superficial areas (about 1000 m^2/g) and internal volumes. In general the zeolites channels are hydrophilic and in normal conditions are occupied from water or from other molecules, especially polar, which critical diameter is not greater than access windows to the channels. It seems clear the function of adsorbents exhibited by zeolites and the possibility of their use in processes of separation of gas and liquid mixtures on the basis of the critical diameter of the molecules that may be smaller or equal to that of the access windows to channels (action of molecular sieving). Moreover the presence and the particular distribution of the charges and ions create a specific electric field within the framework, which permits the control of hydrophilicity and the introduction of ion-exchange properties.

Since Cronstedt's time, about 50 natural zeolite species have been discovered, but their potential for adsorption/separation science did not come to fruition until the twentieth century. Based on the pioneering work of Barrer, synthetic zeolites became available by the early 1950s [Barrer 1978; 1982]. Today, about 100 structurally different synthetic zeolites are known and there are both synthetic analogues of natural zeolites and synthetic zeolites with no natural counterpart. In contrast to natural zeolites, synthetic zeolites may contain inorganic and organic cations, such as quaternary ammonium ions. Meanwhile, in total about 80 different molecular sieve structures are known, which are classified by the Structure Commission of the International Zeolite Association [Meier 1992].

Natural zeolites are traditionally used in construction as dimension stone, cement and concrete lightweight aggregate. Recently they have also found application as cation exchangers in water and wastewater treatment [Ames 1967; Mercer et al. 1970]. Thanks to their environmental friendly composition, some natural zeolites can be also employed in agriculture for animal nutrition and health [Onagi 1966; Kondo et al. 1968], in agronomy and horticulture [Minato 1968], in aquaculture and in animal-waste treatment.

On the other hand synthetic zeolites have found widespread applications as dehydrating agents, selective adsorbents, ion exchangers and, most importantly, catalysts of both high activity and selectivity for a huge number of different reactions [Niwa et al. 2010] in particular hydrocarbon reactions, such as fluid catalytic cracking (FCC) process [Li et al. 2007], hydrocracking, alkylation, and isomerization. In these reactions, the reactivity and selectivity of the zeolites are determined by the charge imbalance between the

silicon and aluminum atoms. Among various other applications, zeolites are used for the drying of refrigerants, removal of atmospheric pollutants such as SO_2, cryopumping, separation of N_2 and O_2, separation of paraffin hydrocarbons, recovery of radioactive ions from waste solutions [Rhodes 1965], catalysis of hydrocarbon reactions and curing of plastics and rubber.

1.6 ZSM-5

ZSM-5 (ZSM = Zeolite Socony Mobil) zeolite belongs to the MFI structure. It is a medium pore size material with straight and sinusoidal channels. The chemical formula of this zeolite is:

$$Na_nAl_nSi_{96-n}O_{192}\cdot 16H_2O \text{ (where } 0<n<27)$$

ZSM-5 is composed of several pentasil units (consists of eight five-membered rings represented in figure 1.8) linked together by oxygen bridges to form pentasil chains.

Figure 1.8: pentasil unit

In these rings, the vertices are Al or Si and an O is assumed to be bonded between the vertices. The pentasil chains are interconnected by oxygen bridges to form corrugated sheets with 10-ring holes. Like the pentasil units, each 10-ring hole has Al or Si as vertices with an O assumed to be bonded between each vertex. Each corrugated sheet is connected by oxygen bridges to form a structure with straight 10-ring channels running parallel to the corrugations and sinusoidal 10-ring channels perpendicular to the sheets. This structure is represented in figure 1.9.

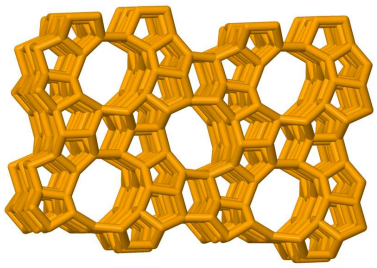

Figure 1.9: structure of ZSM-5

The straight channel has a diameter of 5.3-5.6 Å, whereas the sinusoidal channels have diameters of 5.1-5.5 Å (figure 1.10).

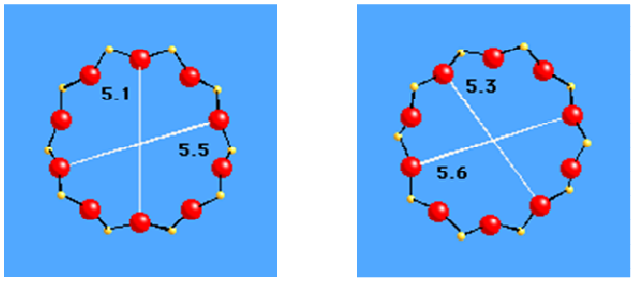

Figure 1.10: dimensions of sinusoidal and straight channels of ZSM-5

The system structure of the pores of ZSM-5 with circular channels in a zigzag linear channels that intersect with elliptical cross-section is shown in figure 1.11.

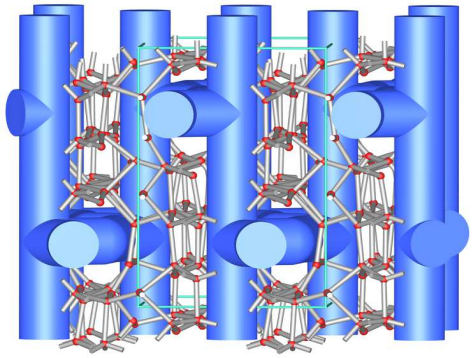

Figure 1.11: system of channels of ZSM-5

FCC process uses a ZSM-5 catalyst due to its high surface area, acidic nature of its pores and well-defined porous structure [Coronas 2010]. Catalytic dehydration of ethanol to ethylene, disproportionate of ethanol to propylene and ethanol to aromatics are some of the examples, where the textural properties of ZSM-5 zeolite, especially its

Si/Al played a vital role in determining the nature of the product [Anastas et al. 2003; Coronas et al. 2008]. Another application of ZSM-5 is in the methylation of benzene that is an alternative low-cost route to produce xylenes, but selectivity to xylene remains low over conventional zeolitic catalysts. This catalyst suffers from low selectivity also towards C5-C10 alkanes, high yields of aromatics and carbon deposition thus requiring frequent regeneration.

1.7 Y (FAUJASITE)

The chemical formula of Y zeolite is:

$$(Ca,Na_2,Mg)_{3,5}\,[Al_7Si_{17}O_{48}]\cdot 32H_2O$$

It exhibits the FAU (faujasite) framework structure consisting of a double 6 ring, cages adjacent to hexagonal prism and supercages placed among the cages. It can be thought of as arising from merging multiple sodalite units (represented in figure 1.12) connected via the hexagonal faces.

Figure 1.12: sodalite unit

The sodalite unit is a structural unit typical of various zeolites whose vertices are the atoms of Si and Al which occupy the centers of the tetrahedra SiO_4 and AlO_4. This type of structure (figure 1.13) makes the presence in the system of a very large cavity, with diameter of 1.20 nm, whose openings (diameter 7.4 Å reported in figure 1.14) are formed by a ring of 12 atoms.

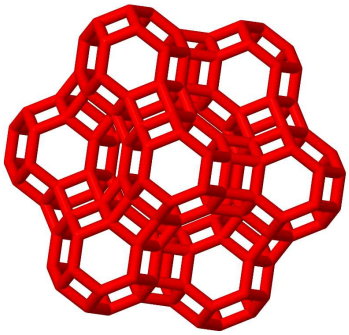

Figure 1.13: structure of zeolite Y

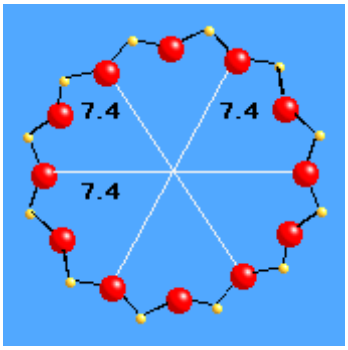

Figure 1.14: dimensions of channel of zeolite Y

Due to the fact that this group of zeolites has the biggest channels and supercages, which permit access to quite large molecules, Y zeolite was for the first time used as catalysts in petrochemical industry and after in additional processes in the fields of petroleum refining and basic petrochemistry. The most important of these processes are hydrocracking of heavy petroleum distillates [Scherzer et al. 1996], octane number enhancement of light gasoline by isomerization [Sic et al. 1998], the synthesis of ethylbenzene (the precursor of styrene and polystyrene) from benzene and ethene after the Mobil-Badger process [Dwyer et al. 1981], the disproportionation of toluene into benzene and xylenes [Chen et al. 1989] and the isomerization of xylenes.

1.8 CHARACTERIZATION OF NANOADSROBENT MATERIALS

The adsorption phenomenon depends on the physico-chemical characteristics of the adsorbent material and of the adsorbate molecule. But, in order to study this process is important to make a physical characterization of the adsorbent material, it means to characterize the superficial area of the material. In this way we need informations about the dimensions (in particular the diameter and the polydispersity) regarding NPs and about the porosity for the NPMs.

The characterization of NPs started in the middle 1980s when the scanning tunnelling microscope (STM) and, shortly after, the atomic force microscope (AFM) were invented. Nowadays there are many methods available to image NPs and to characterise their physical and chemical properties. This methods, together with the properties information which can be obtained, are reported in figure 1.15.

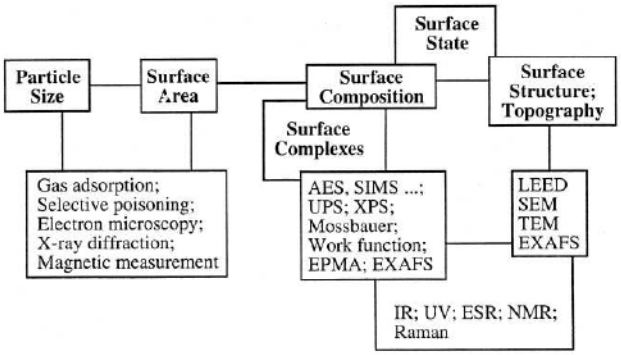

Figure 1.15: common methods for the characterization of NPs [Aiken et al. 1999]

Microscopic techniques are the most employed characterization tools as they create surface

images using a physical probe that scans the specimen. Some of the used microscopic techniques are:

- Atomic Force Microscopy (AFM): which provides qualitative and quantitative information on many physical properties including size, morphology, surface texture and roughness. This technique overestimates the dimensions of the NPs when the geometry of the tip is larger than the NPs themselves [Maurice 1996];
- Scanning Tunneling Microscopy (STM): allows the chemical identification of the atoms and molecules that make up the NPs. STM can operate in a ultrahigh vacuum allowing characterization in liquid and gaseous suspensions [Friedbacher et al. 1999];
- Scanning and Transmission Electron Microscopy (SEM and TEM): provide information about the sample's surface, crystal structure, elemental composition, size, shape and other properties such as electrical conductivity [Goldstein et al. 1992].

However, most of these imaging techniques can lead to imaging artefacts, due to previous treatment of the sample (coating, drying, staining, freezing and embedding)

before measuring and also due to the vacuum conditions in the sample chamber [Tiede et al. 1999]. Other techniques belonging to this class are the Environmental Scanning Electron Microscopy (ESEM) and the WetSEM technology.

Light scattering techniques, such as Dynamic Light Scattering (DLS), are commonly used to determine particle size. Furthermore it is a nonintrusive, sensitive and powerful analytical tool that is commonly employed for the characterization of macromolecules and colloids in solution [Zanetti-Ramos et al. 2009; Chu 1991].

X-ray-based methods such as X-ray Absorption (XAS), X-ray Fluorescence (XRF), X-ray Photoelectron Spectroscopy (XPS), and X-ray Diffraction (XRD) are in general highly surface-specific and can provide information on surface properties and coatings, crystallographic structure or elemental composition. X-ray spectroscopy is often combined with SEM and TEM for the assessment of the elemental composition and quantitative analysis [Mavrocordatos et al. 2004; Nurmi et al. 2005].

Spectroscopic techniques, such as UV-visible, are commonly used in NPs with surface plasmon resonance by collective oscillations of their conduction band electrons in response to electromagnetic waves. This allows obtaining information on NPs size, aggregation, structure, stabilization and surface chemistry [Daniel et al. 2004]. Metal NPs display specific absorbance bands in their spectra when the incident light enters into resonance with the conduction band electrons on their surface.

Field-flow fractionation (FFF) is an emergent analytical technique for size separation of natural and inorganic NPs. Recent applications of FFF include natural and artificial nanoparticles in environmental samples [Stolpe et al. 2013; Koopmans et al. 2015], protein aggregates [Tanase et al. 2015], drug delivery nanocarriers [Zattoni et al. 2014], subcellular organelles [Yang et al. 2015], food applications [Nilsson 2013], quantum dots [Moquin et al. 2015], red blood cells [Moore et al. 2014], and many more. FFF has been applied to separate solutes as small as 1 nm [Von der Kammer et al. 2011; Ratanathanawongs Williams et al. 2011] and as large as 0.1 mm [Giddings et al. 1978; 1993]. The flexibility of FFF results from the large number of potential transverse external fields that can be used: gravitational [Lee et al. 2011], centrifugal sedimentation [Mélin et al. 2012], electrical [Gigault et al. 2011], magnetic [Williams et al. 2010], dielectrophoretic [Shim et al. 2011], acoustic [Budwig et al. 2010], photophoretic [Kononenko et al. 1997], cross-flow (both symmetrical [Cumberland et al. 2009] and asymmetrical [Yohannes et al. 2011]) and thermal [Runyon et al. 2011] fields have all been utilized. In particular in ThFFF retention occurs as a result of an

externally applied thermal gradient, i.e., by thermodiffusion and today there is significant interest in the potential of separation by thermophoresis and as witnessed by the recent increase in the number of articles dealing with the thermodiffusion studies of nanoparticle systems. In these articles, different particles have been studied: biological macromolecules [Braun et al. 2004], ferrocolloids [Blumsa et al. 2002], sodium dodecyl sulfate micelles [Piazza et al. 2002], latex spheres [Putnam et al. 2005] and silica particles [Shiundu et al. 2003].

Capillary electrophoresis (CE) measures the electrophoretic mobility of NPs based on their charge and size distribution in the sample, when an external electric field is applied. Ions move towards the electrode of opposite charge. The separation would be achieved by the mobility of the species depending not only on the solvent medium, but also on the charges, sizes and shapes of the NPs. The ability of capillary electrophoresis as a separating tool for mixed NPs according to their sizes as well as the nature of materials has been demonstrated. However, as the amount of the sample used is rather low a high concentration of NPs is needed [Hwang et al. 2003].

Some of the techniques mentioned before such as electron microscopy and elastic X-ray and neutron scattering are used also for the characterization of various types of porous materials, providing quantitative parameters such as the pore size, surface area and pore volume in addition to the advantage of deliver an optical image of the samples.

In the early 1900s, Von Laue, Bragg and others laid the groundwork for X-ray crystallography, which has become a powerful method of visualizing complex inorganic and organic crystalline materials [Bragg et al. 1913; Ewald 1921; Von Laue 1913]. In spite of the variety of different diffraction techniques currently available, they are all based on the same physical phenomenon, namely the scattering of X-rays and neutrons by the atoms through their electrons or nuclei, respectively. For almost all types of nanoporous materials, no single crystal diffraction datum is obtainable, not even for the crystalline zeolites. Therefore, most of the most prominent types of nanoporous materials (such as zeolites) are studied in diffraction experiments as polycrystalline powders.

Other characterization techniques belong to the family of thermogravimetric analysis which record the changes in percentage of weight loss suffered by a material subjected to increasing heating. The Differential Thermogravimetric analysis (DTG), which corresponds to the first derivate of the thermogravimetric (TG) curve, allows to know the rate of change in weight of the sample as a function of temperature. The Differential

Thermal Analysis (DTA) measures, for all the duration of the heat treatment, the temperature difference (ΔT) between the sample and an inert material (corundum) subjected simultaneously to the same thermal regime. Since the temperature of the inert is constantly in equilibrium with that of the thermoanalyzer, the temperature difference is a function of the absorption or release of heat from the sample examined, in correspondence of certain reactions. The absorption of heat is displayed graphically on the DTA curve as a thermal minimum and corresponds to an endothermic reaction (loss of substance, change of state, structural collapse). The transfer of heat is instead recorded as a thermal maximum, determined by an exothermic reaction (recrystallization, oxidation).

Finally, to characterize NPMs, the study of adsorption represents a widely used technique and provides porosity parameters such as pore size distributions, surface areas and pore volumes. The word "adsorption" was coined in 1881 by German physicist Heinrich Kayser (1853-1940) to indicate the adhesion of atoms, ions or molecules from a gas, liquid or dissolved solid to a surface creating a film of the adsorbate on the surface of the adsorbent. The process of adsorption arises due to presence of unbalanced or residual surface forces at the surface of liquid or solid phase. In fact in a bulk material, all the bonding requirements (be they ionic, covalent or metallic) of the constituent atoms of the material are filled by other atoms in the material. However, atoms on the surface of the adsorbent are not wholly surrounded by other adsorbent atoms and therefore can attract adsorbate molecules. These unbalanced residual forces have tendency to attract and retain the molecular species which it comes in contact with the surface so adsorption is essentially a surface phenomenon. Also IUPAC defined adsorption as the "Increase in the concentration of a substance at the interface of a condensed and a liquid or gaseous layer owing to the operation of surface forces".

On the basis of the type of forces of attraction existing between adsorbate and adsorbent, adsorption can be classified into two types: physical adsorption or chemical adsorption. The first type occurs when the force of attraction existing between adsorbate and adsorbent are weak Van der Waals forces and takes place with formation of multilayer of adsorbate on adsorbent. It has low enthalpy of adsorption (i.e. ΔH adsorption is 20-40 KJ/mol) and it takes place at low temperature below boiling point of adsorbate. This type of adsorption can be easily reversed by heating or by decreasing the pressure. On the other hand when the force of attraction existing between adsorbate

and adsorbent are chemical forces, chemical bonds or electrostatic attraction [Ferrari et al. 2010], the process is called chemical adsorption or chemisorption. It takes place with formation of unilayer of adsorbate on adsorbent. It has high enthalpy of adsorption (i.e. ΔH adsorption is 200-400 KJ/mol) and it can takes place at all temperature. In chemisorption the force of attraction is very strong, therefore adsorption cannot be easily reversed.

A comparison between the two types of adsorption is reported in the following table 1.2:

Physisorption	**Chemisorption**
Low heat of adsorption usually in the range of 20-40 kJ mol^{-1}	High heat of adsorption in the range of 40-400 kJ mol^{-1}
Force of attraction are Van der Waal's forces	Forces of attraction are chemical bond forces
It usually takes place at low temperature and decreases with increasing temperature	It takes place at high temperature
It is reversible	It is irreversible
It is related to the ease of liquefaction of the gas	The extent of adsorption is generally not related to liquefaction of the gas
It is not very specific	It is highly specific
It forms multi-molecular layers	It forms monomolecular layers
It does not require any activation energy	It requires activation energy

Table 1.2: comparison between physi- and chemisorption

Adsorption process is usually studied through graphs known as adsorption isotherms which plot the amount of adsorbate (x) on the adsorbent surface (m) as a function if its pressure (P) or concentration (C) at constant temperature. A generic example of

adsorption isotherm is reported in figure 1.16. The quantity adsorbed is nearly always normalized by the mass of the adsorbent to allow comparison of different materials.

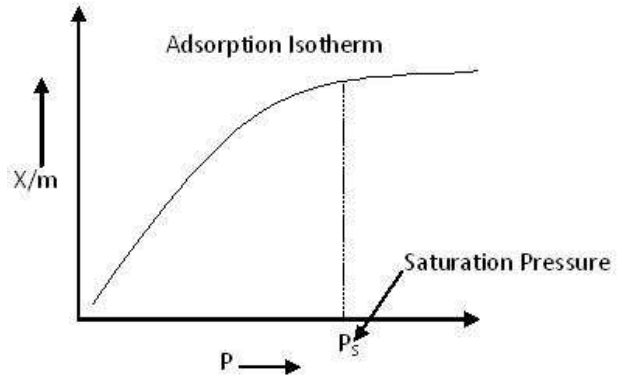

Figure 1.16: example of an adsorption isotherm

From the above graph we can predict that after saturation pressure Ps, adsorption does not occur anymore, that is there are limited numbers of vacancies on the surface of the adsorbent. At high pressure a stage is reached when all the sites are occupied and further increase in pressure does not cause any difference in adsorption process so, in this condition, adsorption is independent of pressure.

The shape of an isotherm allows to distinguish between representative types of nanoporous materials, based on the classifications by de Boer [de Boer 1958] or IUPAC [Sing et al. 1985] (the last classification is reported in figure 1.17).

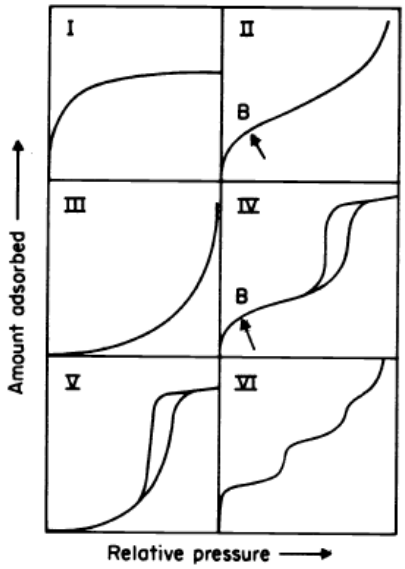

Figure 1.17: IUPAC classification of isotherm type of 1985 [Sing et al. 1985]

The principal characteristics of the isotherm types are given below:

- The reversible Type I isotherm is concave to the relative pressure (P/P°) axis and the amount adsorbed approaches a limiting value as P/P° → 1. Type I isotherms are given by microporous solids having relatively small external surfaces (e.g. activated carbons, molecular sieve zeolites and certain porous oxides), the limiting uptake is being governed by the accessible micropore volume rather than by the internal surface area. Examples of Type I adsorption are adsorption of nitrogen or hydrogen on charcoal at temperature near to -1800° C.
- The reversible Type II isotherm is the normal form of isotherm obtained with a non-porous or macroporous adsorbent. The Type II isotherm represents unrestricted monolayer-multilayer adsorption. Point B, the beginning of the almost linear middle section of the isotherm, is often taken to indicate the stage at which monolayer coverage is complete and multilayer adsorption about to begin. Examples of Type II adsorption are nitrogen adsorbed at -1950° C on iron catalyst and nitrogen adsorbed at -1950° C on silica gel.
- The reversible Type III isotherm is convex to the P/P° axis over its entire range and therefore does not exhibit a Point B. Isotherms of this type are not common, but there are a number of systems (e.g. nitrogen on polyethylene) which give isotherms with gradual curvature and an indistinct Point B. In such cases, the adsorbate-adsorbate interactions play an important role. Examples of Type III adsorption isotherm are bromine at 790° C on silica gel or iodine at 790° C on silica gel.
- Characteristic features of the Type IV isotherm are a capillary condensation taking place in mesopores and the limiting uptake over a range of high P/P°. The initial part of the Type IV isotherm is attributed to monolayer-multilayer adsorption since it follows the same path as the corresponding part of a Type II isotherm obtained with the given adsorptive on the same surface area of the adsorbent in a non-porous form. Type IV isotherms are given by many mesoporous industrial adsorbents. Examples of Type IV adsorption isotherm are the adsorption of benzene on iron oxide at 500° C and adsorption of benzene on silica gel at 500° C.

- The Type V isotherm is uncommon; it is related to the Type III isotherm in that the adsorbent-adsorbate interaction is weak, but is obtained with certain porous adsorbents. Example of Type V adsorption isotherm is adsorption of water at 1000° C on charcoal.
- The Type VI isotherm, in which the sharpness of the steps depends on the system and the temperature, represents stepwise multilayer adsorption on a uniform non-porous surface. The step-height now represents the monolayer capacity for each adsorbed layer and, in the simplest case, remains nearly constant for two or three adsorbed layers. Examples of Type VI isotherms are those obtained with argon or krypton on graphitised carbon blacks at liquid nitrogen temperature.

1.9 SELECTED TYPES OF ADSORPTION ISOTHERM

In this work we determined adsorption isotherms in a wide range of analyte concentration and numerous are the models which can be used. In the following paragraphs are reported the selected types with the characteristics.

1.9.1 LINEAR HENRY ISOTHERM

This is the simplest adsorption isotherm in which the amount of the adsorbate on the surface is represented to be proportional to the concentration of the interested compound in solution [Yıldırım Erbil 2006]:

$$q_e = K_H C_e \tag{1.1}$$

where: q_e is the adsorbed amount at equilibrium, C_e is the concentration at equilibrium and K_H is the Henry's adsorption constant.

The linearity of the adsorption isotherm is, however, limited to a certain low concentration range that is in conditions of infinite dilution in fact this isotherm can be used to describe the initial part of many practical isotherms. It is typically taken as valid for low surface coverages and the adsorption energy is independent of the coverage.

1.9.2 LANGMUIR ISOTHERM

In 1916 Langmuir published a new model isotherm for gases adsorbed to solids [Langmuir 1916]. It is a semi-empirical isotherm derived from a proposed kinetic mechanism. This isotherm was based on different assumptions:

- a dynamic equilibrium exists between adsorbed gaseous molecules and the free gaseous molecules;
- the surface of the adsorbent is uniform, that is, all the adsorption sites are equivalent;
- adsorbed molecules do not interact [Ruthven 1984];
- all adsorption occurs through the same mechanism;
- at the maximum adsorption, only a monolayer is formed: molecules of adsorbate do not deposit on other, already adsorbed, molecules of adsorbate, only on the free surface of the adsorbent.

This model can be extended to a liquid-solid system. The equation which explained the relationship for this system is:

$$q_e = \frac{q_s K C_e}{1 + K C_e} \tag{1.2}$$

Where, q_e is the amount of solute on one unit of adsorbent at equilibrium, C_e is the concentration at equilibrium, K is the equilibrium constant related to the energy of adsorption and q_s is the saturation capacity.

In the case of low concentrations, KC_e is so small, than the factor $(1+KC_e)$ in denominator can almost be ignored. So Langmuir equation reduces to:

$$q_e = q_s K C_e \tag{1.3}$$

$$\theta = \frac{q_e}{q_s} = K C_e \tag{1.4}$$

where θ is called the fractional surface coverage. The slope of the isotherm at infinite dilution defines the Henry's constant of the adsorption $(K_H = q_s K)$.

1.9.3 BI-LANGMUIR ISOTHERM

This model is the simplest one for a non-homogeneous surface [Graham 1953] which is assumed to be paved with two different types of chemical domains characterized by different interaction energies which behave independently. This particular model considers two different types of sites, on which molecules can adsorb independently by following the Langmuir isotherm [Guiochon 1994]. Therefore, the isotherm model is written as a sum of two Langmuir terms:

$$q_e = \frac{q_{s,1} K_1 C_e}{1 + K_1 C_e} + \frac{q_{s,2} K_2 C_e}{1 + K_2 C_e} \tag{1.5}$$

where q_e, K, q_s and C_e have the same meaning as in the previous equation and the subscripts refer to sites 1 and 2, respectively. In this model there are two saturation capacities ($q_{s,1}$ and $q_{s,2}$) corresponding to each one of the two types of sites. The total saturation capacity of the adsorbent is:

$$q_s = q_{s,1} + q_{s.2} \tag{1.6}$$

Also in this case the two equilibrium constants K_1 and K_2 are associated with the adsorption energies.

1.9.4 COMPETITIVE LANGMUIR MODEL

The Langmuir equilibrium isotherm model can be extended to multicomponent system [Schwab 1928, Markham 1931]. However, when different components are simultaneously present in the solution, this compound can interfere. The amount of each of them that is adsorbed at equilibrium is smaller than if these compounds were alone.
Guiochon in 2006 extended the Langmuir isotherm to a multicomponent system. For example for a binary mixture:

$$q_{e,1} = \frac{q_{s,1} K_1 C_{e,1}}{1 + K_1 C_{e,1} + K_2 C_{e,2}} \tag{1.7}$$

$$q_{e,2} = \frac{q_{s,2} K_2 C_{e,2}}{1 + K_1 C_{e,1} + K_2 C_{e,2}} \tag{1.8}$$

where q_e, K, q_s and C_e have the same meaning as in the previous equation and the subscripts refer to components 1 and 2, respectively.

Similar to the Langmuir model also this one assumes a homogeneous surface with respect to the energy of adsorption, no interaction between adsorbed species and all sites are equally available to all adsorbed species.

1.9.5 COMPETITIVE BI-LANGMUIR MODEL

This model is an extension of the competitive Langmuir model considering that two kinds of sites coexist on the surface of the adsorbent. When both the sites are available for the adsorption of the two compounds (i = 1,2), the isotherm can be described by the following relationships:

$$q_{e,i} = \frac{q_{s,a,i} K_{a,i} C_{e,i}}{1 + K_{a,1} C_{e,1} + K_{a,2} C_{e,2}} + \frac{q_{s,b,i} K_{b,i} C_{e,i}}{1 + K_{b,1} C_{e,1} + K_{b,2} C_{e,2}}, (i = 1,2) \qquad (1.9)$$

where q_e, K, q_s and C_e have the same meaning as in the previous equation and the subscripts refer to sites a and b, respectively.

This model can be applied to mixtures of components having similar saturation capacities and it assumes that all adsorption sites are equally available to all adsorbed species.

To account the difference in sites availabilities for the components of the mixture this model has been improved by Jain and Snoyink in 1973. In this latter model two types of regions or sites are assumed: one type of regions or sites can be occupied by both components on which the two species have the same saturated adsorption amount (competitive sites); whereas the other type can be occupied only by the component with the larger saturated adsorption capacity (non-competitive sites). Further, it was assumed that the number of sites for which there was no competition was equal to the quantity:

$$q_{s,1} - q_{s,2} \text{ where } q_{s,1} > q_{s,2}$$

On this bases, the following equations were proposed:

$$q_{e,1} = \frac{(q_{s,1} - q_{s,2})K_1 C_{e,1}}{1 + K_1 C_{e,1}} + \frac{q_{s,2} K_1 C_{e,1}}{1 + K_1 C_{e,1} + K_2 C_{e,2}} \tag{1.10}$$

$$q_{e,2} = \frac{q_{s,2} K_2 C_{e,2}}{1 + K_1 C_{e,1} + K_2 C_{e,2}} \tag{1.11}$$

where q_e, K, q_s and C_e have the same meaning as in the previous equation and the subscripts refer to sites 1 and 2, respectively. The first term on the right side of equation 1.10 is the Langmuir expression for the number of molecules of species 1 that adsorbs without competition on the surface area proportional to $q_{s,1} - q_{s,2}$. The second term, instead, represents the number of species 1 adsorbed on the surface area proportional to $q_{s,2}$ under competition with species 2 and is based on the Langmuir model for competitive adsorption. On the other side the number of molecules of species 2 adsorbed on surface area proportional to $q_{s,2}$ under competition with species 1 can be calculated from the equation 1.11. When $q_{s,1} = q_{s,2}$, the proposed model is the same as the Langmuir one for competitive adsorption.

This model is expected to be valid only when a fraction of the adsorption occurs without competition, such as when the larger of the two adsorbates is unable to enter the smaller pores of a porous adsorbent or when certain accessible sites on the adsorbent are not available to one of the solutes because of the chemical characteristics of the sites and the solute.

1.9.6 JOVANOVIC-FREUNDLICH ISOTHERM

The Jovanovic model keeps the same assumptions contained in the Langmuir model, only considering, in addiction, the possibility of some mechanical contacts between the adsorbing and desorbing molecules [Jovanovic 1969].

This semiempirical model for single component adsorption was recently derived from a differential relationship relating the surface coverage and the bulk concentration of the adsorbate [Quiñones et al. 1996]. The model reduces to the Jovanovic model when the surface is homogeneous and it reduces to the monolayer isotherm at high concentrations but it does not obey the Henry law at low concentrations. For the single component isotherm the relation is:

$$\theta_t = 1 - e^{-(aC)^{\nu}} \tag{1.12}$$

where θ and C have the same meanings as the previous equation, ν is the heterogeneity parameter (with $0 < \nu \leq 1$) and a is a constant, function of the sole temperature, which characterizes the magnitude of the adsorbate-adsorbent interaction energy [Quiñones et al. 1996].

An extension of this model to competitive binary adsorption can be derived following a procedure reported by Jaroniec et al. [Jaroniec et al. 1998]. The method is rigorous if there is a linear correlation between the adsorption energies of the components of the mixture. In this case, the heterogeneity parameter for the mixture ($\bar{\nu}$) should be the same for both compounds. The extension of this model is derived in terms of a localized adsorption model which neglects lateral interactions in the surface phase and assumes the monolayer character of this phase and is represented by the following set of equations:

$$\theta_{t,1} = \frac{a_1 C_1}{a_1 C_1 + a_2 C_2}\left[1 - e^{-(a_1 C_1 + a_2 C_2)\bar{\nu}}\right] \tag{1.13}$$

$$\theta_{t,2} = \frac{a_2 C_2}{a_1 C_1 + a_2 C_2}\left[1 - e^{-(a_1 C_1 + a_2 C_2)\bar{\nu}}\right] \tag{1.14}$$

where θ, C, a have the same meanings as the previous equations and subscripts 1 and 2 stand for the first and second component, respectively.

This model is purely predictive: it means that it is a competitive isotherm model which uses only the coefficients of the single-component isotherms. It allows prediction of competitive isotherm behavior knowing only the single-component adsorption behavior. It is rigorous, as stated earlier, for equal values of the heterogeneity parameter of both components (it means homogeneous surface). It is clear that, in practice, this condition can be satisfied but for a few systems only.

CHAPTER 2: ADSORPTION OF BIOLOGICAL MOLECULES ON AuNPs

In this chapter we investigated the possibility to employ gold nanoparticles as adsorbent materials for pre-concentration and clean-up methods for biological samples in order to optimize biological and biochemical analysis.

The concept of nanoparticle-assisted sample separation and preconcentration plays important roles in many analytical methods [Howard et al. 1993]. The potential capability of NPs has been extensively studied in separation science for several years. Nanoparticles (NPs) have been used to extract and enrich target analytes from different complex matrices thank to their unique property of high surface area to volume ratios which permits higher adsorption capacity for biomolecules to the surface of this type of nanomaterials [Sapsford et al. 2013; Coto-Garcia et al. 2011]. For example there are reports in the literature on the preconcentration and separation of trace elements in biological samples by means of nanometer TiO_2 material and Khajeh et al. in works published from 2009 to 2011 used magnetic nanoparticles for copper, lead, manganese and zinc uptake from water and biological samples.

Among all the different types of NPs we selected AuNPs since the strong affinity of these NPs to thiol-containing biomolecules via a gold-thiolate bond [Li et al. 2002] have been demonstrated. AuNPs have been shown to be efficient to extract aminothiols in plasma [Chang et al. 2010] or to adsorb thiol modified nucleosides [Mourougou-Candoni et al. 2003].

So, starting from this evidence, we studied the adsorption process of the selected target biomolecules which containing a sulphur ether moiety. Although the adsorption of multidentate thioether ligands [Peterle et al. 2008] and also of thiacrown ether macrocycles [Nion et al. 2007] on AuNPs have been reported, the innovation in this work consist in explore the less employed thioether-based coordination chemistry (compared to the thiol- or disulfide-based chemistry which are often exploited in approaches toward nanoparticle assembly) which has not been employed in enrichment phase.

In fact the selected biological molecules are two different synthetic conjugated deoxyadenosines and the two oligonucleotides containing them [Capobianco et al. 2013] which may present antibiotic, antiviral and/or antitumoral activity.

Many data which will be next reported are part of my work of thesis and have been recently published: [Bosi V., Sarti E., Navacchia M. L., Perrone D., Pasti L., Cavazzini

A., Capobianco M. L., Analytical and Bioanalytical Chemistry 407 (18) (2015) 5405-5415] (see Appendix I).

2.1 TAGET MOLECULES

2.1.1 LABELLED NUCLEOSIDES

Nucleosides are glycosylamines that consist of a nucleobase (also named nitrogenous base) and a five-carbon sugar (ribose or deoxyribose and in the last case is named deoxynucleoside) via a β-glycosidic linkage; whereas a nucleotide is composed of a nucleobase, a five-carbon sugar and one or more phosphate groups. A schematic representation of the formation of nucleosides and nucleotides with the possible nitrogenous bases is represented in figure 2.1.

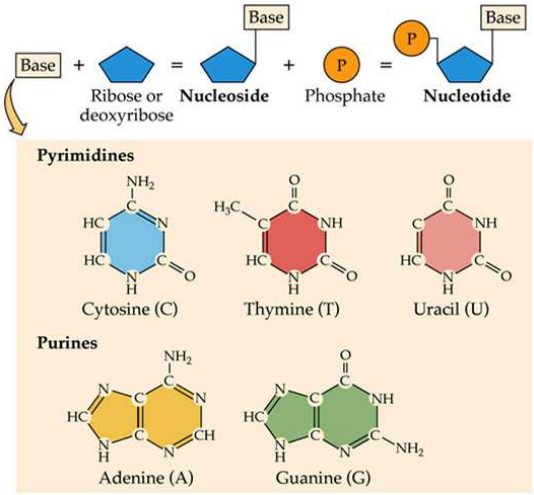

Figure 2.1: structure of nucleosides and nucleotides

Nucleosides are both precursors and break-down products of DNA and RNA and they are intrinsically involved with cell metabolism [Geldart et al. 1997]. Their mutations have been linked to cancer and genetic diseases [Lecoq et al. 1993]. For this reason their triphosphate metabolites must frequently be monitored [Geldart et al. 1998]. Nevertheless some nucleoside analogues are effective drugs in treating AIDS, cancer and other diseases.

The labelled nucleosides used in this thesis were provided by Dott. Massimo L. Capobianco of ISOF-CNR of Bologna and were synthesized in collaboration with Dott. Daniela Perrone of University of Ferrara. The structures are shown in Figure 2.2.

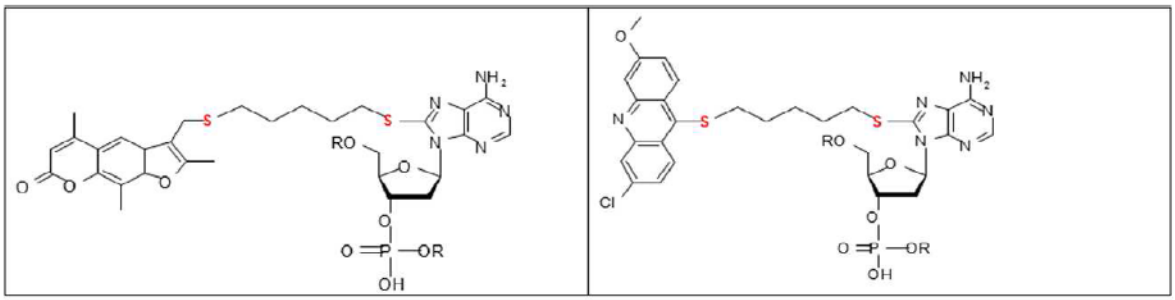

Pso-dA: R = H **Acr-dA**: R = H

Figure 2.2: structure of the analyzed labelled nucleosides

Capobianco [Capobianco et al. 2013] synthetized new nucleic lipids (hybrid molecules formed from a nucleoside and a lipid part which can be formed by one or more alkyl or alkene chains, from a carbocyclic hydrocarbon, a vitamin or a bile acid) highly modified. These compounds are of particular interest for their antibiotic, antiviral and/or antitumor activities explicate by some nucleoside analogues.

In particular, the nucleoside analogues investigated are derived from adenosine substituted in position 8 with groups having a triple bond terminal. The structure of these compounds gives easy access to a further conjugation with molecules containing an azido group via "click chemistry" reaction. The functionalization of the nucleobase is usually performed linking the chosen moiety to the C-6 position of pyrimidines and on the C-8 position of purine bases. In fact this is the preparation of thioderivatives bound to the C-8 position of the deoxyadenosine containing different functional molecules:

- Psoralen: structurally related to coumarin by the addition of a fused furan ring occurs naturally in the seeds of Psoralea corylifolia, as well as in the common fig, celery, parsley, West Indian satinwood and in all citrus fruits. Psoralens are commonly used in combination with ultraviolet A (UVA) light irradiation to treat a number of conditions with a known autoimmune basis such psoriasis, vitiligo, cutaneous T-cell lymphoma, phemphigus vulgaris, systemic sclerosis, rheumatoid arthritis and systemic lupus erythematosus [Gasparro 2000; Dalla Via et al. 2001; Oliven et al. 2001]. The effectiveness of these compounds has been attributed to their DNA photobinding properties [Pathak et al. 1992].
- Acridine: planar molecule structurally related to anthracene with one of the central CH groups replaced by a nitrogen atom. Acridine derivatives possess widely differing activities such as anti-inflammatory and anticancer [Srivastava et al. 2004], antihelmintics [Elslager et al. 1969], insectecidal, rodenticidal

[Mayer et al. 1970], fungicidal [Pathak et al. 1980] and antitumor activities [Takemura et al. 1995]. A number of marketed preparations based on the acridine nucleus are available [Kumar et al. 2012].

2.1.2 LABELLED OLIGONUCLEOTIDIES

Oligonucleotides are short, single-stranded DNA or RNA molecules that have a wide range of applications in genetic testing, research and forensics. Commonly made in the laboratory by solid-phase chemical synthesis, these small bits of nucleic acids can be manufactured with any user-specified sequence and so are vital for artificial gene synthesis, polymerase chain reaction, DNA sequencing, library construction and as molecular probes.

Oligonucleotides are in theory designed to specifically modulate the transfer of the genetic information to protein, but the mechanisms by which an oligonucleotide can induce a biological effect is complex. Although some of these mechanisms of inhibition have been characterized, rigorous proof for others is still frequently lacking.

Like nucleosides they have been chemically bound to a variety of fluorophores, drugs or other active molecules for biochemical and structural studies and to a variety of materials (for example metals, glass, polymers and peptides…) for the realization of biochemical probes and biosensors. They have also been actively employed as down-regulators of genetic expression in cellular studies, where they have been conjugated to a plethora of derivatives to enhance the cellular uptake or increase the binding affinity toward their RNA target (the antisense methodology) or to form more efficient triple helices on the double-stranded DNA (the antigen approach). More recently, oligonucleotides have also been used as molecular scaffolds to exploit their autoassembly properties for the realization of supramolecular aggregates with potential applications in the field of electronics devices.

Also the labelled oligonucleotides were provided by Dott. Massimo L. Capobianco of ISOF-CNR of Bologna.

The most common derivatizations of the oligonucleotides are done at their 5′ or 3′ ends or both (as in the case of the so called ″molecular beacons″); however, for some purposes it is important to be able to link a tether in the middle of a sequence, by modifying a base, a sugar, a phosphate or an entire internucleotidic region. Derivatization of nucleobases enables the incorporation of one or more suitable

functionalities to the desired position of the oligonucleotide, leaving the 5′ and 3′ ends available for further modifications.

The labelled oligonucleotides use in this thesis are 13-mer and the sequence is:

$$^{5'}\text{CGTGC X TCCTAGC}^{3'}$$

in which X denotes the labelled nucleosides Pso-dA (named P-Pso) or Acr-dA (named P-Acr).

The length of the probe was chosen to maximize the effects of modif cations on the duplex stability, expecting at the same time a good degree of duplex formation at room temperature, to facilitate HPLC analysis and to allow the formation of a full helix turn, in order to extend our f nding to real application cases. The arbitrary sequence was chosen to avoid secondary structures, with the modif ed adenosine located in such a way to provide a unique site for psoralen or acridine binding at the center of the duplex and locating a transition mismatch in a sensitive position.

2.2 LOADING OF CONJUGATE ADENOSINES ON AuNPs

To verify whether or not citrate-AuNPs can interact with labelled adenosines, the extinction spectra of the citrate-AuNPs were examined. The Surface Plasmon Resonance (SPR) peak of citrate-AuNPs was located at 520.0 ± 0.5 nm (n = 3) (spectrum A in figure 2.3).

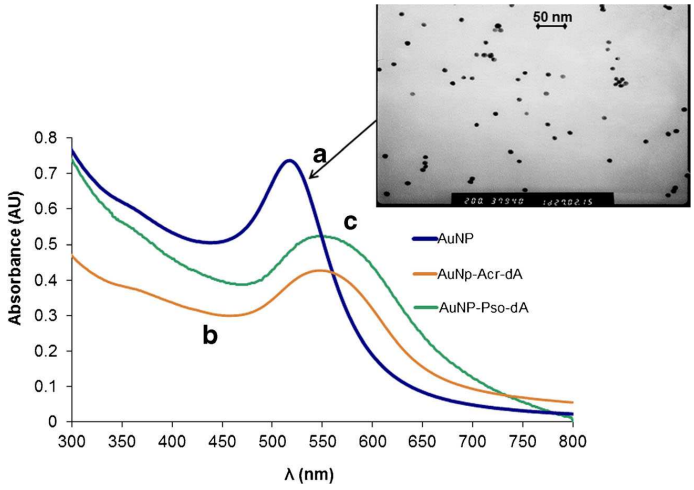

Figure 2.3: Spectra of the AuNPs suspension before (a) and after P-pso (b) and Pso-dA (c) adsorption. Inset: TEM image of AuNPs

As shown from TEM data in the inset of figure 2.3, AuNPs have an average diameter of about 10 nm in agreement with the data from the supplier. Upon the addition of Pso-dA, the SPR peak of the AuNPs was shifted to 543 ± 0.6 nm (spectrum C in figure 2.3) and its intensity decreased. Similar trends were observed in the spectra of Acr-dA, and of P-pso and P-acr (spectrum B in figure 2.3). It has been reported that the adsorption of uncharged nucleosides could cause AuNPs aggregation, in such a case the colloidal solution undergoes an instant red-to-blue color change [Li et al. 2004]. In the studied concentration range, the spectra of the colloid after addition of labelled adenosines do not turn to blue, the shift in the spectra is possibly due to the modification of the dielectric environment close to the NP surface which, in turn, is related to the interaction of the surface with a molecule [Zhang et al. 2012]. The interaction between nucleosides and AuNPs is quite complicated and has been the subject of extensive debate. Briefly, binding of nucleosides to AuNPs through the nitrogen has been reported, [Zhang et al. 2012; Demers et al. 2002], in other work hydrophobic interactions were indicated as the adsorption drive force [Nelson et al. 2011]. These differences in the interaction responsible for adsorption partially derive from different colloidal composition for what concerns both the adsorbate solution, the NPs surface and the media. Moreover, it should also be considered that the compounds investigated in the present study were conjugate nucleosides containing thioether groups and the adsorption of organosulfur compounds on the AuNP surface has also already been reported [Peterle et al. 2008]. In fact, it is well known that alkanethiols are the most popular ligand for AuNPs [Lim et al. 2009], additionally, the use of dialkyl sulphides [Beulen et al. 1996; Angelova et al. 2013] and protected thiols has also been reported [Chen et al. 2002]. The thioether–gold coordination is much weaker than the covalent thiolate–gold interaction and it increases for multidentate ligands comprising more than one thioether unit [Maye et al. 2003; Nion et al. 2003]. In general, monothioethers need longer chain lengths or costabilization in order to give stable, redispersible gold colloids [Hermes et al. 2012]. Nevertheless the detailed study of binding mechanisms lies beyond the scope of the present work. In any case, we observed that for the studied nucleosides, the binding was found to be strong enough to allow their capture on the surface of the AuNPs.

In order to qualitatively understand if this interaction is mainly due to functional molecules and the tioether linker or to the nucleoside, the adsorption of dA (deoxyadenosine) was investigated. In figure 2.4 are reported the electropherograms

obtained by hydrodynamic injection of a solution before and after the contact with AuNPs.

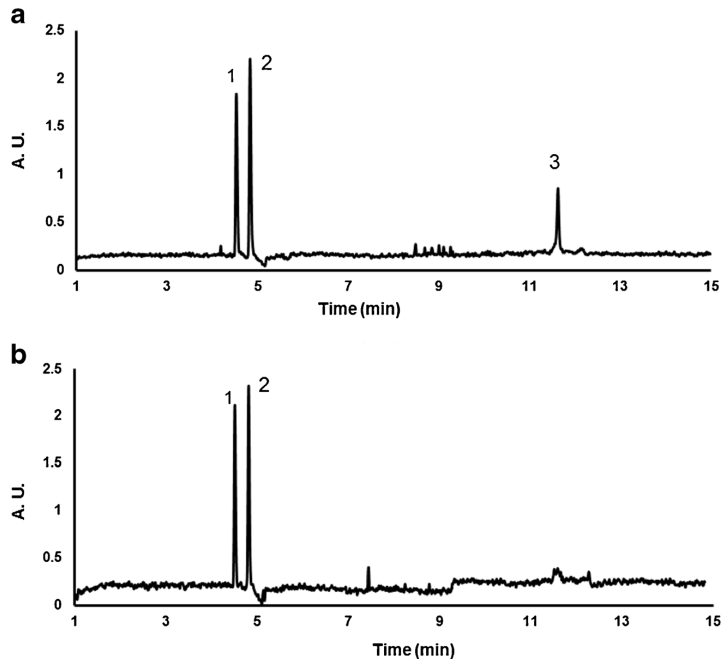

Figure 2.4: Electropherograms of dA (2), and Pso-dA (3) a) before and b) after the contact with AuNPs. Peak 1 is DMSO employed as marker. Capillary: 50 μm inner diameter, 60.5 cm bare silica capillary (detection length, 8.5 cm). Background electrolyte (BGE) Borate buffer 20mM pH=9.3 SDS 20mM. Applied voltage: +20 kV: Temperature: 25 °C. Absorbance detection wavelength: 260 nm

It can be qualitatively seen that the adsorption of dA on AuNPs is negligible when compared to that of Pso-dA.

To quantify the adsorption of labelled adenosines on AuNPs, their concentrations obtained by REPSM-MEKC in the solution before and after the contact with AuNPs were measured. The effect of equilibration time on the adsorption was evaluated by measuring the concentration of the labelled adenosines in contact with AuNPs during time. The concentration observed for the modified adenosines reached a constant value after 30 min of incubation. Consequently, to assure a contact time longer than the equilibration time, 1 h was chosen for the experiments. In addition, the influence of the concentration of the analytes was considered. Figure 2.5 shows the adsorbed quantity as a function of the labelled adenosines in the solution after equilibration.

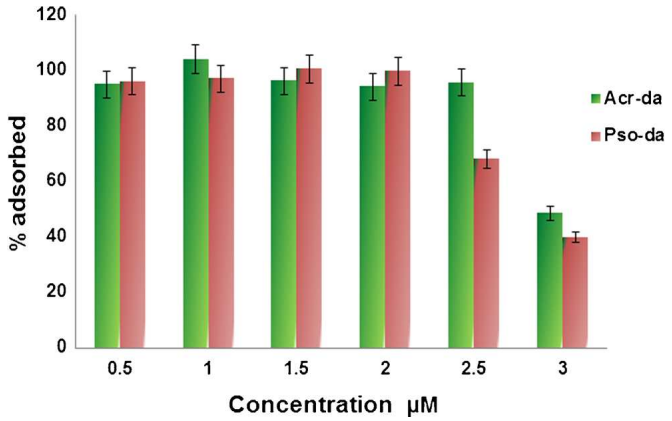

Figure 2.5: Percentage of adsorbed Pso-dA and Acr-dA on AuNPs as a function of conjugated-adenosines concentration in the bulk phase

Extraction was almost complete at concentrations lower of 2 µM for Pso-dA and 2.5 µM for Acr-dA; at higher concentrations the particles were saturated. On the basis of these results, in order to obtain a quantitative adsorption of the two adenosines the quantity were chosen lower than the saturation coverage and the equilibration time was set to 1 h. These adsorption results confirmed that AuNPs could be used for extracting the labelled adenosines from an aqueous solution.

The particles obtained after incubation and centrifugation, were washed by suspension in water and separated by centrifuge, the supernatant was injected in the CE system to determine the concentration of the labelled adenosines eventually released and the procedure was repeated twice. We found that, for both the analytes considered the concentration in the two aqueous solutions was below the detection limit and no peaks were revealed in the electropherograms. This finding indicates that the concentration of released adducts in water (i.e. AuNP-Pso-dA and AuNP-Acr-dA) were lower than the detection limit of the method.

2.3 RELEASE OF LABELLED ADENOSINES FROM THEIR ADDUCTS WITH AuNPs

To evaluate the release of labelled adenosines from their AuNP adducts, the labelled nucleosides adsorbed on the NP surface were suspended in 100 µL of buffered solutions at different pH values. It can be seen in figure 2.6 (a) that the percentage of released Pso-dA is negligible in the 3-9 pH range and increases at pH higher than 10 or lower than 2.

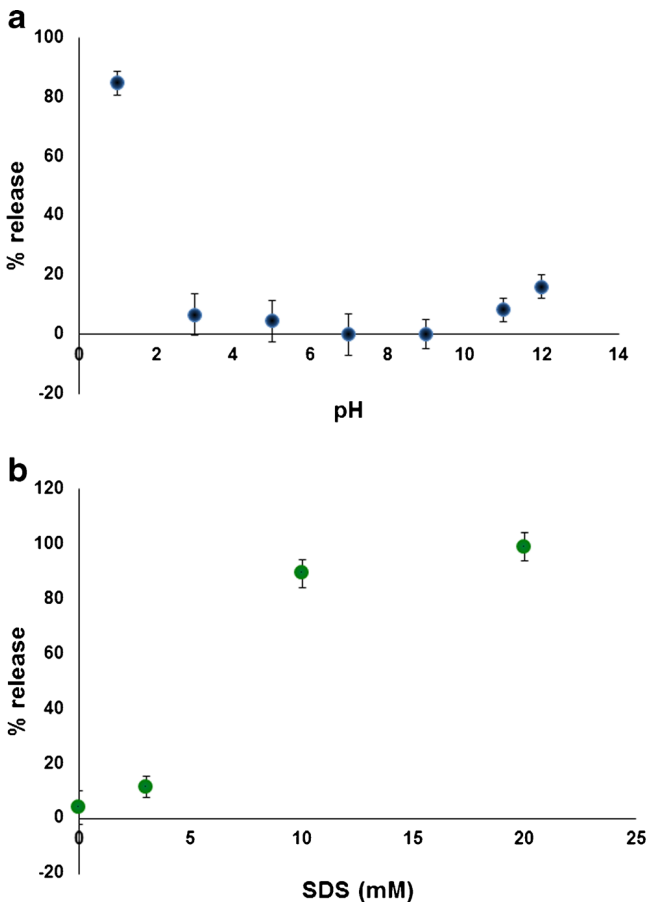

Figure 2.6: Percentage of released Pso-dA (a) vs. pH and (b) vs. SDS concentration

To increase the release of the compounds in the solution the effect of SDS was investigated at pH = 9 (figure 2.6 (b)). When SDS concentration was increased from 0.1 to 10 mM an increase of the area of the analyte in the electropherograms recorded at 260 nm was found; at SDS concentration higher than 10 mM the area of the compounds reached a plateau. The maximum release is thus obtained for SDS concentrations higher than the critical micelle concentration for SDS (8.1 mM) [Cifuentes et al. 1997]. This finding indicates that the labelled adenosines are physisorbed on AuNPs and they are displaced by the surfactant SDS can indeed be adsorbed onto gold surface [Soares et al. 2007; Huang et al. 2003]. Based on the previous results, for the extraction of the labelled nucleosides a buffered solution at pH = 9 with 20 mM SDS was chosen. The electrophoretic mobilities of the released labelled adenosines were equal to those obtained for the compounds before the capture process. Therefore, the concentration step does not affect the labelled adenosines.

Under the conditions above mentioned, the peak areas of the compounds in the electropherograms obtained by MEKC increased significantly after the extraction. In

particular, the extraction with the AuNPs resulted in a 4.2 and 3.8-fold increase in the response of the method (for Pso-dA and Acr-dA, respectively). This result is in agreement with a four-fold improvement in the sensitivity due to a nearly complete adsorption from the initial 400 µL volume (before extraction) and desorption to a final sample volumes of 100 µL (after extraction), confirming that thioether labelled nucleosides can be completely extracted from aqueous solution by using AuNPs.

The effect of the sample volume on the enrichment of the labelled adenosines was also investigated, generally by increasing the sample volume, the peak area in the electropherograms of the analytes after enrichment increases, until the particle saturation is reached. For a given compound, the sample volume to achieve particles saturation depends on the concentration of both the analyte solution and the AuNPs. At the concentration of 0.05 µM (C_i) and by using 100 µL of AuNPs solution and 1.9 mL (V_i) of sample solution, the recovery obtained from three repetition was 101 ± 8.3 %. The recovery was calculated as:

$$R(\%) = 100\frac{C_f V_f}{C_i V_i} \tag{2.1}$$

where C_i and V_i indicates the initial concentration and volume respectively, Cf corresponds to the concentrations of labelled adenosines in the final volume of supernatant of 100 µL (that is V_f). In turn C_f values were calculated from calibration curves built with standard solutions.

The enrichment factor after the extraction procedure (i.e. $\frac{V_i}{V_f}$), was 19.

The obtained LOD for Pso-dA and Acr-dA at a signal to noise ratio of three, in the normal hydrodynamic injection MEKC technique (without extraction) were 1.62 and 0.71 µM respectively and the LOD in the normal hydrodynamic injection MEKC technique (with extraction) were 0.092 and 0.052 µM for Pso-dA and Acr-dA, respectively.

The particles after the release of analytes were washed twice with milliQ water and 10 mM citrate solution and the enrichment of Pso-dA was repeated on the AuNPs recovered by using the procedure above described. The extraction-release procedure was repeated thrice on the same AuNPs particles. The loading percentage of Pso-dA on AuNPs was calculated from its concentration measured by REPSM-MEKC before and after the contact with AuNPs. Loading percentages were 97 %, 100 %, 100 %,

respectively in the first, second and third trial. The release was obtained with the buffered borate solution at pH = 9.3 and 20 mM SDS. Recovery percentages in the first, second and third reuse cycle were 97 %, 98 %, 105 % respectively. This finding indicates that the solid phase of the off-line enrichment procedure can be easily regenerated and can be reused, thus decreasing the waste of materials.

2.4 REVERSE STACKING

REPSM, a CE-based on-line concentration strategy, has been proved increase detection ability for various samples [Bernard et al. 2011; Quirino et al. 2011], including NPs [Lin et al. 2007]. In REPSM the sample is introduced into the capillary hydrodynamically, applying a stacking voltage at negative polarity to concentrate the analytes at the interface between the sample zone and the background electrolyte and then pumping the sample matrix from the capillary under electroosmotic flow (EOF). When the current reaches ca. 97% of its original value, this potential is turned off. A positive potential is then applied to separate the analytes.

The REPSM-MEKC method was optimized with respect to different experimental parameters such as sample loading time, separation buffer concentration, pH of separation buffer and separation voltage.

Different concentrations of borate buffer, 15, 20, 40 and 60 mM and different pH values, 9.3, 10.04 and 12.10 were investigated. As the concentration of borate was increased, a longer migration time was observed. In addition, the retention time of the labelled adenosines increases with the pH. It was also found that by increasing the SDS concentration in the BGE, the separation improves however for concentrations larger than 50 mM long retention times lead to peak broadening. The best resolution of the analytes was obtained using a 20 mM sodium tetraborate buffer at pH 9.30 containing 20 mM SDS, with an applied voltage of 20 kV. Figure 2.7 show the elegropherogram of mixture of Pso-dA and Acr-dA under optimal condition.

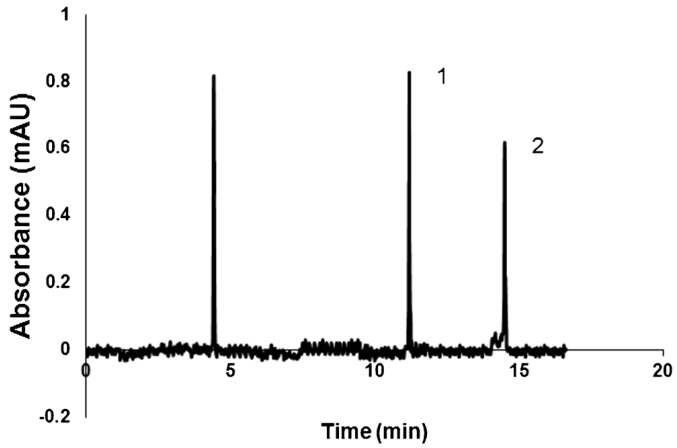

Figure 2.7: Electropherograms of Pso-dA (1) and Acr-dA (1). The concentration of both the analytes was 10 µM. Hydrodynamic injection at a pressure of 10 mbar applied for 30 seconds. The separation conditions were 20 mM SDS, 20 mM borate buffer pH 9.30, fused silica capillary: 50 µm inner diameter, 60.5 cm (detection length, 8.5 cm). Neutral marker: dimethyl sulfoxide. Applied voltage: +20 kV: Temperature: 25 °C. Absorbance detection wavelength: 260 and 268 nm for Pso-dA and Acr-dA respectively.

Different sample plugs were tested in order to determine the highest sample plug length to be injected without worsening the separation profile by REPSM. To improve the sensitivity of the method, the injection time was varied between 25 s and 100 s using a 50 mbar hydrodynamic injection. The peak area of the three analytes increased with the injection time, but injection time longer than 50 s gave lower area reproducibility therefore 50 s were chosen.

To examine the quantitative REPSM method, the results in terms of limit of detection were compared with the conventional MEKC method (see table 2.1).

Compound	**MEKC**			**REPSM**		
	REGRESSION	**Coefficient of correlation (R^2)**	**LOD (µM)**	**REGRESSION**	**Coefficient of correlation (R^2)**	**LOD (µM)**
Pso-dA	y=106.9(6.8) x-0.72 (0.54)	0.9989	1.62±0.097	y=4281(121)x-8(23)	0.9946	0.068±0.011
Acr-dA	y=331.9(5.1) x-0.26 (0.25)	0.9992	0.71±0.088	y=12391(611)x +13(35)	0.9975	0.042±0.010

Table 2.1: Linear regression data and LOD of the studied labelled nucleosides by MEKC and REPSM-MEKC

It can be observed that the REPSM-MEKC method gave around twenty-fold lower limits of detection.

Finally when the REPSM-MEKC method was applied to the extracted solution of labelled nucleosides which was obtained from the release of the analytes from their adducts with AuNPs, an enrichment factor of about 380 was obtained, which is in good agreement with the total enrichment factor given by the product of the enrichment in the extraction procedure (about 19) and that due to REPSM injection (about 20).

The LOD, at a signal to noise ratio of three, in the REPSM-MEKC method (with extraction) were 5.5 and 2.3 nM for Pso-dA and Acr-dA respectively.

It has been reported that REPSM-MEKC method can also be directly applied to AuNPs. For instance, the surfactant CE separation coupled with RESPM injection increases the detection sensitivities of a factor of about 5 for AuNPs with diameter of 5 nm as reported by Lin et al in 2007. The stability of AuNPs suspended in buffer containing SDS, inside silica capillaries commonly employed for electrophoretic separation has been already demonstrated [Lin et al. 2007].

The extraction procedure was also applied to a real sample of female urine in order to explore the feasibility of the methodology in practical cases. When the supernatant obtained from the extraction with AuNPs of urine was analyzed by REPSM-MEKC, no peak corresponding to Pso-dA was detected (see figure 2.8 (a)).

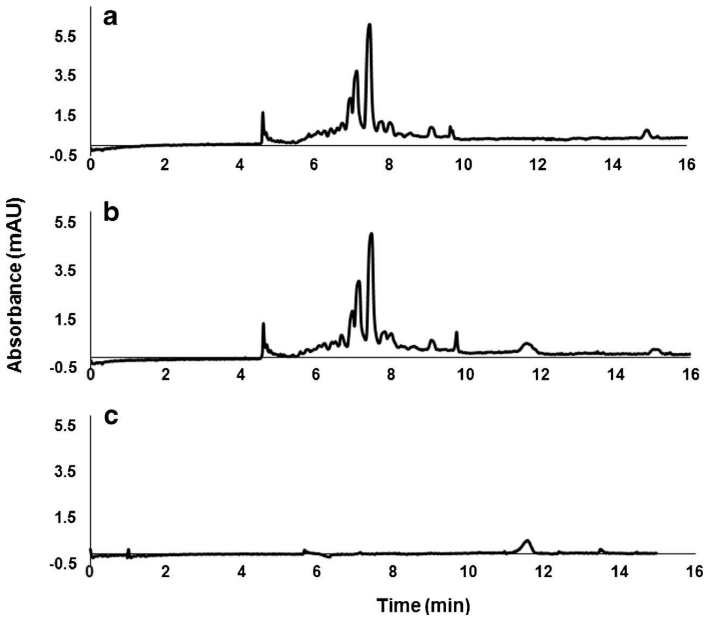

Figure 2.8: Electropherograms of extracted from urine samples. a) urine sample, b) urine sample spiked with Pso-dA, c) spiked water sample. The separation conditions were 20 mM SDS, 20 mM borate buffer pH 9.30, fused silica capillary, 64.5 cm length (56 cm to the detector), 50 µM I.D., 25 °C, sample loading 50 mbar for 50 s, stacking at -15 kV, separation at 20 kV, detection UV wavelength: 260 nm

Instead in the urine sample spiked with Pso-dA, a peak corresponding to the analyte was identified (see figure 2.8 (b)). The identification was carried out by comparing the eletropherogram of the urine sample to that of a water spiked solution prepared with the same procedure of the urine sample (figure 2.8 (c)).

2.5 CAPTURE AND RELEASE OF OLIGONUCLEOTIDES BY USING AuNPs

Oligonucleotide probe-linked AuNPs have found wide application in biosensors, in general they were obtained as alkanethiol-capped oligonucleotides self-assembled on AuNPs by Au-thiol bond. One of the method to prepare those probes was that proposed by Mirkin [Jin et al. 2003] based on the chemisorption step for linking thiol oligo probes to citrate-protected AuNPs. It should be noted that, in addition to terminal linkage of DNA and AuNP through Au-S linkage, nonspecific binding of nucleotides to AuNPs through the nitrogen-containing bases, or not specific interactions were also described [Zhang et al. 2012; 2013]. Nonthiolated DNA was found to protect AuNPs against salt-induced aggregation as long as the DNA was single stranded, short and unfolded [Li et al. 2004]. In this case, the adduct is resulted from an adsorption process. In general, the DNA loading capacity in adsorption is much lower than that can be

achieved by thiolated DNA. However, it has been found that at low pH, the loading capacity of AuNPs for nonthiolated DNA containing polyadenine fragment, can be increased and their conjugates maintain the full functions of DNA, allowing for molecular recognition [Kimura-Suda et al. 2003; Jiang et al. 2013].

In the present work, the adsorption of labelled oligonucleotides was carried out at acid pH. The increase in loading capacity at low pH is due to the decrease of electrostatic repulsion among negatively charged AuNPs and oligonucleotides as reported by Dam et al. in 2015. A small volume of stock solution was diluted in MilliQ water (spiked solution), at this diluted solution AuNPs were added and the suspension was mixed via a brief vortex mixing. A small volume of 500 mM pH 3.00 citrate-HCl buffer was added to the suspension. After brief vortex mixing, the sample was allowed to incubate at room temperature for 4 h, the mixture was centrifuged at 14000 rpm and the supernatant was removed.

The pellets obtained after incubation and centrifugation, were washed by suspension in water and separated by centrifuge. The conjugates were re-suspended in the phosphate buffer and analyzed by CE. As shown in table 2.2, the AuNPs adducts migrated at different rates than AuNPs and in particular the conjugates migrated more slowly.

	AuNP	**AuNP-P-pso**	**AuNP-P-acr**
Migration time (min) **(SD, n=3)**	9.45 (0.045)	22.66 (0.55)	20.85 (0.52)
Mobility ($cm^2V^{-1}s^{-1}$) **(SD, n=3)**	-3.77E-04 (1.5E-06)	-5.39E-04 (2.8E-06)	-5.29E-04 (3.2E-06)

Table 2.2: Migration time and electrophoretic mobility of AuNPs and AuNPs adducts. The separation conditions were 20 mM SDS, 20 mM borate buffer pH 9.30, fused silica capillary, 64.5 cm length (56 cm to the detector), 50 µM I.D., 25 °C, sample loading 50 mbar for 50 s, stacking at -15 kV, separation at 20 kV, detection UV wavelength, 520 nm (AuNP), 543 nm (AuNP-P-pso and AuNP-P-acr).

This finding confirms that the proposed method is able to separate efficiently AuNPs on the basis of their size and surface properties. It should also be noticed that the oligonucleotides employed have a thioether linker which is more easily displaced than a terminal thiol group linker [Takeishi et al. 2004].

The release of adsorbed oligonucleotides was carried out at neutral pH by adding NaCl 0.1 M [Zhang et al. 2013] in SDS borate buffer and the recovery was 88 ± 11 % (see equation 2.1) with an enrichment due to the extraction equal to 17. Release of nonthiolated DNA from their AuNP adducts in neutral pH solution has also been reported by Zhang et al. in 2013. The solutions of the oligonucleotides P-pso and P-acr before extraction were analyzed by REPSM-MEKC method, carried out in the same condition above described for the labelled adenosines. An increase in the sensitivity of the method was obtained (see table 2.3), with an enrichment factor of 21 ± 8 respect to hydrodynamic injections.

Compound	**MEKC**			**REPSM**		
	REGRESSION	**Coefficient of correlation (R^2)**	**LOD (µM)**	**REGRESSION**	**Coefficient of correlation (R^2)**	**LOD (µM)**
P-Pso	y=480(12) x+0.79 (0.48)	0.9987	0.67±0.11	y=19007(712)x +15(29)	0.9931	0.031±0.0087
P-Acr	y=497.8(8.9) x+0.57 (0.62)	0.9991	0.63±0.077	y=13742(523)x +22(24)	0.9968	0.032±0.0081

Table 2.3: Linear regression data and LOD of the studied labelled oligonucleotides by MEKC and REPSM-MEKC

Finally, by coupling the extraction procedure with REPSM method an enrichment factor of about 360 was obtained.

The LOD, at a signal to noise ratio of three, in the REPSM injection technique MEKC (with extraction) were 3.3 and 4.3 nM for P-Pso and P-Acr respectively.

CHAPTER 3: DIFFUSION OF BIOLOGICAL MOLECULES AND Au β-CDSH NPs

In this chapter we explored the diffusion process of some biological active molecules related to their interaction with AuNPs superficially modified with β-cyclodextrines functionalized –SH.

The unique properties of NPs account for their widespread applications in material science, catalysis and biomedicine [Katz et al. 2004]. In particular, in this last field, AuNPs are endowed with considerable potential to be a biomedicine by virtue of their improved stability and their optical and electronic properties. The supramolecular aggregation of gold nanoparticles to host compounds such as the cyclodextrins have been reported [Park et al. 2009; Liu et al. 2000]. This aggregation gives the opportunity to conjugate the biosensing properties of AuNPs to drug transport and controlled release for developing new strategies of specific drug delivery systems.

The ability of Au β-CDSH NPs to act as hosts for biological molecules (more precisely inside the cyclodextrin cavity) was investigated in order to obtain some preliminary information on the interaction of these compounds with AuNPs.

Complexation phenomena were detected by measuring the diffusion coefficients by a TDA-CE method and, the obtained values, were also compared with the measurements reported in literature determined with different technique in particular NMR [Uccello-Barretta et al. 2011] and, since in literature work of this type are lacking, another aim of this part was to verify the developed TDA-CE methodology.

It is known that the diffusion coefficients are very sensitive to complexation phenomena which slow down the diffusion of complexed species and, hence, bring about decreases of the diffusion parameters, which reflect the increase of the apparent sizes of complexed species with respect to uncomplexed ones. In fact, starting from determination of diffusion coefficients, is possible to obtain another important parameter for the description of the interaction between Au β-CDSH NPs and the biological compound that is the ligand fraction.

The results presented in this chapter are a relevant part of a manuscript in preparation.

3.1 TAGET MOLECULES

3.1.1 DEOXYCYTIDINE

Deoxycytidine (which structure is shown in figure 3.1) is a nucleoside compound from the pyrimidine nitrogenous base cytosine which is attached to a ring of ribose via a β-N1-glycosidic bond.

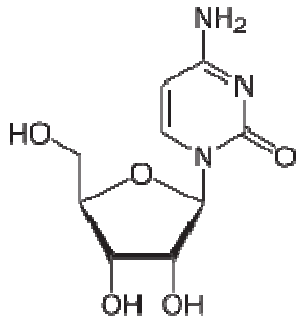

Figure 3.1: deoxycytidine

The utilization of oxygen by aerobic organisms generates large amounts of oxidants, including $O^{\cdot-}$, H_2O_2, 'OH, which in turn alter target biomolecules such as lipid, protein and DNA [Halliwell et al. 1989; Sies 1991; Fraga et al. 1990].This originates some oxidation products of 2'-deoxycytidine (the major are 5-hydroxy-2'-deoxycytidine, 5-hydroxy-2'-deoxyurldine and 5,6-dihydroxy-5,6-dihydro-2'-deoxyuridine). This products of DNA damage leading to cancer [Wagner et al. 1992]. In particular both 5-hydroxy-2'-deoxycytidine and 5-hydroxy-2'-deoxyuridine lesions appear to be mutagenic.

The best known deoxycytidine analogue, 1-P-D-arabinofuranosylcytosine, is commonly used in the treatment of leukemia [Ho 1973; Hagenbeek et al. 1987]. Another analogue, the 2',2'difluorodeoxycytidine, also shows chemotherapeutic activity alone and in combination against a variety of solid tumor types such as ovarian, non-small cell lung, pancreatic, bladder and head/neck squamous cell carcinomas [Belani et al. 2002; Favaretto 2006; Heinemann 2001].

3.1.2 DOXORUBICIN

Doxorubicin (figure 3.2) is a member of the anthracycline group of compounds (anticancer antibiotics with a four-membered ring system containing an anthraquinone chromophore and an aminoglycoside) [Lown 1988] which presents good anticancer

activity against a wide spectrum of tumors and it is one of the most extensively used chemotherapeutic compounds currently in clinical use.

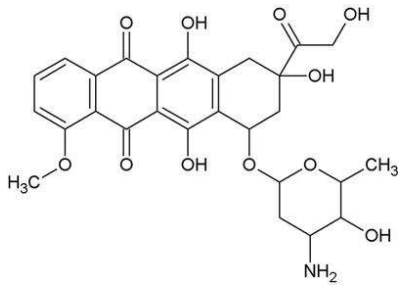

Figure 3.2: structure of doxorubicin

Common adverse effects of doxorubicin include hair loss, myelosuppression (a compromised ability of the body's bone marrow to produce new blood cells), nausea and vomiting, oral mucositis, oesophagitis, diarrhoea, skin reactions and localized swelling and redness along the vein in which the drug is delivered. Less common, yet serious reactions include hypersensitivity reactions (including anaphylaxis), radiation recall, heart damage and liver dysfunction.

3.2 TAYLOR DISPERSION ANALYSIS

Taylor Dispersion Analysis (TDA) is a simple, relatively rapid and absolute (calibration is not required) method for determination of diffusion coefficients [Cottet et al. 2010]. TDA has been used to assess the diffusivity of small molecules [Niesner et al. 2000], macromolecules [Hulse et al. 2011], as well as colloidal particles [Franzen et al. 2011] and was also successfully introduced to characterize complexation phenomena [Jensen et al. 2010]. Recently, TDA studies utilizing two detection points along the capillary have been reported [Chamieh et al. 2012]. However, the potential advantages associated with having more than one detection window have hither not been investigated.

Taylor dispersion analysis was developed by Taylor in the 1950s [Taylor 1953, 1954] and successively improved by Aris [Aris 1956] and others [Alizadeh et al. 1980].

Taylor introduced the idea of measuring the diffusion coefficient by monitoring the concentration profile of solute pulses and fronts (represented in figure 3.3) as they flowed through a uniform, cylindrical tube under laminar, Poiseuille flow.

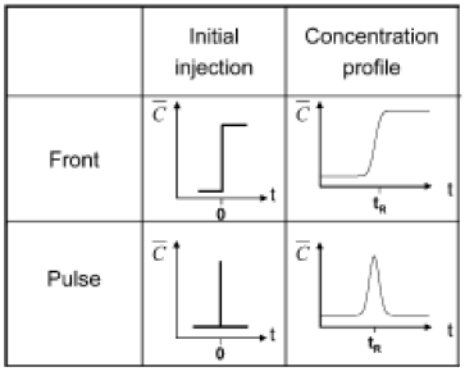

Figure 3.3: concentration profile of solute pulses and fronts [Sharma et al. 2005]

The solute is transported through the capillary by the fluid; the parabolic velocity profile of the fluid produces a concentration gradient between the centre of the capillary and the walls, which causes the solute to diffuse in the radial direction. The overall distribution of the solute due to the combined effects of axial convection and radial diffusion is known as dispersion. By measuring the dispersion of a solute, Taylor was able to determine its diffusivity under conditions when axial diffusion could be neglected. In this way he obtained analytical solutions of the convection-diffusion equation for concentration profiles of fronts and pulses:

$$\frac{\partial C^*}{\partial t}+\frac{u_0}{2}\left(1-\frac{r^2}{R_C^2}\right)\frac{\partial C^*}{\partial z}=D\left[\frac{1}{r}\frac{\partial}{\partial r}\left(r\frac{\partial C^*}{\partial r}\right)+\frac{\partial^2 C^*}{\partial z^2}\right] \tag{3.1}$$

where: t is time, z is axial position, r is radial position, C* is local concentration of the solute and is a function of both r and z, D is the diffusivity of the solute, and R_c is the radius of the tube.

If the mean solute concentration across the cross section of the tube, $\bar{C}$, is monitored as a function of time at a fixed position along the tube, typically by UV absorbance, the solution of equation 3.1 gives equations 3.2 and 3.3 for a front and for a pulse respectively:

$$\frac{\bar{C}}{C_0}=\frac{1}{2}\pm\frac{1}{2}erf\left(\frac{t-t_r}{\sigma\sqrt{2}}\right) \tag{3.2}$$

$$\bar{C}=\frac{M}{2\pi^{3/2}R_C^2\sqrt{kt}}\exp\left(-\frac{(t-t_r)^2}{2\sigma^2}\right) \tag{3.3}$$

where: k is the dispersion coefficient defined as:

$$k = \frac{R_C^2 u_0^2}{48D} \tag{3.4}$$

M is the mass of the solute in the pulse, C_0 is the concentration of the front, t_R is the mean residence time (i.e. the time it takes the solute moving with the mean velocity of the fluid to reach the detector located at a distance L_D from the inlet of the tube) and σ^2 is a measure of the width of the pulse or the sharpness of the front and is related to the dispersion coefficient by:

$$\sigma^2 = \frac{2kt}{u_0^2} \tag{3.5}$$

Taylor's analysis assumed an ideal experiment where a concentration front or a pulse is introduced into a capillary of uniform radius under conditions of steady-state, laminar Poiseuille flow. The concentration profile of the solute is monitored at a fixed cross section of the capillary. In this ideal case, t_R and σ^2 can be determined by fitting the concentration profiles to equations 3.2 and 3.3 (for pulses, t_R and σ^2 correspond to the first and second moments of the distribution of solutes in the profile). The diffusivity of the solute is then determined using equation 3.6:

$$D = \left(\frac{R_C^2}{24\sigma^2} \right) t_r \tag{3.6}$$

The conditions necessary for this equation to be valid are expressed in terms of two dimensionless quantities:

- a dimensionless residence time $\left(\tau = \frac{Dt_r}{R_C^2} \right)$, which is the ratio of the residence time to the time required for a solute to diffuse a distance equal to the radius of the capillary;

- a Peclet number $\left(P_e = \frac{u_0 R_C}{D}\right)$, which describes the relative rates of mass transfer along the axis of the capillary due to convection and diffusion.

Taylor showed that equation 3.6 was valid when:

- τ is greater than the time it takes to decrease variations in radial concentrations by a factor of e ($\tau >> 0.14$)
- diffusion in the axial direction is negligible compared to convection ($P_e >> 7$).

If we assume that a ratio of 10:1 is sufficient for the inequalities given by Taylor, the equation is applicable when $P_e > 70$ and $\tau > 1.4$. Inspection of equation 3.6 shows that capillaries with smaller values of R_c require shorter residence times to produce profiles with the same value of σ^2. Consequently, smaller tubes enable a more rapid measure of D.

A limitation of Taylor's analysis is that diffusivities cannot be determined for slow flows when axial diffusion is no longer negligible (because the condition of Pe > 70 is not satisfied).

Aris extended the analysis of Taylor to overcome this restriction. The alternative method consists in examining the moments of a concentration profile. In this case the diffusivity could be determined when the solute was initially contained within a finite length of the tube.

The analyses of Taylor and Aris for the dispersion of a solute flowing in a tube have been used previously as a method to measure values of diffusivity [Pratt et al. 1974]. Typically, these experiments were performed in tubes that had values of radii up to 1 mm and required long measurement times (on the order of hours).

Bello et al. in 1994, using a commercial CE instrument with a UV detector, introduced the use of narrow-bore glass capillaries (radii $\leq$ 50 μm) for the determination of D of small molecules and proteins from the Taylor-Aris analysis of dispersion. By using capillaries with such small inner diameters, the residence time required to measure D accurately was reduced from hours to minutes. More precisely in their work, a plug of solute was injected into a capillary and the concentration profile was fit to pulse equation 3.3. The diffusivity was then determined from t_R and σ^2 by solving equation 3.7 for D (Aris approach):

$$D + \frac{R_C^2 u_0^2}{48D} = \frac{1}{4} u_0^2 t_r \left(-1 + \sqrt{1 + \frac{4\sigma^2}{t_r^2}} \right) \tag{3.7}$$

When the conditions of Taylor are satisfied (Pe > 70 and $\sigma^2 > 1.4$), this expression gives the same value of D as equation 3.6.

The obtained equations allow measurement of the diffusivity of a solute from its concentration profile in a single experiment, assuming it satisfies the ideal conditions. In practice, the experimental setup often deviates from ideality. Wakeham and co-workers considered a number of experimental departures from ideality and analysed their impact on the analysis by Aris for dispersion of a pulse. A number of these deviations from ideality are applicable to a commercial CE apparatus:

- the finite width of the detection window
- the finite width of the injected plug of solute
- non-uniformities in the radius of the capillary

They assumed that each effect was small and could be treated as an independent first-order perturbation to the system.

They found that errors arising from non-uniformities in the radius of the capillary were insignificant. The corrections they derived for the finite width of the detector are proportional to the ratio of the width of the detector window to L_D. Because this quantity is small (~ 10^{-3}) for the glass capillaries, the correction for the finite width of the detector window is also insignificant and can be neglected.

Corrections for the finite width of an injected plug of volume V_i cannot be neglected typically and are given in equations 3.8 and 3.9:

$$t_r = t_{r,obs} \left[1 - \left(\frac{V_i}{2\pi R_C^2 L_D} \right) \right] \tag{3.8}$$

$$\sigma^2 = \sigma_{obs}^2 - \frac{t_{r,obs}^2}{12} \left(\frac{V_i}{\pi R_C^2 L_D} \right)^2 \tag{3.9}$$

To use these corrections, the concentration profile of a pulse is monitored and fit to pulse equation in order to obtain $t_{R,obs}$ and σ^2_{obs}. The values are corrected using equations 3.8 and 3.9 to obtain t_R and σ^2, which are used to obtain the value of D of the solute with equation 3.7 (Aris approach). Alternatively, when the conditions of Pe > 70

and $\sigma^2 > 1.4$ are satisfied, Taylor's approach can be used; in this case, the corrections given in equations .8 and 3.9 are applied to equation 3.6 for the calculation of D.

Taylor approach offers a number of advantages over other techniques used to measure values of D: diffusivities in solution can be measured for any molecule provided detection of that molecule by CE is possible (typically UV absorbance or fluorescence) in fact a commonly used technique for measuring solute diffusivities, Dynamic Light scattering (DLS), is limited to measuring the diffusivities of macromolecules in solution (greater than ~ 1 nm in size). Another frequently used technique, Fluorescence Recovery after Photobleaching (FRAP), is applicable only to fluorescent or fluorescently tagged solutes.

CE instrument introduced an experimental non-ideality not considered previously in the analysis of the dispersions. The mean fluid velocity u_0 (the fluid velocity averaged over the cross section of the capillary measured as the length of the capillary from inlet to detector divided by the time required for the solute to reach the detector) is not at a constant, steady-state value, as was assumed by Taylor and Aris.

Because the current configuration of commercial CE instruments requires the fluid flow through the capillary to stop for the solute to be injected, there is an initial acceleration of the fluid after injection as the flow rate is increased from zero to the steady state value. The analyses of Taylor and Aris assumed that the fluid velocity was at its steady-state value throughout the experiment; they did not consider the effects of this "ramping up" in velocity. Also Wakeham et al. and Bello et al. did not include this effect in their measurements; but Sharma et al. in 2005 showed that the presence of this ramp in velocity can lead to large errors in values of D (as great as 60 %) and provided a simple method to compensate for the effect of this unsteady-state flow at all values of residence time.

3.2.1 CORRECTION FOR THE EFFECT OF INITIAL RAMP IN FLUID VELOCITY

In the absence of such a ramp, the fluid velocity is assumed constant at a value of u_{ss} that results in an ideal residence time of $t_r = \frac{L_D}{u_{ss}}$; in this instance, D can be obtained from equation 3.6. When an initial ramp in fluid velocity is present, we observe a

residence time, $t_{R,obs}$ that results from an average fluid velocity $u_0 = \frac{L_D}{t_{r,obs}}$. These velocities and residence times can be related as $u_0 t_{r,obs} = u_{ss} t_r$.

To describe the situation quantitatively, we assume that the velocity ramp occurs until time t_i, at which point the steady-state velocity is attained. If the average velocity during this ramp period is u_i, then the overall average fluid velocity is related to the steady-state velocity by equation 3.10:

$$u_0 = u_s \left(1 - \frac{t_i}{t_{r,obs}} + \frac{u_i}{u_{ss}} \frac{t_i}{t_{r,obs}} \right) \tag{3.10}$$

For a commercial CE instrument, the velocity increases at a constant rate. In the case of this simple velocity profile, equation 3.10 is simplified to give equation 3.11 and the ideal residence time is related to the observed residence time by equation 3.12:

$$u_0 = u_{ss} \left(1 - \frac{1}{2} \frac{t_i}{t_{r,obs}} \right) \tag{3.11}$$

$$t_r = t_{r,obs} - \frac{t_i}{2} \tag{3.12}$$

For more complex velocity profiles, the value of u_i must be determined in order to correct for the ramp.

If we assume that the initial ramp in fluid velocity results from a ramp in the applied pressure, we can relate t_i to the rate of increase of applied pressure, r_i, using equation 3.13:

$$t_i = \frac{8 L_T L_D \eta}{t_r R_C^2 r_i} \tag{3.13}$$

Combining equation 3.12 and 3.13 we obtain an expression for the ideal residence time in terms of the observed residence time:

$$t_r = \frac{t_{r,obs} + \sqrt{t_{r,obs}^2 - \frac{16 L_T L_D \eta}{R_C^2 r_i}}}{2} \tag{3.14}$$

Inspection of this equation shows that, in the absence of an initial velocity ramp (i.e., when $r_i = \infty$), $t_R = t_{R,obs}$. In this instance, fitting concentration profiles with equations 3.2 and 3.3 in order to obtain $t_{R,obs}$ and σ^2 and then applying equation 3.6 is sufficient to obtain D. In the presence of a velocity ramp, this approach will lead to errors in the measured value of D since $t_R \neq t_{R,obs}$. As shown by equation 3.14, at shorter observed residence times, the impact of the ramp will be more substantial than at longer times. As the residence time increases, the effect of the initial ramp becomes negligible. We expect that as $t_{R,obs} \rightarrow \infty$, the error in D should approach zero.

In conclusion to obtain accurate measurements of D in the presence of the initial ramp, we must correct for the presence of this initial ramp.

3.3 TDA OF Au β-CDSH NPs AND DEOXYCYTIDINE

Starting from a reported value for the diffusion coefficient of deoxycytidine [Uccello-Barretta et al. 2011] the minimum values for mobilization pressure were found out in order to respect the minimum ideality condition described by Taylor of $\tau = 1.4$ and $Pe = 70$ using equations 3.15 and 3.16:

$$Q = 0.785 D^2 V \tag{3.15}$$

$$Q = \frac{\pi R_C^4 \Delta P}{8 \eta L} \tag{3.16}$$

where: D is the inner diameter of the capillary (measured in m), V is the flow velocity (measured in $\frac{m}{s}$), R_C is the radius of the capillary (measured in m), ΔP is the mobilization pressure (measure in Pa), η is the viscosity of the BGE (measure in Pa s) and L is the length of the capillary (measured in m).

Because of the presence of tailing in DC peak, an optimization of the CE instrument configuration has been necessary. This tailing was probably due to an interaction between the OH groups of DC and the silica wall of the capillary. For this reason a polyvinyl alcohol (PVA) coated capillary, instead of the most common bare fused silica,

was used to avoid this problem. These capillaries contain a permanently adsorbed layer of PVA which minimizes hydrophobic and electrostatic solute/wall interactions and eliminates electroosmotic flow (EOF) so CE separations are based mainly on the electrophoretic mobilities of the analytes. PVA capillaries can be used for a variety of applications, including protein analysis [Glles et al. 1994], isoelectric focusing, small anion analysis, small molecules such as pharmaceutical drugs [Calcara et al. 2005], peptides and DNA fragments [Formenton-Catai et al. 2003].

Once found the optimal working conditions, TDA analysis for DC alone were made varying different experimental parameters such as capillary length and inner diameter, mobilization pressure and analyte concentration.

In figure 3.4 is reported an example of solute front injections with the fitting obtained applying equation 3.2 for four different mobilization pressure: 70, 80, 90 and 100 mbar.

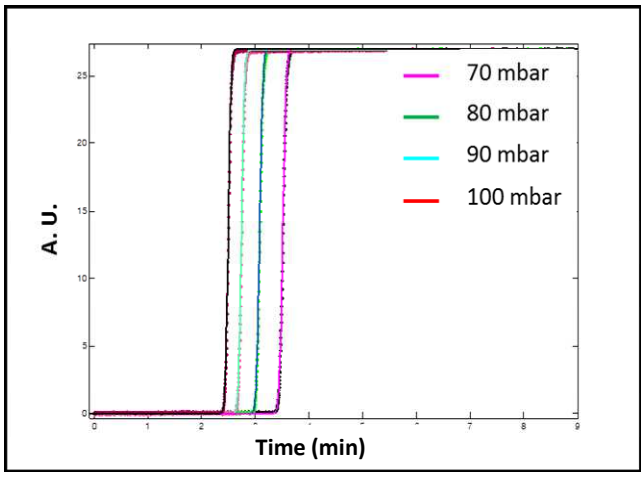

Figure 3.4: Solute front for DC 1 mM in phosphate 50 mM pH 7. Capillary: 50 µm inner diameter, 40 cm PVA coated capillary (detection length, 8.5 cm). Background electrolyte (BGE) phosphate 50 mM pH 7. Temperature: 25 °C. Absorbance detection wavelength: 214 nm

As stated before, because in TDA analysis diffusion coefficient can be obtained with two different types of injection, solute pulse for DC were also made varying the same experimental parameters reported above and, moreover, the pressure and the duration of hydrodynamic injection of the sample.

An example of solute pulse injections for DC with the relative fittings obtained with equation 3.3 for the same values of mobilization pressure of the previous solute front injections is reported in figure 3.5.

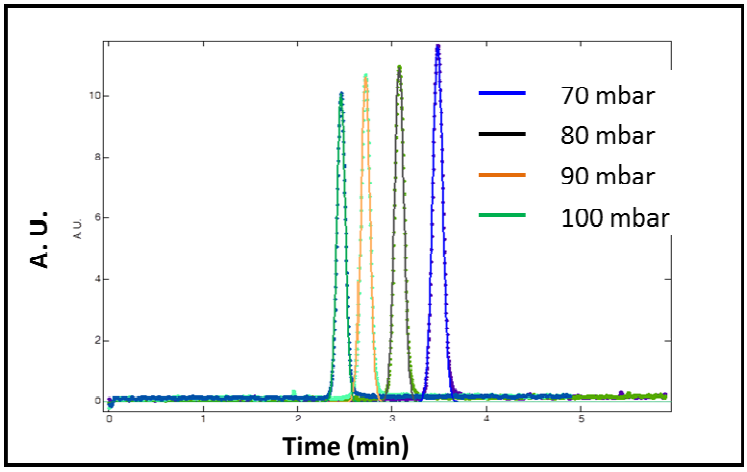

Figure 3.5: Solute pulse for DC 1 mM in phosphate 50 mM pH 7. Capillary: 50 µm inner diameter, 40 cm PVA coated capillary (detection length, 8.5 cm). Background electrolyte (BGE) phosphate 50 mM pH 7. Hydrodinamic injection: 50 mbar for 5 s. Temperature: 25 °C. Absorbance detection wavelength: 214 nm

Also Au β-CDSH NPs were analysed alone to determine the value of diffusion coefficient. In figure 3.6 are reported two examples of solute pulse injections and the relative fittings obtained with equation 3.3 for two mobilization pressure.

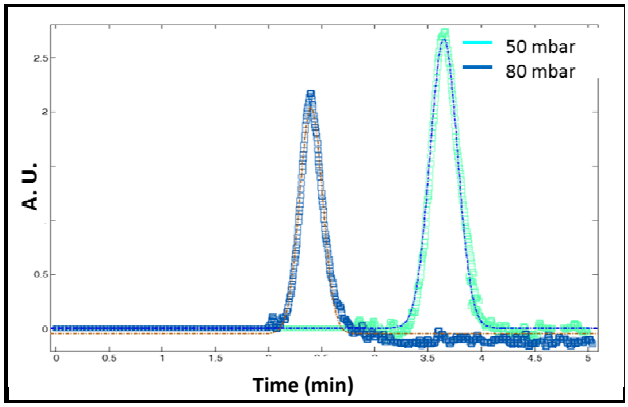

Figure 3.6: Solute pulse for AuNPs β-CDSH 0,1% p/v in MQ water. Capillary: 75 µm inner diameter, 50 cm PVA coated capillary (detection length, 8.5 cm). Background electrolyte (BGE) phosphate 50 mM pH 7. Hydrodinamic injection: 50 mbar for 5 s. Temperature: 25 °C. Absorbance detection wavelength: 214 nm

Successively we studied the interaction between the considered compounds. At this purpose a mixture of AuNPs β-CDSH and DC in ratio 1:1 was prepared, stirred one

hour with vortex and then analysed with solute pulse injection. In figure 3.7 is reported a comparison between the solute pulses of DC and AuNPs β-CDSH alone and two mixtures with different concentration of DC with the relative fittings obtained with equation 3.3.

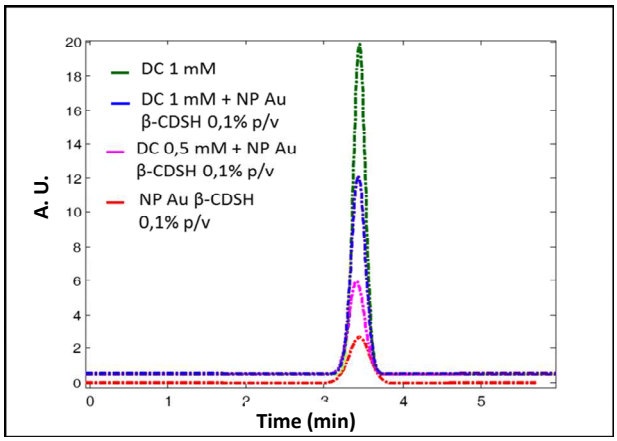

Figure 3.7: Solute pulse for DC 1 mM in phosphate 50 mM pH 7, AuNPs β-CDSH 0,1% p/v in MQ water and two mixtures with different concentrations of DC. Capillary: 75 μm inner diameter, 50 cm PVA coated capillary (detection length, 8.5 cm). Background electrolyte (BGE) phosphate 50 mM pH 7. Hydrodinamic injection: 50 mbar for 5 s. Mobilization pressure: 50 mbar. Temperature: 25 °C. Absorbance detection wavelength: 214 nm

As reported in section 3.2.1, when TDA is use in combination with a commercial CE instrument, is necessary to make a correction for the initial ramp in fluid velocity. As reported by D'Orlyé et al. in 2008 a series of measurements were realized and, obtained the mean residence time t_R and the temporal variance σ^2 of each elution profiles were by fitting the solute and/or front concentration profile to the appropriate equation, the values were plotted (t_R VS. σ^2). The plot for solute pulse injections (figure 3.8) of DC reveals a linear relationship between both temporal moments.

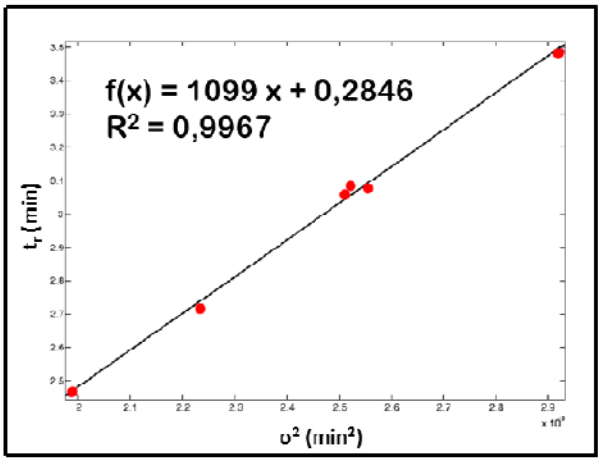

Figure 3.8: correction for the initial velocity ramp for DC 1 mM in phosphate 50 mM pH 7. Capillary: 75 µm inner diameter, 50 cm silica bare capillary (detection length, 8.5 cm). Background electrolyte (BGE) phosphate 50 mM pH 7. Hydrodinamic injection: 50 mbar for 5 s. Mobilization pressure: from 50 to 100 mbar. Temperature: 25 °C. Absorbance detection wavelength: 214 nm

This correlation could be expected from equation 3.6 for the calculation of D when Taylor's conditions are satisfied. Nevertheless, the fact that the y-intercept does not go past origin demonstrates that the observed residence time t_R results from an average fluid velocity and that a certain period of time is necessary for the fluid flow to reach its steady state. In detail the correction consists in apply equation 3.17 to determine a new corrected value for the residence time (t_R'):

$$t_r' = t_r - (y - \text{intercept}) \qquad (3.17)$$

Successively the obtained value (t_R') is inserted in equation 3.6 for the calculation of D (but only if Taylor's conditions are satisfied).

The dimension of capillary inner diameters was verified with two different methodologies.

In the first method, reported by D'Orlyé et al. in 2008 the capillary was first filled with phosphate 50 mM pH 7 by flushing the capillary for 10 min. Then a short plug of a flow marker (dimethylformamide 0.04% v/v in phosphate 50 mM pH 7) was hydrodynamically injected (50 mbar, 5 s) and displaced by flushing the BGE under two different mobilization pressure (60 and 80 mbar) until reaching detection window.

On the other hand, the second method, consists in flushing the capillary with water for 20 minutes and collect the water in an empty vial to weigh it. This value was converted in a volume knowing the density of water and after that in a flow rate.
In both case, using equation 3.18:

$$R_c^2 \Delta P = \frac{32 L_d L_c \eta}{t_r} \tag{3.18}$$

where R_c, ΔP, η and t_r have the same meaning of the previous equations, L_d and L_c are the detection and the total length of the capillary, respectively; the radius (and so the diameter) of the capillary were measured.
Table 3.1 resumes the results obtained with the two method.

	Used method	
Theorical diameter	**D'Orlyé et al. 2008**	**Water weighed**
50 µm	49.5 µm	49.8 µm
75 µm	74.4 µm	74.4 µm

Table 3.1: values of the capillary inner diameters

Instead in table 3.2 the values of diffusion coefficients obtained with the developed TDA-CE method and the calculated capillary inner diameters are reported.

Sample	τ (>1,4)	Pe (>70)	D * 10^{-10} (m^2 s^{-1})	D * 10^{-10} (m^2 s^{-1}) Literature	Ligand fraction	R_H (nm)
dC *	164	78	4.8 ± 0.1	4.8 (1)		
dC #	114	98	4.8 ± 0.1			
Au-βCDSH *	58	219	1.7 ± 0.1	1.7		1.44
Au-βCDSH #	42	268	1.7 ± 0.1			
Au-βCDSH-dC (10 mM) *	157	81	4.4 ± 0.1		0.12	
Au-βCDSH-dC (1 mM) #	85	132	3.5 ± 0.1		0.41	
Au-βCDSH-dC (0.5 mM) #	70	160	2.9 ± 0.1		0.60	

Table 3.2: τ, Pe, diffusion coefficient, ligand fraction and hydrodynamic radius values.
(*Capillary: 49.5 µm inner diameter, 40 cm TDA coated capillary
Capillary: 74.4 µm inner diameter, 50 cm silica bare capillary
(1) [Uccello-Barretta et al. 2011])

Observing table 3.2 it can be note that Taylor ideality conditions were always satisfied and so it was possible to calculate the values diffusion coefficient with equation 3.6. These values were successively compared with NMR measurements reported in literature [Uccello-Barretta et al. 2011] showing a good correlation. This is an important goal of the developed method because, despite the importance of the diffusion coefficient (in particular in biological and pharmaceutical matrices), this physicochemical parameter is not commonly determined experimentally. This is, at least in part, related to the fact the measurements are mostly cumbersome and time consuming.

Because the diffusion coefficient of a substance in a solvent is also related to the size (i.e. the hydrodynamic radius, R_h) of a molecule the good experimental evidence of diffusion coefficients values encouraged us to determine the dimension of AuNPs β-CDSH through the Stokes–Einstein equation:

$$D = \frac{k_B T}{6\pi\eta R_h} \tag{3.19}$$

where k_B is the Boltzmann constant, T is the absolute temperature and η is the viscosity of solution.

Also in this case the value of hydrodynamic radius determined is in good agreement with the AuNPs β-CDSH diameter of 2.9 nm found in literature [Uccello-Barretta et al. 2011].

Finally, for the study of complexation phenomena between Au β-CDSH NPs and DC, the diffusion coefficients of mixtures derived from TDA-CE can be determined as an average value of the individual diffusion coefficients with equation 3.20:

$$D_{obs} = x_1 D_1 + x_{(1-x_1)} D_2 \tag{3.20}$$

where subscripts 1 and 2 indicate the two mixture components (in particular, X_1 indicates the free DC fraction, D_1 is the diffusion coefficient of free DC, $X_{(1-x1)}$ is the bounded DC and D_2 is the diffusion coefficient of Au β-CDSH NPs). In this equation it is assumed that the bounded DC moves like Au β-CDSH NPs.

The diffusion coefficients of mixtures are in agreement with the fact that, when in the mixture in present an high concentration of DC, but only a little part of it (as demonstrated by the ligand fraction values) is bounded to Au β-CDSH NPs, the value is more similar to that of free DC because this one has more importance in the calculation in equation 3.20. In conclusion it was also possible to determine another important parameter to describe the interaction between the selected NPs and the biological molecule that is the ligand fraction.

3.4 TDA OF DOXORUBICIN

An analogue study was made for the interaction between Au β-CDSH NPs and doxorubicin.

In this case the optimization of the instrument configuration did not required the use of PVA coated capillary so a bare silica capillary was used. Moreover, following the same calculations reported in section 3.3, the minimum values of mobilization pressure were determined.

Similarly to what made for DC, also for DOXO alone TDA-CE analysis were made varying different experimental parameters such as capillary length and inner diameter, mobilization pressure and analyte concentration.

In figure 3.9 are reported solute pulse injections for DOXO at four different mobilization pressure (70, 80, 90 and 100 mbar) with the relative fittings obtained with equation 3.3.

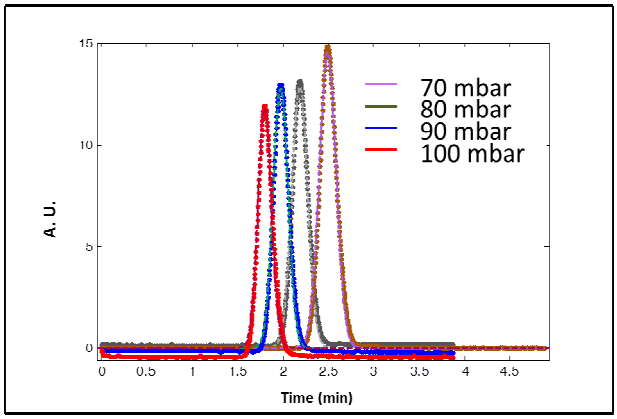

Figure 3.9: Solute pulse for DOXO 0,86 mM in MQ water pH 4. Capillary: 75 µm inner diameter, 50 cm silica bare capillary (detection length, 8.5 cm). Background electrolyte (BGE) phosphate 50 mM pH 4. Hydrodinamic injection: 50 mbar for 5 s. Temperature: 25 °C. Absorbance detection wavelength: 485 nm

The table 3.3 resumes the values of diffusion coefficients obtained with the developed TDA-CE method.

Sample	**τ (>1,4)**	**Pe (>70)**	**D * 10^{-10} (m^2 s^{-1})**
DOXO #	24	470	2.2 ± 0.1

Table 3.3: τ, Pe, diffusion coefficient, ligand fraction and hydrodynamic radius values. (# Capillary: 74.4 µm inner diameter, 50 cm silica bare capillary)

Also in this case it can be note that Taylor ideality conditions where always satisfied and so the diffusion coefficient was determined with equation 3.6.

Future objective of this work is the study of the interaction between AuNPs β-CDSH and DOXO.

CHAPTER 4: ADSORPTION OF ORGANIC POLLUTANTS ON ZEOLITES

With the fast development of various industries, a huge quantity of wastewater produced from industrial processes is discharged into soils and water systems. Wastewater usually contains many pollutants such as cationic and anionic species, volatile organic compounds (VOCs) and polar organic compounds which may have toxic effects on humans. For that which concern VOCs different technologies have been proposed to remove them from the environment [Banat et al. 1996]. Among them, adsorption is a simple and effective technique because of the flexibility of the system, low energy and cheap operation costs.

Nanoporous materials (NPMs), thanks to their large porosity and a very ordered, uniform pore structure, show a very high adsorption capacity which can be used for the removal of contaminants and pollutants from waste gas and water streams [Lu et al. 2004]. In particular, zeolites are NMPs having some desirable properties for environmental applications: they are mechanical and thermal resistant and it has also been reported that they can be thermally regenerated without changing their structure and adsorption properties [Leardini et al. 2014].

The use of natural zeolites for water decontamination (in particular for the removal of cations, heavy metal ions and dyes) has been well documented [Wang et al. 2010]. On the other hand the application of synthetic zeolites with an high SAR for organic contaminant removal has been reported only recently [Cejka et al. 2007; Rossner et al. 2009; Martucci et al. 2014]. For this reason, in this chapter we evaluated the possibility to employ zeolites as adsorbent for some VOCs in aqueous solution with particular attention to the kinetics and the efficiency of the adsorption processes. Additionally, we investigate also the thermal regeneration of zeolites; during this process the zeolite structure was monitored to examine the stability of the adsorbent material at high temperatures. The adsorption properties of the regenerated material were evaluated to verify the possibility for recycling the material. It should be emphasised that this work is the continuation of previous studies in this field of our research group.

Many data which are reported in this chapter are part of my work of thesis and have been recently published: [Martucci A., Rodeghero E., Pasti L., Bosi V., Cruciani G., Microporous and mesoporous materials 215 (2015) 175-182 and Rodeghero E., Martucci A., Cruciani G., Bagatin R., Sarti E., Bosi V., Pasti L., Catalysis today (2015) article in press] (see appendix I). Experimental result related to CB are part of a manuscript in preparation.

In the following part 4.1 the principal properties and applications of the investigated VOCs (DCE, TOL and CB) are reported. MTBE is also described, because it was used for the study of the adsorption of binary mixtures of pollutants which experimental data are reported in chapter 5.

4.1 TARGET MOLECULES

As defined by U.S. Geological Survey in 2005 "VOCs (Volatile Organic Compounds) are organic compounds that can be isolated from the water phase of a sample by purging the water sample with inert gas, such as helium and, subsequently, analyzed by gas chromatography. Many VOCs are human-made chemicals that are used and produced in the manufacture of paints, adhesives, petroleum products, pharmaceuticals and refrigerants. They often are compounds of fuels, solvents, hydraulic fluids, paint thinners, and dry-cleaning agents commonly used in urban settings. VOC contamination of drinking water supplies is a human-health concern because many are toxic and are known or suspected human carcinogens".

Within this category two major classes of pollutants of interest can be distinguished: aromatic and aliphatic compounds. Both classes also include halogenated compounds or compounds containing heteroatoms.

VOCs are produced in large volumes and are associated with a myriad of products, such as plastics, adhesives, paints, gasoline, fumigants, refrigerants and dry-cleaning fluids. Widespread and long-term use of VOCs and their ability to persist and migrate in ground water raise questions about possible adverse effects on the environment. Some of these compounds are only partially removed by conventional water treatment plants and they are found in drinking water. VOCs can be released to the environment and reach ground water through many sources and pathways, including exhaust from gasoline engines, industrial air emissions, leaking storage tanks, landfills, infiltration of urban runoff and wastewater, septic systems and injection through wells. Some of them are known or suspected human carcinogens and their concentrations in drinking water from public water systems are regulated by the U.S. Environmental Protection Agency [US EPA 1998].

In table 4.1 are reported some properties of the considered VOCs.

Compound	MW (g mol^{-1})	Log K_{ow}	Solubility in water (g L^{-1})	Molecule volume ($Å^3$)
TOL	92.14	2.73	0.47	98.87
MTBE	88.15	1.2	26	105.60
DCE	98.95	1.48	8.7	73.30
CB	112.56	2.84	0.5	95.95

Table 4.1: properties of the selected pollutants

4.1.1 BTEX

Environmental Protection Agency in 2010 stated that "BTEX is the term used for benzene, toluene, ethylbenzene and xylene-volatile aromatic compounds typically found in petroleum product, such as gasoline and diesel fuel". European Environment Agency in 2010 defined "BTEX as a group of chemicals which is quantified by one analytical method...Toluene, ethylbenzene and the three isomers of xylene are colourless liquids, immiscible with water but miscible with organic solvents. They have a characteristic strong odour and are highly flammable".

BTEX are made up of naturally occurring chemicals that are found mainly in petroleum products such as gasoline and in many of the common household products we use every day. The primary man-made sources of BTEX into the environment are via emissions from motor vehicles and aircraft exhaust, losses during petrol marketing, spills and cigarette smoke. They are created and used during the processing of refined petroleum products and coal and during the production of chemical intermediates and consumer products such as paints and lacquers, thinners, rubber products, adhesives, inks, cosmetics and pharmaceutical products.

Besides the common daily exposures to BTEX, larger amounts can enter the environment from leaking underground storage tanks, fuel spills from accidents and from landfills. Another way of water contamination is by the introduction into water by industrial effluents and atmospheric pollution, but releases of BTEX to water are mainly related to spills of petrol and petroleum products or proximity to natural deposits of petroleum and natural gas. The majority released into the environment enter the atmosphere directly and usually evaporate quickly but they also easily move through soils and can reach the groundwater, contaminating water systems and the soils in between.

For the removal of BTEX from water various techniques can be used: bioremediation [Sorensen 1996; Yadav et al. 1993], adsorption onto activated carbon [Heilshorn, 1991; Clark et al. 1991], packed tower aeration [Ball et al. 1992; Niramalalakhandan et al. 1991], oxidation [Frank 1987] membrane techniques [Banat et al. 1996] and also oxidative processes with UV/H_2O_2 have been proposed [Daifullah et al. 2004].

4.1.1.1 TOLUENE

Toluene (figure 4.1) is a clear colorless liquid possessing high vapor pressure and low to moderate water solubility with a distinctive smell.

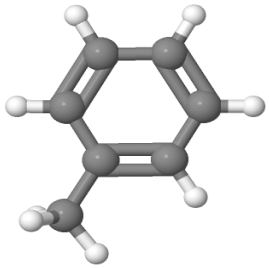

Figure 4.1: structure of toluene

It is produced from the catalytic reforming of refinery streams and its principal use is as solvent used in making paints, paint thinners, fingernail polish, lacquers, adhesives and rubber, in some printing and leather tanning processes and in the production of benzene, nylon, plastics, polyurethane, trinitrotoluene (TNT), benzoic acid, benzoyl chloride and toluene diisocyanate. It is also added to gasoline along with benzene and xylene to improve octane ratings.

Toluene can be released into the air, water and soil where it is produced or used. It is commonly found in air, particularly when there is heavy vehicular traffic, it can enter surface waters and groundwater from solvent and petroleum products spills and can also leak from underground storage tanks at gasoline stations and other facilities (for example when toluene-containing products are placed in landfills or waste disposal sites). It is one the main pollutants of the Mediterranean Sea.

When enter the environment it readily evaporates into the air or it is broken down in surface water primarily by anaerobic microorganisms. Once in the atmosphere, it is principally degraded by reaction with photochemically generated hydroxyl radicals, but

also through reaction with nitrate radicals and ozone. Toluene does not bioconcentrate or bioaccumulate significantly in aquatic organisms.

About human health effect this compound may have a temporary effect on nervous system, such as headaches, dizziness or unconsciousness. However, effects such as incoordination, cognitive impairment and vision and hearing loss may become permanent with repeated exposure, especially at concentrations associated with intentional solvent abuse. High levels of exposure during pregnancy may lead to retardation of mental abilities and growth in children. Other health effects of potential concern may include immune, kidney, liver and reproductive effects such as an increased risk of spontaneous abortions.

4.1.2 1,2 DICHLOROETHANE

1,2-dichloroethane (figure 4.2) is a clear liquid which most common use is to make vinyl chloride, which is used to make a variety of plastic and vinyl products including polyvinyl chloride (PVC) pipes and other important construction and packaging materials, furniture and automobile upholstery, wall coverings, housewares and automobile parts.

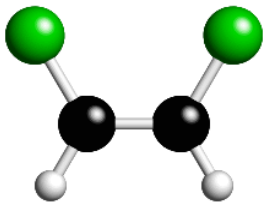

Figure 4.2: structure of DCE

It is mainly used as a solvent and is added to leaded gasoline to remove lead. In the past, it was also found in small amounts in products that industries used to clean cloth, remove grease from metal and break down oils, fats, waxes, resins and rubber. In the household, it was formerly a component of some cleaning solutions, pesticides, adhesives, such as those used to glue wallpaper or carpeting and some paint, varnish and finish removers.

Small amounts of 1,2-dichloroethane released into water or soil evaporate quickly into the air while the amount that remains in soil from a spill or improper disposal can travel through the ground into water. When released in the air, it breaks down by reacting with

other compounds formed by the sunlight and it may also be removed from air in rain or snow. Since it stays in the air, the wind may carry it over large distances. In water, only very small amounts are taken up by plants and fish.

Humans are exposed to 1,2-dichloroethane mainly by breathing air or drinking water that contains it. However, low levels have also been found in the air near industries where it is made or used in manufacturing. Another way of human exposition to low levels is through the skin or air by contact with old products which contains it but such exposure is probably not enough to cause harmful health effects. People who were accidentally exposed to large amounts of 1,2-dichloroethane often developed nervous system disorders, liver and kidney disease and lung effects such as central nervous system depression, nausea and vomiting, corneal opacity, bronchitis, respiratory distress, lung congestion, myocardial lesions, hemorrhagic gastritis and colitis, increased blood clotting time, hepatocellular damage, renal necrosis and histopathological changes in brain tissue.

4.1.3 FUEL OXIGENATED COMPOUND

U.S. Environmental Protection Agency in 2009 defined "Fuel oxygenates as a group of chemicals that raise the oxygen content of gasoline. The presence of oxygen optimizes oxidation during fuel combustion, resulting in a more complete burn and a reduction of harmful tailpipe emissions of partially oxidized gasoline components from motor vehicles". The employ of this compounds as gasoline additives dates back in 1990 with the approval of Clean Air Act amendments.

Oxygenated compounds are either alcohols (such as methanol, ethanol and tert-butyl alcohol (TBA)) or ethers (such as methyl tert-butyl ether (MTBE), ethyl tert-butyl ether (ETBE) and tert-amyl methyl ether (TAME)).

The transportation, transfer and especially storage of oxygenated fuel in underground tanks present a risk to the environment. Leaks and spillage can contaminate ground and waters, representing a significant threat to drinking-water supplies.

4.1.3.1 METHYL TERT-BUTYL ETHER

Methyl tert-butyl ether (figure 4.3) is relatively volatile, moderately soluble in water and very soluble in some organic solvents (for example alcohol and ether), flammable liquid.

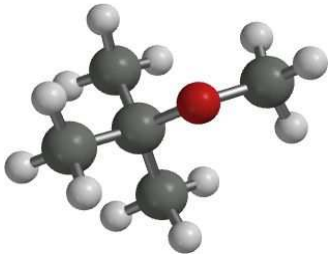

Figure 4.3: structure of MTBE

As stated before the principal use of MTBE is as a fuel oxygenating agent. In fact most of it is mixed with gasoline. It is employed in small quantities as a laboratory reagent to extract semi-volatile organic compounds from such sample types as leachates or solid wastes and it is also a pharmaceutical agent, which can be used as an alternative to surgery in dissolving gallstones when injected intraductally [Bergman et al. 1994; Eidson et al. 1993].

Methyl tert-butyl ether is of particular concerns in water pollution due to its high aqueous solubility and high vapour pressure (about 50 g L^{-1} and 245 mmHg at 25° C, respectively). MTBE is toxic and is a potential human carcinogen, moreover it is not readily biodegradable in natural environment. The U.S. Environmental Protection Agency (EPA) has placed MTBE on the drinking water contaminant candidate list for future and has estimated that its levels in drinking water based on organoleptic effects should not exceed 20 µg L^{-1} in terms of odour and 40 µg L^{-1} in terms of taste.

4.1.4 CHLOROBENZENE

Chlorobenzene (figure 4.4) is volatile and moderately soluble in water liquid with an almond-like odor.

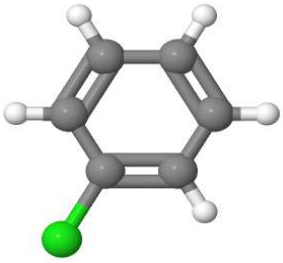

Figure 4.4: structure of chlorobenzene

It is produced by the chlorination of benzene in the presence of a catalyst. This process yields a mixture of chlorobenzene, dichlorobenzene and higher analogues which are distilled and crystallized to obtain pure products [Hughes et al. 1983]. The current primary uses of chlorobenzene are as a solvent for pesticide formulations, diisocyanate manufacture, degreasing automobile parts and for the production of nitrochlorobenzene; the past major use was as an intermediate in phenol and dichlorodiphenyltrichloroethane (DDT) production [Hughes et al. 1983].

Chlorobenzene persists in soil, air and water, adsorbs moderately to soil and is biodegraded comparatively rapidly. The air plays a large role in the environmental transport and degradation of this compound while in water biodegradation is therefore the major degradation process and finally, in soils, biodegradation is rapid.

Exposure in humans could occurs in persons living or working in the vicinity of hazardous waste sites if emissions to water, air and soil are not adequately controlled. Workers exposed to high levels of chlorobenzene complained of headaches, numbness, sleepiness, nausea and vomiting. Moreover this compound can cause severe injury to the liver and kidneys.

4.2 RESULTS

The study of adsorption process of organic pollutants on two different zeolite, ZSM-5 and Y, has been carried out by considering different aspects: kinetics, thermodynamics and the structural modification of the adsorbent material.

Today, adsorption kinetic study still attracts considerable interest because of its particular significance in adsorbent evaluation and application. Kinetic analysis are useful not only for the determination of the time required for completion of adsorption reaction, but also for the description of the mechanism of the process.

Additionally, the adsorption isotherms are usually employed to compare the adsorption capacity of adsorbents for given substances and for characterizing the adsorption system. The isotherms for the adsorption systems investigated were obtained with batch method and the experimental results were fitted by the different models reported in chapter 1.

As stated before another important aspect is the thermodynamics of the phenomena because it also provide very useful information to the adsorption mechanisms. The spontaneity of adsorption process based on these parameters has been reviewed [Milonjic 2007] predicting certain optimum condition for the feasibility of adsorption

process and investigating the range of temperature at which the adsorption process is favourable or unfavourable. For this reason, an investigation of the adsorption at different temperatures, ranging from the typical temperature of surface waters and groundwaters, was made to evaluate the applicability of zeolites in the adsorption of VOCs contaminants in natural waters.

To better understand VOCs adsorption, a structural investigation of the pollutant-zeolite system was accomplished using Rietveld refinement of in situ synchrotron X-Ray powder diffraction data collected in a 30° - 600° C temperature range. This study have allowed to obtain detailed structural information relating to the cell parameters, deformations undergone by the zeolite framework, the position of the extraframework sites, the orientation and the occupancy of molecules guests with which it was possible to enhance the adsorption results using a model which better describe the considered system.

Finally the possibility of a zeolites re-use in different adsorption cycles was evaluated by examining the adsorption properties of the regenerated materials.

4.2.1 ADSORPTION KINETICS

The uptake of VOCs vs time at different initial concentrations was measured. For instance in figure 4.5, the adsorbed quantity of TOL as a function of the contact time is reported, it can be noticed that the kinetic of the process is very fast; the time to reach the equilibrium was only 15 min. This trend has been observed also for other VOCs. Adsorption is initially rapid and then constant, probably due to a greater abundance of adsorption sites available for adsorption during the initial stage.

Various kinetic models have been suggested for describing adsorption processes. Among these, Lagergren's pseudo first order kinetics (PFO) and pseudo second order kinetics (PSO) are those commonly employed to investigate adsorption onto zeolites. These models are mathematically described in equations 4.1 and 4.2:

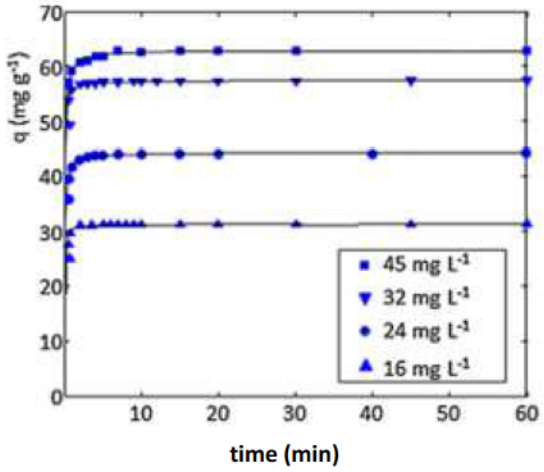

Figure 4.5: TOL uptake on ZSM-5 at different initial concentrations

$$q = q_e[1 - \exp(-k_1 t)] \tag{4.1}$$

$$q = \frac{k_2 q_e^2 t}{1 + k_2 q_e t} \tag{4.2}$$

where q is the amount of solute per unit mass of adsorbent at time t, q_e is the equilibrium value of q, k_1 and k_2 are the PFO and PSO rate constant, respectively.

According to the theoretical analysis proposed by Azizian [Azizian et al. 2008], PFO model better describes adsorption from a solution with a high initial solute concentration, while for initial solute concentrations which are not too high, a sorption PSO fit is generally better. It has also been demonstrated that for systems which are characterized using the PFO model, the observed rate constant is a linear function of the initial solute concentration; whereas the observed rate constant is a complex function of initial solute concentration for PSO kinetics systems. Table 4.2 reports correlation coefficients (R^2), kinetic parameters (k_1, k_2) and calculated $q_{e,cal}$ values obtained by non-linear regression for both models.

		Pseudo-first-order			Pseudo-second-order		
C_0 (mg L^{-1})	**$q_{e,exp}$ (mg g^{-1})**	**k_1 (min^{-1})**	**$q_{e,cal}$ (mg g^{-1})**	**R^2**	**k_2 (g mg^{-1} min^{-1})**	**$q_{e,cal}$ (mg g^{-1})**	**R^2**
16	31.3	9.48	32.1	0.8774	1.68	31.1	0.9934
24	43.9	5.123	43.8	0.8253	0.723	44.2	0.9705
32	57.4	3.821	56.1	0.7767	0.539	57.4	0.9121
45	62.8	2.891	64.1	0.6361	0.159	63.1	0.9233

Table 4.2: Kinetic parameters for the adsorption of TOL onto the ZSM-5

R^2 comparison, obtained for PFO and PSO, suggests that TOL adsorption onto ZSM-5 takes place according to the pseudo second order kinetic model. Moreover, TOL uptake fit on ZSM-5 at 25° C for different initial TOL concentrations in an aqueous solution revealed that the PSO dependence rate constant on the equilibrium concentration follows a complex trend (see figure 4.6).

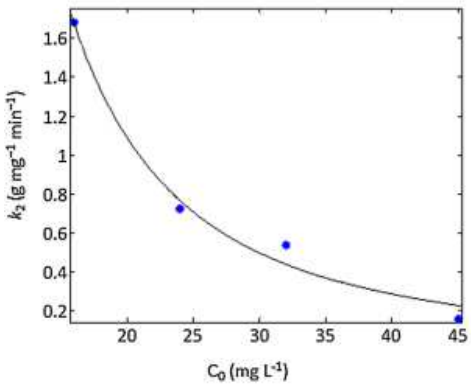

Figure 4.6: Pseudo second order kinetics constant vs. TOL equilibrium concentration

Thus, the PSO model was confirmed [Azizian et al. 2008; Rudzinsky et al. 2006].
In addition, the intraparticle diffusion model was applied in order to identify the adsorption steps:

$$q = k_{i,d} t^{1/2} + c_i \tag{4.3}$$

where k_i is the intraparticle diffusion rate constant and c_i is a constant for the i-th step. Figure 4.7 shows the intraparticle diffusion plots for adsorption for C_0 45 mg L^{-1}.

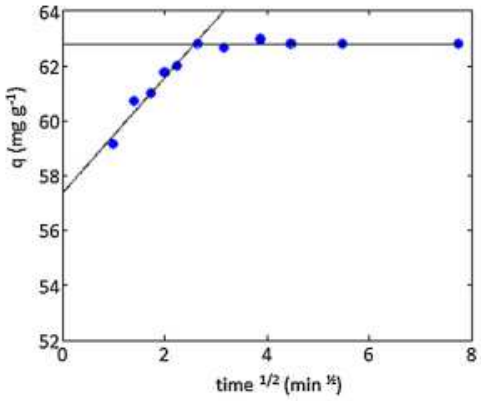

Figure 4.7: Intraparticle diffusion plots for adsorption (C_0 45 mg L^{-1})

As shown, the two-phase plot suggests that the adsorption process proceeds by surface adsorption and TOL intraparticle diffusion into the zeolite micropores. By comparing the slopes of the two lines, it can be observed that $k_{1,d}$ is larger than $k_{2,d}$ (data are reported in table 4.3) for all the investigated concentrations, indicating that film diffusion is a more rapid process than intraparticle diffusion [Ai et al. 2011].

C_0 (mg L^{-1})	**$ki_{,1}$ (mg g^{-1} $min^{-1/2}$)**	**C_1 (mg g^{-1})**	**R^2**	**$ki_{,2}$ (mg g^{-1} $min^{-1/2}$)**	**C_2 (mg g^{-1})**	**R^2**
16	0.54	28.8	0.9647	0.052	31.3	0.8553
24	1.01	41.2	0.8972	0.083	43.9	0.8676
32	1.62	53.1	0.9823	0.081	57.4	0.8662
45	2.11	57.3	0.9637	0.091	62.8	0.8755

Table 4.3: Intraparticle diffusion model parameters for the adsorption of toluene on ZSM-5

Moreover the intercept (C_i value) is significantly different from zero, confirming that the studied zeolites have a high level of initial adsorption.

For that which concerns CB adsorption on ZSM-5 the results of kinetic study are shown in figure 4.8.

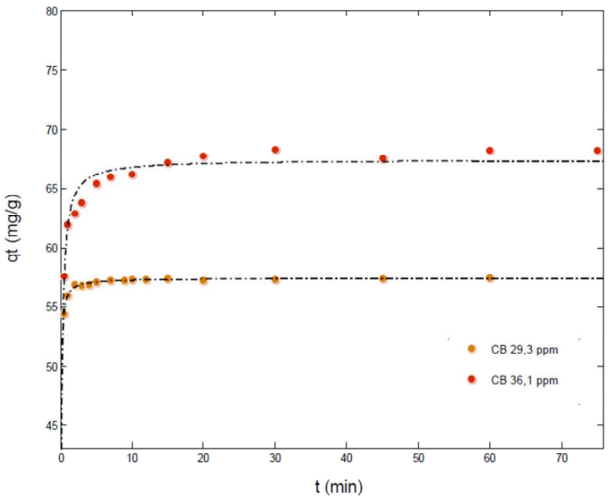

Figure 4.8: CB uptake on ZSM-5 at different contact time for two CB concentrations

Similarly to TOL, also for CB the adsorption process is very fast and, and follows a PSO model. The kinetic parameters obtained by non linear fitting are reported in table 4.4.

CB	**36.1 mg L^{-1}**	**29.3 mg L^{-1}**
k_2 (g/mg·min)	0,1591	0,6497
q_e (mg/g)	67,38	57,37
R^2	0,9154	0,9863

Table 4.4: Kinetic parameters for the adsorption of CB onto the ZSM-5

4.2.2 ADSORPTION ISOTHERM

The experimental isotherm for TOL on ZSM-5 at 22.5° C is reported in figure 4.9.

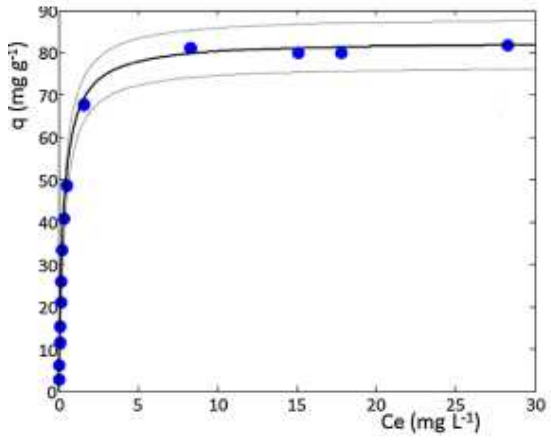

Figure 4.9: TOL uptake on ZSM-5

It can be se that the isotherm shows a Langmuirian shape and for this reason data were fitted to Langmuir (equation 1.2 in chapter 1) and a bi-Langmuir (equation 1.5 in chapter 1) models, which were employed to describe the adsorption of different organic compounds on ZSM-5 [Hansen et al. 2009]. The estimated parameters from non-linear fitting are shown in table 4.5.

	b (L mg^{-1})	**q_S (mg g^{-1})**	**R^2**
Langmuir	3.17 (2.76, 3.59)	82 (77, 87)	0.9565
Bi-Langmuir	2.70 (2.27, 3.14)	65 (61, 70)	0.9865
	3.36 (2.91, 3.80)	26 (22, 30)	0.9865

Table 4.5: Langmuir isotherm parameters for the adsorption of toluene on ZSM-5

The determination coefficients (R^2) of the Langmuir isotherm are not significantly different from the bi-Langmuir isotherm. Since the difference in goodness of fitting parameters for the two isotherm models is not significant, the simplest model (i.e. Langmuir isotherm) can be employed. Moreover, the monolayer adsorption capacity determined using the Langmuir isotherm is about 82 mg/g which approaches experimental data (81.6 mg/g).

The equilibrium parameter R_L [Weber et al. 1974] was given by:

$$R_L = \frac{1}{1 + bC_0} \tag{4.4}$$

where C_0 is the initial concentration.

The determined R_L values are in the 0.009-0.45 range, indicating that TOL adsorption onto ZMS-5 is favourable ($0 < R_L < 1$).

About CB adsorption, isotherms on Y zeolite and ZSM-5 are reported in figure 4.10 and 4.13 respectively.

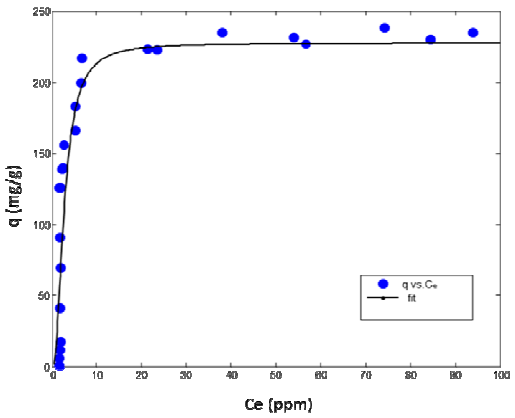

Figure 4.10: CB adsorption isotherms on Y zeolite

Experimental data for Y zeolite were fitted with the Fowler-Guggenheim/Jovanovic-Freundlich (equation 1.12 in chapter 1) isotherm model and the resulted parameters are reported in table 4.6.

		R^2
Fowler-Guggenheim/Jovanovic-Freundlich		
a	229 (212.1, 246)	0.9273
b_1	0.38 (0.34, 0.41)	
c	3.42 (2.10, 4.74)	

Table 4.6: Isotherm parameters for the adsorption of CB on Y zeolite

On the other hand experimental data for ZSM-5 were fitted with the Langmuir isotherm model and the resulted parameters are reported in table 4.7.

	b ($L\ mg^{-1}$)	**q_S ($mg\ g^{-1}$)**	**R^2**
Langmuir	2.7 (2.3, 3.1)	74 (71, 78)	0.9831

Table 4.7: Isotherm parameters for the adsorption of CB on ZSM-5

Comparing the experimental data it can be noticed that CB is efficiently absorbed on ZSM-5 in particular in the range of low concentrations, while the adsorption on Y zeolite is relatively poor. On the other hand, Y zeolite adsorbed very effectively at higher concentrations with saturation values about three times more respect to ZSM-5.

4.2.3 POLLUTANT UPTAKE AT DIFFERENT TEMPERATURES

DCE adsorption isotherms at four different temperatures are shown in figure 4.11 and the relative fitting parameters are reported in table 4.8.

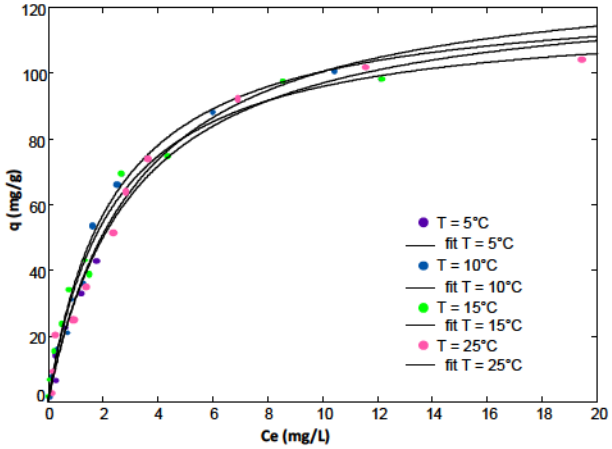

Figure 4.11: Adsorption isotherms of DCE on ZSM-5 at four temperatures

Temperature (° C)	b (L/mg)	qs (mg/g)
25	0.18	121
15	0.362	120
10	0.5922	120
5	0.8595	122

Table 4.8: Parameters estimated by non linear fitting, according to Langmuir model, of DCE adsorption on ZSM-5 at four temperatures. The confidence limits at 95% of probability of parameters are reported in brackets

It could be noted that the q_S values are not statistically different in the considered temperature range, while the adsorption constant b increases as temperature decreases and, therefore, adsorption is exothermic for these systems.

Since the b parameter represents the equilibrium constant (K_{ads}), it is possible to substitute its value into the Van't Hoff equation (equation 4.5), in order to calculate the enthalpy of the adsorption process.

$$\frac{\ln K_{ads,2}}{\ln K_{ads,1}} = -\frac{\Delta H}{R}\left(\frac{1}{T_2} - \frac{1}{T_1}\right) \qquad (4.5)$$

where $K_{ads,2}$ and $K_{ads,1}$ are the equilibrium constants at temperatures T_2 and T_1, respectively, ΔH is the enthalpy change for the process and R is the universal gas constant. The resulting Van't Hoff plot is shown in figure 4.12.

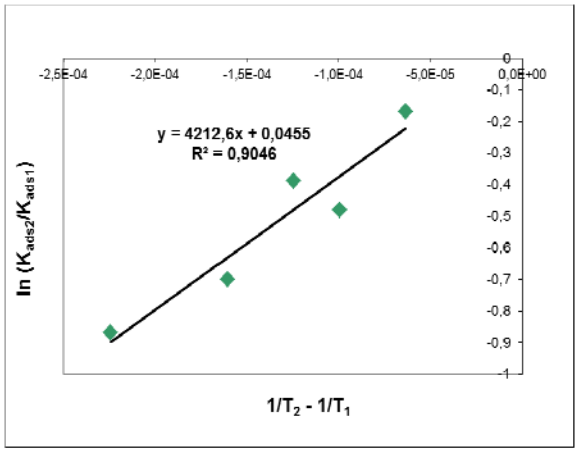

Figure 4.12: Van't Hoff plot for DCE adsorption on ZSM-5

By multiplying the slope and the gas constant, a ΔH value of -35 kJ mol^{-1} has been obtained. This value is in agreement with some literature data: Intriago et al. [Intriago et al. 2006] used IGC experiments to find that the adsorption enthalpies on H-ZSM-5 for DCM (-58 kJ mol^{-1}) and TCE (-55 kJ mol^{-1}).

Since the Henry's constant, enthalpy and temperature are known, the process entropy change (ΔS) can be calculated for each temperature using equation 4.6:

$$-RT\ln K_{ads} = \Delta H - T\Delta S \qquad (4.6)$$

The mean value obtained for ΔS is -33 J mol^{-1} K^{-1}.

A similar investigation was made for the CB-ZSM-5 system. The adsorption isotherms at four different temperatures are shown in figure 4.13 and the relative fitting parameters are reported in table 4.9.

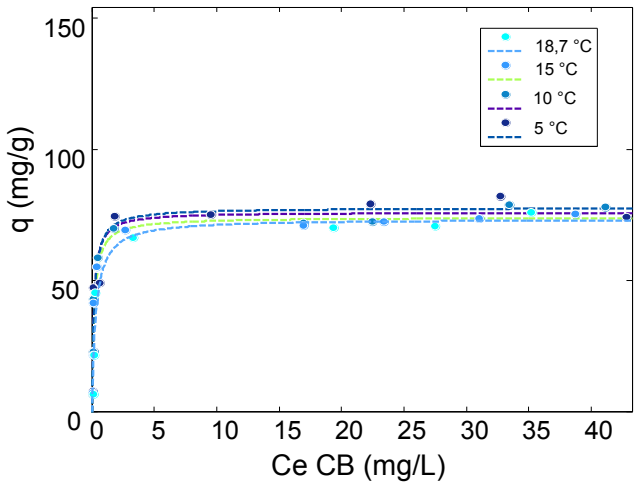

Figure 4.13: Adsorption isotherms of CB on ZSM-5 at four temperatures

Temperature (° C)	**b (L/mg)**	**qs (mg/g)**
18.7	2.7	74
15.0	3.1	74
10.0	4.6	76
5.0	6.4	77

Table 4.9: Parameters estimated by non linear fitting, according to Langmuir model, of CB adsorption on ZSM-5 at four temperatures.

Similirarly to DCE-ZSM-5 system q_S values are not statistically different in the considered temperature range, while the adsorption constant b increases as temperature decreases and, therefore, adsorption is exothermic for these systems.

The Van't Hoff plot, shown in figure 4.14, was determined to obtain the enthalpy of the adsorption process.

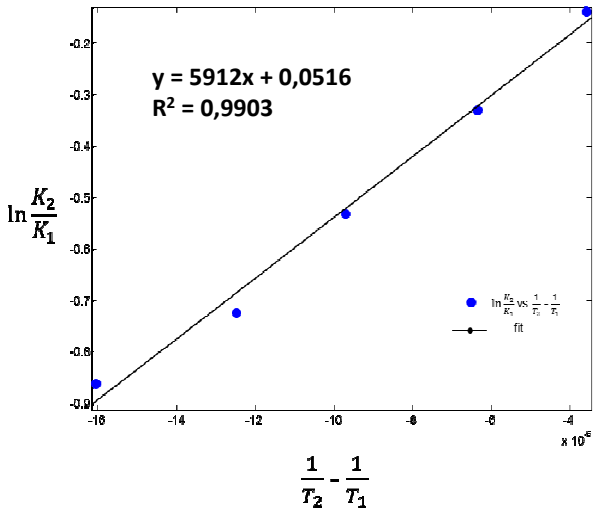

Figure 4.14: Van't Hoff plot for CB adsorption on ZSM-5

By multiplying the slope and the gas constant, a ΔH value of -49 kJ mol^{-1} has been obtained.

Also the process entropy variation (ΔS) was calculated and the mean value obtained for ΔS is -60.9 J mol^{-1} K^{-1}.

4.2.4 IN SITU SYNCHROTRON X-RAY POWDER DIFFRACTION AND RIETVELD REFINEMENTS

For ZSM-5-DCE system the difference Fourier map confirmed the distribution of the DCE molecules over the two crystallographically independent sites (DCE1 and DCE2 sites) (figure 4.15) localized by Pasti et al. [Pasti et al. 2012].

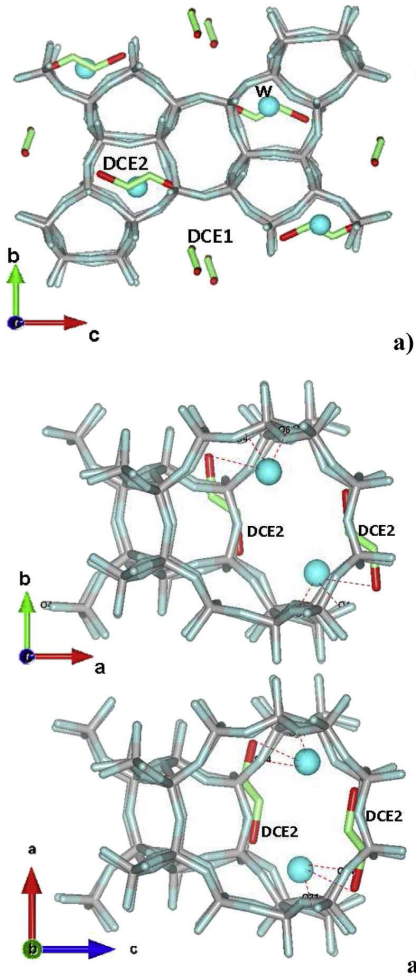

Figure 4.15: Location of DCE and water molecules in ZSM-5 along [100] and [010] directions, in ZSM-5-DCE. Chlorine (red), carbon (green), water molecules (light blue circle), framework oxygens (light blue line) and silicium (green line) atoms are reported.

The sites are located in the straight (DCE1) and sinusoidal (DCE2) channels and the location of co-adsorbed water molecules (W site, ~ 3.0 water/u.c, corresponding to ~ 1.5 % in weight) was also confirmed. DCE molecules (~ 6.5 molecules/u.c., corresponding to ~ 9.5 % in weight) can interact with water thus forming DCE-water molecule complexes (clusters or short chains) bridged via W to framework oxygen atoms.

A similar situation was observed for ZSM-5-TOL system. In this case the two crystallographic independent sites (TOL 1 and TOL2 sites) are located in the straight channel and at the intersection between straight and sinusoidal channels, respectively (figure 4.16).

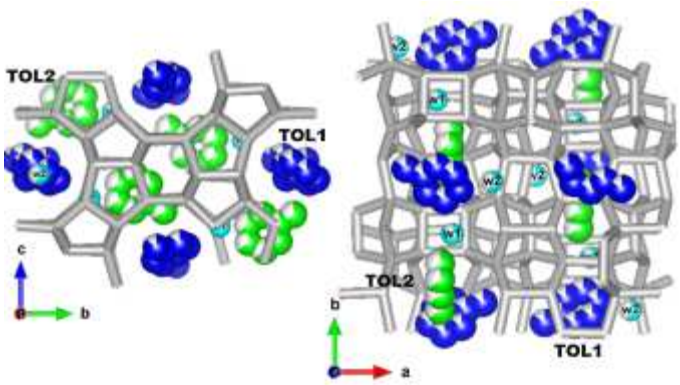

Figure 4.16: Location of toluene and water molecules in ZSM-5 along [001] and [001] directions, respectively

Also co-adsorbed water molecules (W1 and W2 sites, respectively) were detected. On the whole, 6 toluene molecules (which correspond to about 8.55 % in weight) and approximately 2 water molecules (approximately 2.0 % in weight) were localised. The refined distances suggest the presence of water-toluene oligomers interacting with framework oxygens. At the same time, toluene and W1 water molecules are connected to each other to form TOL1-W1-TOL2 molecular oligomer which are bonded to framework oxygen atoms.

Finally, about CB Rietveld structural refinements allowed to localize the molecule inside the two considered zeolites. The positions are shown in figure 4.17 (a) and (b) for ZSM-5 and Y zeolite respectively.

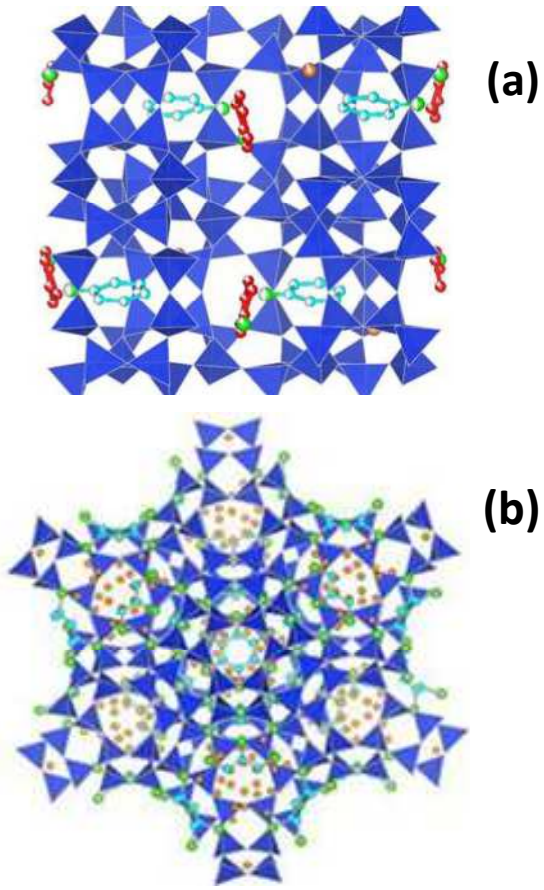

Figure 4.17: Location of CB molecules in ZSM-5 (a) and in Y zeolite (b)

Inside ZSM-5 CB occupies both the sinusoidal and straight channel. On the other hand, inside the Y zeolite it occupies only the interior of the supercage assuming 6 different orientations.

About the content of CB adsorbed by the ZSM-5 is about 10 % by weight and about 23.7 % by weight for Y zeolite. This is in agree with thermal analysis reported in figure 4.18.

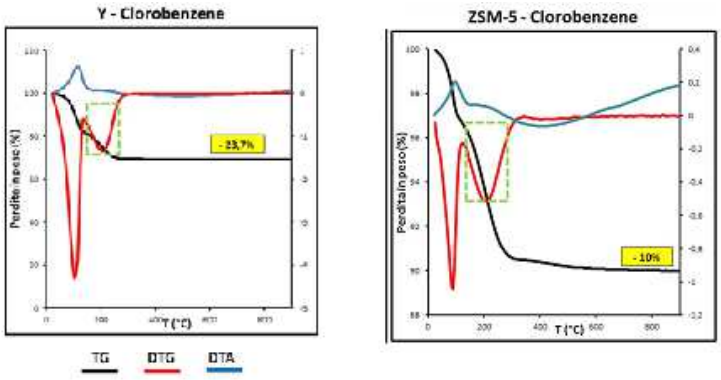

Figure 4.18: TG analysis for Y-CB (left) and ZSM-5-CB (right)

Also CB interacts with co-adsorbed water in the channels, even if present in low concentrations (approximately 3 %), creating complex W-CB interacting with the oxygens of the framework.

The evolution content of pollutant and water molecules was studied in the synchrotron analysis T-range (30°-600° C). The refined occupancies for ZSM-5-DCE are reported in figure 4.19.

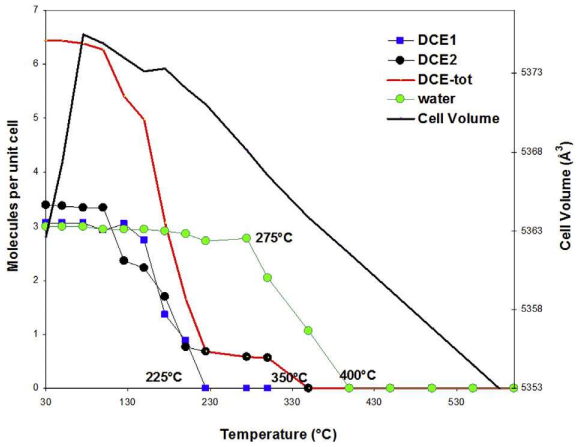

Figure 4.19: Variation of DCE and water molecules per unit cell as a function of temperature

This plot shows that, in the considered temperature range, the DCE1 site progressively decrease its occupancy and it is emptied at a temperature (225° C) lower than that found for the organic hosted in DCE2 site (350° C), which is forced into the sinusoidal channel. At 350° C all sites are emptied, thus confirming the completion of the thermal degradation of DCE at this temperature. A similar behaviour was observed for the water molecules. The parallelism in the decrease of DCE and water occupancies with temperature increase, can be explained by the disassembly of water-DCE clusters caused by the DCE thermal degradation. At temperature higher than 400° C, the host molecule decomposition and expulsion process is completed.

Furthermore, the data reported in figure 4.19 can be also utilized to obtain information of the interaction energies, this investigation will be developed in the close future. A possible relationship to interpret the distribution is based on the Frenkel-De Boer equation [De Boer 1968]:

$$\tau = g_0 \exp\left(\frac{E}{RT}\right) \tag{4.7}$$

where τ is the site distribution (therefore related to the sites occupancy), g_0 is a configurational factor (a constant), E is the (mean) adsorption energy, R is the gas constant and T is the temperature.

An examination of this equation shows that when temperature increases, τ might decrease.

Also for ZSM-5-TOL the organic evolution content as a function of temperature (figure 4.20) shows a similar trend.

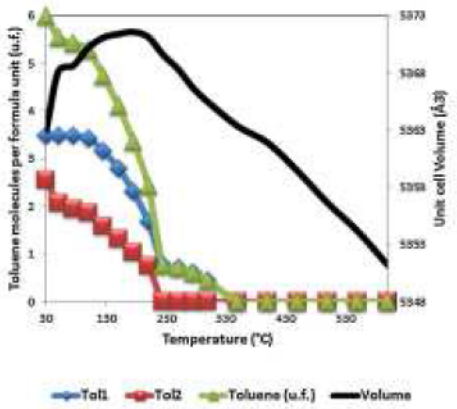

Figure 4.20: variation in TOL molecules per unit cell as a function of temperature

TOL molecules remained confined within the straight channel (TOL1 site) as well as at the intersection between straight and sinusoidal channels (TOL2 site). TOL removal starts in the 75° C < T < 200° C T-range but toluene release is only partially started from the TOL2 site. At T > 250° C TOL1 content was reduced by about 50 % and, at the same time, the TOL2 molecules are almost completely decomposed.

4.2.5 ADSORPTION BEHAVIOUR OF REGENERATED ADSORBENT

After ZSM-5 regeneration (named ZSM-5-r), the structural study indicated that the material retain its original crystallinity.

For this reason ZSM-5-r was tested again for DCE adsorption and in figure 4.21 is shown the comparison between the adsorption performance of fresh and regenerated zeolite.

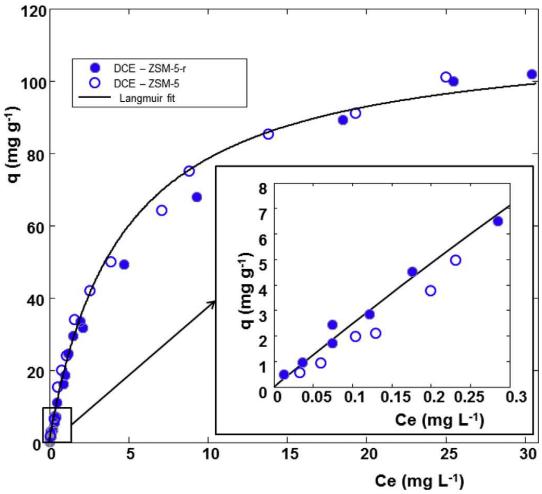

Figure 4.21: Adsorption isotherms of DCE on fresh (ZSM-5) and thermally regenerated (ZSM-5-r) zeolites. The data obtained on the low concentration range are enlarged in the inset

The regenerated sample produced slightly higher adsorption in the low concentration range than the fresh one as shown in the inset of figure 4.21. Possibly, this is due to the decomposition of a low amount of NH_4 in the starting material.

The adsorption data of ZSM-5-r were fitted by using a Langmuir equation and the parameters found for DCE adsorption on regenerated material were not statistically different to those characterizing the fresh material reported in Pasti et al. [Pasti et al. 2012] (see table 4.10).

	b (L mg^{-1})	**q_s(mg g^{-1})**	**R^2**
DCE-ZSM-5-r	0.20 (0.17-0.23)	117 (111-123)	0.9925
DCE-ZSM-5	0.19 (0.16-0.21)	120 (113-127)	0.9927

Table 4.10: Comparison of fitting results of the adsorption data of DCE on regenerated zeolite (ZSM-5-r) and on fresh material (ZSM-5). The fitting parameters are reported together with the confidence limits calculated at 95% of probability

Structural analysis demonstrates that the regenerated and reloaded zeolite does not show any significant crystallinity loss, as well as perfectly regains the unit-cell parameters of fresh material and without any significant deformations in the channel apertures. The

Rietveld refinement indicates minor differences in DCE location and, on the basis of the occupancies, indicates that the organic content remains substantially unchanged thus confirming that, after regeneration, ZSM-5 is able to re-adsorb DCE in amounts comparable to that adsorbed in the first cycle [Pasti et al. 2012]. The occurrence of DCE-water molecule complexes (clusters or short chains) bridged via W to framework oxygen atoms was also confirmed. On the whole, ~ 6.6/u.c. DCE molecules (corresponding to ~ 10.3 % in weight) and ~ 5 H_2O/u.c, (corresponding to ~ 1.5 % in weight) were re-adsorbed in the channels systems.

ZSM-5-r after TOL adsorption was also tested for TOL re-adsorption. The adsorption/desorption cycle was repeated twice on the same material. Figure 4.22 reports the comparison of fresh and regenerated zeolite adsorption capacities.

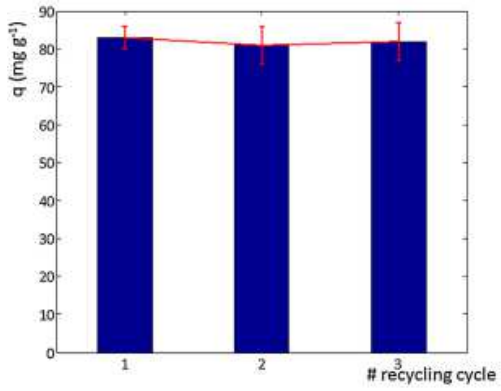

Figure 4.22: TOL saturation capacity vs. number of recycling cycle on ZSM-5 after thermal regeneration

It is clearly shown that the saturation capacity of the regenerated sample does not significantly differ from fresh material.

From the obtained results we can conclude that ZSM-5-r behave as an adsorbent with undiminished adsorption capacity and so the possibility for a re-use of the material with clear benefits on the cost/performance ratio of the whole water treatment process exists.

CHAPTER 5: ADSORPTION OF BINARY MIXTURES OF ORGANIC POLLUTANTS ON ZEOLITES

Chapter 4 reports the results of the studies devoted to prove the efficiency of hydrophobic zeolites in the adsorption of a single component from aqueous solution. However, real samples often contain complex mixtures of hazardous chemicals and their adsorption involve solute-adsorbate interactions and competitive adsorption of water on the adsorbent materials other than adsorbate-adsorbate and the adsorbate-adsorbent interactions. Generally, in the adsorption of mixtures, the adsorbate-sorbent interactions of single components can be altered (i.e. competition occurs) by the presence and quantity of other sorbates and from the solvent. Competitive phenomena can occur when molecules with similar size and polarity are adsorbed on a limited number of sorption sites. Therefore, at low adsorbate concentrations, comparable to those usually found in surface waters, and with low solution/sorbent ratio, competitive interactions are not expected to play a significant role in the adsorption process. However, in the case of a highly concentrated accidental release or during the life time of the adsorbent a full understanding of the competitive interactions among adsorbates would be necessary to predict adsorbent performances.

In literature only few works have been published regarding adsorption of complex mixtures of hazardous chemicals and many of them deals with gaseous mixtures [Pires et al. 2001, Brosillon et al. 2001] or liquid binary mixtures of organic compounds [Denayer et al. 2003]. The literature on the evaluation of competitive adsorption from aqueous solution is relatively scarce, Li et al. in 2010 studied the competitive sorption mechanism of trichloroethene (TCE) and tetrachloroethene (PCE) using different adsorbents.

To gain knowledge on the competitive phenomena that can affect adsorption, the adsorption properties of a commercial hydrophobic zeolite toward binary mixtures of three representative water contaminants chosen as VOCs representative compounds (i.e. methyl tert butyl ether (MTBE), toluene (TOL), and 1,2 dichloroethane (DCE)) was investigate. Additionally, thanks to the different properties of the selected VOCs, this work would provide insight into the zeolite selectivity in the VOCs removal process.

The results presented in this chapter are a relevant part of a manuscript in preparation.

5.1 TARGET MOLECULES

The target molecules used for this part of the work are the same presented in the previous chapter 4 (toluene, 1,2 dichloroetane, methyl tert-butyl ether and chlorobenzene).

5.2 CHARACTERIZATION OF BINARY MIXTURES OF POLLUTANTS BY X-RAY DIFFRACTION

A summary of the location of MTBE, DCE and TOL inside ZSM-5 after adsorption from single component aqueous solutions is given in table 5.1.

Pollutant	Site 1	Site 2
DCE	at the intersection of sinusoidal and straight channels closer to straight channel	in the sinusoidal channel
TOL	at the intersection of sinusoidal and straight channels closer to straight channel	at the intersection of straight and sinusoidal channels
MTBE	near the intersection of sinusoidal and straight channels	in the sinusoidal channel

Table 5.1: summary of pollutants location inside ZSM-5

For sake of simplicity, we gave a general indication about the positions. For the exact localization of the solute molecules, the reader is referred to the tables reporting the lattice parameters and the atomic coordinates.

5.2.1 ZSM-5 LOADED WITH MTBE-TOL AND MTBE-DCE MIXTURES

After MTBE-DCE and TOL-MTBE mixtures adsorption, the ZSM-5 diffraction data are quite similar to those reported for the untreated materials and consequently, unit-cell parameters are not remarkably modified but they suggest the guest molecules entering in the ZSM-5 channels. Considering the geometry of the DCE, MTBE and TOL molecules, the Fourier maps suggest the presence of more than the one molecular species with different orientations in the channel systems.

In MTBE-TOL-ZSM-5 system, TOL molecules are confined only in the TOL1 site (~ 2.8 molecules, corresponding to ~ 4 % in zeolite dw) at the intersection of sinusoidal and straight channels closer to straight channel. TOL2 site (at the intersection near the straight channel) is now empty. Instead MTBE molecules are now confined in MTBE2

site (sinusoidal channel) (~ 3.2 MTBE molecules per unit cell). Thermogravimetric data confirmed this level of incorporation of organics. The total weight loss at 900° C is ~ 13 % dw/w, in very good agreement with the refined occupancies as well as the adsorption data. The TG curve reported a first weight loss below ~ 100° C which can be ascribed to the elimination of species weakly bonded to the surface (~ 3 % zeolite dw/w). Above this temperature, the sudden slope change can be related to the decomposition of extraframework species (MTBE, TOL and water molecules) embedded within the MFI pores (weight loss ~ 10.0 % dw/w).

A similar trend was also observed for MTBE-DCE-ZSM-5. As far as concerns the relative position of the MTBE and DCE molecules inside the structure, two independent extraframework sites are again localised. MTBE (4 molecules p.u.c. corresponding to ~ 5.4 % in zeolite dw) is confined at the intersections of sinusoidal and straight channels (MTBE1 site), whereas DCE (3.3 molecules p.u.c. corresponding to ~ 5 % in zeolite dw) is in the sinusoidal channel (DCE2 site).

Difference Fourier maps calculated for both ZSM-5-DCE-MTBE and ZSM-5-TOL-MTBE revealed the occurrence of a low amount of co-adsorbed water (both ~ 4.0 molecule p.u.c. corresponding to ~ 1 % in zeolite dw). The refined distances between the framework oxygen, water oxygen atoms and organics molecules suggested the occurrence of water-MTBE and water-MTBE-DCE complexes interacting with the framework.

5.3 ADSORPTION FROM BINARY MIXTURES

Isotherm profiles obtained with batch experiments with DCE alone and with a DCE-MTBE mixtures at different ratio are shown in figure 5.1.

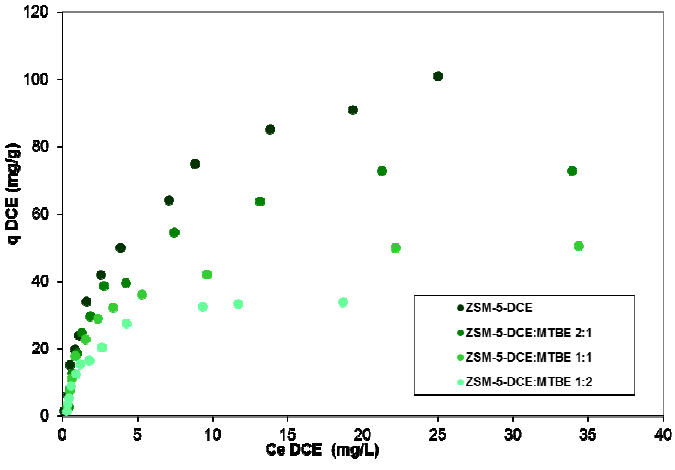

Figure 5.1: comparison of isotherms of DCE alone and DCE-MTBE mixtures

For mixture experiments, it can be noticed that the isotherm profiles for DCE in the presence of MTBE are below isotherm profiles for DCE alone in at least a portion of the measured concentration range, indicating that MTBE and DCE compete in the adsorption onto ZSM-5 within the concentration range shown. In particular the isotherm profiles for DCE alone and for DCE in the presence of MTBE mainly diverge at the highest concentration and then maintain a uniform separation distance thus suggesting that the extent of competition can change with concentration.

A similar trend was also observed for the adsorption of TOL and of TOL-MTBE mixtures at different ratio as demonstrated in figure 5.2.

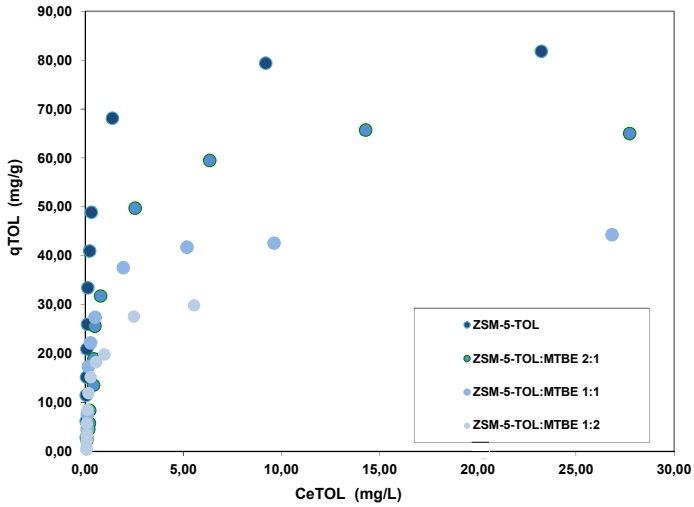

Figure 5.2: comparison of isotherms of TOL alone and TOL-MTBE mixtures

This experimental evidences indicate the competition of the adsorption process of VOCs mixtures on zeolites.

To describe competitive adsorption from liquid phase many models have been proposed and, among them, the Competitive Bi-Langmuir Model (CBLM equation 1.9 in chapter 1) seems the one that better agree with the results of the structural investigation. In fact, two different adsorption sites were localized for all of the three compounds inside the zeolite from unary adsorption systems and the short intermolecular distances between the site occupied in the single component adsorption (MTBE1-DCE2 0.43 (1), MTBE2-DCE1 0.57 (1), MTBE1-TOL2 0.69 (1), MTBE2-DCE1 1.10 (1), TOL1-DCE1 0.58

(1), TOL2-DCE2 0.50 (1)) , clearly prevent their simultaneous occupancy when adsorbed as mixture.

However, from the unary adsorption isotherm, the fitting goodness obtained with a dual sites model does not significantly encompass that obtained with a single site model [Rodeghero et al. 2015].

From this evidence also the classical Competitive Langmuir Model (CLM equations 1.7 and 1.8 in chapter 1) seems to be appropriate to fit the experimental data. This isotherm model has been improved to account of difference in sites availabilities for the components of the mixture by Jain and Snoeyink in 1973 (equations 1.10 and 1.11 n chapter 1); but the situation described in this model is not the case of the selected VOCs. In fact, the saturation capacity (reported in table 5.2) obtained from the single component adsorption isotherms of MTBE, TOL and DCE are roughly similar from each other, in particular, by considering the confidence levels at 95% of probability, they differ of about 10 %, which was considered to be a value acceptable for the applicability of CLM.

Compound	**Saturation capacity (mg g^{-1})**
MTBE	88-100
TOL	77-87
DCE	113-127

Table 5.2: experimental saturation capacities for the selected VOCs

Another methodology often adopted in dealing with adsorption from binary mixtures is the Ideal Adsorbed Solution Theory (IAST) of Myers and Prausnitz [Myers et al. 1965]. However, it has been shown that IAST does not provide reliable results for the adsorption of VOCs onto hydrophobic zeolites, probably due to the fact that these adsorbates have not access to the same area of surface, because the area accessible to each adsorbent is dependent upon the size of the adsorbate or due to framework deformation upon adsorption. For this reason CLM and CBLM have been used to fit experimental adsorption data of organic pollutants mixtures on ZSM-5.

The adsorption of both components of the aqueous binary mixtures on zeolite ZSM-5 at different concentrations have been determined. In figure 5.3 and 5.4 are shown the three dimensional plot of the experimental data of the adsorbed amount of MTBE (q MTBE) or TOL (q TOL) as a function of the concentration of TOL and MTBE, respectively.

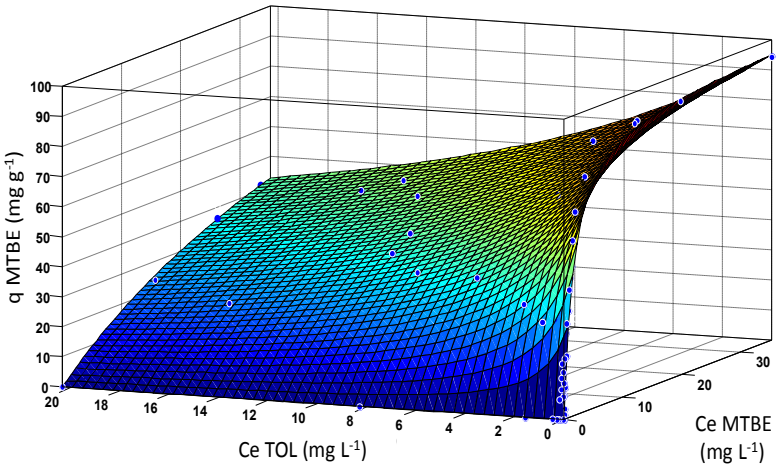

Figure 5.3: 3D plot of q MTBE as a function of the concentration of TOL and MTBE

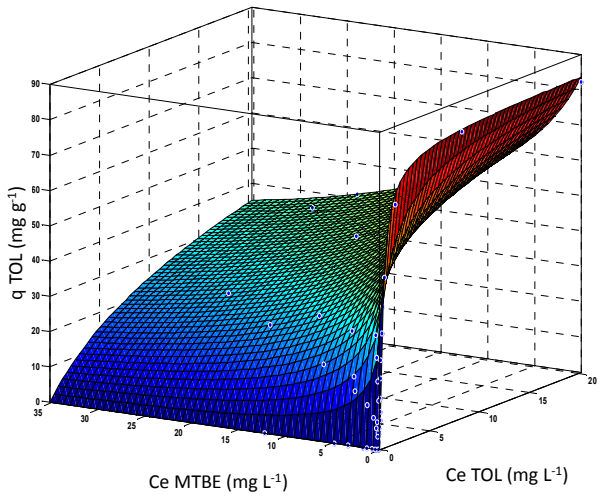

Figure 5.4: 3D plot of q TOL as a function of the concentration of TOL and MTBE

The contour surfaces are the competitive dual site Langmuir isotherms generated by non-linear fitting procedure. The results of estimated parameter for the CBLM and CLM are reported in table 5.3.

				R^2
TOL-MTBE-ZSM-5	**TOL**	**Langmuir**		
		q_s	83.7	0.9476
		B	2.418	
		Bilangmuir		
		$q_{s,A}$	48.2	0.9879
		b_1	0.683	
		$q_{s,B}$	37.1	
		b_2	0.234	
	MTBE	**Langmuir**		0.9374
		q_s	97.7	
		B	0.408	
		Bilangmuir		
		$q_{s,A}$	62	0.9821
		b_1	0.731	
		$q_{s,B}$	38	
		b_2	0.314	
DCE-MTBE-ZSM-5	**DCE**	**Langmuir**		
		q_s	108	0.9146
		B	0.219	
		Bilangmuir		
		$q_{s,A}$	64	0.9759
		b_1	0.283	
		$q_{s,B}$	48	
		b_2	0.144	
	MTBE	**Langmuir**		
		q_s	96.8	0.8926
		B	0.427	
		Bilangmuir		
		$q_{s,A}$	62	0.9721
		b_1	0.661	
		$q_{s,B}$	34	
		b_2	0.247	

Table 5.3: Isotherm parameters for the adsorption of TOL-MTBE and DCE-MTBE on ZSM-5 (at 25 °C).

It can be seen that for binary mixture the determination coefficients (R^2) of the CBLM gave a better fit than CLM. For that which concerns the parameters estimated from fitting it can be seen in table 5.3 that the adsorption capacities well agree with the results of structural refining and the adsorption constant of TOL is higher than that of MTBE and DCE, probably due to its higher hydrophobicity.

The effect of MTBE on the competitive adsorption of TOL and DCE has been also evaluated determining the selectivity (α) applying equation 5.1:

$$\alpha_{1/2} = \frac{D_1}{D_2} \tag{5.1}$$

where D_1 and D_2 represent the distribution coefficient of two solutes, calculated as:

$$D = \frac{q_e}{C_e} \tag{5.2}$$

where q_e is the adsorbed amount at equilibrium and C_e is the concentration at equilibrium.

In figure 5.5 (a) the selectivity for the TOL-MTBE mixture was plotted as a function of C_e TOL and in figure 5.5 (b) the selectivity for the DCE-MTBE mixture as a function of C_e DCE is shown.

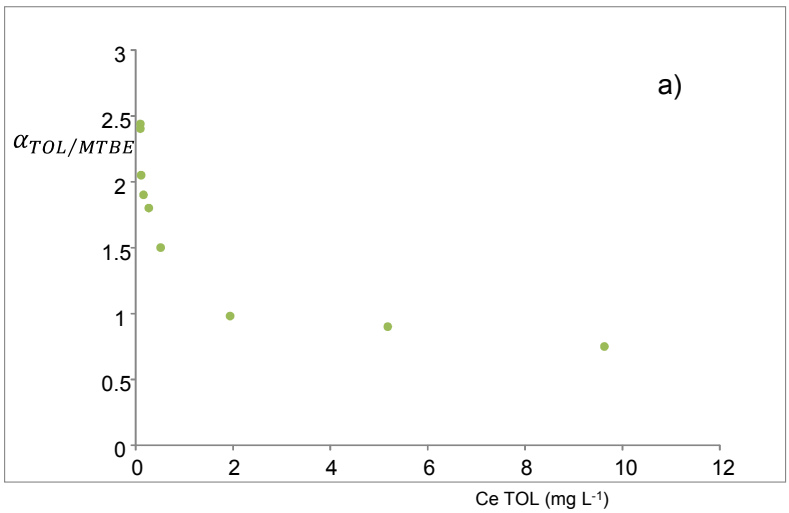

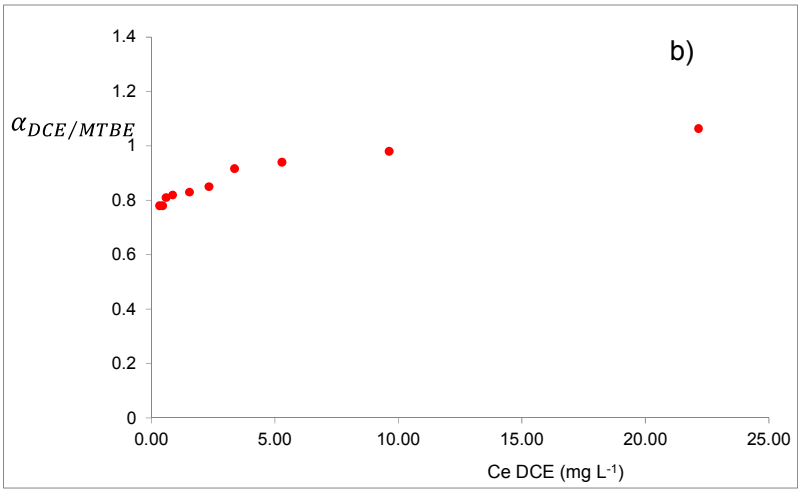

Figure 5.5: selectivity plots of TOL-MTBE mixture (a) and of DCE-MTBE mixture (b)

From figure 5.5 (a) it can be deduced that the ZSM-5 selectivity toward TOL with respect to MTBE decreases with increasing MTBE concentration. At higher concentrations, the adsorption is selective to MTBE which has a higher saturation capacity. In contrast, at low concentration range, zeolite is selective to TOL which has a higher adsorption strength as determined in unary adsorption isotherm.

On the other hand, the selectivity of ZSM-5 for DCE (figure 5.5 (b)) slightly increases with increasing MTBE concentration, thus confirming that the saturation capacities and adsorption constants of these compound are similar.

Focusing our attention in the low concentration range (usually found in surface waters) a selectivity order was obtained: $TOL > MTBE > DCE$.

This means that, in this concentration range, ZSM-5 preferentially adsorbs TOL compared to MTBE and finally DCE.

BIBLIOGRAPHY

Ai L. H., Zhang C. Z., Liao F., Wang Y., Li M., Meng L. Y., Jiang J., Journal of Hazardous Materials 198 (2011) 282-290

Aiken J. D., Finke R. G., Journal of Molecular Catalysis A: Chemical 145 (1999) 1-44

Alizadeh A., Nieto de Castro C. A., Wakeham W. A., International Journal Thermophysics 1 (1980) 243

Ames L. L., Proceedings of the 13th Pacific Northwest Industrial Waste Conference (1967) (Washington State University, Pullman) 135-152

Anastas P.T., Kirchhoff M.M., Williamson T.C., Applied Catalysis A: Generalty 221 (2003) 3-13

Angelova P., Solel E., Parvari G., Turchanin A., Botoshansky M., Gölzhauser A., Keinan E., Langmuir 29 (2013) 2217-2223

Appenzeller T., Science 254 (1991) 1300

Aris R., Proceedings Royal Society London Series A 235 (1956) 67-77

Azizian S., Bashiri H., Langmuir 24 (20) (2008) 11669-11676

Baer D. R., Gaspar D. J., Nachimuthu P., Techane S. D., Castner D. G., Analytican and Bioanalytical Chemistry 396 (2010) 983

Balasubramanian S. K., Jittiwat J., Manikandan J., Ong C. N., Yu L. E., Ong W. Y., Biomaterials 8 (2010) 2034-2042

Ball B. R., Edward M. D., Journal of Environmental Program 11 (1992) 39

Banat F., Ph.D. thesis, 1995, McGill University, Canada

Barrer R. M., (1978 and 1982) Academic Press of London

Belani C. P., Langer C., Lung Cancer 38 (4) (2002) 13

Bello M. S., Rezzonico R., Righetti P. G., Science 226 (1994) 773-776

Bergman J.J., Groen A.K., Huibregste K., et al. Journal of Gastroenterology and Hepatology 35 (1994) 1553-1658

Bernad J. O., Damascelli A., Nunez O., Galceran M. T., Electrophoresis 32 (2011) 2123-2130

Beulen M. W. J., Huisman B. H., van der Heijden P. A., van Veggel F. C. J. M., Simons M. G., Biemond E. M. E. F., de Lange P. J., Reinhoudt D. N., Langmuir 12 (1996) 6170-6172

Blumsa E. Mezulisa A., Buskeb N., Maiorov M., Jornal of Magnetism and Magnetic Materials 252 (2002) 215-217

Bragg W. H., Bragg W. L., Proceedings of Royal Society of London 88 (1913) 428

Braun D., Libchaber A., Physical Biology 1 (2004) P1-P8

Brosillon S., Manero M. H., Foussard J. N., Environmental science & technology 35 (17) (2001) 3571-3575

Budwig R., Anderson M., Putnam G., Manning C., Ultrasonics 50 (2010) 26-31

Calcara M., Enea V., Pricoco A., Miano F., Journal of Pharmaceutical and Biomedical Analysis 38 (2005) 344-348

Capobianco M. L., Marchesi E., Perrone D., Navacchia M. L., Bioconjugate Chemistry 24 (2013) 1398-1405

Cejka J., van Bekkum H., Corma A., Schueth F., (2007) Elsevier, The Netherland

Chamieh J., Cottet H., Journal of Chromatography A 1241 (2012) 123-127

Chang C. W., Tseng W. L., Analytical Chemistry 82 (2010) 2696-2702

Chen N.Y., Garwood W.E., Dwyer F.G., (1989) Marcel Dekker, New York, Basel

Chen M. M. Y., Katz A., Langmuir 18 (2002) 2413-2420

Cheng M.M.C., Cuda G., Bunimovich Y.L., Gaspari M., Heath J.R., Hill H.D., Mirkin C.A., Nijdam A.J., Terracciano R., Thundat T., Ferrari M., Current Opinion in Chemical Biology 10 (2006) 11-19

Chu B., (1991) Academic Press, New York, 2nd edn

Cifuentes A., Bernal J. L., Diez-Masa J. C., Analytical Chemistry 69 (1997) 4271-4274

Clark R. M., Adams J. Q., Journal of Environmental Engineering 9 (117) (1991) 247

Conde J., Larguinho M., Cordeiro A., Raposo L.R., Costa P.M., Santos S., Diniz M.S., Fernandes A.R., Baptista P.V., Nanotoxicology 8 (2014) 521-532

Connor E.E., Mwamuka J., Gole A., Murphy C.J., Wyatt M.D., Small 1 (2005) 325-327

Coronas J., Chemical Engineering Journal 156 (2010) 236-242

Coto-García A. M., Sotelo-González E., Fernández-Argüelles M. T., Pereiro R., Costa-Fernández J. M., Sanz-Medel A., Analytical and Bioanalytical Chemistry 399 (2011) 29-42

Cottet H., Biron J.P., Cipelletti L., Matmour R., Martin M., Analytical Chemistry 82 (2010) 1793-1802

Cumberland S., Lead J., Journal of Chromatography A 1216 (2009) 9099-9105

D'Orlyé F., Varenne A., Gareil P., Journal of Chromatography A 1204 (2008) 226-232

Daifullah A. H. A. M., Mohamed M. M., Journal of Chemical Technology and Biotechnology 79 (2004) 468-474

Dalla Via L., Marciami M. S., Current Medicinal Chemistry 8 (2001) 1405-1418

Dam D. H. M., Lee H., Lee R. C., Kim K. H., Kelleher N. L., Odom T. W., Bioconjugate Chemistry (2015)

Daniel M. C. , Astruc D., Chemical Review 104 (2004) 293-346

Davies A. G., Thompson J. M. T., (2007) Imperial College Press, London

De Boer J. H., (1958) Butterworths, London

De Boer J. H., (1968) Clarendon Press: Oxford

Demers L. M., Östblom M., Zhang H., Jang N. H., Liedberg B., Mirkin C. A., Journal of American Chemical Society 124 (38) (2002) 11248-11249

Denayer J. F. M., De Meyer K., Martens J. A., Baron G. V., Angewandte Chemie International Edition 42 (2003) 2774-2777

Dobson J., Gene Therapy 13 (2006) 283-287

Dwyer F.G., Moser W.R., (1981) Marcel Dekker, New York, Basel

Eidson S. A., Maier M., Kohler B., et al. American Journal of Gastroenterology 88 (8) (1993) 1242-l248

Elslager E. F., Worth D. F., Journal of Medicinal Chemistry 12 (1969) 955

EUROPEAN COMMISSION NANOTECHNOLOGIES (2013); Directorate General for Research and Innovation Industrial technologies

Ewald P. P., Zeitschrift für Kristallographie 56 (1921) 129

Faulk W. P., Taylor G. M., Immunochemistry 8 (11) (1971) 1081-1083

Favaretto A.G., Annuals of Oncology 17 (5) (2006) 82

Ferrari L., Kaufmann J., Winnefeld F., Plank J., Journal of Colloid and Interface Science 347 (2010) 15-24

Formenton-Catai A. P., Carrilho E., Analytical and Bioanalytical Chemistry 376 (2003) 138-141

Frank C., Ozone Science Engineering 9 (1987) 265

Franzen U., Vermehren C., Jensen H., Østergaard J., Electrophoresis 32 (2011) 738-748

Fraga M. F., Centeno M. L., Valdés A. E., Moncaleán P., Fernández B., Cañal M. J., Rodríguez R., (2000) Vitoria 495-506

Frens G., Colloidal Polymer Science 250 (1972) 736-741

Friedbacher G. , Fuchs H., Pure and Applied Chemistry 71 (7) 1999 1337-1357

Gasparro F. P., American Journal of Clinical Dermatology 1 (2000) 337-358

Geldart S. E., Brown P. R., Journal of Chromatography A 792 (1997) 67-73

Geldart S. E., Brown P. R., Journal of Microcolumn Separation 10 (1998) 65-73

Geldart S. E., Brown P. R., Journal of Chromatography A 828 (1998) 317-336

Giddings J., Myers M., Separation Science Technologies 13 (1978) 637-645

Giddings J., Williams P. S., Am. Lab. 95 (1993) 88-95

Gigault J., Gale B., Le Hecho I., Lespes G., Analytical Chemistry 83 (2011) 6565-6572

Gllges M., Kleemlss M. H., Schomburg G., Analytical Chemistry 66 (1994) 2038-2046

Goldstein J. I., Newbury D. E., Echlin P., Joy D. C., Roming A. D., (1992) Plenum Press, New York, 2nd edn

Gosh P., Man G., De M., Chae K. K., Rotello V. M., Advanced delivery reviews 60 (2008) 1307-1315

Graham D., Journal of Physical Chemistry 57 (1953) 665

Guiochon G., Golshan-Shirazi S., Katti A.M., (1994) Academic Press, Boston

Guiochon G., Shirazi D. G., Felinger A., Katti A. M., (2006) Academic Press

Gunduz S., Akman S., Baysal A., Culha M., Microchimica Acta 172 (2011) 403

Hagenbeek A., Martens A. C. M., Golly L. P., Seminary Oncology 14 (1987) 202-206

Halliwell B., Gutteridge J. M. C., (1989) Clarendon, Oxford, U.K.2nd Ed.

Hanley C., Thurber A., Hanna C., Punnoose A., Zhang J., Wingett D. G., Nanoscale Research Letters 4 (12) (2009) 1409-1420

Hansen N., Krishna R., van Baten J. M., Bell A. T., Keil F. J., Journal of Physical Chemistry C 113 (1) (2009) 235-246

Heilshorn E. D., Chemical Engineering 98 (1991) 120

Heinemann V., Hertel L. W., Grindey G. B., Plunkett W., Cancer Research 48 (1988) 4024-4031

Hermes J. P., Sander F., Fluch U., Peterle T., Thompson D., Urbani R., Pfohl T., Mayor M., Journal of American Chemical Society 134 (2012) 14674-14677

Ho D. H. W., Cancer Research 33 (1973) 2816-2820

Holsapple M. P., Farland W. H., Landry T. D., et al. Toxicological Science 88 (2005) 12-17

Howard A. G., Statham P. J., (1993) Wiley: Chichester, U.K.

Huang Y. F., Huang C. C., Chang H. T., Langmuir 19 (2003) 7498-7502

Huang C., Notten A., Rasters N., Journal of Technology Transfer 36 (2011) 145-172

Hughes C. S., Cox W., Kamatari O., (1983) Menlo Park, CA: SRI International

Hulse W. L., Forbes R. T., International Journal of Pharmaceuticals 411 (2011) 64-68

Hwang W. M., Lee C. Y., Boo D. W., Choi J. G., Bulletin Korean Chemical Society 24 (5) (2003) 684-686

Hyuk S. W., Suslick S. K., Stucky Galen D., Suh Y. H., Progress in Neurobiology 87 (3) (2009) 133-170

Intriago L., Dıaz E., Ordoñez S., Vega A., Microporous and Mesoporous Materials 91 (2006) 161-169

Jain S. J., Snoeyink V. L., Journal (Water Pollution Control Federation) 45 (12) (1973) 2463-2479

Jaroniec M., Madey R., (1998) Elsevier, Amsterdam

Jiang H., Materon E. M., Sotomayor M. D. P. T., Liu J., Journal of Colloidal Interface Science 411 (2013) 92-97

Jimenez-Soto J. M., Lucena R., Cardenas S., Valcarcel M., (2010) Ed.; InTech: New York

Jin R., Wu G., Li Z., Mirkin C. A., Schatz G. C., Journal of American Chemical Society 125 (2003) 1643-1654

Jovanovic D. S., Colloidal Polymer Science 235 (1969) 1203

Kalfa O. M., Yalcinkaya O., Turker A. R., Journal of Hazardous Materials 166 (2009) 455

Kang Y.S., Risbud S., Rabolt J.F., Stroeve P., Chemical Materials 8 (1996) 2209-2211

Kassing R., Petkov P., Kulisch W., Popov C., (2005) Springer

Katz E., Willner I., Angewandte Chemie International Edition 43 (2004) 6042

Khajeh M., Laurent S., Dastafkan K., Chemical Review 113 (2013) 7728-7768

Kim K. T., Zaikova T., Hutchison J. E., Tanguay R. L., Toxicological Science 133 (2) (2013) 275-288

Kimura-Suda H., Petrovykh D. Y., Tarlov M. J., Whitman L. J., Journal of American Chemical Society 125 (2003) 9014-9015

Klabunde K. J., (2001) Wiley: New York

Kohli P., Harrell C. C., Cao Z., Gasparac R., Tan W., Martin C. R., Science 305 (2004) 984

Kondo N., Wagai B., Yotonkai (1968) 1-4

Kononenko V., Giddings J., Myers M., Journal of Microcolumn Separations 9 (1997) 321-327

Koopmans G., Hiemstra T., Regelink I., Molleman B., Comans R., Journal of Chromatography A 1392 (2015) 100-109

Kumar R., Kaur M., Kumari M., Acta Poloniae Pharmaceutica Drug Research 69 (1) (2012) 3-9

Langmuir I., Journal of the American Chemical Society 38 (11) (1916) 2221-2295

Leardini L., Martucci A., Braschi I., Blasioli S., Quartieri S., Mineralogical Magazine 78
(2014) 1141-1159

Lecoq A. F., Di Biase S., Montanarella L., Journal of Chromatography 638 (1993) 363-373

Lee S., Kang D., Park M., Williams P., Analytical Chemistry 83 (2011) 3343-3351

Leopold K., Foulkes M., Worsfold P. J., Analytical Chemistry 81 (2009) 3421

Li Z., Jin R. C., Mirkin C. A., Letsinger R. L., Nucleic Acids Research 30 (2002) 1558-1562

Li H., Rothberg L., Protocol Natural Academy of Science USA 101 (39) (2004) 14036-14039

Li W. S. L., Z. F. Jing F. Y., Yang X. G., Li X. J., Pei F. K., Wang X. X., Lei H., Acta Chimica Sinica 65 (2007) 2029

Li N., Chen Y., Zhang Y. M., Yang Y., Su Y., Chen J. T., Liu Y., Scientific reports 4 (2014) 1-7

Lim I. I. S., Mott D., Engelhard M. H., Pan Y., Kamodia S., Luo J., Njoki P. N., Zhou S., Wang L., Zhong C. J., Analytical Chemistry 81 (2009) 689-698

Lin K. H., Chua T. C., Liu F. K., Journal of Chromatography A 1161 (2007) 314-332

Lin Y., Yu X., Wang Z., Tu S., Wang Z., Analytica Chimica Acta. 667 (2010) 103-112

Linak W. P., Miller C. A., Wendt J. O. Journal of the Air & Waste Management Association 50 (2000) 1532-1544

Liu J., Alvarez J., Kaifer A. E., Advanced Materials 12 (2000) 1381-1383

Lown J. W. (1988) Elsevier, Amsterdam

Lu G.Q., Zhao X. S., (2004) Imperial college Press, London

Markham E. C., Benton A. F., Journal of American Chemical Society 53 (1931) 497

Martucci A., Braschi I., Marchese L., Quartieri S., Mineralogical Magazine 78 (2014) 1115-1140

Maurice P. A., Colloids and Surface A 107 (1996) 57-75

Mavrocordatos D., Pronk W., Boller M., Water Science Technology 50 (2004) 9-18

Maye M. M., Chun S. C., Han L., Rabinovich D., Zhong C. J., Journal of American chemical society 124 (2002) 4958-4959

Mayer D., Hermann G., Sasse K., German Offen 1 (1970) 811

Myers A. L., Prausnitz J. M., AiCHE Journal 11 (1) (1965) 121-127

Meier W. M., (1992) Butterworths Zeolites

Mélin C., Perraud A., Akil H., Jauberteau M. O., Cardot P., Mathonnet M., Battu S., Analytical Chemistry 84 (2012) 1549-1556

Mercer B. W., Ames L. L., Touhill C. J., Van Slyke W. J., Dean R. B. Journal of Water Pollution Control Federation 42 (1970) R95-R107

Milonjic S. K., Journal of Serbian chemical society 72 (2007) 1363-1367

Minato H., Koatsu Gasu 5 (1968) 536-547

Mirkin C. A., Letsinger R. L., Mucic R. C., Storhoff J. J., Nature 382 (1996) 607-609

Moore L., Williams P., Nehl F., Abe K., Chalmers J., Zborowski M., Analytical and Bioanalytical Chemistry 406 (2014) 1661-1670

Moquin A., Neibert K. D., Maysinger D., Winnik F. M., European Journal of Pharmaceutics and Biopharmaceutics 89 (2015) 290-299

Mourougou-Candoni N., Naud C., Thibaudau F., Langmuir 19 (2003) 682-686

Mühlfeld C., Gehr P., Rothen-Rutishauser B., Swiss Medical Weakly 138 (2008) 387-391

Nelson E. M., Rothberg L. J., Langmuir 27 (5) (2011) 1770-1777

Niemeyer C. M., Angewandte Chemie International Edition 40 (2001) 4128

Niesner R., Heintz A., Journal of Chemical Engineering Data 45 (2000) 1121-1124

Nilsson L., Food Hydrocolloids 30 (2013) 1-11

Nion A., Jiang P., Popoff A., Fichou D., Journal of American Chemical Society 125 (2003) 9906-9907

Niramalalakhandan N., Jang W., Speece R., Journal of Environmental Engineering 117 (1991) 788

Niwa M., Katada N., Okumura K., (2010) Springer Series in Materials Science 141

Nurmi J. T., Tratnyek P. G., Sarathy V., Baer D. R., Amonette J. E., Pecher K., Wang C. M., Linehan J. C., Matson D. W., Penn R. L., Driessen M. D., Environmental Science Technology 39 (2005) 1221-1230

Oliven A., Shechter Y., Blood Review 15 (2001) 103-108

Onagi T., Republic Yamagata Stock Raising Insttute (1966) 11-22

Paciotti G. F., Myer L., Weinreich D., Goia D., Pavel N., McLaughlin R. E., Tamarkin L., Drug Delivery 11 (2004) 169-183

Paciotti G. F., Kingston D. G. I., Tamarkin L., Drug Development Research 67 (2006) 47-54

Pankhurst Q.A., Connolly J., Jones S.K., Dobson J., Journal of Physics D Applied Physics 36 (2003) R167

Park C., Youn H., Kim H., Noh T., Kook Y. H., Oh E. T., Park H. J., Kim C., Journal of Material Chemistry 19 (2009) 2310-2315

Pasti L., Martucci A., Nassi M., Cavazzini A., Alberti A., Bagatin R., Microporous and Mesopororous Materials 160 (2012) 182-193

Pathak R. B., Bahel S. C., Journal of Antibacterial and Antifungine Agents 8 (1980) 15

Pathak M. A., Fitzpatrick T. B., Journal of Photochemistry and Photobiology 14 (1992) 3-22

Peterle T., Leifert A., Timper J., Sologubenko A., Simon U., Mayor M., Chemical Communications (2008) 3438-3440

Piazza R., Guarino A., Physical Review Letters 88 (20) (2002) 208302(1-4)

Pires J., Carvalho A., de Carvalho M. B., Microporous and Mesoporous Materials 43 (3) (2001) 277-287

Pratt K. C., Wakeham W. A., Proceedings Royal Society London Series A 336 (1974) 393-406

Putnam S. A., Cahill D. G., Langmuir 21 (12) (2005) 5317-5323

Qian X., Peng X. H., Ansari D. O., Yin-Goen Q., Chen G. Z., Shin D. M., Yang L., Young A. N., Wang M. D., Nie S., Natural Biotechnology 26 (1) (2008) 83-90

Quinones I., Guiochon G., Journal of Chromatography A 734 (1996) 83

Quirino J. P., Anres P., Sirieix-Plènet J., Delaunay N., Gareil P., Journal of Chromatography A 218 (2011) 5718-5724

Ratanathanawongs Williams S., Runyon J., Ashames A., Analytical Chemistry 83 (2011) 634-642

Rhodes D. W., Wilding M. W., (1965) AEC, Washington, DC Publ. No. IDO-14657

Rogers F., Arnott P., Zielinska B., Sagebiel J., Kelly K. E., Wagner D., Lighty J. S., Sarofim A. F., Journal of the Air & Waste Management Association 55 (2005) 583-593

Rosi N. L., Mirkin C. A., Chemical Review 105 (2005) 1547-1562

Rossner A., Snyder S. A., Knappe D. R. U., Water Research 43 (2009) 3787

Rudge S., Peterson C., Vessely C., Koda J., Stevens S., Catterall L., Journal of Controlled Release 74 (2001) 335-340

Rudzinski W., Plazinski W., Journal of Physical Chemistry B 110 (33) (2006) 16514-16525

Runyon J., Williams S. R., Journal of Chromatography A 1218 (2011) 7016-7022

Rutishauser R., Mühlfeld C., Blank F., Musso C., Gehr P., Paricles andt Fibre Toxicology 4 (2007) 9-15

Ruthven D. G., (1984) John Wiley & Sons, N.Y. (USA)

Sapsford K. E., Algar W. R., Berti L., Boeneman Gemmill K., Casey B. J., Oh E., Stewart M. H., Medintz I. L., Chemical Review 113 (3) (2013) 1904-2074

Savage N., Diallo M. S., Journal of Nanoparticle Research 7 (2005) 331–342

Savage N., Diallo M., Duncan J., Street A., Sutich R., (2009) William Andrew Inc, Norwich

Scherzer J., Gruia A. J., (1996) Marcel Dekker, New York, Basel, Hong Kong

Schlesinger R. B., Inhaationl Toxicology 7 (1995) 99-109

Schwab G. M., (1928) Julius Springer Berlin

Sharma U., Gleason N. J., Carbeck J. D., Analytical Chemistry 77 (2005) 806-813

Shim S., Gascoyne P., Noshari J., Stemke Hale K., Integrative Biology 3 (2011) 850-862

Shiundu P. M., Munguti S. M., Ratanathanawongs Williams S. K., Journal of Chromatography A 984 (2003) 67-79

Sic S.T., (1997) Wiley-VCH, Weinheim

Sies H., (1991) (Academic, New York)

Sing K. S. W. , Everett D. H. , Haul R. A. W. , Moscou L. , Pierotti R. A., Rouquerol J. , Siemieniewska T., Pure & Applied Chemistry 57 (4) (1985) 603-619

Skirtach A. G., Javier A. M., Kreft O., Kohler K., Alberola A. P., Mohwald H., Parak W. J., Sukhorukov G. B., Angewandte Chemie International Edition 45 (2006) 4612-4617

Slocik J. M., Crouse C. A., Spowart J. E., Naik R. R.,Nano Letters 13 (6) (2013) 2535-2540

Soares D. M., Gomes W. E., Tenan M. A., Langmuir 23 (2007) 4383-4388

Soerensen P. L. Ingenioeren (1996) 39

Srivastava A., Nizamuddin N., Indian Journal of Heterocyclic Chemistry 13 (2004) 261

Stolpe B., Guo L., Shiller A.M., Aiken G.R., Geochimica et Cosmochimica Acta 105 (2013) 221-239

Takeishi S., Rant U., Fujiwara T., Buchholz K., Usuki T., Arinaga K., Takemoto K., Yamaguchi Y., Tornow M., Fujita S., Abstreiter G., Yokoyama N., Journal of Chemical Physics 120 (2004) 5501-5504

Takemura Y., Juichi M., Ito C., Furukawa H., Tokuda H., Planta Medica 61 (1995) 366

Tanase M., Zolla V., Clement C. C., Borghi F., Urbanska A. M., Rodriguez-Navarro J. A.,
Roda B., Zattoni A., Reschiglian P., Cuervo A. M., et al. Natural Protocol 10 (2015) 134-148

Taylor G. I., Proceeding Royal Society London Series A 219 (1953) 186-203

Taylor G. I., Proceeding Royal Society London Series A 225 (1954) 473-477

Tiede K., Tear S. P., David H., Boxall A. B. A., Water Research 43 (2009) 3335-3343

Turkevich J., Stevenson P.C., Hillier J., Discuss Faraday Society 11 (1951) 55-75

Uccello-Barretta G., Evangelisti C., Balzano F., Vanni L., Aiello F., Jicsinszky L., Carbohydrate Research 346 (2011) 753-758

Von der Kammer F., Legros S., Hofmann T., Larsen E., Loeschner K., Trends in Analytical Chemistry 30 (2011) 425-436
Von Laue M., Zeitschrift für Physik 14 (1913) 1075

Yacobi N. R., Phuleria H. C., Demaio L., Liang C. H., Peng C. A., Sioutas C., et al., Toxicology In Vitro 21 (2007) 1373-1381

Yadav J., Reddy C., Applied environmental microbiology 59 (1993) 756-763

Yang J. S., Lee J. Y., Moon M. H., Analytical Chemistry 87 (2015) 6342-6348

Yıldırım Erbil H., (2006) Blackwell Publishing

Yohannes G., Jussila M., Hartonen K., Riekkola M. L., Journal of Chromatography A 1218 (2011) 4104-4116

Wagner J. R., Van Lier J. E., Decarroz C., Berger M., Cadet J. Methods Enzymology 186 (1990) 502-511

Wang S., Peng Y., Chemical Engineering Journal 156 (2010) 11-24

Weber T. W., Chakravorti R. K., AIChE Journal 20 (1974) 228-238

Wigginton N. S., Haus K. L., Hochella M. F., Journal of Environmental Monitoring 9 (2007) 1306

Williams P., Carpino F., Zborowski M., Philosophical Transactions of Royal Society A 368 (2010) 4419-4437

Zanetti-Ramos B., Fritzen-Garcia M. B., de Oliveira C. S., Pasa A. A., Soldi V., Borsali R., Creczynski-Pasa T. B., Material Science Engineering C 29 (2009) 638-640

Zattoni A., Roda B., Borghi F., Marassi V., Reschiglian P., Journal of Pharmaceutical and Biomedical Analysis 87 (2014) 53-61

Zhai Y., Chang X., Cui Y., Lian N., Lai S., Zhen H., He Q., Microchimical Acta 154 (2006) 253

Zhang Q. W., Kusaka Y., Sato K., Nakakuki K., Kohyama N., Donaldson K., Journal of Toxicol Environmental Heath 53 (1998) 423-438

Zhang X., Liu B., Dave N., Servos M. R., Liu J., Langmuir 28 (2012) 17053-17060

Zhang X., Liu B., Servos M. R., Liu J., Langmuir 29 (2013) 6091-6098

Zhang Z., Zhang F., Liu Y., Journal of Chromatographic Science 51 (2013) 666-683

ACKNOWLEDGEMENTS

I would like to thank Dr. Luisa Pasti for the time, the energy and all the support she gave me during my years of PhD.

I would like to thank Prof. Alberto Cavazzini and the entire group of Analytical Chemistry.

I would like to give thanks Dott. M. L. Capobianco and the entire group of ISOF-CNR of Bologna, Dott. Daniela Perrore of the group of organic chemistry of Department of Pharmaceutical and Chemical Science of University of Ferrara, Prof. Gloria Uccello-Barretta of University of Pisa, ENI for their financial support on this project and the group of Earth Science of University of Ferrara (in particular Prof. Alberto Alberti and Dr. Annalisa Martucci) for their collaboration.

Lots of thanks also to my family and friends.

APPENDIX I

PAPERS

1. "Gold-nanoparticle extraction and reversed-electrode-polarity stacking mode combined to enhance capillary electrophoresis sensitivity for conjugated ucleosides and oligonucleotides containing thioether linkers", Valentina Bosi, Elena Sarti, Maria Luisa Navacchia, Daniela Perrone, Luisa Pasti, Alberto Cavazzini, Massimo L. Capobianco, Analytical and Bioanalytical Chemistry 407 (18) (2015) 5405-5415
2. "Adsorption of 1,2-dichloroethane on ZSM-5 and desorption dynamics by in situ synchrotron powder X-ray diffraction", A. Martucci, E. Rodeghero, L. Pasti, V. Bosi, G. Cruciani, Microporous and Mesoporous Materials 215 (2015) 175-182
3. "Kinetics and dynamic behaviour of toluene desorption from ZSM-5using in situ high-temperature synchrotron powder X-ray diffractionand chromatographic techniques", E. Rodeghero, A. Martucci, G. Cruciani, R. Bagatin, E. Sarti, V. Bosi, L. Pasti, Catalysis Today (2015) article in press
4. "Microscopic models of liquid chromatography: From ensemble-averaged information to resolution of fundamental viewpoint at single-molecule level", Luisa Pasti, Nicola Marchetti, Roberta Guzzinati, Martina Catani, Valentina Bosi, Francesco Dondi, Annamária Sepsey, Attila Felinger, Alberto Cavazzini, Trends in Analytical Chemistry (2015) article in press

Anal Bioanal Chem
DOI 10.1007/s00216-015-8702-6

RESEARCH PAPER

Gold-nanoparticle extraction and reversed-electrode-polarity stacking mode combined to enhance capillary electrophoresis sensitivity for conjugated nucleosides and oligonucleotides containing thioether linkers

Valentina Bosi[1] · Elena Sarti[1] · Maria Luisa Navacchia[2] · Daniela Perrone[1] · Luisa Pasti[1] · Alberto Cavazzini[1] · Massimo L. Capobianco[2]

Received: 10 February 2015 / Revised: 2 April 2015 / Accepted: 13 April 2015

Abstract We present a capillary electrophoresis method for determining two different C8-conjugated deoxyadenosines, and for oligonucleotides containing them, in which a psoralen or an acridine molecule is bonded to the base via a short alkyl chain containing sulfur ethers at both ends. The sensitivity of the micellar electrokinetic chromatography (MEKC) method was increased by using two preconcentration techniques, micro solid-phase extraction (μSPE) followed by reversed-electrode-polarity stacking mode (REPSM). Variables that affect the efficiency of the extraction in μSPE and preconcentration by REPSM, including the type and volume of extraction nanoparticle, concentration, and injection time, were investigated. Under the optimum conditions, enrichment factors obtained were in the range 360–400. The limits of detection (LODs) at a signal-to-noise ratio of 3 ranged from 2 to 5 nmol L^{-1}. The relative recoveries of labelled adenosines from water samples were 95–103 %. The proposed method provided high enrichment factors and good precision and accuracy with a short analysis time. On the basis of the advantages of simplicity, high selectivity, high sensitivity, and good reproducibility, the proposed method may have great potential for biochemical applications.

Keywords Labelled adenosines · Gold nanoparticles · Field-amplified sample stacking · Micellar electrokinetic capillary electrophoresis

Abbreviations

Acr-dA	Acridine-deoxyadenosine
AuNP	Gold nanoparticle
BGE	Background electrolyte
CE	Capillary electrophoresis
CZE	Capillary-zone electrophoresis
dA	Deoxyadenosine
MEKC	Micellar electrokinetic chromatography
NP	Nanoparticle
Pso-dA	Psoralen-deoxyadenosine
P-pso	$^{5'}$CGTGCxTCCTAGC$^{3'}$, for x=Pso-dA
P-acr	$^{5'}$CGTGCxTCCTAGC$^{3'}$, for x=Acr-dA
REPSM	Reversed-electrode-polarity stacking mode
SDS	Sodium dodecyl sulfate

Introduction

Oligonucleotides are widely used for a variety of applications, from molecular probes to downregulation of gene expression in cellular studies and, more recently, as molecular scaffolds for the bottom-up construction of ordered aggregates [1] with potential use in devices [2]. In all these applications, extended functionality can be added to natural oligonucleotides by conjugation with molecules, while maintaining the basic and well-known hydrogen-bond arrangements [3, 4] that enable the predictable supramolecular assembly of the oligonucleotides.

✉ Luisa Pasti
luisa.pasti@unife.it

[1] Department of Chemistry and Pharmaceutical Sciences, University of Ferrara, via L. Borsari 46, 44121 Ferrara, Italy

[2] Istituto per la Sintesi Organica e la Fotoreattività del Consiglio Nazionale delle Ricerche (ISOF-CNR), via P. Gobetti 101, 40129 Bologna, Italy

Published online: 10 May 2015

One way of preparing conjugated oligonucleotides is synthesizing a conjugated nucleoside and incorporating it into the chosen position inside the oligonucleotide. The natural ability of the oligonucleotide to bind specifically to its predetermined target makes it then possible to locate the functional molecule in a specific predetermined position in the final complex.

Because many uses of oligonucleotides involve cellular studies, if not in vivo, it is important to be able to analyze them at the lowest possible concentration with minimal interference from possible interfering components.

Determination of normal and conjugate nucleosides and oligonucleotides in a variety of samples can be performed with different techniques, including immunoassays [5], high-performance liquid chromatography (HPLC), and capillary electrophoresis (CE) conjugated with UV detection [6, 7] and mass spectrometry (MS) [8–10]. High-performance capillary electrophoresis (HPCE) has proved to be a rapid and simple technique for separating charged biomolecules and nanoparticles with very high resolution [11]. Its unique advantages, including relatively short analysis time and high separation efficiency with consumption of a minimal amount of sample and buffer solution, make HPCE a valuable technique for the determination of biomolecules [12], especially when a small amount of sample is available for the analysis. Micellar electrokinetic chromatography (MEKC) methods with sodium dodecyl sulfate (SDS) and borate phosphate buffers have been used for the determination of nucleosides by many researchers [13–15]. One of the well-recognized disadvantages of CE is the poor concentration sensitivity, especially when a photometric detector is used. To solve this problem several techniques have been developed. One is the use of high-sensitivity detectors [16], and another is sample preconcentration before (off-line) or after (on-line) sample injection. Among the on-line enrichment methods, sample stacking in CE analyses is a particularly useful technique because it is simple to perform, economical, and requires no additional instrumentation [17–19]. In particular, so-called reversed-electrode-polarity stacking mode (REPSM), a modified version of the field-amplified sample-stacking technique [20], has good potential for sample enrichment. For off-line enrichment, nanoparticles (NPs) have been used to extract and enrich target analytes from complex matrices because of their high surface-area-to-volume ratios, which result in higher adsorption capacity for analytes and enable attachment of biomolecules to the surface of nanomaterials [21, 22]. The binding mechanisms of NPs with target analytes include different interactions, for example electrostatic or hydrophobic interactions [23]. In addition to these nonspecific interactions, unmodified NPs can also be used to capture specific analytes through the formation of chemical bonds. The strong affinity of AuNPs for thiol-containing biomolecules via a gold–thiolate bond has been revealed [24], and on this basis AuNPs have been revealed to be an efficient method of extracting aminothiols in plasma [25] or adsorbing thiol-modified nucleosides [26]. However, some reports have also revealed the possibility of disulfide [27] and thioether [28, 29] monolayer encapsulation on gold nanoparticles. Whereas the thiol or disulfide-based chemistry is often exploited in approaches for nanoparticle assembly, investigation of thioether-based coordination chemistry for similar purposes is less frequent, and the technique has not been used for enrichment. In this paper we present the optimization of a capillary-electrophoresis method for determining two different C8-conjugated deoxyadenosines, and oligonucleotides containing them [30], in which the functional molecule is either a psoralen or an acridine derivative. Those molecules are bound to the base via a short alkyl chain containing sulfur ethers at both ends (Fig. 1).

The determination involves the following steps:

1. Capture of labelled adenosines using AuNPs;
2. Centrifuging and washing adenosine-adsorbed AuNPs;
3. Release of adenosines from the Au surface through ligand-exchange reaction; and
4. Separation of released adenosines by CE.

We investigated the effect of the number of AuNPs and the concentration of analytes on the loading and release steps. Our objective was the development of an analytical strategy combined with off-line (i.e., SPE) and on-line REPSM–MEKC for the separation and sensitive determination of conjugated thioether nucleosides and oligonucleotides.

Materials and methods

Apparatus

An Agilent Technologies Capillary Electrophoresis series 7100 system (Santa Clara, CA, USA) was used for the REPSM and surfactant-modified CE separation of the analytes and of their adducts with AuNPs. The CE system was equipped with diode-array detection (DAD). For separations, extended light path (bubble cell) bare-fused-silica capillaries (red G1600-61232 I.D.: 50 μm, total length: 60.5 cm, effective length: 52 cm, or 64.5 cm length (56 cm to the detector) bubble factor: 3) were obtained from Agilent Technologies (Santa Clara, CA, USA).

Hydrodynamic injection of the AuNP sample was performed at a pressure of 10 mbar applied for 30 s. The detection wavelength of the CE system was 520 nm for AuNPs, 260 nm and 268 nm for Pso-dA and Acr-dA, respectively, and 260 nm for oligonucleotides. Positive polarity (20 kV) was applied at the capillary inlet for the duration of the separation. The pH of the electrolyte was measured using an AMEL pHmeter (Milano, Italy). Before use, the capillary was pretreated by

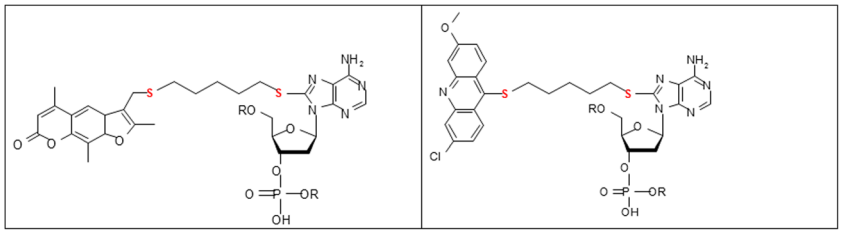

Fig. 1 Structures of the analyzed compounds

sequential flushing with 1 mol L^{-1} NaOH for 5 min, 0.1 mol L^{-1} NaOH for 5 min, and Milli-Q (Millipore, Bedford, MA, USA)-grade water for 15 min. The capillary was also rinsed with water for 3 min, 0.1 mol L^{-1} NaOH for 2 min, water for 3 min, and running buffer for 5 min between each run.

For the REPSM separation the capillary was rinsed with 0.1 mol L^{-1} NaOH for 3 min, water for 3 min, and running buffer for 3 min between each run. The injection of the AuNP sample was performed throughout at a pressure of 50 mbar applied for a given time, followed by an application of voltage at negative polarity (−15 kV) for 24 s, switching polarity from negative to positive when the current reached 97–99 % of the predetermined current at negative polarity and with a waiting time of 5 s. All CE experiments were performed at 25 °C.

Reagents

Sodium dodecyl sulfate (SDS purity 95 %) (J. T. Baker, Avantor, Center Valley, PA, USA), sodium hydroxide (Tiolchimica, Rovigo, Italy), hydrochloric acid (Carlo Erba, Milano, Italy), borate buffer ($Na_2B_4O_7$), sodium dihydrogen phosphate (NaH_2PO_4), dimethyl sulfoxide (DMSO), and citrate were obtained from Sigma–Aldrich (Steinheim, Germany). The AuNPs used in this study were obtained from commercial sources; their sizes were determined through TEM analysis. Standard AuNPs having a mean diameter of 10 nm with standard deviation (SD) 0.5 nm were obtained from Sigma–Aldrich (Steinheim, Germany). Milli-Q (Millipore, Bedford, MA, USA)-grade water (>18 MΩ•cm) was used throughout the experiments.

Psoralen-deoxyadenosine (Pso-dA) and acridine-deoxyadenosine (Acr-dA) and their oligonucleotides P-pso and P-acr (Fig. 1) were synthesized as described in Ref. [30].

Preparation of BGE

The BGE solutions containing 20 mmol L^{-1} $Na_2B_4O_7$ and SDS at mmol L^{-1} concentrations (10, 20, 30, 40, and 50 mmol L^{-1}) were prepared with Milli-Q water, and their pH was adjusted to a given value (9.3, 10, or 12) by adding 1.0 mol L^{-1} or 0.1 mol L^{-1} NaOH into the buffer after diluting it to the final volume. The buffer solutions were filtered through the 0.22 μm PVDF membrane filter Overmolded Millex Millipore (Bedford, MA, USA) before use.

Preparation of standard solutions

The 5 mmol L^{-1} stock solutions of modified adenosines (Pso-dA, Acr-dA) were prepared in DMSO. All stock solutions were kept at −20 °C. The working solutions of labelled adenosines were prepared by diluting the stock solutions with Milli-Q water to concentrations of 1, 10, 20, 25, and 50 μmol L^{-1} for hydrodynamic injection and 0.05, 0.1, 2, 5, and 10 μmol L^{-1} for REPSM injection. The 0.014 mmol L^{-1} stock solutions of oligonucleotides were prepared in Milli-Q water. All stock solutions were kept at 4 °C. The working solutions of oligonucleotides were prepared by diluting the stock solutions with Milli-Q water to concentrations of 0.0035, 0.007, 0.014, 0.035, and 0.07 mmol L^{-1} for P-acr and P-pso for hydrodynamic injection and 0.05, 0.1, 2, 5, and 10 μmol L^{-1} for REPSM injection.

Characterization of AuNPs

A double-beam UV–visible spectrophotometer (Jasco V-570 UV-VIS-NIR, Easton, MD, USA) was used to record the absorption spectra of AuNPs.

Transmission electron microscopy (TEM) experiments were performed on a Hitachi (Tokyo, Japan) H-800 microscope using an acceleration voltage of 100 kV. The thermionic source was a tungsten filament. Samples for TEM analysis were prepared by placing a drop of the colloidal AuNPs on a clean, dry copper grid coated with a carbon film; this was allowed to dry in air and then used for measurements.

Preparation of AuNPs with labelled adenosines and modified oligonucleotides

The maximum absorption wavelength of the AuNPs, which was measured by visible spectrophotometer, was 520 nm. The concentration of 10 nm diameter AuNPs in the used solution, determined on the basis of a molar absorptivity of 1.01×10^{8} mol^{-1} L cm^{-1} at 520 nm, was 5.98×10^{12} nanoparticles mL^{-1} (9.89 nmol L^{-1}). This concentration is denoted as C1.

A known amount of labelled adenosines (0.05–5 μmol L^{-1} for Acr-dA; 0.1–7.5 μmol L^{-1} for Pso-dA) was added to a measured volume of C1 AuNPs and mixed for 1 h by vortex (VV3, VWR, Milano, Italy). The resulting mixture was centrifuged at 14,000 rpm (Eppendorf 5418, Hamburg, Germany) for 30 min and the supernatant was carefully removed up to a residual volume of 20 μL. To remove the excess of labelled adenosines from the pellets, the AuNPs were resuspended in 500 μL Milli-Q water, mixed by vortex for 20 min and then centrifuged, and the supernatant was analyzed by CE. The capped AuNPs were then analyzed by CE and their release was investigated. To remove labelled adenosines from the gold surface, the AuNPs were resuspended in known amounts of solutions having different compositions (i.e. pH and SDS concentration) and containing 20 mmol L^{-1} $Na_2B_4O_7$. After 20 min, the released labelled adenosines were isolated from AuNPs by centrifugation at 14,000 rpm for 30 min. The supernatant was directly analyzed by CE. A known amount of 1.9 mL oligonucleotides (obtained by diluting 50 μL 0.014 mmol L^{-1} for P-pso and 0.014 mmol L^{-1} for P-acr, both prepared in Milli-Q water) was added to a measured volume of 10 nm AuNP solution at concentration C1; 500 mmol L^{-1} pH 3 citrate HCl buffer was added to the suspension and mixed by vortex; and the mixture was incubated at room temperature for 4 h. The solution was centrifuged at 14,000 rpm for 30 min to separate the AuNPs from the excess of reagent, and the supernatant was analyzed by CE. The AuNPs were then washed three times with 400 μL Milli-Q water and then centrifuged, and the supernatant was analyzed by CE. Finally the AuNPs were dispersed in a solution which contained 20 mmol L^{-1} $Na_2B_4O_7$ and 20 mmol L^{-1} SDS. After 48 h, the released oligonucleotides were isolated from the AuNPs by centrifugation at 14,000 rpm for 30 min. The supernatant was directly analyzed by CE.

Analysis of Pso-dA in urine

Urine samples (8 mL) were collected from healthy adult females. An aliquot of 3.6 mL urine was spiked with 40 μL 20 μmol L^{-1} Pso-dA. C1 AuNPs (400 μL) were added to both urine and spiked urine and mixed for 1 h by vortex. After centrifugation at 14,000 rpm the supernatant was carefully removed up to a residual volume of 20 μL, and the precipitates were suspended in 500 μL Milli-Q water, mixed by vortex for 20 min, and then centrifuged. The pellets were resuspended in 400 μL borate buffer at pH 9.3 with SDS 20 mmol L^{-1}. After 20 min, the suspensions were separated by centrifugation at 14,000 rpm for 30 min. The supernatants were directly analyzed by MEKC.

Results and discussion

Reverse stacking

To increase the applicability of CE for biomolecule monitoring we developed a stacking REPSM-MEKC method. REPSM, a CE-based on-line concentration strategy, has been proved to increase detection ability for a variety of samples [31, 32], including NPs [33]. In REPSM the sample is introduced into the capillary hydrodynamically, applying a stacking voltage at negative polarity to concentrate the analytes at the interface between the sample zone and the background electrolyte, and then pumping the sample matrix from the capillary under electroosmotic flow (EOF). When the current reaches ca.97 % of its original value, this potential is turned off. A positive potential is then applied to separate the analytes.

The REPSM-MEKC method was optimized with respect to sample loading time, separation buffer concentration, pH of separation buffer, and separation voltage.

Different concentrations of borate buffer, 15, 20, 40, and 60 mmol L^{-1}, and different pH values, 9.3, 10.04, and 12.10, were investigated. As the concentration of borate was increased, a longer migration time was observed. In addition, the retention time of the labelled adenosines increased with increasing pH. It was also found that by increasing the SDS concentration in the BGE, the separation improved; however, for concentrations larger than 50 mmol L^{-1} long retention times lead to peak broadening. The best resolution of the analytes was obtained using a 20 mmol L^{-1} sodium tetraborate buffer at pH 9.30 containing 20 mmol L^{-1} SDS, with an applied voltage of 20 kV (Fig. 2).

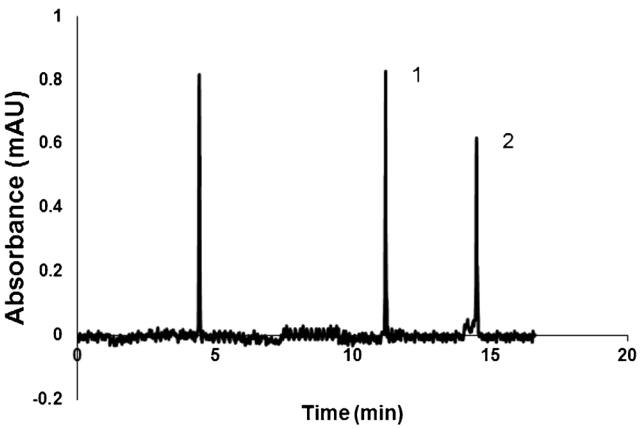

Fig. 2 Electropherograms of Pso-dA(1) and Acr-dA(*2*). The concentration of both analytes was 10 μmol L^{-1}. Hydrodynamic injection at a pressure of 10 mbar applied for 30 s. The separation conditions were 20 mmol L^{-1} SDS, 20 mmol L^{-1} borate buffer pH 9.30, fused-silica capillary: 50 μm inner diameter, 60.5 cm (detection length, 8.5 cm). Neutral marker: dimethyl sulfoxide. Applied voltage: +20 kV: Temperature: 25 °C. Absorbance detection wavelength: 260 and 268 nm for Pso-dA and Acr-dA, respectively

Different sample plugs were tested to determine the greatest sample-plug length that could be injected without worsening the separation profile by REPSM. To improve the sensitivity of the method, the injection time was varied in the range 25–100 s using a 50 mbar hydrodynamic injection. The peak area of the three analytes increased with increasing injection time, but injection times longer than 50 s resulted in lower area reproducibility. Therefore an injection time of 50 s was chosen.

To investigate the quantitative REPSM method, the limits of detection were compared with those of the conventional MEKC method (Table 1). It can be observed that the REPSM-MEKC method gave approximately twentyfold lower limits of detection.

Loading of conjugate adenosines onto AuNPs

To determine whether citrate–AuNPs can interact with labelled adenosines, the extinction spectra of the citrate–AuNPs were investigated. The surface-plasmon-resonance (SPR) peak of citrate–AuNPs was located at 520.0±0.5 nm (n=3) (spectrum A in Fig. 3). As shown by the TEM data in the inset of Fig. 3, the AuNPs have an average diameter of approximately 10 nm, in agreement with the data from the supplier. Upon the addition of Pso-dA, the SPR peak of the AuNPs was shifted to 543±0.6 nm (spectrum B in Fig. 3) and its intensity decreased. Similar trends were observed in the spectra of Acr-dA, and of P-pso and P-acr (spectrum C in Fig. 3). It has been reported that the adsorption of uncharged nucleosides (e.g. adenosine and inosine) could cause AuNP aggregation; in such a case the colloidal solution undergoes an instant red-to-blue color change [34]. In the studied concentration range, the spectra of the colloid after addition of labelled adenosines do not shift toward blue; the previous shift in the spectra was possibly caused by modification of the dielectric environment close to the NP surface which, in turn, is related to the interaction of the surface with a molecule [35]. The interaction between nucleosides and AuNPs is quite complicated and has been the subject of extensive debate. Briefly, binding of nucleosides to AuNPs via nitrogen has been reported [35, 36], and in other work hydrophobic interactions were indicated as the main mechanism of adsorption [37]. These differences in the interaction responsible for adsorption partially derive from different colloidal compositions of the adsorbate solution, the NP surface, and the media. It should also be taken into account that the compounds investigated in the present study were conjugate nucleosides containing thioether groups, and the adsorption of organosulfur compounds on the AuNP surface has been reported elsewhere [28]. It is well known that alkanethiols are the most popular ligand for AuNPs [38], and the use of dialkyl sulfides [39, 40] and protected thiols has also been reported [41]. The thioether–gold coordination is much weaker than the covalent thiolate–gold interaction, and it increases for multidentate ligands comprising more than one thioether unit [42, 43]. In general, monothioethers need longer chain lengths or costabilization to give stable, redispersible gold colloids [44]. The detailed study of binding mechanisms is beyond the scope of this work. However, we observed that for the studied nucleosides, the binding was strong enough to enable their capture on the surface of the AuNPs. To qualitatively understand whether this interaction is mainly brought about by functional molecules and the thioether linker or by the nucleoside, the adsorption of dA (deoxyadenosine) was investigated. Figure 4 shows the electropherograms obtained by hydrodynamic injection of a solution before and after contact with AuNPs. It can be qualitatively seen that the adsorption of dA on AuNPs is negligible compared with that of Pso-dA. To quantify the adsorption of labelled adenosines on AuNPs, the concentrations obtained by REPSM-MEKC of the solution before and after the contact with AuNPs were measured. The effect of equilibration time on the adsorption was evaluated by measuring the concentration of the labelled adenosines in contact with AuNPs during equilibration. The concentration observed for the modified adenosines reached a constant value after 30 min incubation. Consequently, to assure a contact time longer than the equilibration time, 1 h was chosen for the experiments. In addition, the effect of the concentration of the analytes was considered. Figure 5 shows the adsorbed quantity as a function of the labelled adenosines in the solution after equilibration. Extraction with 400 μL AuNP at C1 concentration with 400 μL solution was almost complete at concentrations below 2 μmol L^{-1} for Pso-dA and 2.5 μmol L^{-1} for Acr-dA; at higher

Table 1 Linear regression data and LOD of the studied compounds obtained by MEKC and REPSM-MEKC

Compound	MEKC			REPSM		
	Regression	Correlation coefficient (R^2)	LOD (μmol L^{-1})	Regression	Correlation coefficient (R^2)	LOD (μmol L^{-1})
Pso-dA	y=106.9(6.8)x−0.72(0.54)	0.9989	1.62±0.097	y=4281(121)x−8(23)	0.9946	0.068±0.011
Acr-dA	y=331.9(5.1)x−0.26(0.25)	0.9992	0.71±0.088	y=12391(611)x+13(35)	0.9975	0.042±0.010
P-Pso	y=480(12)x+0.79(0.48)	0.9987	0.67±0.11	y=19007(712)x+15(29)	0.9931	0.031±0.0087
P-Acr	y=497.8(8.9)x+0.57(0.62)	0.9991	0.63±0.077	y=13742(523)x+22(24)	0.9968	0.032±0.0081

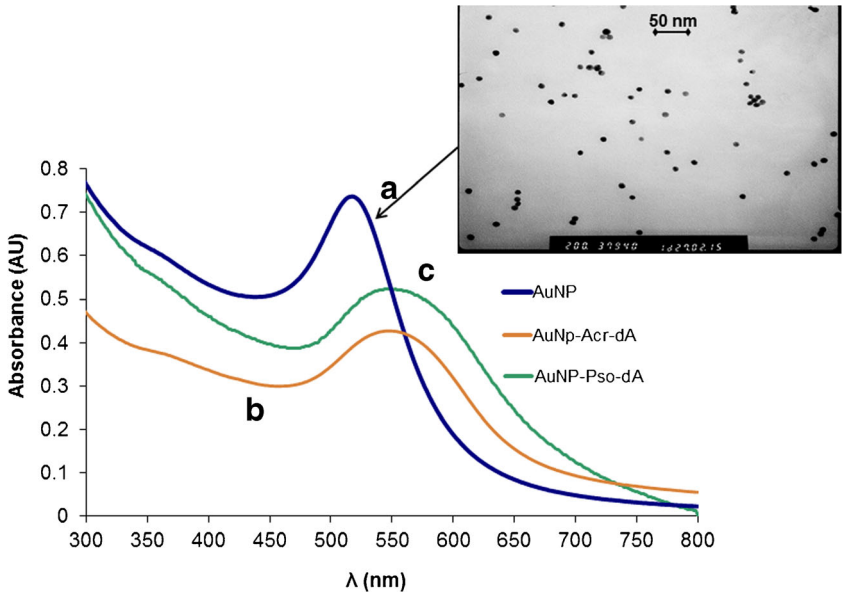

Fig.3 Spectra of the AuNPs suspension before(**a**) and after Pso-dA(**b**) and P-pso(**c**) adsorption. *Inset*: TEM image of AuNPs

concentrations the particles were saturated. On the basis of these results, to obtain a quantitative adsorption of the two adenosines the quantities were chosen to be lower than the saturation coverage and the equilibration time was set to 1 h. These adsorption results confirmed that AuNPs could be used for extracting the labelled adenosines from an aqueous solution.

The particles obtained after incubation and centrifugation were washed by suspension in water and separated by centrifuge, the supernatant was injected into the CE system to determine the concentration of the labelled adenosines eventually released, and the procedure was repeated twice. We found that, for both the analytes considered (i.e. Pso-dA and Acr-dA), the concentration in the two aqueous solutions was below the detection limit and no peaks were revealed in the electropherograms. This finding indicates that the concentrations of released adducts in water (i.e. AuNP–Pso-dA and AuNP–Acr-dA) were below the detection limit of the method.

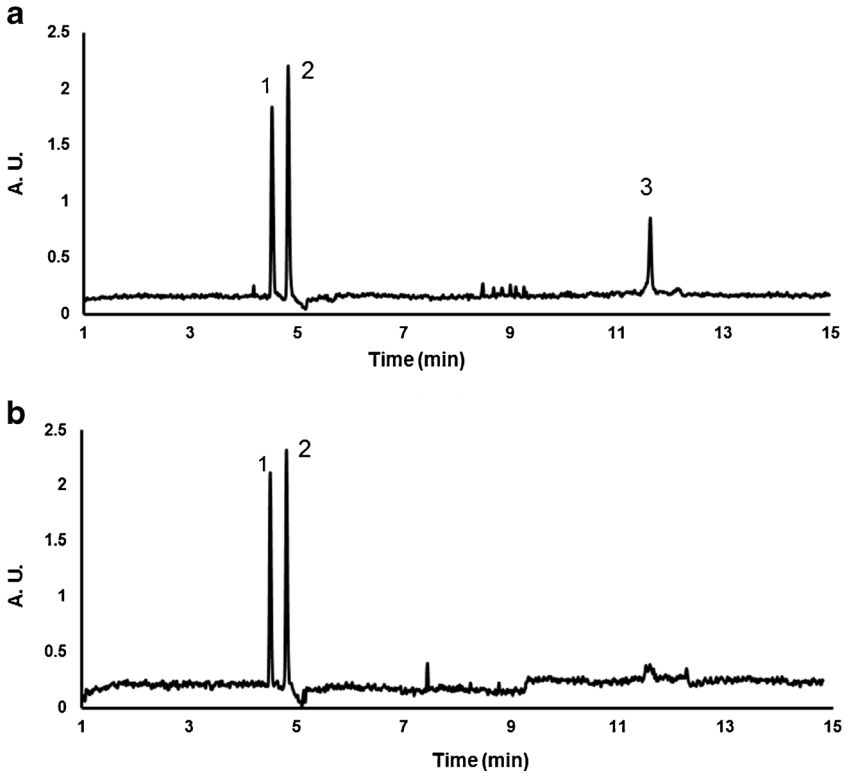

Fig.4 Electropherograms of dA(*2*), and Pso-dA(*3*), with DMSO used as marker(1), (**a**) before and (**b**)after the contact with AuNPs. Capillary: 50 μm inner diameter, 60.5 cm bare-silica capillary (detection length, 8.5 cm). Background electrolyte (BGE) borate buffer 20 mmol L^{-1} pH 9.3 SDS 20 mmol L^{-1}. Applied voltage: +20 kV: Temperature: 25 °C. Absorbance detection wavelength: 260 nm

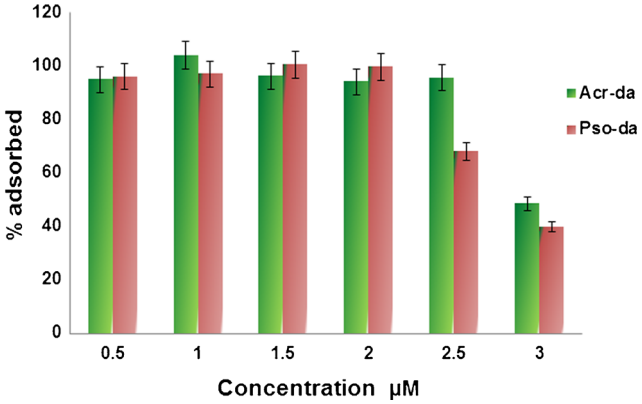

Fig.5 Percentage of adsorbed Pso-dA and Acr-dA on AuNPs as a function of conjugated-adenosines concentration in the bulk phase

Release of labelled adenosines from their adducts with AuNPs

To evaluate the release of labelled adenosines from their AuNP adducts, the labelled nucleosides adsorbed on the NP surface were suspended in 100 μL of buffered solutions at different pH values (the conjugated particles were prepared as described in the section "Loading of conjugate adenosines onto AuNPs"). It can be seen from Fig. 6a that the percentage of released Pso-dA is negligible in the 3–9 pH range and increases at pH above 10 or below 2. To increase the release of the compounds in the solution the effect of SDS was investigated at pH 9 (Fig. 6b). When SDS concentration was increased from 0.1 to 10 mmol L^{-1} an increase of the area of the analyte in the electropherograms recorded at 260 nm was observed, and at SDS concentrations higher than 10 mmol L^{-1} the area of the compounds reached a plateau. The maximum release is thus obtained for SDS concentrations higher than the critical micelle concentration for SDS (8.1 mmol L^{-1}) [45]. This finding indicates that the labelled adenosines are physisorbed onto AuNP, and that they are displaced by the surfactant. SDS can therefore be adsorbed onto the gold surface [46, 47].

On the basis of these results, for the extraction of the labelled nucleosides a buffered solution at pH 9 with 20 mmol L^{-1} SDS was chosen. The electrophoretic mobilities of the released labelled adenosines were equal to those obtained for the compounds before the capture process. Therefore the concentration step does not affect the labelled adenosines.

Under the above conditions, the peak areas of the compounds in the electropherograms obtained by MEKC increased significantly after the extraction. In particular, the extraction with the AuNPs resulted in a 4.2 and 3.8-fold increase in the response of the method for Pso-dA and Acr-dA, respectively (peak area recorded at 260 and 268 nm for Pso-dA and Acr-dA, respectively). This result is in agreement with a fourfold improvement in the sensitivity resulting from nearly complete adsorption from the initial 400 μL volume (before

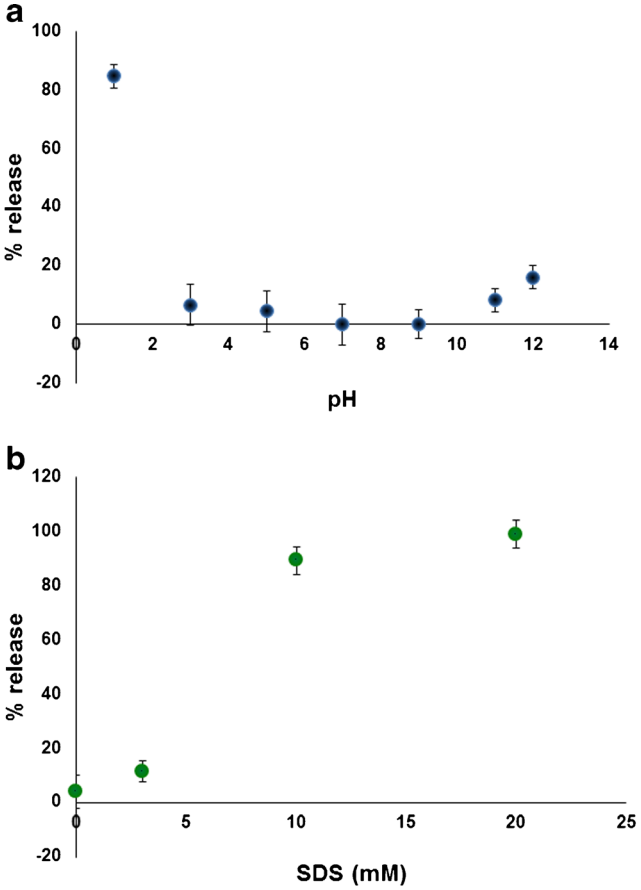

Fig.6 Percentage of released Pso-dA (**a**)vs. pH, (**b**)vs. SDS concentration

extraction) and desorption to a final sample volume of 100 μL (after extraction), confirming that thioether labelled nucleosides can be completely extracted from aqueous solution by using AuNPs. The effect of the sample volume on the enrichment of the labelled adenosines was also investigated. Generally, on increasing the sample volume the peak area in the electropherograms of the analytes after enrichment increases, until particle saturation is reached. For a given compound, the sample volume to achieve particle saturation depends on the concentration of both the analyte solution and the AuNPs. At an analyte solution concentration of 0.05 μmol L^{-1} (C_i) and using 100 μL C1 AuNP solution and 1.9 mL (V_i) sample solution, the recovery obtained from three repetitions was 101±8.3 %. The recovery was calculated as:

$$R(\%) = 100\frac{C_f V_f}{C_i V_i} \quad (1)$$

where C_f corresponds to the concentration of labelled adenosines in the final volume of supernatant and V_f=100 μL. C_f values were calculated from calibration curves built with standard solutions.

The enrichment factor after the extraction procedure (i.e. V_i/V_f), was 19.

The LOD for Pso-dA and Acr-dA at a signal-to-noise ratio of three, for the normal hydrodynamic injection technique MEKC (without extraction), were 1.62 and 0.71 μmol L^{-1}, respectively, and the LOD for the normal hydrodynamic injection technique MEKC (with extraction) were 0.092 and 0.052 μmol L^{-1}, respectively.

After the release of analytes, the particles were washed twice with Milli-Q water and 10 mmol L^{-1} citrate solution and the enrichment of Pso-dA was repeated on the AuNPs recovered by using the procedure described above. The extraction–release procedure was repeated thrice on the same AuNP particles. The extraction was performed with 400 μL AuNP at C1 concentration, with 400 μL 2 μmol L^{-1} Pso-dA solution and a contact time of 1 h. The loading percentage of Pso-dA on AuNPs was calculated from the concentration measured by REPSM-MEKC before and after the contact with AuNPs. Loading percentages were 97 %, 100 %, and 100 %, respectively, in the first, second, and third trial. The release was obtained with 400 μL buffered borate solution at pH 9.3 and with 20 mmol L^{-1} SDS. Recovery percentages in the first, second, and third reuse cycle were 97 %, 98 %, and 105 %, respectively. This finding indicates that the solid phase of the off-line enrichment procedure can be easily regenerated and can be reused, thus decreasing the waste of materials.

Finally, when the REPSM-MEKC method was applied to the extracted solution of labelled nucleosides, which was obtained by the release of the analytes from their adducts with AuNPs, an enrichment factor of approximately 380 was obtained, which is in good agreement with the total enrichment factor given by the product of the enrichment in the extraction procedure (approximately 19) and that resulting from REPSM injection (approximately 20). As far as we are aware, this is the first example of the use of citrate–AuNPs for the successful extraction of labelled adenosines combined with stacking injection to increase the sensitivity of CE analysis. The LOD, at a signal-to-noise ratio of three, for the REPSM injection technique combined with MEKC (with extraction) were 5.5 and 2.3 nmol L^{-1} for Pso-dA and Acr-dA, respectively.

It has been reported that the REPSM-MEKC method can also be directly applied to AuNPs. For instance, the surfactant CE separation coupled with RESPM injection increases the detection sensitivity by a factor of approximately five for AuNPs with a diameter of 5 nm, as reported in Ref. [33]. The stability of AuNPs suspended in buffer containing SDS, inside silica capillaries commonly used for electrophoretic separation, has been reported elsewhere [33]. On the basis of this finding, AuNP-labelled adenosines adducts were analyzed by CE.

Figure 7 shows the separation of the two components, Pso-dA and its AuNP adduct, obtained at different concentrations of SDS. The adducts were partially dissociated during the electrophoretic separation in SDS buffers and both the free Pso-dA and its AuNP conjugate were detected, thus indicating

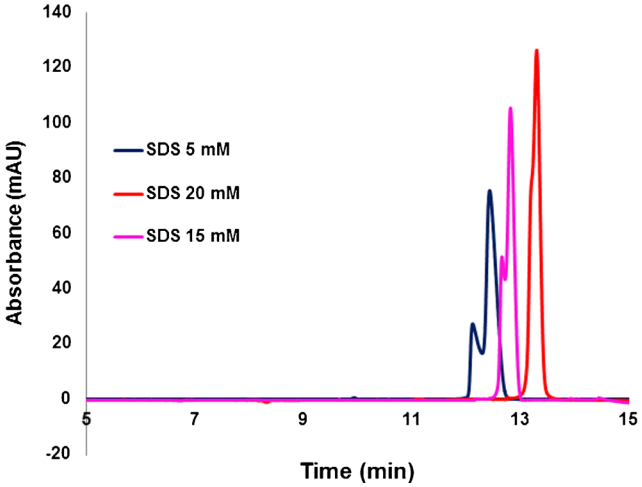

Fig. 7 Electropherograms of AuNPs–Pso-dA. Electropherograms obtained on injection of AuNPs–Pso-dA adduct. Capillary: 50 μm inner diameter, 60.5 cm bare-silica capillary (detection length, 8.5 cm). Background electrolyte (BGE) borate buffer 20 mmol L^{-1} pH 9.3. Applied voltage: +20 kV: Temperature: 25 °C. Absorbance detection wavelength: 260 nm

that adduct suspensions were not stable in the running buffer. It can be also noticed that the separation increases with decreasing surfactant concentration in the BGE. It is outside of the scope of this study to investigate the kinetics of the Pso-dA release in SDS buffer. However, from this experiment it can be hypothesized that the CE–diode-array-detection technique could also enable separation and identification of surface-labelled nanoparticles, if performed under stable conditions.

The extraction procedure was applied to a urine sample to investigate the feasibility of the method in practical cases. When the supernatant obtained from the extraction of urine with AuNPs was analyzed by REPSM-MEKC, no peak corresponding to Pso-dA was detected (Fig. 8a). However, for the urine sample spiked with Pso-dA a peak corresponding to Pso-dA was identified (Fig. 8b). The identification was performed by comparing the electropherogram of the urine sample with that of a spiked water solution prepared using the same procedure used for the urine sample (Fig. 8c).

Capture and release of oligonucleotides by using AuNPs

Oligonucleotide probe-linked AuNPs have found wide application in biosensors, usually being obtained as alkanethiol-capped oligonucleotides self-assembled on AuNPs by an Au–thiol bond. One of the methods of preparing those probes is that proposed by Mirkin [48], based on the chemisorption step for linking thiol oligo probes to citrate-protected AuNPs. It should be noted that, in addition to terminal linkage of DNA and AuNP through Au–S linkage, nonspecific binding of nucleotides to AuNP through the nitrogen-containing bases or nonspecific interactions has also been described [35, 49]. Nonthiolated DNA was found to protect AuNPs against salt-

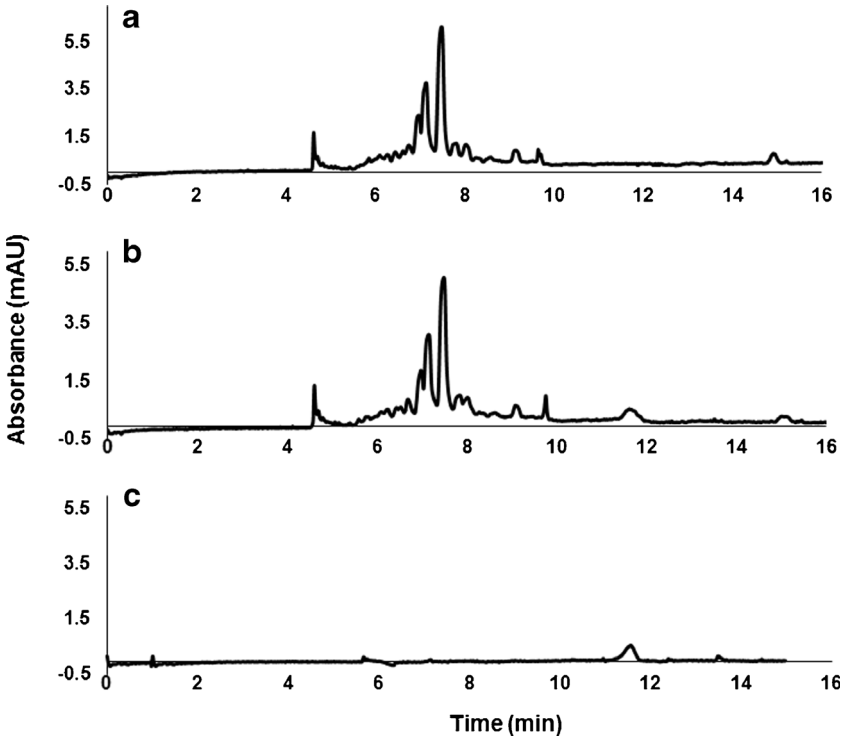

Fig. 8 Electropherograms of extracted from urine samples. (**a**) Urine sample, (**b**)urine sample spiked with Pso-dA, (**c**)spiked water sample. The separation conditions were 20 mmol L^{-1} SDS, 20 mmol L^{-1} borate buffer pH 9.30, fused-silica capillary, 64.5 cm length (56 cm to the detector), 50 μmol L^{-1} I.D., 25 °C, sample loading 50 mbar for 50 s, stacking at −15 kV, separation at 20 kV, detection UV wavelength: 260 nm

induced aggregation as long as the DNA was single stranded, short, and unfolded [34]. In this case, the adduct resulted from an adsorption process. In general, the DNA loading capacity in adsorption is much lower than can be achieved by thiolated DNA. However, it has been found that at low pH the loading capacity of AuNPs for non-thiolated DNA containing a polyadenine fragment can be increased and their conjugates maintain the full functions of DNA, enabling molecular recognition [50, 51]. In this work, the adsorption of labelled oligonucleotides (Fig. 1) was performed at acid pH. The increase in loading capacity at low pH is brought about by the reduction in electrostatic repulsion among negatively charged AuNPs and oligonucleotides, as reported in Ref. [52]. A small volume (50 μL) of stock solution (14 μmol L^{-1}) was diluted in 1.9 mL Milli-Q water (spiked solution), 100 μL C1 AuNPs was added to this diluted solution, and the suspension was mixed by a brief vortex mixing. A small volume of 500 mmol L^{-1} pH 3.00 citrate–HCl buffer was added to the suspension. After brief vortex mixing, the sample was allowed to incubate at room temperature for 4 h, the mixture was centrifuged at 14,000 rpm, and the supernatant was removed.

The pellets obtained after incubation and centrifugation were washed by suspension in water and separated by centrifuge. The conjugates were resuspended in the phosphate buffer and the suspensions of the AuNPs superficially labelled with oligonucleotides were analyzed by CE. As shown in Table 2, the AuNP adducts migrated at different rates from AuNPs and, in particular, the conjugates migrated more slowly.

This finding confirms that the proposed method is able to efficiently separate AuNPs on the basis of their size and surface properties. It should also be noticed that in this study the oligonucleotides used have a thioether linker, which is more easily displaced than a terminal thiol group linker [53].

The release of adsorbed oligonucleotides was performed at neutral pH by adding NaCl 0.1 mol L^{-1} [49] in 100 μL SDS borate buffer, and the recovery was 88±11 % (Eq. 1) with an enrichment factor of 17 resulting from the extraction. Release of nonthiolated DNA from its AuNP adducts in neutral pH solution has also been reported in Ref. [49]. The solutions of the oligonucleotides P-pso and P-acr before extraction were analyzed by REPSM-MEKC, performed under the same

Table 2 Migration time and electrophoretic mobility of AuNPs and AuNP adducts. The separation conditions were 20 mmol L^{-1} SDS, 20 mmol L^{-1} borate buffer pH 9.30, fused-silica capillary, 64.5 cm length (56 cm to the detector), 50 μm I.D., 25 °C, sample loading 50 mbar for 50 s, stacking at −15 kV, separation at 20 kV, detection at UV wavelength, 520 nm (AuNP), 543 nm (AuNP–P-pso and AuNP–P-acr)

	AuNP	AuNP–P-pso	AuNP–P-acr
Migration time (min) (SD, n=3)	9.45 (0.045)	22.66 (0.55)	20.85 (0.52)
Mobility (cm^2 V^{-1} s^{-1}) (SD, n=3)	−3.77E−04 (1.5E−06)	−5.39E−04 (2.8E−06)	−5.29E−04 (3.2E−06)

conditions as were described above for the labelled adenosines. An increase in the sensitivity of the method was obtained (Table 1), with an enrichment factor of 21±8 compared with hydrodynamic injections. Finally, by coupling the extraction procedure with REPSM, an enrichment factor of approximately 360 was obtained. The LOD, at a signal-to-noise ratio of three, of the REPSM injection technique coupled with MEKC (with extraction) were 3.3 and 4.3 nmol L^{-1} for P-pso and P-acr, respectively.

Conclusions

In this paper we present the optimization of a capillary-electrophoresis method for determining two different C8-conjugated deoxyadenosines, and oligonucleotides containing them, in which either a psoralen or an acridine moiety is linked to the adenosine through an alkyl linker containing two thioether functional groups. The choice of the linker enables a reversible capture of the compounds on gold nanoparticles, and also ensures enrichment and separation from possible interfering components (at least in aqueous solutions).

The combined two-step enrichment method, based on off-line micro solid-phase extraction (μSPE) on gold nanoparticles followed by REPSM-MEKC, can be used for the separation and analysis of labelled nucleosides and oligonucleotides. The enrichment procedure is simple and does not require additional instrumentation. The method does not use solvent and the gold nanoparticles used as solid phase can be reused, meaning the method satisfies the criteria for a green analytical-chemistry procedure. The proposed enrichment method substantially increases the sensitivity of capillary electrophoresis. In addition, the separation strategy developed can also be used to investigate surface-modified nanoparticles.

Acknowledgments The authors thank the Italian University and Scientific Research Ministry PRIN 2012-393 ATMNJ 003, and the University of Ferrara (FAR 2013) for financial support. The authors thank Daniela Palmeri of the Electronic Microscopy Centre of the University of Ferrara for the TEM images.

References

1. Usmann N, Ogilvie KK, Jiang MY, Cedergren RJ (1987) Automated chemical synthesis of long oligoribonucleotides using 2'-O-silylated ribonucleoside 3'-O-phosphoramidites on a controlled-pore glass support: synthesis of a 43-nucleotide sequence similar to the 3'-half molecule of an Escherichia coli formylmethionine tRNA. J Am Chem Soc 109:7845–7854
2. Gu HZ, Chao J, Xiao SJ, Seeman NC (2010) A proximity-based programmable DNA nanoscale assembly line. Nature 465: 202–205
3. Tyagi S, Kramer FR (1996) Molecular beacons: probes that fluoresce upon hybridization. Nat Biotechnol 14(3):303–308
4. Garbesi A, Bonazzi S, Zanella S, Capobianco ML, Giannini G, Arcamone F (1997) Synthesis and binding properties of conjugates between oligodeoxynucleotides and daunorubicin derivatives. Nucleic Acids Res 25(11):2121–2128
5. Sasco AJ, Rey F, Reynaud C, Bobin YJ, Clavel M, Niveleau A (1996) Breast cancer prognostic significance of some modified urinary nucleosides. Cancer Lett 108:157–162
6. Struck W, Waszczuk-Jankowska M, Kaliszan R, Markuszewski MJ (2011) The state-of-the-art determination of urinary nucleosides using chromatographic techniques "hyphenated" with advanced bioinformatic methods. Anal Bioanal Chem 401:2039–2050
7. Jiang Y, Ma Y (2009) A fast capillary electrophoresis method for separation and quantification of modified nucleosides in urinary samples. Anal Chem 81:6474–6480
8. Hsu WY, Chen WTL, Lin WD, Tsai FJ, Tsai Y, Lin CT, Lo WY, Jeng LB, Lai CC (2009) Analysis of urinary nucleosides as potential tumor markers in human colorectal cancer by high performance liquid chromatography/electrospray ionization tandem mass spectrometry. Clin Chim Acta 402:31–37
9. Kammerer B, Frickenschmidt A, Gleiter CH, Laufer S, Liebich H (2005) MALDI-TOF MS analysis of urinary nucleosides. J Am Soc Mass Spectrom 16:940–947
10. Mao Y, Zhao X, Wang S, Cheng Y (2007) Urinary nucleosides based potential biomarker selection by support vector machine for bladder cancer recognition. Anal Chim Acta 598:34–40
11. Breadmore MC, Shallan AI, Rabanes HR, Gstoettenmayr D, Abdul Keyon AS, Gaspar A, Dawod M, Quirino JP (2013) Recent advances in enhancing the sensitivity of electrophoresis and electrochromatography in capillaries and microchips (2010–2012). Electrophoresis 34:29–54
12. Righetti PG, Sebastiano R, Citterio A (2013) Capillary electrophoresis and isoelectric focusing in peptide and protein analysis. Proteomics 13(2):325–340
13. Iqbal J, Müller CE (2011) High-sensitivity capillary electrophoresis method for monitoring purine nucleoside phosphorylase and adenosine deaminase reactions by a reversed electrode polarity switching mode. J Chromatogr A 1218:4764–4771
14. Szymanska E, Markuszewski MJ, Bodzioch K, Kaliszan R (2007) Development and validation of urinary nucleosides and creatinine assay by capillary electrophoresis with solid phase extraction. J Pharm Biomed Anal 44:1118–1126
15. Rageh AH, Kaltz A, Pyell U (2014) Determination of urinary nucleosides via borate complexation capillary electrophoresis combined with dynamic pH junction-sweeping-large volume sample stacking as three sequential steps for their on-line enrichment. Anal Bioanal Chem 406:5877–5895
16. Whitmore CD, Essaka D, Dovichi NJ (2009) Six orders of magnitude dynamic range in capillary electrophoresis with ultrasensitive laser-induced fluorescence detection. Talanta 80:744–748
17. Zhang Z, Zhang F, Liu Y (2013) Recent advances in enhancing the sensitivity and resolution of capillary electrophoresis. J Chromatogr Sci 51:666–683
18. Malá Z, Šlampová A, Křivánková L, Gebauer P, Boček P (2015) Contemporary sample stacking in analytical electrophoresis. Electrophoresis 36(1):15–35
19. Anres P, Delaunay N, Vial J, Gareil P (2012) A chemometric approach for the elucidation of the parameter impact in the hyphenation of field-enhanced sample injection and sweeping in capillary electrophoresis. Electrophoresis 33:1169–1181
20. Kitagawa F, Otsuka K (2014) Recent applications of on-line sample preconcentration techniques in capillary electrophoresis. J Chromatogr A 1335:43–60
21. Sapsford KE, Algar WR, Berti L, Boeneman Gemmill K, Casey BJ, Oh E, Stewart MH, Medintz IL (2013) Functionalizing nanoparticles with biological molecules: developing chemistries that facilitate nanotechnology. Chem Rev 113(3):1904–2074

22. Coto-García AM, Sotelo-González E, Fernández-Argüelles MT, Pereiro R, Costa-Fernández JM, Sanz- Medel A (2011) Nanoparticles as fluorescent labels for optical imaging and sensing in genomics and proteomics. Anal Bioanal Chem 399:29–42
23. Klinkova A, Choueiri RM, Kumacheva E (2014) Self-assembled plasmonic nanostructures. Chem Soc Rev 43:3976–3991
24. Li Z, Jin RC, Mirkin CA, Letsinger RL (2002) Multiple thiol-anchor capped DNA-gold nanoparticle conjugates. Nucleic Acids Res 30:1558–1562
25. Chang CW, Tseng WL (2010) Gold nanoparticle extraction followed by capillary electrophoresis to determine the total, free, and protein-bound aminothiols in plasma. Anal Chem 82:2696–2702
26. Mourougou-Candoni N, Naud C, Thibaudau F (2003) Adsorption of thiolated oligonucleotides on gold surfaces: an atomic force microscopy study. Langmuir 19:682–686
27. Letsinger RL, Elghanian R, Viswanadham G, Mirkin CA (2000) Use of a steroid cyclic disulfide anchor in constructing gold nanoparticle-oligonucleotide conjugates. Bioconjug Chem 11:289–291
28. Peterle T, Leifert A, Timper J, Sologubenko A, Simon U, Mayor M (2008) Multidentate thioether ligands coating gold nanoparticles. Chem Commun 3438–3440
29. Maye MM, Chun SC, Han L, Rabinovich D, Zhong CJ (2002) Novel spherical assembly of gold nanoparticles mediated by a tetradentate thioether. J Am Chem Soc 124:4958–4959
30. Capobianco ML, Marchesi E, Perrone D, Navacchia ML (2013) Labeling deoxyadenosine for the preparation of functional conjugated oligonucleotides. Bioconjug Chem 24:1398–1407
31. Bernad JO, Damascelli A, Nuñez O, Galceran MT (2011) In-line preconcentration capillary zone electrophoresis for the analysis of haloacetic acids in water. Electrophoresis 32:2123–2130
32. Quirino JP, Anres P, Sirieix-Plènet J, Delaunay N, Gareil P (2011) Potential of long chain ionic liquids for on-line sample concentration techniques: application to micelle to solvent stacking. J Chromatogr A 1218:5718–5724
33. Lin KH, Chu TC, Liu FK (2007) On-line enhancement and separation of nanoparticles using capillary electrophoresis. J Chromatogr A 1161:314–321
34. Li H, Rothberg L (2004) Colorimetric detection of DNA sequences based on electrostatic interactions with unmodified gold nanoparticles. Proc Natl Acad Sci U S A 101(39):14036–14039
35. Zhang X, Liu B, Dave N, Servos MR, Liu J (2012) Instantaneous attachment of an ultrahigh density of nonthiolated DNA to gold nanoparticles and its applications. Langmuir 28:17053–17060
36. Demers LM, Östblom M, Zhang H, Jang NH, Liedberg B, Mirkin CA (2002) Thermal desorption behavior and binding properties of DNA bases and nucleosides on gold. J Am Chem Soc 124(38): 11248–11249
37. Nelson EM, Rothberg LJ (2011) Kinetics and mechanism of single-stranded DNA adsorption onto citrate- stabilized gold nanoparticles in colloidal solution. Langmuir 27(5):1770–1777
38. Lim IIS, Mott D, Engelhard MH, Pan Y, Kamodia S, Luo J, Njoki PN, Zhou S, Wang L, Zhong CJ (2009) Interparticle chiral recognition of enantiomers: a nanoparticle-based regulation strategy. Anal Chem 81(2):689–698
39. Beulen MWJ, Huisman BH, van der Heijden PA, van Veggel FCJM, Simons MG, Biemond EMEF, de Lange PJ, Reinhoudt DN (1996) Evidence for nondestructive adsorption of dialkyl sulfides on gold. Langmuir 12:6170–6172
40. Angelova P, Solel E, Parvari G, Turchanin A, Botoshansky M, Gölzhauser A, Keinan E (2013) Chemisorbed monolayers of corannulene penta-thioethers on gold. Langmuir 29:2217–2223
41. Chen MMY, Katz A (2002) Steady-state fluorescence-based investigation of the interaction between protected thiols and gold nanoparticles. Langmuir 18:2413–2420
42. Maye MM, Luo J, Lim IIS, Han L, Kariuki NN, Rabinovich D, Liu T, Zhong CJ (2003) Size-controlled assembly of gold nanoparticles induced by a tridentate thioether ligand. J Am Chem Soc 125(33): 9906–9907
43. Nion A, Jiang P, Popoff A, Fichou D (2007) Rectangular nanostructuring of Au(111) surfaces by self-assembly of size-selected thiacrown ether macrocycles. J Am Chem Soc 129(9):2450–2451
44. Hermes JP, Sander F, Fluch U, Peterle T, Thompson D, Urbani R, Pfohl T, Mayor M (2012) Monofunctionalized gold nanoparticles stabilized by a single dendrimer form dumbbell structures upon homocoupling. J Am Chem Soc 134(36):14674–14677
45. Cifuentes A, Bernal JL, Diez-Masa JC (1997) Determination of critical micelle concentration values using capillary electrophoresis instrumentation. Anal Chem 69(20):4271–4274
46. Soares DM, Gomes WE, Tenan MA (2007) Sodium dodecyl sulfate adsorbed monolayers on gold electrodes. Langmuir 23:4383–4388
47. Huang YF, Huang CC, Chang HT (2003) Exploring the activity and specificity of gold nanoparticle-bound trypsin by capillary electrophoresis with laser-induced fluorescence detection. Langmuir 19: 7498–7502
48. Jin R, Wu G, Li Z, Mirkin CA, Schatz GC (2003) What controls the melting properties of DNA-linked gold nanoparticle assemblies? J Am Chem Soc 125:1643–1654
49. Zhang X, Liu B, Servos MR, Liu J (2013) Polarity control for nonthiolated DNA adsorption onto gold nanoparticles. Langmuir 29(20):6091–6098
50. Kimura-Suda H, Petrovykh DY, Tarlov MJ, Whitman LJ (2003) Base-dependent competitive adsorption of single-stranded DNA on gold. J Am Chem Soc 125(30):9014–9015
51. Jiang H, Materon EM, Sotomayor MDPT, Liu J (2013) Fast assembly of non-thiolated DNA on gold surface at lower pH. J Colloid Interface Sci 411:92–97
52. Dam DHM, Lee H, Lee RC, Kim KH, Kelleher NL, Odom TW (2015) Tunable loading of oligonucleotides with secondary structure on gold nanoparticles through a pH-driven method. Bioconjug Chem 26:279–285
53. Takeishi S, Rant U, Fujiwara T, Buchholz K, Usuki T, Arinaga K, Takemoto K, Yamaguchi Y, Tornow M, Fujita S, Abstreiter G, Yokoyama N (2004) Observation of electrostatically released DNA from gold electrodes with controlled threshold voltages. J Chem Phys 120:5501–5504

myDesk @unife

Valentina Bosi <bsovnt@unife.it>

Fwd: Thank you for your RightsLink / Springer transaction

Luisa Pasti <psu@unife.it> 11 febbraio 2016 11:58
A: VALENTINA BOSI <valentina.bosi@student.unife.it>

---------- Forwarded message ----------
From: **Copyright Clearance Center** <rightslink@marketing.copyright.com>
Date: 2016-02-11 11:57 GMT+01:00
Subject: Thank you for your RightsLink / Springer transaction
To: psu@unife.it

To view this email as a web page, go here.

Do Not Reply Directly to This Email

To ensure that you continue to receive our emails,
please add rightslink@marketing.copyright.com to your address book.

RightsLink | Copyright Clearance Center

Thank You For Your Order!

Dear Mrs. Luisa Pasti,

Thank you for placing your order through Copyright Clearance Center's RightsLink service. Springer has partnered with RightsLink to license its content. This notice is a confirmation that your order was successful.

Your order details and publisher terms and conditions are available by clicking the link below:
http://s100.copyright.com/CustomerAdmin/PLF.jsp?ref=0ef8548d-c271-4bec-bd3d-f0cd657eb9e0

Order Details
Licensee: Luisa Pasti
License Date: Feb 11, 2016
License Number: 3805850843842
Publication: Analytical and Bioanalytical Chemistry
Title: Gold-nanoparticle extraction and reversed-electrode-polarity stacking mode combined to enhance capillaryelectrophoresis sensitivity for conjugated nucleosides and oligonucleotides containing thioether linkers
Type Of Use: Thesis/Dissertation
Total: 0.00 USD

To access your account, please visit https://myaccount.copyright.com.

Please note: Online payments are charged immediately after order confirmation; invoices are issued daily and are payable immediately upon receipt.

To ensure that we are continuously improving our services, please take a moment to

complete our customer satisfaction survey.

B.1:v4.2

+1-855-239-3415 / Tel: +1-978-646-2777
customercare@copyright.com
http://www.copyright.com

This email was sent to: **psu@unife.it**

Please visit Copyright Clearance Center for more information.

This email was sent by Copyright Clearance Center
222 Rosewood Drive Danvers, MA 01923 USA

To view the privacy policy, please go here.

--

Luisa Pasti Ph.D
Department of Chemistry and Pharmaceutical Sciences
University of Ferrara
Via L. Borsari, 46
44123 Ferrara, ITALY

e-mail: luisa.pasti@unife.it
tel:+39 0532 455346
fax:+39 0532 240709

Microporous and Mesoporous Materials 215 (2015) 175–182

Contents lists available at ScienceDirect

Microporous and Mesoporous Materials

journal homepage: www.elsevier.com/locate/micromeso

Adsorption of 1,2-dichloroethane on ZSM-5 and desorption dynamics by *in situ* synchrotron powder X-ray diffraction

A. Martucci [a,*], E. Rodeghero [b], L. Pasti [b], V. Bosi [b], G. Cruciani [a]

[a] Department of Physics and Earth Sciences Department, University of Ferrara, Via Saragat, 1, I-44122 Ferrara, Italy
[b] Department of Chemistry, University of Ferrara, Via L. Borsari, 46, I-44123 Ferrara, Italy

ARTICLE INFO

Article history:
Received 30 January 2015
Received in revised form
25 April 2015
Accepted 18 May 2015
Available online 27 May 2015

Keywords:
Thermal regeneration
1,2-dichloroethane
Adsorption
In situ synchrotron X-ray powder diffraction

ABSTRACT

The adsorption/desorption behaviour of ZSM-5 loaded with 1,2-dichloroethane was studied using the *in situ* synchrotron X-ray powder-diffraction technique in the temperature range 30°–600 °C. Rietveld refinements allowed to monitor the DCE decomposition process as well as the structural modifications undergoing on ZSM-5 upon a temperature-programmed thermal treatment. These results clearly demonstrated that regeneration of ZSM-5 is effective when thermally treating the adsorbent at about 300 °C thus minimising the cost of the regeneration step of the adsorption process. Once regenerated and reloaded the Rietveld refinement indicates that both DCE location and content remain substantially unchanged thus confirming ZSM-5 is able to re-adsorb DCE in amounts comparable to that adsorbed in the first cycle, in very good agreement with the chromatographic results. In conclusion, the use of this adsorbent with unchanged adsorption performances after thermal regeneration under mild conditions appears very promising also over several cycles of the adsorption/desorption process.

1. Introduction

Chlorinated volatile organic compounds (VOCs), such as 1,2-dichloroethane (DCE) constitute an important environmental pollutants class. VOC have been used extensively in the past for many industrial and domestic applications. Leaks, spills, and wrong disposal practices have led to widespread contamination of groundwater. Because of their diffusion in the environment, their human toxicity, and tendency to persist in ground-water [1] these contaminants are of particular concern for human health. Moreover, many VOC are mutagens and teratogens, and, furthermore, are known or suspected human carcinogens." [2]. Adsorption is a reliable alternative to eliminate these organic compounds from wastewaters because of the flexibility of the system, low energy and cheap operation costs.

Recently, high-silica zeolites characterized by a silica/alumina ratio >50, have been shown to be environmental friendly materials able to efficiently sorb from water emerging organic contaminants such VOCs more efficiently than activated carbon [1,3–9]. Zeolite advantages concerning high organic contaminant selectivity, high specific capacity, rapid kinetics, absence of salt and humic substance interference, excellent resistance to chemical, biological, mechanical or thermal stress have been reported [10].

In particular, the mechanisms and effectiveness of high-silica zeolite adsorbents (ZSM-5, mordenite, and Y zeolites) for DCE removal from water have investigated by combing X-ray diffraction, gas-chromathography and thermal analyses (TG, DTA) [6,11]. The presence of DCE molecules inside the zeolite pores was revealed by unit cell parameters variations and structural deformations obtained from conventional X-ray structure analyses carried out using the Rietveld method on exhausted zeolite samples. Very interestingly, structure refinements demonstrated that these changes are strongly related to the complexation of the guest species with water molecules. Therefore, these results allowed to select the isotherm models which better explained the experimental adsorption data. In particular, zeolite ZSM-5 (MFI-type framework topology, [12]) with high SiO_2/Al_2O_3 ratio was found to be very effective in DCE removal from water [6].

Moreover, it has been reported that zeolites can be easily thermally regenerated at low cost without changing their initial adsorption or catalytic properties [13–15]. After adsorption, the exhausted zeolites are normally subjected to a regeneration process by operating under particularly mild conditions at temperatures ranging from 250° to 350 °C, for a time ranging from

* Corresponding author.
E-mail addresses: mrs@unife.it, psu@unife.it (A. Martucci).

http://dx.doi.org/10.1016/j.micromeso.2015.05.035
1387-1811/

0.5 to 1.5 h, in the presence of an air flow ranging from 1.5 to 2.5 m^3/hr [13].

In this work, the *in situ* high-temperature (HT) synchrotron X-ray powder diffraction (XRPD), is used as a key to continuous monitoring of DCE decomposition process as well as the structural modifications undergoing on ZSM-5 upon a temperature-programmed thermal treatment. Understanding the transient and dynamic features of desorption processes can contribute to better design and optimize the regeneration treatment of hydrophobic zeolites. Achieving the (re)activation of the microporous adsorbents under mild conditions would expand their capabilities in environmental applications.

With this purpose, the structural rearrangements on the zeolitic framework were analysed and the adsorption capacity of ZSM-5 after thermal regeneration and were also tested in order to verify whether the reactivated material can be further used for DCE removal from wastewater.

2. Experimental

2.1. Diffraction methods

The powder sample of ZSM-5 organophilic zeolite (CBV28014, Zeolyst International, SiO_2/Al_2O_3 ~ 280, Na_2O content ‹0.05 wt.%, NH_4^+ content <0.1% w/w, Surface Area of 400 m^2/g) loaded with 1,2 dichloroethane has been studied *in situ* by synchrotron radiation powder diffraction. The details of sample preparation are reported elsewhere [6]. Time – resolved diffraction data were collected (temperature range 30°–600 °C) on the ID31 beamline at ESRF (Grenoble), using a fixed wavelength of 0.400031(1) Å. The sample diffracted X-rays were collected in parallel by means of nine Si 111 analyser crystals and scintillation detectors. Measurements of X-ray powder diffraction (XRPD) patterns at room temperature of both the calcined and reloaded ZSM-5 samples were performed on a Bruker AXS D8 Advance diffractometer equipped with Si(Li) solid state detector (Sol-X). The experimental conditions were the following: Cu $K\alpha_1,\alpha_2$ radiation, 2θ range: 3–110°, step size: 0.02°, time/step: 12 s, scattering, divergence, and receiving slits: 0.6, 0.6 and 0.1 mm, respectively.

2.2. Structure refinement

The structure refinements by full profile Rietveld analysis was carried out using the GSAS [16] package and the EXPGUI graphical interface [17] starting from the atom site positions reported by Pasti et al. [6]. Extraframework site were located by difference Fourier synthesis. The Bragg peak shape was modelled using a modified pseudo-Voigt function with 0.01% cut-off peak intensity. The instrumental background was empirically fitted using a Chebyschev polynomial of the first kind with 16 variable coefficients for room temperature and 24 variable coefficients for high temperature data set. The 2θ-zero shift, scale factor and unit-cell parameters were accurately refined. Soft constraints were imposed on Si–O and O–O framework distances (1.60 and 2.60 Å, respectively) and on C–C (1.34 Å), C–Cl (1.74 and 2.76 Å) and Cl–Cl (4.34 Å) DCE distances and the weight was gradually released after the initial stages of refinement, H-atoms were not considered in the structure refinement due to their low scattering factors. In the final cycles, all positional parameters, site occupancy, and isotropic atomic displacement parameters (ADPs) were refined. The structural model obtained at ambient conditions was then used for the high temperature pattern analysis by adopting the same structure refinement strategies. The 2θ-zero shift and the reflection intensity were preliminary refined with Le Bail extraction method and then kept fixed at the mean value in all patterns of the data set. No evidence was found to support a change in symmetry on the powder patterns until 75 °C: the monoclinic $P2_1/n$ space group was used at room and 50 °C temperature, orthorhombic P*nma* space group was used in all the crystal structure refinements in the 75°–600 °C temperature range.

Lattice parameters and refinement details of ZSM-5-DCE at 30 °C (ZSM-5-DCE-30), regenerated (ZSM-5-R), and regenerated and reloaded ZSM-5 (ZSM-5-R-DCE) are reported in Table 1. The features of unloaded material [6] are also listed for comparison. Framework atoms site positions and isotropic ADPs, extraframework atomic coordinates, occupancy and temperature factors of ZSM-5-DCE at 30 °C (ZSM-5-DCE-30), regenerated (ZSM-5-R), and regenerated and reloaded ZSM-5 (ZSM-5-R-DCE) respectively, are provided as Supporting Information in Table1S and Table2S, respectively; the dimensions of the 10-membered rings (10MRs) together with their Crystallographic Free Area (C. F. A) and their ellipticity (ε) are reported in Table 2. Mol Files of all refined structures are also uploaded as SI.

2.3. Thermal analysis

Thermogravimetric (TG) and differential thermal analysis (DTA) measurements of both the calcined and reloaded ZSM-5 samples were performed in air at up to 600 °C using a Netzsch STA 409 PC LUXX® - simultaneous TG/DTA thermogravimetric analyzer operating at 5 °C/min heating rate. The thermal curves are reported in Fig. 1.

2.4. Gas chromatography

The DCE concentration in the aqueous solutions was determined using a Gas Chromatography – Electron Capture Detector (GC-ECD). Prior to this, the DCE was extracted from the water sample by Head Space - Solid Phase Micro Extraction (HS-SPME). The head space mode was used to extract DCE from 10 ml of solution in 25-ml glass flasks sealed with Teflon screw caps. 2 mL of a 300 g L^{-1} NaCl solution were added to the sample. Samples were immersed in a thermostatic water bath at 40 °C (±0.5 °C) and maintained under controlled agitation with a magnetic stirrer (300 rpm) for 10 min to reach equilibrium conditions before SPME insertion. The fibre was inserted into the GC injector for analysis and kept at 250 °C. The

Table 1
Lattice parameters and refinement details of unloaded ZSM-5 (ZSM-5)[a], after thermal regeneration (ZSM-5-R), after DCE adsorption (ZSM-5-DCE-30), and for regenerated and reloaded sample (ZSM-5-R-DCE).

	ZSM-5[a]	ZSM-5-DCE-30	ZSM-5-R	ZSM-5-R-DCE
Space group	$P2_1/n$	$P2_1/n$	$P2_1/n$	$P2_1/n$
a (Å)	19.8999(5)	19.9052(3)	19.8935(5)	19.8954(5)
b (Å)	20.1174(6)	20.1199(3)	20.1165(5)	20.1177(5)
c (Å)	13.3892(4)	13.3909(2)	13.3818(4)	13.3835(4)
β	90.546(3)	90.578(1)	90.5598(23)	90.5641(25)
V (Å^3)	5359.9(3)	5362.7(1)	5354.97(25)	5356.46(26)
Wavelength of incident radiation (Å)	1.5417(1)	0.400031(1)	1.5417(1)	1.5417(1)
Refined pattern 2θ range (°)	3–110	0.7–25	3–110	3–110
R_{wp} (%)	9.12	9.2	11.90	12.94
R_p (%)	8.4	8.5	8.76	10.07
R_F^2 (%)	9.1	7.50	5.75	5.57
No. of contributing reflections	14142	12252	6039	10258
N_{obs}	5601	7239	8911	6223
N_{var}	289	282	250	282

$R_p = \sum[Y_{io}-Y_{ic}]/\sum Y_{io}$; $R_{wp} = [\sum w_i(Y_{io}-Y_{ic})^2/\sum w_i Y_{io}^2]^{0.5}$; $R_F^2 = \sum|F_o^2-F_c^2|/\sum|F_o^2|$

[a] Pasti et al., 2012 [6].

Table 2
Dimensions (Å) of the apertures of unloaded ZSM-5 (ZSM-5)[a], after thermal regeneration (ZSM-5-R), after DCE adsorption (ZSM-5-DCE-30), and for regenerated and reloaded sample (ZSM-5-R-DCE) assuming an oxygen ionic radius of 1.35 Å. The ellipticity (ε = largest/shortest oxygen–oxygen distances) and C.F.A. were also reported.

Straight channel (SC-A)	ZSM-5[a]	ZSM-5-R	ZSM-5-DCE-30	ZSM-5-R-DCE
O7–O1	7.98(1)	7.96(1)	8.21(1)	8.40(1)
O8–O2	8.08(1)	8.00(1)	8.11(1)	7.97(1)
O31–O37	8.20(1)	8.00(1)	8.28(1)	8.01(1)
O44–O46	8.19(1)	8.28(1)	8.63(1)	8.72(1)
O47–O48	7.93(1)	7.80(1)	7.96(1)	7.95(1)
C.F.A.	22.68	22.16	24.14	23.88
ε	1.03	1.06	1.08	1.10
Straight channel (SC-A)	ZSM-5[a] [6]	ZSM-5-R	ZSM-5-DCE-30	ZSM-5-R-DCE
O11_O5	8.23(1)	8.19(1)	8.15(1)	8.19(1)
O20_O18	8.21(1)	8.19(1)	8.49(1)	8.33(1)
O21_O22	8.04(1)	8.02(1)	8.01(1)	7.98(1)
O27_O33	8.03(1)	7.95(1)	8.38(1)	8.31(1)
O28_O34	8.07(1)	7.86(1)	7.081(1)	8.00(1)
C.F.A.	22.68	22.45	23.51	23.47
ε	1.02	1.04	1.08	1.04
Sinosuidal channel (ZZ-B)	ZSM-5[a]	ZSM-5-R	ZSM-5-RT	ZSM-5-R-DCE
O17–O18	7.81(1)	7.59(1)	7.71(1)	7.59(1)
O23–O25	8.20(1)	8.11(1)	8.49(1)	8.54(1)
O30–O5	8.31(1)	8.26(1)	8.59(1)	8.31(1)
O31–O4	7.91(1)	7.63(1)	7.64(1)	7.69(1)
O44–O43	8.13(1)	8.07(1)	8.18(1)	8.29(1)
C.F.A.	22.65	21.51	23.12	22.80
ε	1.06	1.08	1.12	1.12
Sinosuidal channel (ZZ-A)	ZSM-5[a]	ZSM-5-R	ZSM-5-RT	ZSM-5-R-DCE
O20–O15	7.95(1)	7.90(1)	8.28(1)	8.38(1)
O24–O26	7.84(1)	7.77(1)	8.26(1)	8.24(1)
O27–O2	7.85(1)	7.89(1)	8.16(1)	7.95(1)
O28–O1	7.90(1)	7.83(1)	7.96(1)	8.13(1)
O41–O46	8.22(1)	8.29(1)	8.68(1)	8.57(1)
C.F.A.	21.65	21.54	24.37	24.24
ε	1.04	1.06	1.09	1.08

[a] Pasti et al., 2012 [6].

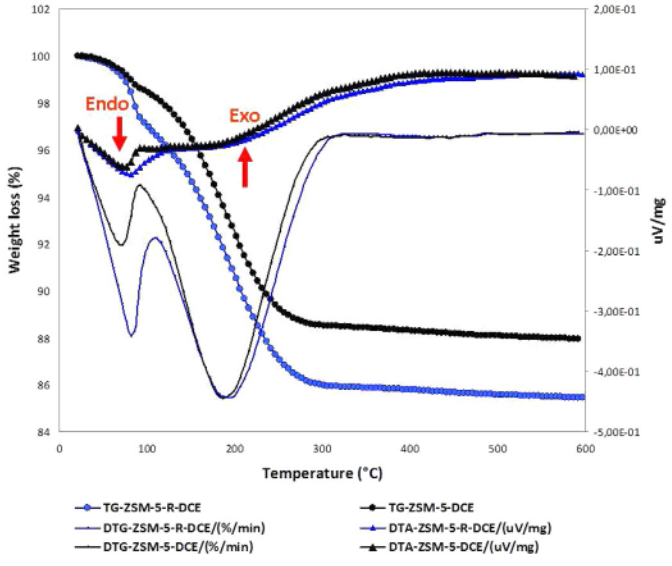

Fig. 1. Thermogravimetric (TG), differential thermogravimetric (DTG) and differential thermal analysis (DTA) curves in ZSM-5-DCE (TG, black circle; DTG, black line; DTA, black triangle) and ZSM-5-R-DCE (TG, blue circle; DTG, blue line; DTA, blue triangle) dry air atmosphere.(For interpretation of the references to colour in this figure legend, the reader is referred to the web version of this article.)

desorption time was 1 min. The GC used in this work was an HRGC 5160 MEGA SERIES Instrument (Carlo Erba, Mi, I) equipped with a split/splitless injector and an electron capture detector (ECD,^{63}Ni). A fused-silica DB-5 capillary column (60 m × 0.25 mm I.D:, 0.25 μm film thickness; J&W Scientific, USA) was employed. Helium (99.999%) was used as a carrier gas at a constant head pressure of 50 kPa and nitrogen (196 KPa) was employed as a make-up gas at a constant flow-rate (1 mL min^{-1}). The detector temperature was kept constant at 250 °C. The GC oven was programmed as follows: 40 °C (5 min), 5 C min^{-1} to 80 °C (5 min), 30 C min^{-1} to 100 °C (5 min).

2.5. Adsorption isotherm

The adsorption isotherm was determined using the batch method. Batch experiments were carried out in duplicate in 20 ml crimp top reaction glass flasks sealed with PTFE septa (Supelco, PA, USA). The flasks were filled in order to have the minimum headspace, a solid/solution ratio of 1:4 (mg mL^{-1}) was employed. After equilibration, (24 h) at a temperature of 25.3 ± 0.5 °C under stirring, the solids were separated from the aqueous solution using centrifugation (14000 rpm for 30 min). To determine the adsorbed quantities (q) and the equilibrium concentrations (Ce), the DCE concentrations were determined in the solutions before and after equilibration with the regenerated zeolite by HS-SPME-GC_ECD (see 2.4 Gas Chromatography).

3. Results and discussion

3.1. In situ synchrotron X-ray powder diffraction and Rietveld refinements

ZSM-5 is a pentasil zeolite widely used as shape-selective catalysts and sorbents due to its shape selectivity, solid acidity, ion exchangeability, pore size and thermal stability. The MFI framework is characterized by two intersecting sets of tubular channels, a linear or 'straight' (SC = straight channel) one parallel to the [010] direction, (apertures opening ~5.4–5.6 Å), and a sinusoidal or zigzag, (ZZ) one parallel to the [100] direction, (apertures opening ~5.1–5.5 Å) [18] (Fig. 1SI).

The topological symmetry is orthorhombic *Pnma*, but its real symmetry strongly depends by the synthesis and post synthesis treatment, SiO_2/Al_2O_3 ratio, structural defects, temperature, nature and amount sorbate organic molecules [18–22]. After DCE adsorption [6] the automatic indexing of the peaks as well as the β values confirmed the $P2_1/n$ monoclinic symmetry [6]. Rietveld refinement has revealed that different DCE molecules could be connected by means of hydrogen bonds through water, to form DCE–water complexes, thus influencing the DCE trans–gauche conformational equilibrium [6]. A similar result has been recently found in hydrophobic mordenite after DCE adsorption [11].

In this work, Rietveld structure refinement of ZSM-5-DCE using *in situ* synchrotron X-ray powder diffraction data was performed starting from the structural model reported at room temperature by Pasti et al. [6]. The difference Fourier map, generated using the GSAS package, confirmed the distribution of the DCE molecules over the two crystallographically independent sites (DCE1 = C1, C2, Cl1, Cl2 sites; DCE2 = C3, C4, Cl3, Cl4 sites) (Fig. 2a, Table S2) localized by Pasti et al. [6]. They are located in both the straight (DCE1) and sinusoidal (DCE2) channels and lye parallel to c and a, b directions, respectively. The location of co-adsorbed water molecules (W site, ~3.0 water/u.c, corresponding to ~1.5% in weight) was also confirmed. According to the starting model, all the DCE molecules (~6.5molecules/u.c., corresponding to ~9.5% in weight) assume a trans (anti)configuration

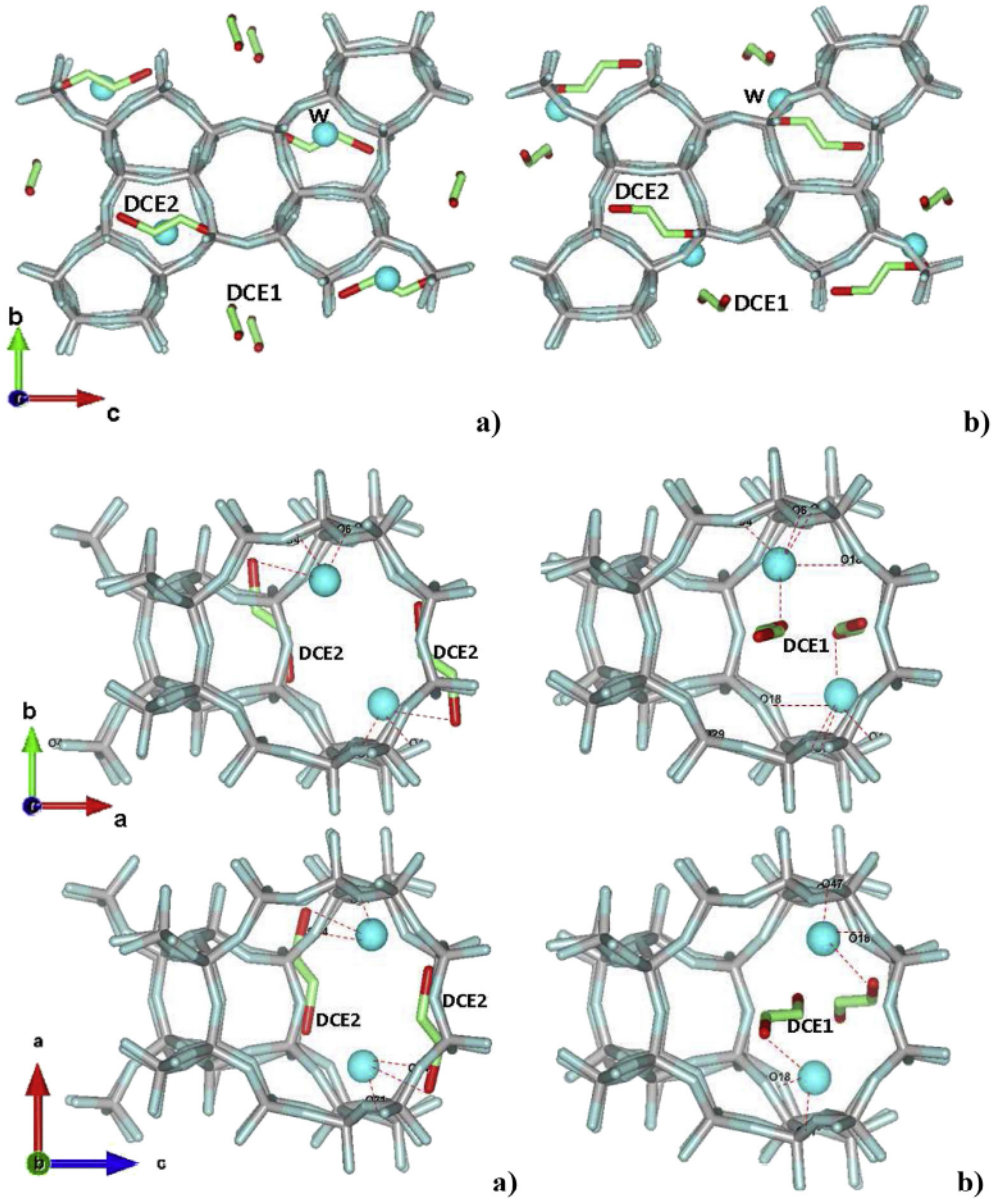

Fig. 2. Location of DCE and water molecules in ZSM-5 along [100] and [010] directions, in ZSM-5-DCE-30 (a) and ZSM-5-R-DCE(b), respectively. Chlorine (red), carbon (green), water molecules (light blue circle), framework oxygens (light blue line) and silicium (green line) atoms are reported.(For interpretation of the references to colour in this figure legend, the reader is referred to the web version of this article.)

and can interact with water thus forming DCE–water molecule complexes (clusters or short chains) bridged via W to framework oxygen atoms (Fig. 2b). Thermogravimetric analysis (TG) was used to determine the amount of DCE molecules embedded in the ZSM-5 framework, and to monitor the decomposition process of organic molecules during the heating procedure. The TG curve of the ZSM-5-DCE (Fig. 1) showed that, apart from the elimination of species (water and/or DCE) weakly bonded to the surface ($T < 100\,^{\circ}C$, weigh loss 1.5%), a sudden change in its slope occurs at higher temperatures, which is reasonably due to the elimination of DCE and/or H_2O molecules trapped within the zeolite pores. Total weight loss at 900 °C is about 12.0% compared to 2.5% in the as-synthesised sample [6]. This result is in very good agreement with the extraframework content given by the refined occupancies and with the saturation capacity determined by the adsorption isotherms [6].

The gradual overlapping of groups of peaks (Fig. 3) reveals that the monoclinic $P2_1/n$ to orthorhombic *Pnma* phase transition, occurs with a Tc close to $70 \pm 5\,^{\circ}C$. As recently reported by Ardit et al. [23], the same phase transition occurs in the same as-synthesized material used in this work, as demonstrated by *in situ* synchrotron X-ray diffraction data. The authors highlighted the tricritical character of this transition from ferroelastic (monoclinic) to paraelastic (orthorhombic) phase in ZSM-5 [23].

The occurrence of this phase transition also confirms the well-known crucial influence of the Si/Al ratio [18–22,24,25] as well of the adsorbed extra-framework molecules [6,11,18–22,26–31] on the monoclinic-orthorhombic phase transition undergone by this zeolite. Since no evidence was found to support another change in symmetry on the powder patterns until 600 °C, the same orthorhombic *Pnma* space group was used in all the crystal structure refinements in the 70–600 °C temperature range.

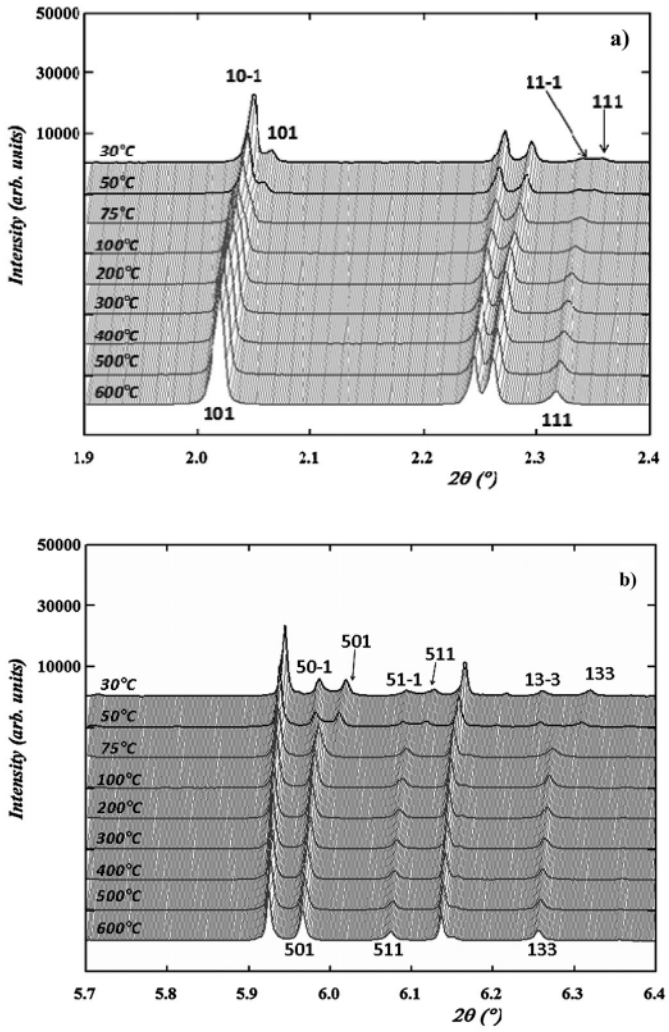

Fig. 3. Plot of ZSM-5-DCE-30 in the 1.9–2.4 (a) and 5.7–6.4 (b) °2θ ranges within the 30–600 °C temperature interval.

Table 3
High-temperature lattice parameters of ZSM-5-DCE in the temperature range 30°–600 °C. Figures in parentheses represent the estimated standard-deviation.

T(°C)	a(Å)	b(Å)	c(Å)	Volume(Å^3)	β(°)
30	19.9052(3)	20.1199(3)	13.3909(2)	5362.65(1)	90.58(1)
40	19.9080(3)	20.1218(3)	13.3938(2)	5365.10(1)	90.54(1)
50	19.9118(3)	20.1213(3)	13.3962(2)	5367.36(1)	90.50(1)
60	19.9164(3)	20.1241(3)	13.4006(2)	5370.79(1)	90.43(1)
75	19.9336(3)	20.1129(3)	13.4077(9)	5375.46(1)	90
100	19.9378(6)	20.1067(5)	13.4076(6)	5374.90(1)	90
125	19.9394(5)	20.1024(5)	13.4066(2)	5373.99(2)	90
150	19.9392(4)	20.1022(4)	13.4054(2)	5373.15(2)	90
175	19.9373(5)	20.1031(5)	13.4042(3)	5373.30(2)	90
200	19.9348(4)	20.1054(4)	13.4034(3)	5372.05(2)	90
225	19.9339(4)	20.1040(4)	13.4024(3)	5371.04(2)	90
250	19.9331(4)	20.1014(4)	13.4014(3)	5369.72(2)	90
275	19.9321(4)	20.0978(4)	13.4004(3)	5368.10(2)	90
300	19.9311(4)	20.0942(3)	13.3996(2)	5366.51(2)	90
350	19.9290(4)	20.0886(3)	13.3980(2)	5363.84(2)	90
400	19.9274(4)	20.0832(2)	13.3969(2)	5361.53(2)	90
450	19.9254(3)	20.0785(3)	13.3956(2)	5359.20(2)	90
500	19.9229(3)	20.0743(3)	13.3941(2)	5356.83(2)	90
550	19.9203(4)	20.0708(4)	13.3924(2)	5354.51(2)	90
600	19.9175(4)	20.0675(4)	13.3906(2)	5352.14(2)	90

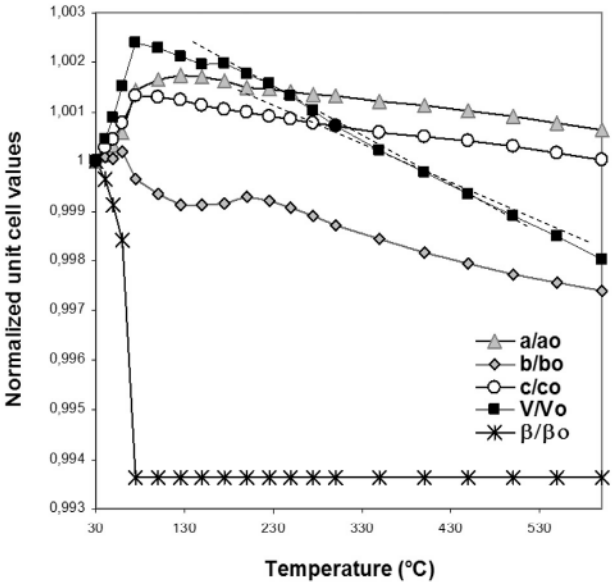

Fig. 4. Temperature evolution of the unit cell parameters of ZSM-5-DCE during the *in situ* thermal burning of the organic. Broken lines highlight the subtle discontinuity on the cell volume trend occurring at about 380 °C.

The complete set of lattice parameters is given in Table 3 and illustrated as a function of temperature in Fig. 4. To allow a better comparison between them, we report normalised values of cell parameters defined as $V(T)/V_0$, $a(T)/a_0$, $b(T)/b_0$, and $c(T)/c_0$, being the reference values those obtained in the refinement of the first orthorhombic pattern recorded at T = 30 °C.

The slight increase of unit cell volume (ΔV~1%) up to 70 °C can be reasonably related to the relaxation of the bonding interactions between the DCE–water molecule complexes and framework oxygen atoms. The refined distances of the DCE atoms from the O atoms in both framework and water molecules indicate that bonding between the water-DCE oligomer and the framework oxygen atoms breaks down during the first stage of temperature increase. As a consequence this attractive force, exerting a kind of negative pressure on the surrounding framework, disappears. The oxygen framework is thus free to relax and expand as demonstrated by the ellipticity decrease in the zeolite channel systems. The formation of more regular wide-open apertures upon heating is likely associated to the observed relative expansion of the framework thus explaining the evolution of the unit cell parameters and the positive cell volume expansion at low temperature. A similar framework expansion was also observed upon heating in B-ZSM-5 [30], as well as in other microporous materials such as wairakite [31], analcime [32], hydro-sodalite $Na_6[AlSiO_4]_6 \cdot 8H_2O$ [33] and silica sodalite [34].

The refined occupancies reported in Fig. 5 showed that in this temperature range the DCE1 site progressively decrease its occupancy and it is emptied at temperature (225 °C) lower than that found for the organic hosted in DCE2 site (350 °C), which is forced into the sinusoidal channel. This is in agreement with the thermogravimetric analysis reported by Pasti et al. [6], according which the state of the DCE-ZSM-5 system is altered in the temperature range ~150°–350 °C.

This finding indicated that DCE molecules preferentially diffuse through the straight channel of orthorhombic ZSM-5. At 350 °C all the Cl and C sites are emptied, thus confirming the completion of the thermal degradation of DCE at this temperature. A similar behaviour was observed for site occupancy of water molecules. The parallelism in the decrease of DCE and water occupancies with

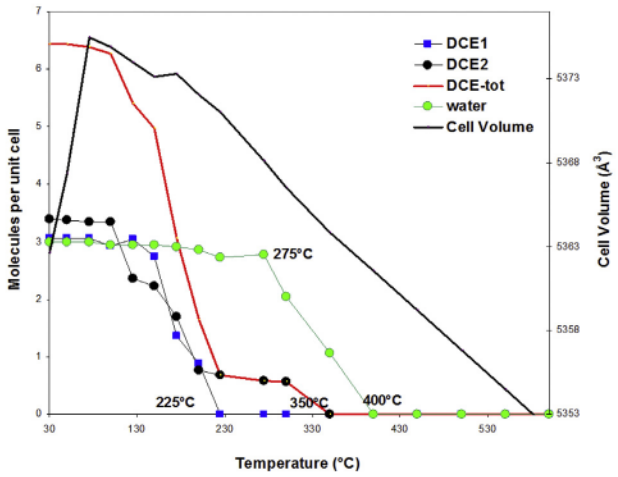

Fig. 5. Variation of DCE and water molecules per unit cell as a function of temperature. The evolution of unit cell volume is also shown for comparison.

temperature increase, can be explained by the disassembly of water–DCE clusters caused by the DCE thermal degradation. The serial structural refinements during the thermal ramp provide information on the way in which the occupancy of the extraframework sites affect the geometry of the framework.

In Fig. 6a and b are reported the Crystallographic Free Areas (C.F.A.) and the ellipticity of the 10 MR channels as a function of temperature. The opening of the zeolite framework pore system change with temperature increase due the continuous structural changes associated with the heating process (see Fig. 6a and b). Consequently, the Crystallographic Free Areas (C.F.A.) that depends on channel ellipticity also vary with temperature [10](see Fig. 6a). The decrease of channel ellipticity with temperature increase reported in Fig. 6b is due to the framework flexibility of ZSM-5 [35–37]. In particular, the straight (SC) 10-ring channel become narrower and its ellipticity (ε) (defined as the ratio between the smaller (O–O) and larger (O–O)"free diameters" of the 10-rings) decreases. A similar contraction was also observed in the sinusoidal channels which become more regular: the resulting cumulative effect explains the unit-cell contraction registered upon heating (Fig. 5b). Once all DCE and water molecules are completely decomposed, no further significant variations are registered in the dimension of the 10 MR channels.

At temperature higher than 400 °C, the host molecule decomposition and expulsion process is completed, therefore the unit cell contraction of ZSM-5 above this temperature can be described as a proper negative thermal expansion (NTE) process (Fig. 4). This behaviour is similar to that observed in MFI-type materials synthesized in the presence of tetrapropylammonium as well in their calcined forms e.g. silicalite-1 [38] titanium silicalite-1 (TS-1) [39] and Fe-silicalite (Fe-MFI) [40]. In particular, in TS-1 and Fe-MFI a negative thermal expansion (NTE) was reported above the temperature which marks the end of the calcination process.

3.2. Adsorption behaviour of regenerated adsorbent

The regeneration of ZSM-5 loaded with DCE was conducted by high temperature calcination using the TG/DTA thermogravimetric analyzer operating at 5 °C/min heating rate from room temperature to 600 °C for completely burning off the organics. After regeneration, the X-ray powder diffraction pattern (ZSM-5-r) was collected and then indexed on a monoclinic unit cell that is consistent with

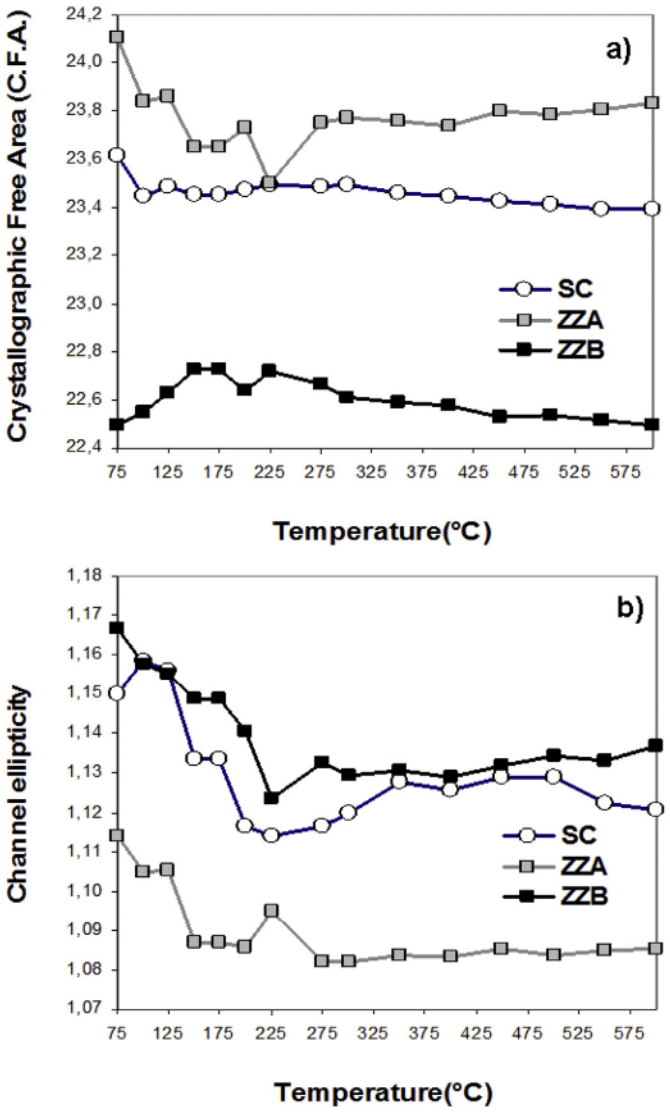

Fig. 6. (a) Evolution of Crystallographic Free Area CFA sensu (Baerlocher et al., 2007) and (b) channel ellipticity for the 10 MR channels as a function of temperature.

that also observed for the unloaded material. According to Leardini et al. [15] the splitting of (131) and (133) peaks reveals the reversibility of the orthorhombic *Pnma* to monoclinic $P2_1/n$ to phase transition. Fig. 7 shows that after regeneration the diffraction peaks are very sharp, indicating that ZSM-5 retain its original crystallinity upon heating.

The regenerated ZSM-5-r was then tested again for DCE adsorption. Fig. 8 shows the comparison of the adsorption performance of fresh and regenerated zeolite. The regenerated sample from air calcination produced slightly higher adsorption in the low concentration range than the fresh one as shown in the inset of Fig. 8. Possibly, this is due to the decomposition of the low amount of NH_4 in the starting material. This result perfectly agrees with the weight loss estimated on the basis of thermal analyses (weight loss ~14.5%) reported in Fig. 1, which is slightly higher than that observed in ZSM-5-DCE (12.0% in weight).

The adsorption data were fitted by using a Langmuir equation (see Table 4, 2nd column) and the parameters found for the adsorption od DCE on regenerated material were not statistically different to those charactering the fresh material reported in Pasti et al. [6].

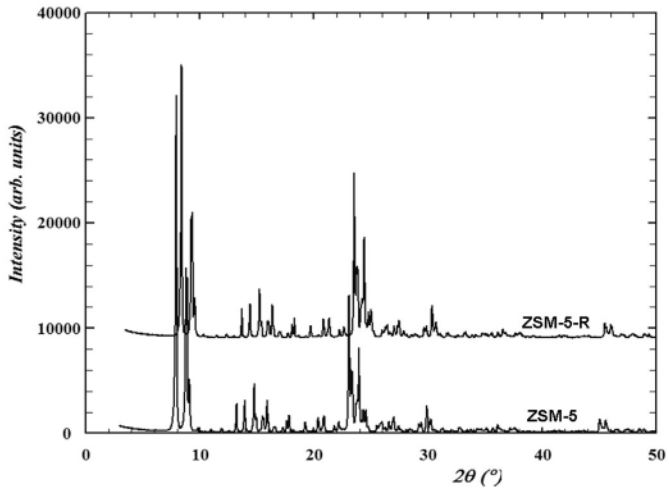

Fig. 7. Powder diffraction patterns of unloaded (ZSM-5) and thermally regenerated (ZSM-5-R) zeolites, respectively (the stacked plots have been shifted for easy comparison).

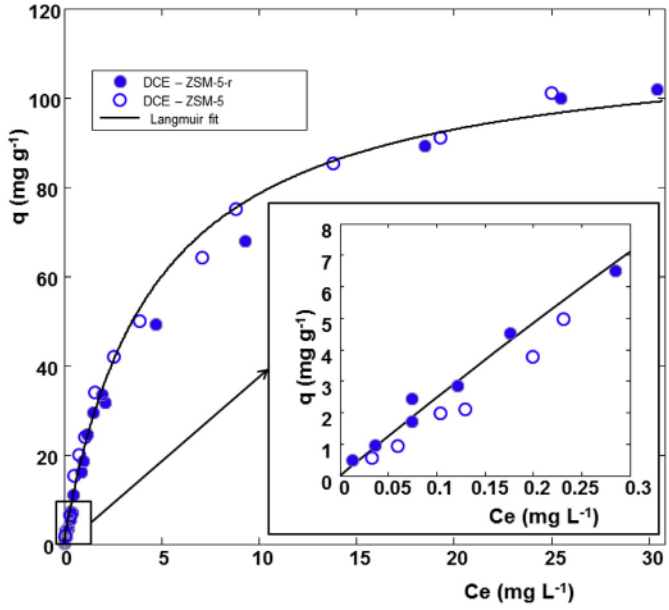

Fig. 8. Adsorption isotherms (T = 298 K) of DCE on fresh (ZSM-5) and thermally regenerated (ZSM-5-r) zeolites. The data obtained on the low concentration range are enlarged in the inset.

XRD analysis demonstrates that the regenerated and reloaded zeolite does not show any significant crystallinity loss, as well as perfectly regains the unit-cell parameters of fresh material (Fig. 7). The regeneration/adsorption process also occurs without any significant deformations in the channel apertures. The refined atomic fractional coordinates obtained by the Rietveld method indicates minor differences in both the DCE location (Fig. 2a and b). On the basis of the occupancies, Rietveld refinement of ZSM-5-DCE-30 (Fig. 2a) indicates that the organic content remains substantially unchanged thus confirming that, after regeneration, ZSM-5 is able to re-adsorb DCE in amounts comparable to that adsorbed in the first cycle [6]. The occurrence of DCE–water molecule complexes (clusters or short chains) bridged via W to framework oxygen atoms (Fig. 2b) was also confirmed. On the whole, ~6.6/u.c. DCE molecules (corresponding to ~10.3% in weight) and ~5H_2O/u.c, (corresponding to ~1.5% in weight) were re-adsorbed in the channels systems, in very good agreement with the weight loss reported on the basis of thermal analysis (Fig. 1). This results suggest that the regenerated ZSM-5 behave as an adsorbent with undiminished adsorption capacity and opens up the possibility for a re-use of such materials with clear benefits on the cost/performance ratio of the whole water treatment process. How many cycles the ZSM-5 can withstand towards DCE adsorption will be matter of future investigation.

Table 4
Fitting Results of the adsorption data of DCE on regenerated zeolite (ZSM-5-r). The fitting parameters are reported together with the confidence limits calculated at 95% of probability.

Organic -zeolite	Equation	Parameters		R^2
DCE-ZSM-5-r	$q = \frac{q_s K_L C_e}{1 + K_L C_e}$	K_L (L mg^{-1})	q_s (mg g^{-1})	0.9925
		0.20	117	
		(0.17, 0.23)	(111, 123)	

4. Conclusions

The adsorption/desorption behaviour of ZSM-5 loaded with 1,2-dichloroethane was studied using the *in situ* synchrotron X-ray powder-diffraction technique. Upon heating the relaxation of the host molecules determines a slight narrowing of both the sinusoidal and straight channels thus causing a unit-cell contraction in all temperature range investigated. Once regenerated and reloaded the ZSM-5 zeolite does not show any significant difference in the saturation capacity. Moreover, regenerated zeolite does not exhibit crystallinity loss or deformations in the channel apertures, as well as perfectly regain the unit-cell parameters of fresh material. The refined occupancies obtained by the Rietveld method indicates that both DCE location and content remain substantially unchanged thus confirming that, after regeneration, ZSM-5 is able to re-adsorb DCE in amounts comparable to that adsorbed in the first cycle. These results clearly demonstrated that regeneration of ZSM-5 is effective when thermally treating this environmentally friendly and highly efficient adsorbent at about 300 °C thus minimising the cost of the regeneration step of the adsorption process. In conclusion, the use of this adsorbent with unchanged adsorption performances after thermal regeneration under mild conditions appears very promising also over several cycles of the adsorption/desorption process.

Acknowledgements

This study was carried out within a project founded by the "SoWaZe" PRIN program of the Italian Ministry for University and Research (MIUR). We acknowledge the European Synchrotron Radiation Facility (ESRF, Grenoble) for provision of beamtime to proposal CH-3510 "In situ XRD study of structural modifications and desorption kinetics of zeolites used for removal of non polar organic compounds from contaminated water".

Appendix A. Supplementary data

Supplementary data related to this article can be found at http://dx.doi.org/10.1016/j.micromeso.2015.05.035.

References

[1] A.R. Gavaskar, B.C. Kim, S.H. Rosansky, S.K. Ong, E.G. Marchand, Environ. Prog. 14 (1995) 33–40.
[2] J.S. Zogorski, J.M. Carter, T. Ivahnenko, W.W. Lapham, M.J. Moran, B.L. Rowe, P.J. Squillace, P.L. Toccalino, U. S. Geol. Surv. Circ. 1292 (2006) 1–101.
[3] M.A. Anderson, Environ. Sci. Technol. 34 (2000) 725–727.

[4] A. Martucci, L. Pasti, N. Marchetti, A. Cavazzini, F. Dondi, A. Alberti, Micropor. Mesopor. Mater. 148 (2012) 174–183.
[5] I. Braschi, S. Blasioli, L. Gigli, C.E. Gessa, A. Alberti, A. Martucci, J. Hazard, Mater 17 (2010) 218–225.
[6] L. Pasti, A. Martucci, M. Nassi, A. Cavazzini, A. Alberti, R. Bagatin, Micropor. Mesopor. Mater. 160 (2012) 182–193.
[7] A. Martucci, L. Leardini, M. Nassi, E. Sarti, R. Bagatin, L. Pasti, Mineral. Magaz 78 (2014) 1161–1175.
[8] A. Martucci, I. Braschi, L. Marchese, S. Quartieri, Mineral. Magaz 78 (2014) 1115–1140.
[9] V. Sacchetto, G. Gatti, G. Paul, I. Braschi, G. Berlier, M. Cossi, L. Marchese, R. Bagatin, C. Bisio, Phys. Chem. Chem. Phys. 15 (2013) 13275–13287.
[10] J. Weitkamp, Solid State Ionics 131 (2000) 175–188.
[11] A. Martucci, L. Pasti, M. Nassi, A. Alberti, R. Arletti, R. Bagatin, R. Vignola, R. Sticca, Micropor. Mesopor. Mater. 151 (2012) 358–367.
[12] L.B. Ch Baerlocher, D.H. McCusker, Olson Atlas of Zeolite Framework Types, sixth Rev ed., Elsevier, Amsterdam (, 2007.
[13] R. Vignola, U. Cova, F. Fabiani, T. Sbardellati, R. Sisto, WO 2009/000429 A1 Patent (2009).
[14] E. Harlin, J. Makkonen, M. Tiitta, WO 2004080591 Al Patent (2004).
[15] L. Leardini, A. Martucci, I. Braschi, S. Blasioli, S. Quartieri, Mineral. Magaz 78 (2014) 1141–1159.
[16] A.C. Larson, R.B. Von Dreele, General Structure Analysis System (GSAS), Los Alamos National Laboratory Report LAUR, 2000, pp. 86–748.
[17] B.H. Toby, J. Appl, Cryst 34 (2001) 210–213.
[18] H. Van Koningsveld, J.C. Jansen, Micropor. Mesopor. Mat. 6 (1996) 159–167.
[19] K. Nishi, A. Hidaka, Y. Yokomori, Acta Cryst. B61 (2005) 160–163.
[20] N. Kamiya, T. Oshiro, S. Tan, K. Nishi, Y. Yokomori, Micropor. Mesopor. Mat. 169 (2013) 168–175.
[21] H. Van Koningsveld, F. Tuinstra, J.C. Jansen, H. Van Bekkum, Zeolites 9 (1989) 253–256.
[22] H. Van Koningsveld, J.C. Jansen, H. Van Bekkum, Zeolites 10 (1990) 235–242.
[23] M. Ardit, A. Martucci, G. Cruciani, J. Phys. Chem. C 119 (13) (2015) 7351–7359.
[24] B.F. Mentzen, Mat. Res. Bull. 27 (1992) 831–838.
[25] E.L. Wu, S.L. Lawton, D.H. Olson, A.C. Rohrman Jr., G.T. Kokotailo, J. Phys. Chem. 83 (1979) 2777–2781.
[26] S. Fujiyama, N. Kamiya, K. Nishi, Y.Z. Yokomori, Z. Kristallogr. 228 (2013) 180–186.
[27] H. Van Koningsveld, F. Tuinstra, Acta Cryst B45 (1989) 423–431 [22].
[28] H. Van Koningsveld, J.C. Jansen, A.J.M. De Man, Acta Cryst. B52 (1996) 131–139.
[29] H. Van Koningsveld, J.C. Jansen, H. Van Bekkum, Acta Cryst. B52 (1996) 140–144.
[30] L. Leardini, A. Martucci, G. Cruciani, Micropor. Mesopor. Mater. 173 (2013) 6–14.
[31] Y.V. Seryotkin, W. Joswig, V.V. Bakakin, I.A. Belitsky, B.A. Fursenko, Eur. J. Min. 15 (2003) 475–484.
[32] G. Cruciani, A.F. Gualtieri, Am. Min. 84 (1999) 112–119.
[33] J. Felsche, S. Luger, Ber. Bunsen. Phys. Chem. 90 (1986) 731–736.
[34] L. Leardini, A. Martucci, G. Cruciani, Micropor. Mesopor. Mat. 151 (2012) 163–171.
[35] A. Alberti, A. Martucci, Micropor. Mesopor. Mat. 141 (2011) 192–198.
[36] A. Alberti, A. Martucci, Stud. Surf. Sci. Catal. 155 (2005) 19–43.
[37] M.L. Gualtieri, A.F. Gualtieri, J. Hedlund, Micropor. Mesopor. Mater. 89 (2006) 1–8.
[38] D.S. Bhange, V. Ramaswamy, Micropor. Mesopor. Mat. 103 (2007) 235–242.
[39] D.S. Bhange, V. Ramaswamy, Microporous Mesoporous Mater. 130 (2010) 322–326.
[40] M. Milanesio, G. Artioli, A.F. Gualtieri, L. Palin, C. Lamberti, J. Am, Chem. Soc. 125 (2003) 14549–14558.

myDesk @unife

Valentina Bosi <bsovnt@unife.it>

Fwd: Thank you for your RightsLink / Elsevier transaction

Luisa Pasti <psu@unife.it> 11 febbraio 2016 11:47
A: Valentina Bosi <bsovnt@unife.it>

---------- Forwarded message ----------
From: **Copyright Clearance Center** <rightslink@marketing.copyright.com>
Date: 2016-02-11 11:46 GMT+01:00
Subject: Thank you for your RightsLink / Elsevier transaction
To: psu@unife.it

To view this email as a web page, go here.

Do Not Reply Directly to This Email

To ensure that you continue to receive our emails,
please add rightslink@marketing.copyright.com to your address book.

RightsLink | Copyright Clearance Center

Thank You For Your Order!

Dear Mrs. Luisa Pasti,

Thank you for placing your order through Copyright Clearance Center's RightsLink service. Elsevier has partnered with RightsLink to license its content. This notice is a confirmation that your order was successful.

Your order details and publisher terms and conditions are available by clicking the link below:
http://s100.copyright.com/CustomerAdmin/PLF.jsp?ref=a8f7bd13-145a-469c-b2fa-614d457b11be

Order Details
Licensee: Luisa Pasti
License Date: Feb 11, 2016
License Number: 3805850268873
Publication: Microporous and Mesoporous Materials
Title: Adsorption of 1,2-dichloroethane on ZSM-5 and desorption dynamics by in situ synchrotron powder X-ray diffraction
Type Of Use: reuse in a thesis/dissertation
Total: 0.00 USD

To access your account, please visit https://myaccount.copyright.com.

Please note: Online payments are charged immediately after order confirmation; invoices are issued daily and are payable immediately upon receipt.

To ensure that we are continuously improving our services, please take a moment to complete our customer satisfaction survey.

B.1:v4.2

+1-855-239-3415 / Tel: +1-978-646-2777
customercare@copyright.com
http://www.copyright.com

This email was sent to: **psu@unife.it**

Please visit Copyright Clearance Center for more information.

This email was sent by Copyright Clearance Center
222 Rosewood Drive Danvers, MA 01923 USA

To view the privacy policy, please go here.

--

Luisa Pasti Ph.D
Department of Chemistry and Pharmaceutical Sciences
University of Ferrara
Via L. Borsari, 46
44123 Ferrara, ITALY

e-mail: luisa.pasti@unife.it
tel:+39 0532 455346
fax:+39 0532 240709

Catalysis Today xxx (2015) xxx–xxx

Contents lists available at ScienceDirect

Catalysis Today

journal homepage: www.elsevier.com/locate/cattod

Kinetics and dynamic behaviour of toluene desorption from ZSM-5 using *in situ* high-temperature synchrotron powder X-ray diffraction and chromatographic techniques

E. Rodeghero [a], A. Martucci [a,*], G. Cruciani [a], R. Bagatin [b], E. Sarti [c], V. Bosi [c], L. Pasti [c,**]

[a] Department of Physics and Earth Sciences, University of Ferrara, Via Saragat, 1, I-44123 Ferrara, Italy
[b] Research Centre for Non-Conventional Energy – Istituto Eni Donegani Environmental Technologies, via Felice Maritano, 26, San Donato Milanese (MI), I-20097 Milan, Italy
[c] Department of Chemistry and Pharmaceutical Sciences, University of Ferrara, Via L. Borsari, 46, I-44123 Ferrara, Italy

ARTICLE INFO

Article history:
Received 17 August 2015
Received in revised form 26 October 2015
Accepted 23 November 2015
Available online xxx

Keywords:
ZSM-5
Toluene
Ad/desorption
In situ synchrotron X-ray powder diffraction

ABSTRACT

In situ high-temperature (HT) synchrotron X-ray powder diffraction (XRPD), was used in this study as a tool to understand the adsorption/desorption process features of toluene adsorbed in organophilic ZSM-5 zeolite (SiO_2/Al_2O_3 ~280), as well as framework structural modifications upon thermal treatment from room temperature to 600 °C. Rietveld refinements showed that toluene release starts in the 75 °C< T < 200 °C temperature range. Furthermore, extraframework structural changes take place when toluene removal starts. Significant internal pressure is developed with the composition product diffusion causing a corresponding transient expansion in the 10-ring channels. Our results clearly demonstrated that ZSM-5 regeneration is effective when it is thermally treated at about 400 °C. Above this temperature, when all the organic have been ejected, non-equilibrium distortions in the framework are relaxed and channel apertures become more circular. ZSM-5 shows no significant difference in saturation capacity once regenerated after toluene reloading, thus demonstrating that thermal regeneration under mild conditions appears to be both very effective even after several cycles of adsorption/desorption.

1. Introduction

Zeolites are microporous materials which are widely used in many industrial adsorption and catalytic processes due to their excellent thermal and chemical resistance. Furthermore, great potential is offered by zeolites in terms of tailoring their structure and physical-chemical properties. To date, organic compound adsorption in zeolites has been widely studied [1–4], especially in vapour or gas systems, since this process is relevant in many catalysed reactions, organic synthesis and depollution processes. In particular, the characteristics of zeolites – such as high organic contaminant selectivity, high specific capacity, rapid kinetics, absence of salt and humic substance interference and excellent resistance to chemical, biological, mechanical or thermal stress – make these materials particularly suitable as adsorbents for water treatment plants [5–11]. With regard to the latter application, a variety of organic compounds are potential water pollutants. Amongst these, BTEX (Benzene, Toluene, Ethylbenzene, and Xylenes) constitute one of the main marine environment pollutants due to accidental spills or leaks. The US environmental protection agency (USEPA) has classified BTEX as priority pollutants and has fixed concentration levels in water and wastewater [12]. According to the World Health Organisation (WHO) guidelines, the maximum permissible concentration of benzene, toluene, ethylbenzene and xylene in drinking water is 0.01, 0.7, 0.3 and 0.5 mg/l, respectively [13]. Indeed, BTEX compounds can cause adverse health effects on humans, including central nervous system impairment, respiratory problems and liver and kidney damage [14,15]. Therefore, BTEX removal from water and wastewater is an important issue. Adsorption based treatment technology offers several advantages, such as low operation costs and reduced waste generation in as much as adsorbent reuse is possible. In several cases, zeolites were proved to be easily thermally regenerated without changing their initial adsorption or catalytic properties [16–19]. However, these studies are rather limited and most deal with organic compound adsorption in gas phase systems. Zeolite ZSM-5 (MFI topology) is an important member of a class of high silica zeolites. It has been largely exploited due to its shape

* Corresponding author. Fax: +39 (0)532 974730.
** Corresponding author.
E-mail addresses: mrs@unife.it (A. Martucci), psu@unife.i (L. Pasti).

http://dx.doi.org/10.1016/j.cattod.2015.11.031
0920-5861/

selectivity, solid acidity, ion exchangeability, pore size and high thermal stability. Moreover, ZSM-5 is the synthetic counterpart of the mineral mutinaite, $(Na_{2.76}K_{0.11}Mg_{0.21}Ca_{3.78})(Al_{11.20}Si_{84.91}) \cdot 60\,H_2O$ [20], a very rich calcium zeolite with a 7.6 Si/Al ratio, the highest ever found in natural zeolites.

Its MFI topological symmetry is orthorhombic *Pnma*. However, a polymorphic monoclinic ($P2_1/n$) -to- orthorhombic (*Pnma*, $Pn2_1a$ or $P2_12_12_1$) phase transition was reported with varying framework defect density, temperature, or nature and amount of guest compounds in the channel systems [21–25]. Usually low-loaded ZSM-5 (4 or less sorbate per unit cell) are orthorhombic, with a *Pnma* or $Pn2_1a$ [21,26–28], space group. On the contrary, high-loaded ZSM-5 (over 4 sorbate per unit cell) is orthorhombic, with a $P2_12_12_1$ space group [29]. This latter was also reported for a high-loaded ZSM-5 with 6.4 toluene molecules per unit cell on the basis of single-crystal XRD data by Nishi et al [30].

Very recently, Ardit et al. [31]. reported on spontaneous strain variation analysis across ferroelastic (monoclinic) and paraelastic (orthorhombic) phases in the ZM-5 zeolite transition using *in situ* synchrotron XRD data. The authors highlighted the tricritical character of this transition from ferroelastic to paraelastic phases in ZSM-5. The adsorption properties of a hydrophobic ZSM-5 zeolite compared to a toluene aqueous solution (TOL) were investigated in this work in order to obtain information on the kinetic and thermodynamics of the adsorption process. Additionally, *in situ* high-temperature (HT) synchrotron X-ray powder diffraction (XRPD) was carried out on ZSM-5 after toluene adsorption (known as ZSM-5-TOL to follow). Saturated material was used as a key to continuously monitoring TOL decomposition process, as well as structural modifications on ZSM-5 upon temperature-programmed treatment. Understanding the features of both adsorption and desorption processes can help in the opting and design water treatment appliances based on microporous materials, as well in their catalytic applications. Furthermore, it can provide insight for the reuse of adsorbing material.

2. Material and methods

2.1. Materials

The zeolite sample used in this study is a hydrophobic ZSM-5 (CBV28014, Zeolyst International) characterized by SiO_2/Al_2O_3 ~280, Na_2O content <0.05 wt.%, NH_4^+ content <0.1% w/w, with a 400 m^2/g surface area. The TOL-loaded form of ZSM-5 was obtained by preparing TOL aqueous solutions and mixing them with the zeolite powder in a 1:4 (mg mL^{-1}) solid/solution ratio as detailed in the following sections.

2.2. Gas chromatography

The TOL concentration in the aqueous solutions was determined by a Gas Chromatography–Flame Ionization Detector (GC–FID). Prior to this, TOL was extracted from the water sample by Head Space-Solid Phase Micro Extraction (HS-SPME). The head space mode was used to extract TOL from 10 ml of solution in 25-ml glass flasks sealed with Teflon screw caps. 2 mL of a 300 g L^{-1} NaCl solution were added to the sample. Samples were immersed in a thermostatic water bath at 40 °C (±0.5 °C) and maintained under controlled agitation with a magnetic stirrer (300 rpm) for 10 min to reach equilibrium conditions before SPME insertion. The fibre was inserted into the GC injector for analysis and kept at 250 °C. Desorption time was 1 min. The GC used in this work was an HRGC 5160 MEGA SERIES Instrument (Carlo Erba, Mi, I) equipped with a split/splitless injector and an FID detector. A fused-silica capillary column OV-1 (30 m × 0.32 mm I.D:, 0.1 μm film thickness; MEGA, MI, I) was used. Helium (99.999%) was used as a carrier gas at 30 kPa constant head pressure. The detector temperature was kept constant at 250 °C. The GC oven was programmed as follows: 40 °C (5 min), 5 °C min^{-1} to 80 °C (5 min), 30 °C min^{-1} to 100 °C (5 min).

2.3. Adsorption isotherm

The adsorption isotherm was determined using the batch method. Batch experiments were carried out in duplicate in 20 ml crimp top reaction glass flasks sealed with PTFE septa (Supelco, PA, USA). The flasks were filled in order to have minimum headspace, a solid/solution 1:4 (mg mL^{-1}) ratio was employed. The solids were separated from the aqueous solution using centrifugation (14,000 rpm for 30 min) after equilibration, for 24 h at a temperature of 25.3 ± 0.5 °C under stirring. TOL concentrations in solutions with regenerated zeolite were read before and after equilibration by HS-SPME-GC-FID in order to determine the adsorbed quantities (q) and the equilibrium concentrations (Ce).

2.4. Synchrotron powder XRD data collection and Rietveld refinements

A TOL-loaded zeolite ZSM-5 powder sample (ZSM-5-TOL) was used for *in situ* time-resolved XRPD. XRD data were collected at the European Synchrotron Radiation Facility (ESRF) ID31 beam line, Grenoble, using a fixed wavelength of 0.40003(1)Å. A series of XRD patterns were measured through nine parallel scintillation counters behind Si (111) analyser crystals in the 0.5–19.5 2θ range, in steps of 25 °C as a function of temperature while the sample was heated from room temperature to 600 °C in air with a heating rate of 0.083 K s-1. Rietveld refinements were performed using the Larson and Von Dreele [32] General Structure Analysis System (GSAS) with an EXPGUI graphical interface [33]. After toluene adsorption, automatic peak indexing was performed using High Score Plus v.3.0 software, revealing the presence of several doublets (i.e. 131 + 13-1 and 311 + 31-1, and 133 + 13-3 and 313 + 31-3) suggesting monoclinic symmetry. As a consequence, structure refinement of this sample (TOL–ZSM-5) was then performed in the $P2_1/n$ space group starting from the framework atom site positions reported by Pasti et al [7]. for the initial unloaded sample. The refined β (90.545 (1)) value confirms the assumption of the monoclinic symmetry after toluene adsorption (Table 1S).

Extra-framework sites were located by difference Fourier synthesis. H-atoms were not considered within the structure refinement due to their low scattering factors. Refined structural parameters for each data histogram were the follows: fractional coordinates and isotropic displacement factors for all atoms (one for each tetrahedral site and framework oxygen atom, one for each toluene molecule). Toluene occupancy factors were refined in blocks e.g. all the carbon atoms for each toluene molecule were constrained to have same value. The occupancy and isotropic displacement factors were varied in alternate cycles. Fig. 1, shows the powder pattern evolution of the investigated ZSM-5-TOL sample when close to the monoclinic ($P2_1/n$) to orthorhombic ($P2_12_12_1$) phase transition at a Tc = 75 °C ± 5 in the 1.7–4.7 (a) and 4.7–7.1 (b) °2θ ranges. The symmetry change was marked by the gradual merging of several peaks doublet into single ones. The Rietveld refinement in the orthorhombic s.g. was carried out starting from the framework atomic coordinates reported by Nishi et al [30]. The structural model obtained after the phase transition was then used for the ZSM-5L high temperature (HT) patterns, by adopting the same structure refinement strategies. After the desorption of the organic molecules (Tc close to 400 °C ± 5), the slope variation of the unit cell volume suggested a new displacive phase transition from orthorohombic $P2_12_12_1$ to *Pnma*. As a consequence, all Rietveld refinements up to 400 °C were performed in this latter space group,

Please cite this article in press as: E. Rodeghero, et al., Kinetics and dynamic behaviour of toluene desorption from ZSM-5 using *in situ* high-temperature synchrotron powder X-ray diffraction and chromatographic techniques, Catal. Today (2015), http://dx.doi.org/10.1016/j.cattod.2015.11.031

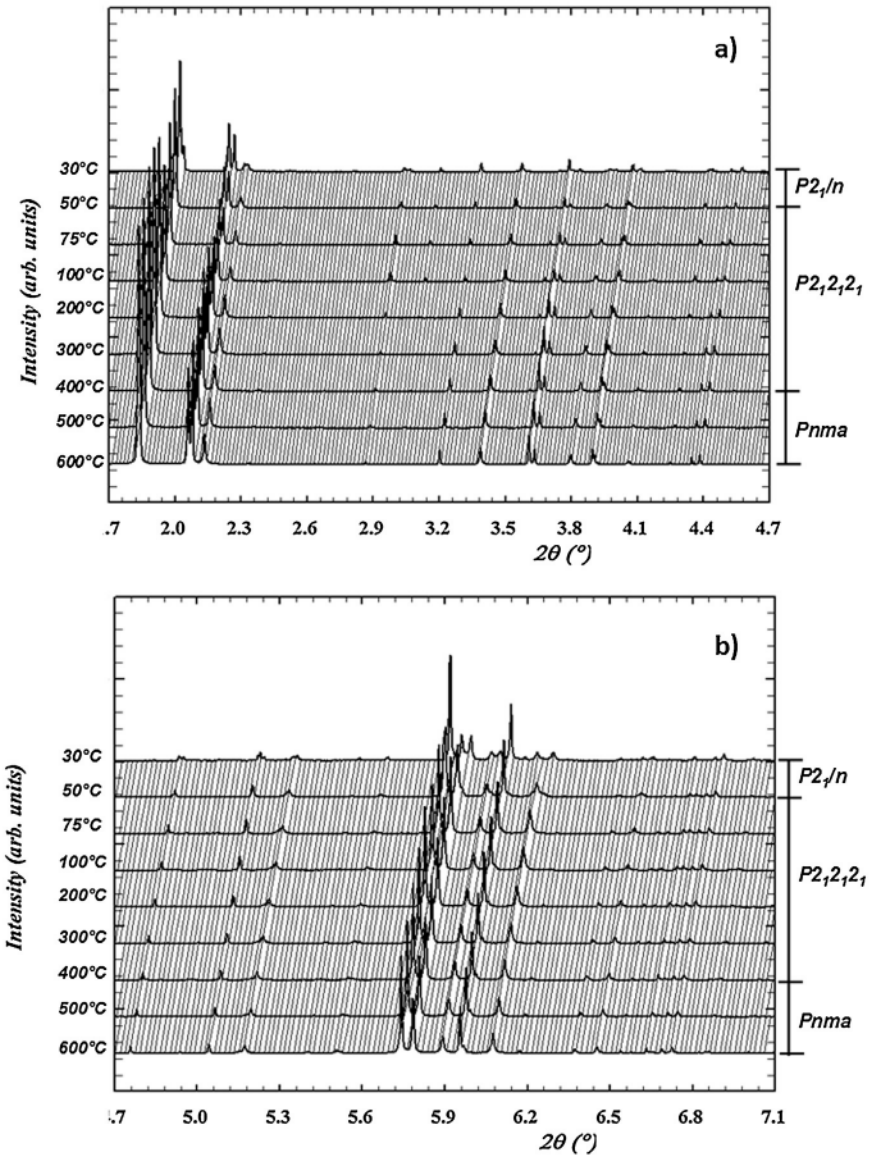

Fig. 1. Plot of selected *in situ* time resolved XRPD patterns as a function of temperature/time for ZSM-5-TOL in (a) the 1.7–4.7 and (b) 4.7–7.1 2θ ranges within the 30–600 °C temperature interval.

starting from the atomic model of van Koningsveld et al [24]. Using the this crystal structure model, based on the latter space group, appreciably improved the quality of the Rietveld refinement, as testified by the lower R_{wp} and R_p parameters. Soft constraints were imposed on Si-O (1.60(1) Å), O-O (2.60(1) Å) and C-C (1.34 Å) distances and their weight was gradually released after the initial refinement stages of rement. The instrumental background was empirically fitted using a Chebyschev polynomial of the first kind with 16 variable coefficients for room temperature and 24 variable coefficients for HT data set. The 2θ-zshift, scale factor and unit-cell parameters were accurately refined and the reflection intensity were was preliminary refined with Le Bail extraction method and then kept fixed at the mean value in all patterns of the data set. Peak intensity profiles (0.01% cut-off peak intensity) were modelled by means of a pseudo-Voigt profile function using Gaussian U, V, and W coefficients, which is a Lorentzian particle-size broadening term. All positional parameters, site occupancy and isotropic atomic displacement parameters (ADPs) were refined in the final cycles. Lattice parameters and refinement details have been summarized for four selected temperatures (30 °C, 75 °C, 400 °C and 600 °C) in Table 1S, the corresponding refined atomic parameters for both framework and extraframework atoms are given as Supporting Information (Tables 2SI-7SI, respectively).

3. Results and discussion

3.1. Adsorption kinetics

The effect of contact time on TOL adsorption onto ZSM-5 was studied at different initial concentrations, as shown in Fig. 2a. The time to reach equilibrium was only 15 min. Adsorption is initially rapid, and then constant, possibly due to a greater abundance of adsorption sites available for adsorption during the initial stage. Various kinetic models have been suggested for describing adsorption processes. Amongst these, Lagergren's pseudo-first-order kinetics (PFO) and pseudo second order kinetics (PSO) are those commonly employed to investigate adsorption onto zeolites. These models are expressed in Eqs. (1) and (2) as shown below:

$$q = q_e[1 - \exp(-k_1 t)] \quad (1)$$

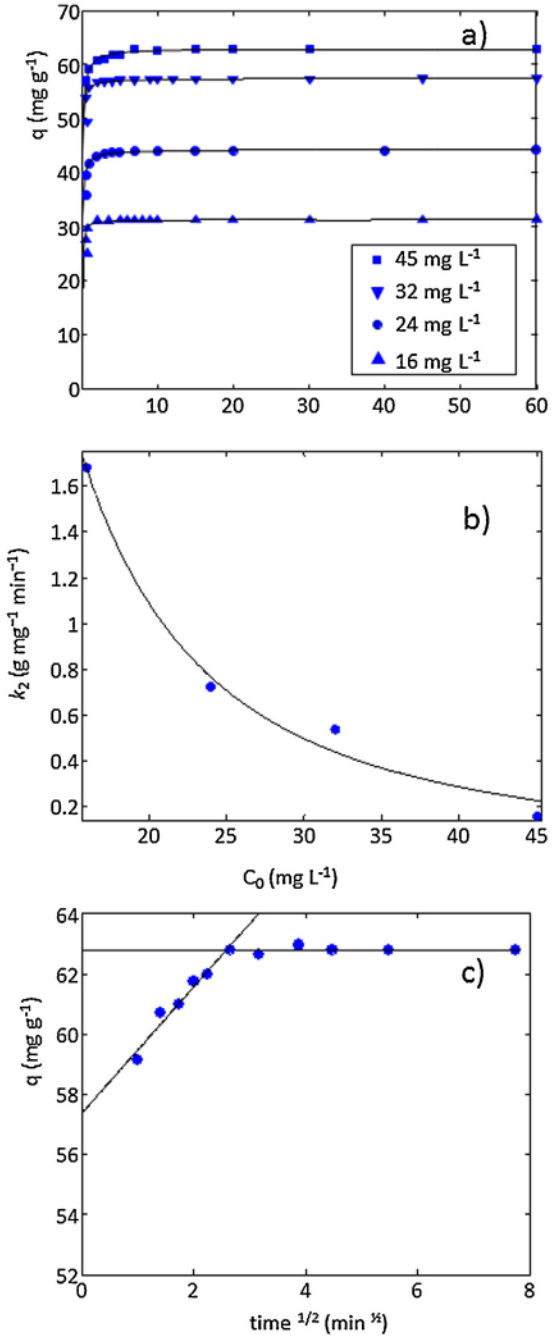

Fig. 2. Adsorption kinetics of TOL on ZSM-5. a) TOL uptake on ZSM-5 at different initial concentrations; b) Pseudo second order kinetics constant vs. TOL equilibrium concentration; c) Intraparticle diffusion plots for adsorption (C_0 45 mg L^{-1}).

$$q = \frac{k_2 q_e^2 t}{1 + k_2 q_e^t} \tag{2}$$

where q is the amount of solute per unit mass of adsorbent at time t, q_e is the equilibrium value of q, $k_1$and k_2 are the PFO and PSO rate constant, respectively. According to the theoretical analysis proposed by Azizian [34], PFO model better describes adsorption from a solution with a high initial solute concentration, while for initial solute concentrations which are not too high, a sorption PSO fit is generally better. It has also been demonstrated that for systems which are characterized using the PFO model, the observed rate constant is a linear function of the initial solute concentration; whereas the observed rate constant is a complex function of initial solute concentration for PSO kinetics systems. Table 1, reports correlation coefficients (R^2), kinetic parameters (k_1, k_2) and calculated $qe_{,cal}$ values obtained by non-linear regression. R^2 comparison, obtained for PFO and PSO, suggests that TOL adsorption onto ZSM-5 takes place according to the pseudo-second-order kinetic model (Fig. 2b). Moreover, TOL uptake fit on ZSM-5 at 25 °C for different initial TOL concentrations (see Fig. 2a) in an aqueous solution revealed that the PSO dependence rate constant on the equilibrium concentration follows a complex trend (see Fig. 2a). Thus, the PSO model was confirmed [34,35].

In addition, the intraparticle diffusion model was applied in order to identify the adsorption steps:

$$q = k_{i,d} t^{1/2} + c_i \tag{3}$$

where k_i is the intraparticle diffusion rate constant and c_i is a constant for the i-th step.

As shown in Fig. 2c, the two-phase plot suggests that the adsorption process proceeds by surface adsorption and TOL intraparticle diffusion into the zeolite micropores for an initial TOL concentration of 45 mg L^{-1}. By comparing the slopes of the two lines, it can be observed that $k_{1,d}$ is larger than $k_{2,d}$ (see Table 8 SI) for all the investigated concentrations, indicating that film diffusion is a more rapid process than intraparticle diffusion [36].

The intercept ($c_i$value) is significantly different from zero, confirming that the studied zeolites have a high level of initial adsorption.

3.2. Adsorption isotherm

The equilibrium adsorption isotherm provides the relationship between the concentration of organic contaminant in solution and how much is adsorbed on the solid phase when the two-phase system is in equilibrium. The experimental data reported in Fig. 3a, shows the Langmuirian shape and consequently the data were fitted to Langmuir and a bi-Langmuir models, which were employed to describe the adsorption of different organic compounds on ZSM-5 [37]. These two models are expressed by Eqs. (4) and (5),

$$q = \frac{q_s b C_e}{1 + b C_e} \tag{4}$$

$$q = \frac{q_{s1} b_1 C_e}{1 + b_1 C_e} + \frac{q_{s2} b_2 C_e}{1 + b_2 C_e} \tag{5}$$

where q_s is the saturation capacity of the adsorbent material, C_e the equilibrium concentration in the solution and b the binding constant, the subscripts refer to the type of adsorption sites.

The estimated parameters from non-linear fitting are shown in Table 9SI. The determination coefficients (R^2) of the Langmuir isotherm (0.9565) are not significantly different from the Langmuir isotherm (0.9865) obtained for adsorption data at 22.5 °C. Since the difference in goodness of fitting parameters for the two isotherm models is not significant, the simplest model (i.e. Langmuir isotherm) can be employed to describe TOL adsorption onto ZSM-5. Moreover, the monolayer adsorption capacity determined using the Langmuir isotherm is about 82 mg/g which approaches experimental data (81.6 mg/g). Finally, the equilibrium parameter R_L [38]. was given by:

$$R_L = \frac{1}{1 + b C_0} \tag{6}$$

where C_0 is the initial concentration R_L values are in the 0.009–0.45 range, indicating that TOL adsorption onto ZMS-5 is favourable ($0 < R_L < 1$).

3.3. ZSM-5-TOL structure refinement at room temperature

The ZSM-5 framework is characterized by two interconnected channel systems: sinusoidal 10-membered ring (ZZ ring A and ZZ

Please cite this article in press as: E. Rodeghero, et al., Kinetics and dynamic behaviour of toluene desorption from ZSM-5 using *in situ* high-temperature synchrotron powder X-ray diffraction and chromatographic techniques, Catal. Today (2015), http://dx.doi.org/10.1016/j.cattod.2015.11.031

Table 1
Kinetic parameters for the adsorption of TOL onto the ZSM-5

C_0 (mg L^{-1})	$qe_{,exp}$ (mg g^{-1})	Pseudo-first-order			Pseudo-second-order		
		k_1 (min^{-1})	$qe_{,cal}$ (mg g^{-1})	R^2	k_2 (g mg^{-1} min^{-1})	$qe_{,cal}$ (mg g^{-1})	R^2
16	31.3	9.48	32.1	0.8774	1.68	31.1	0.9934
24	43.9	5.123	43.8	0.8253	0.723	44.2	0.9705
32	57.4	3.821	56.1	0.7767	0.539	57.4	0.9121
45	62.8	2.891	64.1	0.6361	0.159	63.1	0.9233

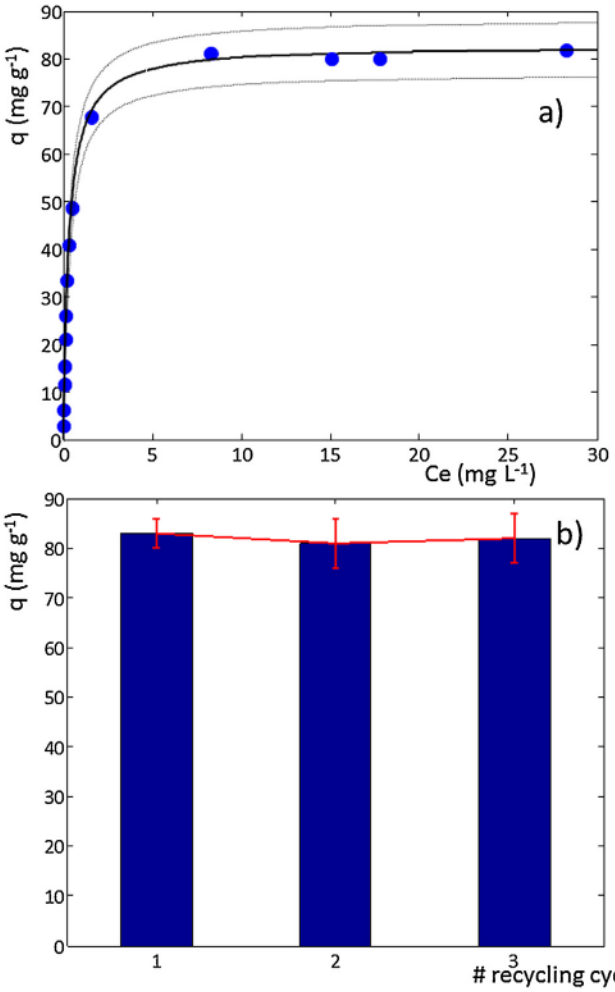

Fig. 3. a) Isotherm for TOL adsorption onto ZSM-5; b) Pseudo second order kinetics constant vs. TOL saturation capacity on ZSM-5 after thermal regeneration.

ring B, respectively) channels along the [1 0 0] direction and straight 10-membered channels parallel to the [0 1 0] direction (SC ring A and SC ring B, respectively). A tortuous pore path runs along the [0 0 1] direction.

The ZSM-5 topological symmetry is orthorhombic *Pnma*, but its real symmetry strongly depends on temperature changes, mechanical stress, synthesis and post synthesis treatment, SiO_2/Al_2O_3 ratio, structural defects and the nature and amount of guest organic molecules [21–26]. The crystal system is monoclinic $P2_1/n$ after small guest molecules adsorption. The same space group was also reported for the same highly siliceous ZSM-5 zeolite used in this work in its as-synthesized form (Pasti et al. [7]; Ardit et al. [31]), as well as after adsorption of other fuel-based pollutants (Martucci et al. [9–11,39].

In our study, the presence of peak doublets such as 131/13-1, 311/31-1, 133/13-3, and 313/31-3 (Fig. 1) in the ZSM-5-TOL pattern at room temperature clearly indicated monoclinic $P2_1/n$ symmetry. The difference Fourier map, generated using the GSAS package, indicated TOL molecules distribution over two crystallographic independent sites (TOL 1 = C1, C2, C3, C4, C5,C6,C7 sites; TOL 2 = C8, C9, C10, C11, C12, C13, C14 sites) (Fig. 4a, Table 3SI). TOL1 is located in the straight channel, while TOL2 molecules are located at the intersection between straight and sinusoidal channels. The final difference Fourier map showed two other peaks which were attributed to co-adsorbed water molecules (W1 and W2 sites, respectively). Both the toluene and water sites are partially occupied: TOL1 and TOL2 sites in 85% and 65% of cases, whereas W1 and W2 were occupied (Table 3 SI) in 85% and 55% of cases, respectively in 85% and 55%. On the whole, 6 toluene molecules (which correspond to about 8.55% in weight) and approximately 2 water molecules (which correspond to approximately 2.0% in weight) were localised inside the ZSM-5 channel system. Therefore, structure refinement gave toluene content levels in very good agreement with the adsorption capacity (81.6 mg/g).

The O atom refined distances for the water molecules from themselves (W2-W2 3.24(1) Å) and the toluene atoms (C1-w1 = 3.02(1) Å, C2-w2 = 2.46(1) Å, C5-w2 = 2.96 (1) Å,C11-w1 = 2.68(1) Å, C8-w1 = 2.34(1) Å, w1-C11 = 2.68(2) Å, w2-C5 = 2.96 (3) Å,) suggest the presence of water-toluene oligomers (TOL1-W1, TOL1-W2, TOL2-W1, TOL1-W2-W2) interacting with framework oxygens (C8-O18 = 3.15(4)Å,C9-O18 = 3.00(3)Å,C10-O17 = 3.04(4)Å,C10-O23 = 2.74(3)Å, C10-O43 = 2.67(3)Å)). At the same time, toluene and W1 water molecules are connected to each other to form TOL1-W1-TOL2 molecular oligomer parallel to the **b** direction which are bonded to framework oxygen atoms. Water-organic complexes interacting with the framework were also detected by XRPD in ZSM-5 after dichloroethane [7]. and methyl *tert* buthyl ether [39] adsorption.

3.4. In situ *XRD data refinements: temperature-dependent structural modifications*

The evolution of the powder diffraction patterns as a function of temperature (Fig. 1) indicated that ZSM-5 maintains its crystallinity up to the highest investigated temperature. *T*-dependent variations in unit cell parameters in the 30°–600 °C *T*-range are reported in Fig. 5a. Cell parameter values defined as $V(T)/V_0$, $a(T)/a_0$, $b(T)/b_0$, and $c(T)/c_0$, are normalised compared to the reference values refined at $T = 30$ °C.

In situ synchrotron XRD data revealed a rapid increase in cell volume (Figs. 5a) in the $30° < T < 75$ °C *T* range. The linear expansion coefficients along *a*, *b* and *c* directions were $\alpha_a = 3.269 \times 10^{-5}$, $\alpha_b = -2.810 \times 10^{-5}$ and $\alpha_c = 1{,}771 \times 10^{-5}$, respectively. The volume thermal expansion coefficient is $\alpha_V = 2.325 \times 10^{-5}$. 131 and 13–1 peak overlapping is still incomplete at 50 °C, and broadening in the 2θ region is observed in the ZSM-5 pattern. This suggests that conversion to the orthorhombic symmetry is still occurring. Complete overlapping for this group of peaks is reached at about 70 ± 5 °C (*Tc*), as a result of a complete monoclinic $P2_1/n$ to orthorhombic $P2_12_12_1$ phase transition. The latter space group was also adopted in the single-crystal XRD study by Nishi et al [30]. for an all-silica MFI material which was highly-loaded with toluene. Nishi et al [30]. reported three kinds of toluene molecules in the unit cell: two

Please cite this article in press as: E. Rodeghero, et al., Kinetics and dynamic behaviour of toluene desorption from ZSM-5 using *in situ* high-temperature synchrotron powder X-ray diffraction and chromatographic techniques, Catal. Today (2015), http://dx.doi.org/10.1016/j.cattod.2015.11.031

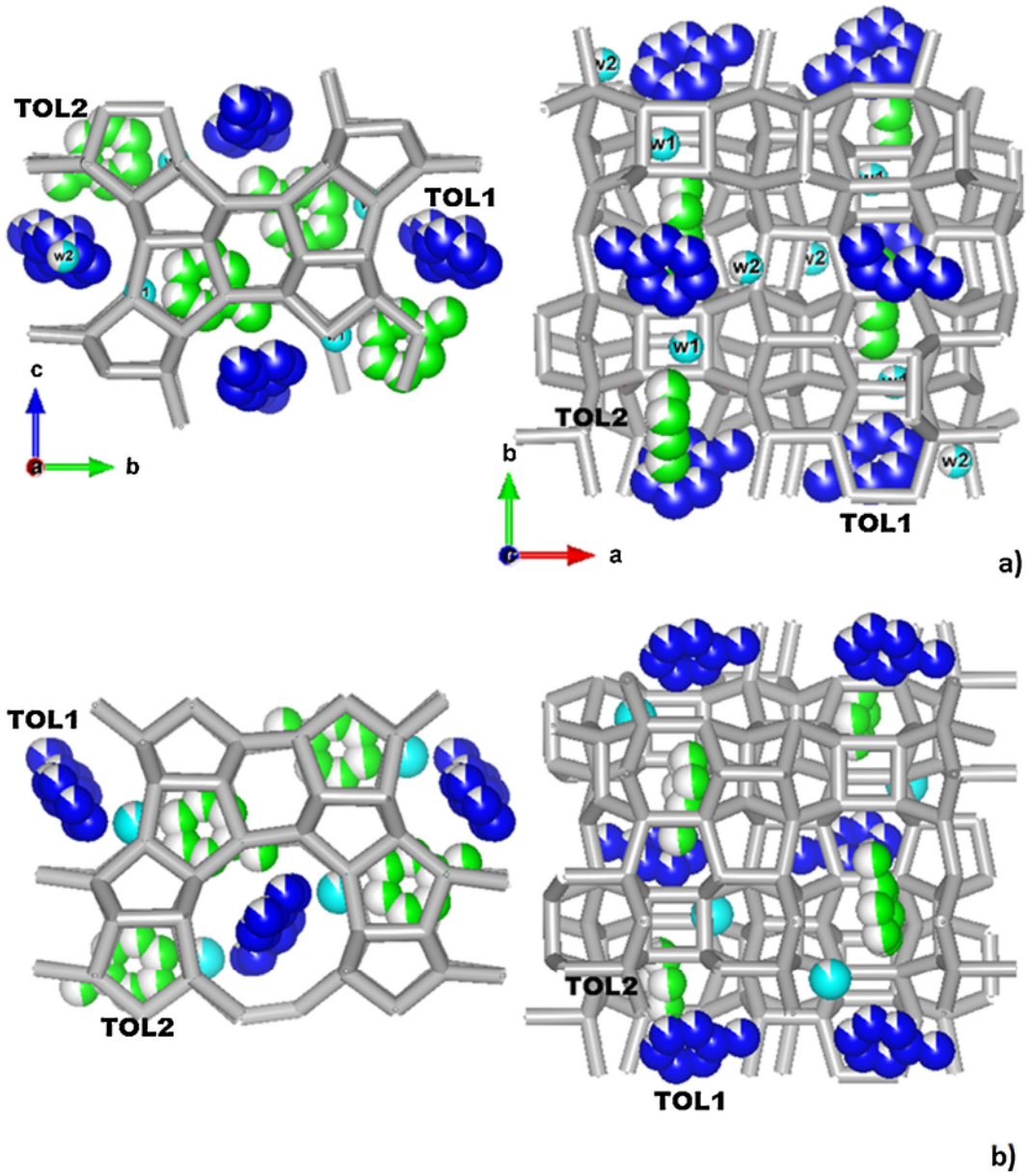

Fig. 4. Location of toluene and water molecules in ZSM-5 along [0 0 1] and [0 0 1] directions, respectively, before (30 °C) (a) and after (75 °C) (b) the monoclinic to orthorhombic phase transition.

of these were located at the intersection of between the straight sinusoidal channels, the third one in the sinusoidal channel.

Our Rietveld refinement highlighted that $P2_1/n$-$P2_12_12_1$ phase transition is accompanied by clear discontinuity in $V(T)/V_0$, $a(T)/a_0$, $b(T)/b_0$, and $c(T)/c_0$ curves (Fig. 5a). Initial cell expansion occurred even if toluene removal was only partially started, as demonstrated by the evolution of toluene content as a function of temperature (Fig. 5b). After phase transition, toluene molecules remained confined within the straight channel (TOL1 site) as well as at the intersection between straight and sinusoidal channels (TOL2 site), (Fig. 4b). Difference Fourier maps also showed the occurrence of a clear weak maximum which is attributed to co-adsorbed water hosted in a fully occupied site (siteW in Table 5SI). At the same time, the simultaneous presence of small diffused maxima indicates that a few other water molecules are spread over a number of low occupied positions, which remained unlocalized by Rietveld structure refinement. The refined distances of toluene and water molecules oligomers (W-C5 = 2.55 Å; W-C11 = 2.76 Å) confirm their interaction with framework oxygens (W-O27 = 2.60 Å; W-O28 = 2.61 Å; C12-O44 2.80 Å). The refined occupancies indicate that the toluene release is only partially started from the TOL2 site. This process is accompanied by an increase in the opening of the zeolite framework pore system and consequently, in the Crystallographic Free Areas (C.F.A.) (Fig. 1SI). This result also jjustifies the volume expansion in this stage of the experiment (Fig. 5a). The same cell volume increase was also reported on the same ZSM-5 sample after dichloroethane adsorption upon heating at T_c close to 70 ± 5 °C [19]. Structure refinements of the occupancies show that the toluene removal starts in the 75 °C< T < 200 °C temperature range. The linear expansion coefficients along a, b and c directions at 200 °C are $\alpha_a = -1.846 \times 10^{-7}$, $\alpha_b = 3.922 \times 10^{-6}$ and $\alpha_c = -5.969 \times 10^{-9}$, respectively. TOL1 content was reduced by about 50% as indicated by the decrease in toluene molecules per unit cell *vs.* temperature (Fig. 5b). At the same time, the TOL2 molecules are almost completely decomposed.

Please cite this article in press as: E. Rodeghero, et al., Kinetics and dynamic behaviour of toluene desorption from ZSM-5 using *in situ* high-temperature synchrotron powder X-ray diffraction and chromatographic techniques, Catal. Today (2015), http://dx.doi.org/10.1016/j.cattod.2015.11.031

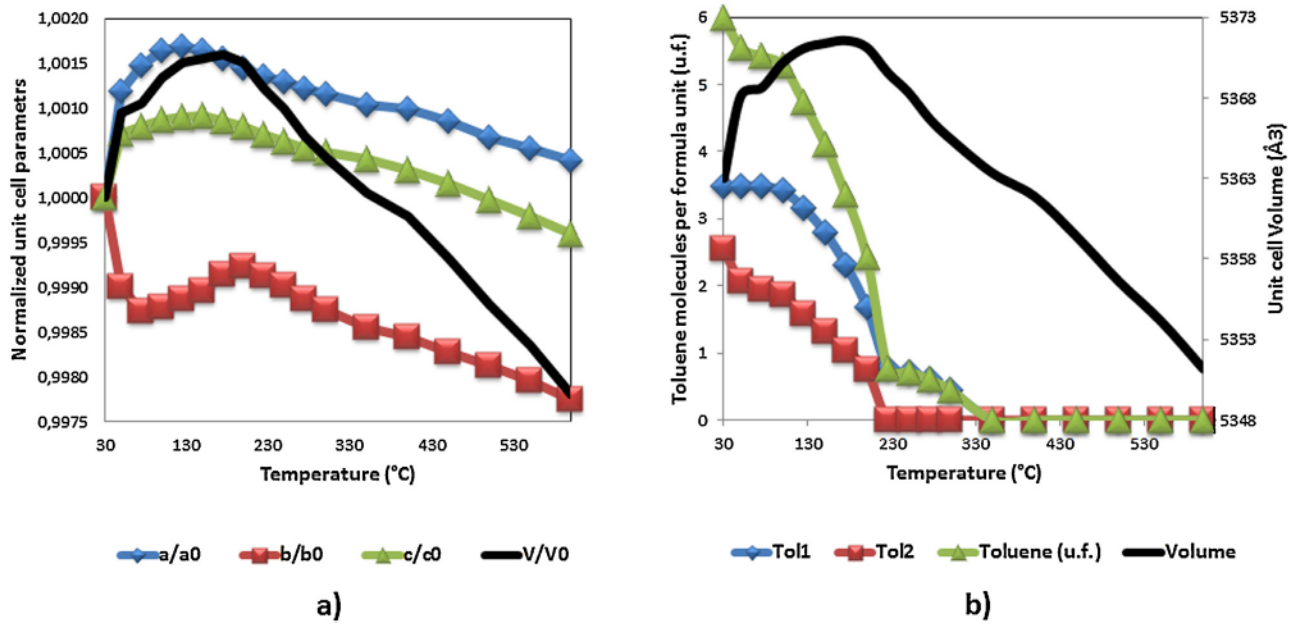

Fig. 5. a) Temperature evolution of ZSM-5-TOL unit cell parameters during in situ thermal burning of the organic. All values are normalized compared to those refined at room temperature; b) variation in toluene molecules per unit cell as a function of temperature. The evolution of unit cell volume (black line) is also shown for comparison.

A *T*-dependent distortion mechanism in the framework takes place in correspondence with guest organic molecule release. Adsorbate diffusion led to significant internal pressure and caused a corresponding transient expansion ($\alpha_V = 3{,}740 \times 10^{-6}$) in the 10-ring channels.

This trend suddenly changes between 200 °C and 400 °C as a result of structural modifications induced by complete toluene removal, in good agreement with the evolution of refined organic occupancy fractions (Fig. 5b). In this *T* range, all the cell parameters decrease, the linear expansion coefficients along *a*, *b* and *c* directions at 400 °C being $\alpha_a = -2.267 \times 10^{-6}$, $\alpha_b = -3.916 \times 10^{-6}$ and $\alpha_c = -2.443 \times 10^{-6}$. The negative volume expansion associated with organics removal is $\alpha V = -8.620 \times 10^{-6}$. Apertures sterical features indicated that the straight channel along the *b* axis is the more viable direction for toluene decomposition product. The unit cell parameter variations and the change in the cell volume slope *vs. T* dependence suggested a new displacive phase transition from orthorhombic $P2_12_12_1$ to *Pnma* at around 400 °C. The quality of the Rietveld refinement based on this crystal structure model was appreciably better, as testified by lower R_{wp} and R_p parameters (see Table 1 SI). The structure maintained this symmetry up to the highest investigated temperatures. The axial and volume thermal expansion coefficients in the 400°–600 °C *T*-range are $\alpha_a = -2.896 \times 10^{-6}$, $\alpha_b = -3.512 \times 10^{-6}$ and $\alpha_c = -3.534 \times 10^{-6}$, $\alpha_V = -9.941 \times 10^{-6}$, respectively. Volume contraction in this *T*-range is true negative thermal expansion (NTE) since it occurs without any mass loss. This mechanism, which has been clearly documented in MFI-materials such as ZSM-5-loaded with dichloroethane [19], silicalite-1 [40], titanium silicalite-1 (TS-1) [41], Fe-silicalite (Fe-MFI), TS-1 and Fe-MFI [42], as well as in other microporous materials [43–45] and zeolites (e.g. zeolite omega [46], B-levyne [47] all silica sodalite [48] and all silica-faujasite [49], can also be explained by relaxation in the framework distortions induced by water molecules passing through the zeolite tetrahedral rings during the preceding dehydration stage (e.g. analcime [50]).

When all the volatile species have been expelled, the non-equilibrium framework distortions are relaxed and the window apertures progressively decrease and become more circular, as demonstrated by the evolution in ellipticity (defined as the ratio between the smaller (O—O) and larger (O—O)"free diameters" in the 10-rings) values reported in Fig. 1SI.

3.5. Regenerated adsorbent adsorption behaviour

The TOL saturated ZSM-5 was regenerated by calcination at 500 °C for 2 h, in order to completely remove the organics. After regeneration, ZSM-5 was then tested for TOL re-adsorption under a solution concentration enabling zeolite saturation. The adsorption/desorption cycle was repeated twice on the same material. Fig. 3b, reports the comparison of fresh and regenerated zeolite adsorption capacities. It is clearly shown that the saturation capacity of the regenerated sample after air calcination does not significantly differ from fresh material.

4. Conclusion

Combined *in situ* high-temperature synchrotron XRPD and chromatographic study was carried out to understand the kinetics and dynamics of the toluene adsorption/desorption process in organophilic ZSM-5 zeolite. Rietveld structure refinements of the occupancies show that toluene removal starts in the 75 °C< *T* < 200 °C temperature range. Adsorbate diffusion leads to significant internal pressure and causes corresponding transient expansion in the 10-ring channels. Our results clearly demonstrated that ZSM-5 regeneration is effective when thermally treated at about 400 °C. Above this temperature, non-equilibrium distortions in the framework are relaxed and channel apertures becomes more circular. ZSM-5 shows no significant difference in saturation capacity once regenerated and reloaded with toluene, thus demonstrating that thermal regeneration under mild conditions appears to be as very promising method even over several adsorption/desorption cycles. Additionally, understanding this process can help in optimizing and the design the water remediation technologies (e.g. Permeable Reactive Barriers) and using zeolites as "molecular sieves" to remove fuels-based pollutants from water.

Please cite this article in press as: E. Rodeghero, et al., Kinetics and dynamic behaviour of toluene desorption from ZSM-5 using *in situ* high-temperature synchrotron powder X-ray diffraction and chromatographic techniques, Catal. Today (2015), http://dx.doi.org/10.1016/j.cattod.2015.11.031

Acknowledgements

Research was co-funded by the Research Centre for Unconventional Energies, Istituto ENI G. Donegani Environmental Technologies(San Donato Milanese (MI), Italy) and by the Italian Ministry for University and Research (MIUR) (PRIN project " SoWaZe", prot.2010EARRRZ_009). We would like to acknowledge the European Synchrotron Radiation Facility (ESRF, Grenoble) for providing beamtime for proposal CH-3510 "*In situ* XRD study of structural modifications and desorption kinetics of zeolites used for removal of non-polar organic compounds from contaminated water". We are also grateful to the Associazione Italiana Zeoliti (AIZ) for the grant for the CIS-6Conference. Thanks to Georgia Emma Gili for the revision of the English language.

Appendix A. Supplementary data

Supplementary data associated with this article can be found, in the online version, at http://dx.doi.org/10.1016/j.cattod.2015.11.031.

References

[1] A. Rossner, S.A. Snyder, D.R.U. Knappe, Water Res. 43 (2009) 3787–3796.
[2] Y.-S. Bae, R.Q. SnurrAngew, Chem. Int. Ed. 50 (2011) 11586–11596.
[3] M.W. Ackley, S.U. Rege, H. Saxena, Microporous Mesoporous Mater. 61 (2003) 25–42.
[4] E. Díaz, S. Ordóñez, A. Auroux, J. Chromatogr. A 1095 (2005) 131–137.
[5] M.A. Anderson, Environ. Sci. Technol. 34 (2000) 725–727.
[6] I. Braschi, S. Blasioli, L. Gigli, C.E. Gessa, A. Alberti, Martucci, J. Hazard. Mater. 17 (2010) 218–225.
[7] L. Pasti, A. Martucci, M. Nassi, A. Cavazzini, R. Alberti, Bagatin, Microporous Mesoporous Mater. 160 (2012) 182–193.
[8] L. Pasti, E. Sarti, A. Cavazzini, N. Marchetti, F. Dondi, Martucci, J. Sep. Sci. 36 (2013) 1604–1611.
[9] A. Martucci, I. Braschi, L. Marchese, S. Quartieri, Mineral. Mag. 78 (2014) 1115–1140.
[10] A. Martucci, L. Pasti, N. Marchetti, A. Cavazzini, F. Dondi, A. Alberti, Microporous Mesoporous Mater. 148 (2012) 174–184.
[11] A. Martucci, L. Pasti, M. Nassi, A. Alberti, R. Arletti, R. Bagatin, R. Vignola, R. Sticca, Microporous Mesoporous Mater. 151 (2012) 358–367.
[12] U.S. Environmental Protection Agency, Waste and cleanup risk assesment glossary. U.S. Environmental Protection Agency. access date May 26 2010.
[13] World Health Organization, Guidelines for drinking-water quality, in: WHO Library Cataloguing-in-Publication Data, 4th ed., World Health Organization, 2011.
[14] E. Durmusoglu, F. Taspinar, A. Karademir, J. Hazard. Mater. 176 (2010) 870–877.
[15] L.M. McKenzie, R.Z. Witter, L.S. Newman, J.L. Adgate, Sci. Total Environ. 424 (2012) 79–87.
[16] R. Vignola, U. Cova, F. Fabiani, T. Sbardellati, R. Sisto, W.O. 2009/000429 (2009). A1 Patent.
[17] E. Harlin, J. Makkonen, M. Tiitta, WO2004080591 (2004). A1 Patent.
[18] L. Leardini, A. Martucci, I. Braschi, S. Blasioli, S. Quartieri, Mineral. Mag. 78 (2014) 1141–1159.
[19] A. Martucci, E. Rodeghero, L. Pasti, V. Bosi, G. Cruciani, Microporous Mesoporous Mater. 215 (2015) 175–182.
[20] G. Vezzalini, S. Quartieri, E. Galli, A. Alberti, G. Cruciani, Å. Kvik, Zeolites 19 (1997) 323–325.
[21] H. Van Koningsveld, J.C. Jansen, Microporous Mesoporous Mater. 6 (1996) 159–167.
[22] N. Kamiya, T. Oshiro, S. Tan, K. Nishi, Y. Yokomori, Microporous Mesoporous Mater. 169 (2013) 168–175.
[23] H. Van Koningsveld, F. Tuinstra, J.C. Jansen, H. Van Bekkum, Zeolites 9 (1989) 253–256.
[24] H. Van Koningsveld, J.C. Jansen, H. Van Bekkum, Zeolites 10 (1990) 235–242.
[25] S. Fujiyama, N. Kamiya, K. Nishi, Y. Yokomori, Langmuir 30 (2014) 3749–3753.
[26] H. Van Koningsveld, J.C. Jansen, H. de Man, Acta Cryst. B 52 (1996) 131–139.
[27] G. Reck, F. Marlow, J. Kornatowski, W. Hill, J. Caro, J. Phys. Chem. 100 (1996) 1698–1704.
[28] H. Klein, H. Fuess, K. Ernst, Weitkamps, Microporous Mesoporous Mater. 3 (1994) 291–304.
[29] H. van Koningsveld, F. Tuinstra, H. van Bekkum, J.C. Jansen, Acta Crystallogr. B 45 (1989) 423–431.
[30] K. Nishi, Y. Hidaka, Yokomori, Acta Cryst. B 61 (2005) 160–163.
[31] M. Ardit, A. Martucci, G. Cruciani, J. Phys. Chem. C 119 (13) (2015) 7351–7359.
[32] A.C. Larson, General structure analysis system (GSAS), Los Alamos Nat. Lab. Rep. LAUR (2000) 86–748.
[33] B.H. Toby, J. Appl. Cryst. 34 (2001) 210–213.
[34] S. Azizian, H. Bashiri, Langmuir 24 (20) (2008) 11669–11676.
[35] W. Rudzinski, W. Plazinski, J. Phys. Chem. B 110 (33) (2006) 16514–16525.
[36] L.H. Ai, C.Z. Zhang, F. Liao, Y. Wang, M. Li, L.Y. Meng, J. Jiang, J. Hazard. Mater. 198 (2011) 282–290.
[37] N. Hansen, R. Krishna, J.M. van Baten, A.T. Bell, F.J. Keil, J. Phys. Chem. C 113 (1) (2009) 235–246.
[38] T.W. Weber, R.K. Chakravorti, AIChE J. 20 (1974) 228–238.
[39] A. Martucci, I. Braschi, C. Bisio, E. Sarti, E. Rodeghero, R. Bagatin, L. Pasti, RSC Adv. (2015), http://dx.doi.org/10.1039/c5ra15201a.
[40] D.S. Bhange, V. Ramaswamy, Microporous Mesoporous Mater. 103 (2007) 235–242.
[41] D.S. Bhange, V. Ramaswamy, Microporous Mesoporous Mater. 130 (2010) 322–326.
[42] M. Milanesio, G. Artioli, A.F. Gualtieri, L. Palin, C. Lamberti, J. Am. Chem. Soc. 125 (2003) 14549–14558.
[43] A. Alberti, A. Martucci, Microporous Mesoporous Mater. 141 (2011) 192–198.
[44] A. Alberti, A. Martucci, Stud. Surf. Sci. Catal. 155 (2005) 19–43.
[45] G. Cruciani, J. Phys. Chem. Solids 67 (2006) 1973–1994.
[46] A. Martucci, M. de, L. Guzman-Castillo, F. Di Renzo, F. Fajula, A. Alberti, Microporous Mesoporous Mater. 104 (2007) 257–268.
[47] L. Leardini, A. Martucci, A. Alberti, G. Cruciani, Microporous Mesoporous Mater. 167 (2013) 117–126.
[48] L. Leardini, A. Martucci, G. Cruciani, Microporous Mesoporous Mater. 151 (2012) 163–171.
[49] L. Leardini, S. Quartieri, G. Vezzalini, R. Arletti, Microporous Mesoporous Mater. 202 (2015) 226–233.
[50] G. Cruciani, A.F. Gualtieri, Am. Miner. 84 (1999) 112–119.

Please cite this article in press as: E. Rodeghero, et al., Kinetics and dynamic behaviour of toluene desorption from ZSM-5 using *in situ* high-temperature synchrotron powder X-ray diffraction and chromatographic techniques, Catal. Today (2015), http://dx.doi.org/10.1016/j.cattod.2015.11.031

myDesk @unife

Valentina Bosi <bsovnt@unife.it>

Fwd: Thank you for your RightsLink / Elsevier transaction

Luisa Pasti <psu@unife.it> 15 febbraio 2016 10:10
A: Valentina Bosi <bsovnt@unife.it>

---------- Forwarded message ----------
From: **Copyright Clearance Center** <rightslink@marketing.copyright.com>
Date: 2016-02-15 10:06 GMT+01:00
Subject: Thank you for your RightsLink / Elsevier transaction
To: psu@unife.it

To view this email as a web page, go here.

Do Not Reply Directly to This Email

To ensure that you continue to receive our emails,
please add rightslink@marketing.copyright.com to your address book.

RightsLink | Copyright Clearance Center

Thank You For Your Order!

Dear Mrs. Luisa Pasti,

Thank you for placing your order through Copyright Clearance Center's RightsLink service. Elsevier has partnered with RightsLink to license its content. This notice is a confirmation that your order was successful.

Your order details and publisher terms and conditions are available by clicking the link below:
http://s100.copyright.com/CustomerAdmin/PLF.jsp?ref=4ffb75f8-25c1-4896-af9d-1e9866e98b2d

Order Details
Licensee: Luisa Pasti
License Date: Feb 15, 2016
License Number: 3810091112589
Publication: Catalysis Today
Title: Kinetics and dynamic behaviour of toluene desorption from ZSM-5 using in situ high-temperature synchrotron powder X-ray diffraction and chromatographic techniques

[Testo tra virgolette nascosto]

[Testo tra virgolette nascosto]

+1-855-239-3415 / Tel: +1-978-646-2777
customercare@copyright.com
http://www.copyright.com

[Testo tra virgolette nascosto]
[Testo tra virgolette nascosto]

Trends in Analytical Chemistry ■■ (2015) ■■–■■

Contents lists available at ScienceDirect

Trends in Analytical Chemistry

journal homepage: www.elsevier.com/locate/trac

Microscopic models of liquid chromatography: From ensemble-averaged information to resolution of fundamental viewpoint at single-molecule level

Luisa Pasti [a], Nicola Marchetti [a], Roberta Guzzinati [a,b], Martina Catani [a], Valentina Bosi [a], Francesco Dondi [a], Annamária Sepsey [c], Attila Felinger [c,d], Alberto Cavazzini [a,*]

[a] Department of Chemical and Pharmaceutical Sciences, University of Ferrara, Ferrara, Italy
[b] Italian National Agency for New Technologies, Energy and Sustainable Economic Development (ENEA), Rome, Italy
[c] MTA-PTE Molecular Interactions in Separation Science Research Group, Ifjúság útja 6, H-7624 Pécs, Hungary
[d] Department of Analytical and Environmental Chemistry, University of Pécs, Ifjúság útja 6, H-7624 Pécs, Hungary

ARTICLE INFO

Keywords:
Single molecule
Microscopic probabilistic theory of chromatography
Ensemble-averaged methods
Statistical fluctuations
Molecular viewpoint
Lévy stochastic process
Liquid chromatography

ABSTRACT

In this study, a microscopic probabilistic model of chromatography that establishes a conceptual link between single-molecule dynamics observation at liquid–solid interfaces and chromatographic experiments is described. This model is based on the discrete Lévy representation of stochastic processes and has the great advantage that it can be directly applied to the raw data set of single-molecule observations. The information contained in the molecular measurements includes some erratic rare events that are potentially very informative. Because experimental data need not be processed by mathematical–statistical transformation, application of this model preserves all the information that could be lost in an ensemble-averaged representation. In this approach, single-molecule experiments and stochastic interpretation are combined. It is of great importance to investigate superficial and interfacial phenomena in different areas, such as adsorption mechanisms in chromatography and mechanisms of biological activity, and to track the behavior of individual molecules in living cells.

Contents

1. Introduction

The basis of any microscopic model of chromatography is the description of the behavior of a lone molecule during its migration through a chromatographic column. This is different from the macroscopic approach, which considers the evolution of chromatographic bands in terms of bulk transport properties. The pathway of a single molecule is determined by a number of statistical processes, including the Brownian motion responsible for molecular diffusion, adsorption/desorption process on the stationary phase and flow pattern effects (flow unevenness) in the column [1]. Microscopic (molecular) models of chromatography have also been defined as random or stochastic models. As pointed out by Feller [2], however, the terms random and stochastic are essentially equivalent, the latter is more appropriate when time is a variable, as in chromatography. Because the statistical fluctuations around the average are the origin of zone broadening [3], the basis to understand and model the dynamic character of

* Corresponding author. Tel.: +39 0532 455331; Fax: +39 0532 240709.
E-mail address: cvz@unife.it (A. Cavazzini).

http://dx.doi.org/10.1016/j.trac.2015.08.007
0165-9936/

Please cite this article in press as: Luisa Pasti, et al., Microscopic models of liquid chromatography: From ensemble-averaged information to resolution of fundamental viewpoint at single-molecule level, Trends in Analytical Chemistry (2015), doi: 10.1016/j.trac.2015.08.007

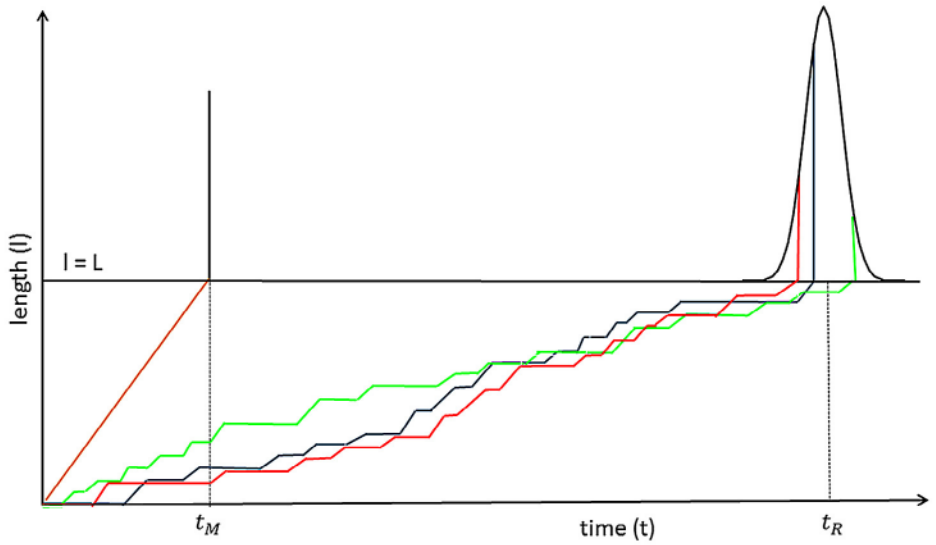

Fig. 1. Graphical representation of chromatography as a stochastic process on a time (t)–length (l) bidimensional plot. Black continuous line: the chromatographic peak as the probability density function of the residence times of molecules in the column. Broken colored lines: examples of random trajectories followed by molecules during their migration through the column. L: column length; t_M: retention time of unretained molecules (if mobile-phase dispersion is absent); t_R: retention time of the chromatographic peak. See text for details.

chromatography is the study of the chaotic pathway of a single molecule.

Fig. 1 shows a simple chromatographic separation as a stochastic process, in the case where when molecular diffusion in the mobile phase is neglected. The same process was proposed in the original description of the stochastic theory by Giddings and Eyring in their study in 1955 [4]. In this figure, migration pathways of several molecules are shown as a bidimensional plot in the time–space (t, l) plane during their separation in the chromatographic column. The broken colored lines pass from the moment of injection (at $t = 0$ and $l = 0$) to the elution of molecules from the column (at $t = t_R$ and $l = L$, where L is the length of the column). In stochastic processes, these trajectories are commonly referred to as molecular histories. Each history is made by the combination of many segments whose slope is either zero (i.e., parallel to the time axis) or equal to the mobile-phase velocity (u_0). These segments represent the two states in which a molecule can be found in the column. The segments parallel to the time axis represent the states of immobilized adsorption on the stationary phase (during which no progression in length occurs), whereas the ones with constant slope (u_0) are the times spent by molecules in the mobile phase, where they identically move at the mobile-phase velocity (in the absence of mobile-phase diffusion). Both the number and lengths of segments are random variables, and hence – from a statistical viewpoint – the history of a molecule is the sum of random numbers (number of adsorption/desorption steps) of random variables (times spent by molecules during the adsorption/desorption events and times spent in the mobile phase between two successive adsorption/desorption steps).

In Fig. 1, the first peak (at t_M) represents the retention time of an unretained compound that travels through the column without performing any adsorption/desorption process. This peak is illustrated as a Dirac delta function, because by neglecting molecular diffusion in the mobile phase, all the unretained molecules move at the same velocity of the mobile phase and are thus eluted exactly at the same time; furthermore, an infinitely narrow injection profile is assumed. On the contrary, the chromatographic peak of a retained compound (peak #2 in Fig. 1) can be interpreted as the probability density function of either trajectory cross sections with the horizontal axis located at $l = L$ or the times spent by molecules in the chromatographic column [5]. When the number of adsorption/desorption steps is large enough (or under the so-called long-time assumption, described later) and the surface is homogeneous [6,7], the shape of this peak tends to a Gaussian distribution, according to the central limit theorem of probability theory [8].

Since the very beginning, one of the most relevant aspects that can be recognized in most of the chromatographic models is the tendency to develop asymptotic theories. This is driven by the concept that an effective chromatographic operation needs sufficient time to produce well-separated peaks. When this is achieved (long-time assumption), an important approximation can be assumed that adsorption/desorption kinetics occur with only a slight deviation from equilibrium [1]. Under the long-time assumption, the convergence of microscopic and macroscopic models has been demonstrated both theoretically [9] and numerically [10].

The stochastic theory of chromatography has been applied to one-, two-, and multisite adsorption processes [7], diffusion-controlled processes [11–13], and different modes of chromatography, including size-exclusion chromatography [14–16], reaction and dynamic chromatography [17–19], ion-exchange chromatography [20], reversed-phase chromatography [21–25], chiral chromatography [26], and – by means of a simulation-based approach – nonlinear chromatography [10,27] to cite some of the most interesting cases.

This study focuses on a unified description of stochastic models through the so-called Lévy process representation or formalism [28,29], which has allowed for the establishment of a conceptual bridge between single-molecule dynamics observation and chromatographic experiments [30]. Paul Lévy (1886–1971) is universally recognized as the one "who has influenced the establishment and growth of probability theory more than any other." [31] He became a professor of analysis at École Polytechnique at Paris, France, in 1920, where he served until his retirement in 1959 [32]. Georges Guiochon (1931–2014) is remembered as one of the masters of modern chromatography and one of the students of Lévy, who graduated from École Polytechnique in 1951.

The continuous developments in analytical science and technology, which have decreased the limits of detection (in the order of femtomoles and yoctomoles [33,34]), have opened new,

Please cite this article in press as: Luisa Pasti, et al., Microscopic models of liquid chromatography: From ensemble-averaged information to resolution of fundamental viewpoint at single-molecule level, Trends in Analytical Chemistry (2015), doi: 10.1016/j.trac.2015.08.007

exciting frontiers of research and revived the stochastic models of chromatography. Indeed, experimental visualization of the erratic behavior of single molecules (e.g., by single-molecule fluorescence, optical tweezers, scanning probe microscopy, and mass spectrometry imaging [35]) has become feasible. These measurements can provide more information on the dynamic character of chromatography (in all of its fundamental aspects) than the ensemble-averaged data obtained from the classical analysis of a large number of molecules, as statistical fluctuations from the average lead to zone broadening [1,3,30].

The description of chromatographic separation as a Lévy process will be revised in the following section, with particular attention paid to its basic principles and physical meaning. Its applications and future possibilities of development will also be discussed.

2. Discussion

2.1. The microscopic stochastic model of chromatography

In the stochastic description of the chromatographic process, the chromatographic peak is measured by the probability density function of the time spent by the molecules inside the column. The retention time of a single molecule j is a random variable ($t_{R,j}$), which is calculated as the sum of all elementary times (τ) spent by that molecule in the mobile (M) and stationary (S) phases:

$$t_{R,j} = \sum_{i=1}^{n} \tau_{M,j,i} + \sum_{i=1}^{n} \tau_{S,j,i} \tag{1}$$

where n represents the random number of adsorption/desorption steps executed by the molecule during the chromatographic migration (with the index i representing the ith elementary step).

Again considering the separation process described in Fig. 1, where diffusion in the mobile phase is neglected, the number of adsorption events per unit time – also referred to as adsorption frequency (μ) – is related to the time t_M spent by an unretained molecule in the column. Indeed, in this case, the average number of adsorption events ($\bar{n}$) is constant for all molecules, and is given by

$$\bar{n} = t_M \mu = \frac{t_M}{\bar{\tau}_M} \tag{2}$$

where $\bar{\tau}_M$ is the average time spent in the mobile phase between two consecutive adsorptions (τ_M). In this case, Equation (1) reduces to

$$t_{R,j} = t_M + \sum_{i=1}^{n} \tau_{S,j,i} \tag{3}$$

It is well known that, in order to find the density function of a random variable, that is, the sum of two or more independent random variables, it is necessary to calculate the convolution integral of the density functions of the individual random variables. When the number of random variables becomes relevant, the convolution integral may become a very complex mathematical expression that could be analytically unsolved.

2.2. The Lévy model of chromatography

The problem of addition of random variables can be overcome by the use of a mathematical tool known as the *characteristic function* ($\varphi_t(\omega)$), that is, the Fourier–Stieltjes transform [36,37] of the frequency function in time domain. Then, the density function can be calculated by the inversion of the characteristic function obtained as the product of the characteristic functions of the individual random variables [38]. Furthermore, the statistical moments can be obtained directly from the derivatives of the characteristic function.

The fundamental contribution to this field was made by Paul Lévy. In particular, he proved the central limit theorem using the characteristic functions and also introduced the concept of stochastic processes with independent and stationary increments. At present, these are commonly known as Lévy processes [39]. By means of the Lévy approach, it can be demonstrated that the chromatographic peak describing the model represented in Fig. 1 is given in the frequency domain by

$$\varphi_t(\omega) = \exp\left(\mathrm{i}\omega t_M + t_M \int_0^{\infty} (e_S^{i\omega\tau} - 1) M(\mathrm{d}\tau_S) \right) \tag{4a}$$

$$\varphi_t(\omega) = \exp\left(\mathrm{i}\omega t_M + \sum\nolimits_k (e_{S,k}^{i\omega\tau} - 1) \Delta M(\tau_{S,k}) \right), \tag{4b}$$

where i is the imaginary unit and $M(d\tau_S)$ (or in the discrete case $\Delta M(\tau_{S,k})$) is the differential of the Lévy "spectral function" $M(\tau_S)$. $M(d\tau_S)$ essentially represents the number of adsorption events with duration between τ_S and $\tau_S + d\tau_S$ per unit time. $M(\tau_S)$ can be obtained by the product of cumulative distribution function of the adsorption time, $F(\tau_S)$, and the adsorption frequency, μ, as

$$M(\tau_S) = \mu F(\tau_S), \tag{5a}$$

where the definition of adsorption time depends on whether desorption time is continuous ($f(\tau_S)$) or discrete ($f_j(\tau_{S,j})$):

$$F(\tau_S \le \tau_S^*) = \begin{cases} \int_0^{\tau_S^*} f(\tau_S) d\tau_S & \text{continuous} \\ \sum_j f_j(\tau_{S,j}) & \text{discrete} \end{cases} \tag{5b}$$

On the basis of the model used to describe the adsorption surface characteristics (e.g., homogeneity or heterogeneity), kinetics of the adsorption/desorption event (order of the reaction), and other attributes, the random variables in Equations (4) and (5) will be described by different probability distributions.

The physical meaning of the Lévy representation of the chromatographic process can be illustrated by considering a series of examples. Let us assume first a very simple case where the duration of any adsorption step is constant and equal to $\tau_{S,1}$ (with unit probability). Under this hypothesis, the spectral function $M(\tau_S)$ is a single Dirac delta function located at $\tau_{S,1}$, whose intensity μ will correspond to the number of molecules detected at that site per unit time (Equation 5). Let us assume furthermore that the number of transitions n between the mobile phase and stationary phase has a Poisson distribution, the most often used distribution to describe discrete stochastic processes (such as the number of adsorption events in chromatography). It designates the so-called memoryless processes, in which the probability that a given event occurs is only proportional to the observation length [4]. This simple model is represented in Fig. 2, whose bottom part shows the differential spectral function. The top part of the figure shows two different molecular trajectories followed by two molecules (A and B) injected simultaneously into the column (at (0,0)), which are presented by broken lines. Assuming that the time spent by either molecule in the mobile phase is constant, t_M, the total time spent in the stationary phase, and thus the total time spent in the column (t_R), will be clearly different, because of the randomness of the entry process. This randomness causes dispersion of arrival times at the column end, and thus peak broadening (even if the time τ_S is constant). The chromatographic peak in this simple case is represented as

$$\varphi_t(\omega) = \exp\left(i\omega t_M + t\mu \left(e_{S,1}^{i\omega\tau} - 1 \right) \right) \tag{6}$$

An adsorption surface paved by m different adsorption sites, each of which is characterized again by a constant adsorption time $\tau_{S,k}$ ($k = 1, \ldots, m$), is considered as the second example. $\tau_{S,k}$ depends on

Please cite this article in press as: Luisa Pasti, et al., Microscopic models of liquid chromatography: From ensemble-averaged information to resolution of fundamental viewpoint at single-molecule level, Trends in Analytical Chemistry (2015), doi: 10.1016/j.trac.2015.08.007

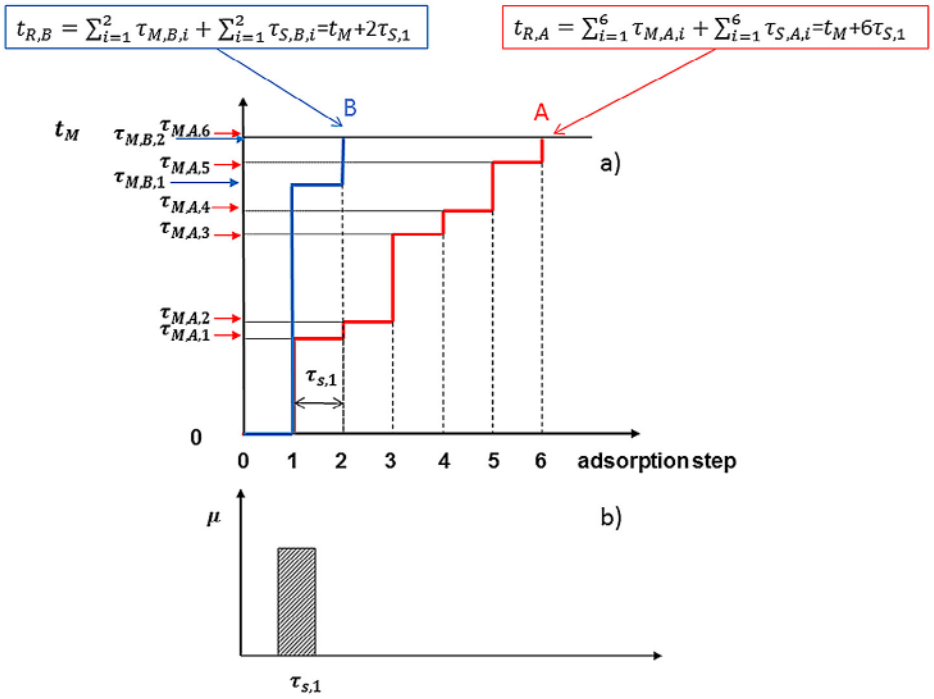

Fig. 2. (a) Molecular trajectories followed by two molecules (A and B) injected simultaneously into the column, at the point (0,0). The duration of any adsorption step is constant and equal to $\tau_{s,1}$; the number of adsorption steps follows a Poisson distribution. The time spent by both molecules in the mobile phase is constant and equal to t_M. (b) Differential spectral function of the process. The intensity μ represents the number of molecules detected per unit time by single-molecule experiments at the surface.

the adsorption energy of the kth site [28]; the larger the τ_{Sk} the stronger the adsorption site is [40]. The spectral function describing this case will be made by a series of Dirac delta functions located at $t_k = \tau_{Sk}$ with an amplitude μ_k, that is, the number of molecules detected at the kth site per unit time (or the abundance of kth-type site on the surface). For example, if $m = 4$, the differential spectral function will be similar to the distribution given in the bottom part of Fig. 3, where, in addition, it has been assumed that the number of molecules (per unit time) detected at the sites of types 1, 2, and 4 is equal and that twice as much molecules detected at site 3 ($\mu_1 = \mu_2 = \mu_4 = \mu_3/2$). In other words, sites 1, 2, and 4 are equally abundant on the surface, whereas the abundance of site 3 is twofold. In analogy with Fig. 2, the top part of Fig. 3 shows two random trajectories followed by two molecules (A and B). By assuming again that the time spent in the mobile phase is constant (t_M), the total time spent by the molecules in the column (t_R) will clearly depend on not only the number of adsorption steps (a random variable, n), but also the type of site visited in each adsorption step (being $\tau_{S,1} \neq \tau_{S,2} \neq \tau_{S,3} \neq \tau_{S,4}$). The corresponding representation of the chromatographic peak in frequency domain is

$$\varphi_t(\omega) = \exp\left(i\omega t_M + \frac{1}{\mu_t} \sum_{k=1}^{m} t\mu_k \left(e^{i\omega\tau_{Sk}} - 1 \right) \right) \tag{7}$$

where

$$\mu_t = \sum_{k=1}^{m} \mu_k. \tag{7a}$$

So far, we have considered cases where the random variables n and τ_s are described by discrete distributions. In the traditional Giddings–Eyring model (Fig. 1), the time spent by the molecule in the (homogeneous) stationary phase is considered as a random variable governed by exponential distribution (with average $\overline{\tau}_s$), whereas the number of adsorption/desorption steps follows a Poisson distribution (as in the discrete cases considered earlier). The resulting

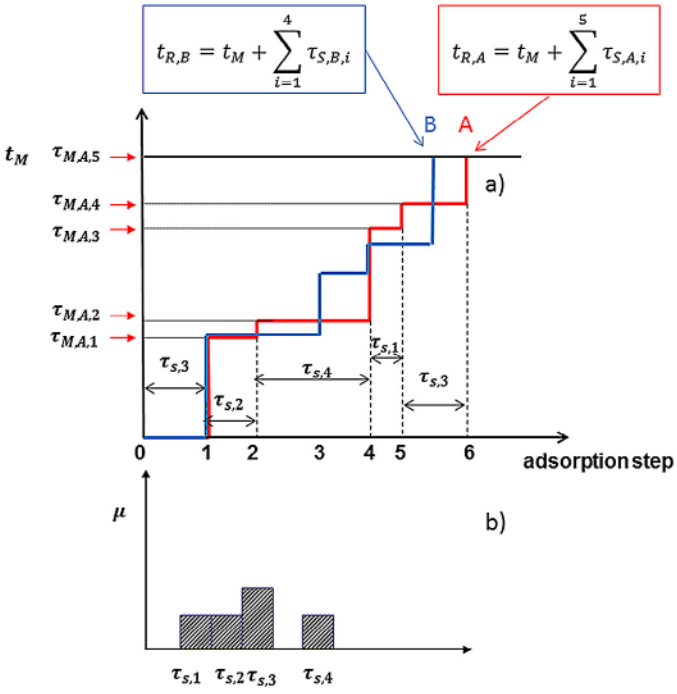

Fig. 3. The same as Fig. 2, but by assuming a heterogeneous surface made of four different adsorption sites. The duration of the adsorption events depends on the site where the molecule stops and may assume four different values (τ_{sk} ($k = 1, \ldots, 4$)). (a) Molecular trajectories followed by two molecules (A and B). (b) Differential spectral function of the process. Intensities μ_k represent the number of molecules detected per unit time at the kth site (or the relative abundance of kth site on the surface). See text for details.

Please cite this article in press as: Luisa Pasti, et al., Microscopic models of liquid chromatography: From ensemble-averaged information to resolution of fundamental viewpoint at single-molecule level, Trends in Analytical Chemistry (2015), doi: 10.1016/j.trac.2015.08.007

process can be classified as a *compound Poisson process*, and the chromatographic peak in the frequency domain takes the following form [9]:

$$\varphi_t(\omega) = \exp\left(i\omega t_M + \overline{n}\left[\frac{1}{1-i\omega\overline{\tau}_s} - 1\right]\right) \quad (8)$$

From a probabilistic viewpoint, it can be demonstrated that, if the frequency μ follows an exponential distribution and the number of adsorption sites (m) is sufficiently large [41], the discontinuous Lévy model of chromatography (Equation 4b) converges to the original Giddings–Eyring model.

However, the importance of the Lévy model for the interpretation of single-molecule experiments lies in its ability to deal with discrete distributions of residence times. Indeed, the experimental information that can be derived from single-molecule observation is usually in the form of number of molecules (or frequency) versus residence time [30] (Fig. 3). Therefore, by using the discrete Lévy representation, the experimental data can be used without any statistical–mathematical manipulation (e.g., nonlinear fitting procedures) to estimate average n or τ_s values based on a given model. In particular, for sparse events, additional manipulation may not only introduce bias in the estimation of the parameters, but also entail loss of information associated with rare events (e.g., adsorption on low-abundance sites). As it will be shown in the next section, important information about the molecular nature of the adsorption mechanisms has been deduced from the interpretation of these events. The major advantage of the Lévy representation over other microscopic stochastic models of chromatography is that it allows moving from an ensemble-averaged description of the process to the resolution of fundamental information at a single-molecular viewpoint.

2.3. *Insights into adsorption mechanisms by combining single-molecule observation and the stochastic theory of chromatography*

This section intends to provide a short overview of some of the most relevant results that have been achieved through single-molecule investigation and traditional chromatographic measurements for liquid–solid interfacial phenomena.

In one of the pioneering works where single-molecule spectroscopy has been used to investigate surface heterogeneity in reversed-phase liquid chromatography (RPLC), by studying the chromatographic behavior of a lipophilic cationic fluorescent dye on C_{18} stationary phase, Wirth et al. demonstrated the presence of two different "populations" of interactions [42]. Almost all molecules (~99%) diffused quickly at the solid–liquid interface (with a diffusion coefficient $D_S = 1.3\times10^{-6}$ cm^2/s), whereas about 1% of them was found to be stuck on the surface for a significantly longer time, in the order of several seconds. This behavior was successfully correlated to the presence of "strong" silanols on the surface by single-molecule imaging coupled to fluorescence correlation spectroscopy (FCS).

Later, those data were used to examine the applicability of the discrete Lévy model (Equation 7) to experimental data [28]. By considering a two-site heterogeneous adsorption surface made of 99% of weak sites and only 1% of strong ones, Pasti et al. demonstrated that the simulated peak obtained by the numerical inversion of Equation (7) was in good agreement with the experimental chromatograms provided in Ref. [43], as the time average is equivalent to the ensemble average, and the percentages of molecules found in Wirth's work correspond to the populations of the two types of sites on the surface.

In another interesting work, Wirth and coworkers indicated the presence of strong adsorption sites of topographical origin on the surface of C_{18} silica gel [44]. According to this work, which was using the same single-molecule techniques as in Ref. [42], the strong adsorption sites were considered equally important as acidic isolated silanols that explain the silanol activity of bonded silica phases. This information would have never been obtained without single-molecule measurements.

Recently, Mabry et al. [23] have studied the adsorption kinetics of a fluorescent lipid on a trimethylsilyl interface by combining single-molecule observations and ensemble-averaged data collected by RPLC experiments. By using the discrete Lévy representation of the chromatographic process (Equation 7), they were able to significantly interpret the dependence of peak tailing on the mobile-phase composition based on the correlation of the number of "active" strong sites (detected by single-molecule experiments) and the amount of organic modifier in aqueous organic eluents.

Further examples of combining single-molecule observations and chromatographic experiments have been provided by Landes et al. [45], who used superresolution single-molecule spectroscopy (SSMS) to study, with the aid of the stochastic theory, single-protein ion-exchange interactions on ligand-functionalized agarose stationary phases. This study demonstrated that, among the different ion exchangers considered, including pentaargininamide- and monoargininamide-functionalized and bare agarose, the protein was able to provide specific interactions solely on the pentaargininamide-based stationary phase. The adsorption/desorption times of single protein–ligand adsorption events were measured, through which a residence time versus frequency distribution (conceptually analogous to the one provided in the bottom part of Fig. 3) was obtained. Using the discrete Lévy model, the authors were able to reconstruct the chromatographic peak and provide an explanation, based on steric effect, for the heterogeneous single-protein adsorption/desorption kinetics observed with different molecules. In particular, they indicated that steric effect causes a reduction of interaction energy between protein surface and charged ligands, which leads to shorter desorption times and longer adsorption times, thereby causing peak fronting. In addition, they also compared the results of the discrete model with those obtained using the traditional Giddings–Eyring model (Equation 8), where the average number of adsorption steps ($\overline{n}$) and the average time spent in each step ($\overline{\tau}_s$) were obtained by fitting the experimental frequency distribution to an exponential function. The results clearly showed that only the discrete Lévy approach maintains the information contained in the experimental data, which, on the contrary, is irrecoverably lost by the ensemble-averaged representation.

The behavior of single proteins at ion-exchange interfaces was further investigated by Larson et al. [46], who, in particular, focused on the effect of ionic strength on these interactions. Their results support the hypothesis of spatial variations in adsorbent structural/energetic properties as a function of ionic strength to explain the observed heterogeneity of protein ion-exchange adsorption isotherms. They were also able to provide the first direct observation of mechanisms, leading to the narrowing of the functional-site population as ionic strength increases.

3. Conclusions

The combination of single-molecule observations and chromatographic experiments according to the representation of the discrete Lévy model represents a formidable tool for the investigation of interfacial processes of different nature. It is assumed that, in the near future, this approach will be particularly useful for the characterization and interpretation of biological systems, with the possibility offered by the model, in terms of not only revealing mechanisms of action at molecular viewpoint, but also by tracking the behavior of molecules in living cells [35].

It may reasonably be supposed that this methodology will contribute to the understanding of the differences between the molecular-scale environment and macroscopic world. In

Please cite this article in press as: Luisa Pasti, et al., Microscopic models of liquid chromatography: From ensemble-averaged information to resolution of fundamental viewpoint at single-molecule level, Trends in Analytical Chemistry (2015), doi: 10.1016/j.trac.2015.08.007

particular, it has been indicated [47] that there are two critical aspects where these differences become relevant: the Brownian motion and the relative importance of viscous forces over inertial forces. It has been shown that the actual motion of an object depends on not only the thermal forces exerted on the object, but also constraints (if any, e.g., viscous drag from the medium) on its motion. In order to gain a deep understanding of these aspects, single-molecule observations are needed in addition to the mean value of thermal energy. Inertial forces are dominant in macroscopic objects, whereas viscous drag force is more important than inertia at the microscopic level. This means that, at the microscopic scale, objects stop moving more rapidly than macroscopic ones when the force is no longer applied. The investigation of these features requires models that are capable of interpreting single-molecule behavior.

In conclusion, the major advantage of working with the raw, single-molecule data set is that far more information can be extracted from them than from ensemble-averaged distributions obtained from the classical analysis of a large number of molecules. Indeed, ensemble methods do not resolve the fundamental molecular viewpoint that reveals unique features of the process under investigation.

Acknowledgments

The authors thank the Italian University and Scientific Research Ministry (PRIN 2012ATMNJ_003). Nicola Marchetti thanks Laboratory Terra&Acqua Tech, member of Energy and Environment Cluster, Technopole of Ferrara of Emilia-Romagna High Technology Network. The work was supported in part by the OTKA K 106044 grant. Dr Valentina Costa is acknowledged for her technical support.

References

[1] J.C. Giddings, Dynamics of Chromatography, Part 1, Marcel Dekker, Inc., New York, 1965.
[2] W. Feller, Probability Theory and Its Applications, Wiley, New York, 1950.
[3] J.C. Giddings, Unified Separation Science, John Wiley & Sons, Inc., New York, 1991.
[4] J.C. Giddings, H. Eyring, A molecular dynamic theory of chromatography, J. Phys. Chem. 59 (1955) 416–421.
[5] F. Dondi, M. Remelli, The characteristic function method in the stochastic theory of chromatography, J. Phys. Chem. 90 (1989) 1885–1891.
[6] A. Cavazzini, M. Remelli, F. Dondi, Stochastic theory of two-site adsorption chromatography by the characteristic function method, J. Microcolumn Sep. 9 (1997) 295–302.
[7] A. Cavazzini, M. Remelli, F. Dondi, A. Felinger, Stochastic theory of multiple-site linear adsorption chromatography, Anal. Chem. 71 (1999) 3453–3462.
[8] S. Deming, Y. Michotte, D. Massart, L. Kaufman, B. Vandeginste, Chemometrics: A Text Book, Elsevier, Amsterdam, 1988.
[9] A. Felinger, A. Cavazzini, F. Dondi, Equivalence of the microscopic and macroscopic models of chromatography: stochastic-dispersive versus lumped kinetic model, J. Chromatogr. A 1043 (2004) 149–157.
[10] A. Cavazzini, F. Dondi, A. Jaulmes, C. Vidal-Madjar, A. Felinger, Monte Carlo model of nonlinear chromatography: correspondence between the microscopic stochastic model and the macroscopic Thomas kinetic model, Anal. Chem. 74 (2002) 6269–6278.
[11] A. Felinger, A. Cavazzini, M. Remelli, F. Dondi, Stochastic-dispersive theory of chromatography, Anal. Chem. 71 (1999) 4472–4479.
[12] A. Felinger, Diffusion time in core-shell packing materials, J. Chromatogr. A 1218 (2011) 1939–1941.
[13] A. Felinger, Molecular dynamic theories in chromatography, J. Chromatogr. A 1184 (2008) 20–41.
[14] F. Dondi, A. Cavazzini, M. Remelli, A. Felinger, M. Martin, Stochastic theory of size exclusion chromatography by the characteristic function approach, J. Chromatogr. A 943 (2002) 185–207.
[15] A. Felinger, L. Pasti, F. Dondi, M. van Hulst, P.J. Schoenmakers, M. Martin, Stochastic theory of size exclusion chromatography: peak shape analysis on single columns, Anal. Chem. 77 (2005) 3138–3148.
[16] A. Sepsey, I. Bacskay, A. Felinger, Polydispersity in size-exclusion chromatography: a stochastic approach, J. Chromatogr. A 1365 (2014) 156–163.
[17] L. Pasti, A. Cavazzini, M. Nassi, F. Dondi, Dynamic chromatography: a stochastic approach, J. Chromatogr. A 1217 (2010) 1000–1009.
[18] R. Sabia, A. Ciogli, M. Pierini, F. Gasparrini, C. Villani, Dynamic high performance liquid chromatography on chiral stationary phases. Low temperature separation of the interconverting enantiomers of diazepam, flunitrazepam, prazepam and tetrazepam, J. Chromatogr. A 1363 (2014) 144–149.
[19] O. Trapp, Unified equation for access to rate constants of first-order reactions in dynamic and on-column reaction chromatography, Anal. Chem. 78 (2006) 189–198.
[20] K. Horváth, M. Olajos, A. Felinger, P. Hajós, Retention controlling and peak shape simulation in anion chromatography using multiple equilibrium model and stochastic theory, J. Chromatogr. A 1189 (2008) 42–51.
[21] A. Felinger, Molecular movement in an HPLC column: a stochastic analysis, LC GC N. Am. 22 (2004) 103–106.
[22] N. Lambert, I. Kiss, A. Felinger, Mass-transfer properties of insulin on core-shell and fully porous stationary phases, J. Chromatogr. A 1366 (2014) 84–91.
[23] J.N. Mabry, M.J. Skaug, D.K. Schwartz, Single-molecule insights into retention at a reversed-phase chromatographic interface, Anal. Chem. 86 (2014) 9451–9458.
[24] D. Hlushkou, F. Gritti, A. Daneyko, G. Guiochon, U. Tallarek, How microscopic characteristics of the adsorption kinetics impact macroscale transport in chromatographic beds, J. Phys. Chem. C 117 (2013) 22974–22985.
[25] D. Hlushkou, F. Gritti, G. Guiochon, A. Seidel-Morgenstern, U. Tallarek, Effect of adsorption on solute dispersion: a microscopic stochastic approach, Anal. Chem. 86 (2014) 4463–4470.
[26] P. Jandera, V. Backovska, A. Felinger, Analysis of the band profiles of the enantiomers of phenylglycine in liquid chromatography on bonded teicoplanin columns using the stochastic theory of chromatography, J. Chromatogr. A 919 (2001) 67–77.
[27] F. Dondi, P. Munari, M. Remelli, A. Cavazzini, Monte Carlo model of nonlinear chromatography, Anal. Chem. 72 (2000) 4353–4362.
[28] L. Pasti, A. Cavazzini, A. Felinger, M. Martin, F. Dondi, Single-molecule observation and chromatography unified by levy process representation, Anal. Chem. 77 (2005) 2524–2535.
[29] F. Dondi, A. Cavazzini, L. Pasti, Chromatography as Levy Stochastic process, J. Chromatogr. A 1126 (2006) 257–267.
[30] L. Kisley, C.F. Landes, Molecular approaches to chromatography using single molecule spectroscopy, Anal. Chem. 87 (2015) 83–98.
[31] S. Taylor, Paul Lévy, Bull. London Math. Soc. 7 (1975) 300–320.
[32] <http://www.annales.org/archives/x/paullevy.html>.
[33] M.E. Kurczy, T.R. Northen, S.A. Trauger, G. Siuzdak, Nanostructure imaging mass spectrometry: the role of fluorocarbons in metabolite analysis and yoctomole level sensitivity, mass spectrometry imaging of small molecules, Methods Mol. Biol. 1203 (2015) 141–149.
[34] H. Zhang, F. Li, X.-F. Li, X.C. Le, Yoctomole detection of proteins using solid phase binding-induced DNA assembly, Methods 64 (2013) 322–330.
[35] A.E. Knight, Single Molecule Biology, Academic Press, San Diego, CA, 2008.
[36] D.A. McQuarrie, Statistical Thermodynamics, University Science Book, Mill Valley, CA, 1973.
[37] N.G. Van Kampen, Stochastic Processes in Physics and Chemistry, North Holland, Amsterdam, 1981.
[38] F. Dondi, Approximation properties of the edgeworth cramer series and determination of peak parameters of chromatographic peaks, Anal. Chem. 54 (1982) 473–477.
[39] P. Lévy, Théorie de L'addition des Variables Aléatoires, Gauthier-Villars, Paris, 1954.
[40] J.H. De Boer, The Dynamical Character of Adsorption, Clarendon Press, Oxford, 1969.
[41] K. Sato, Lévy Processes Theory and Applications, Birkhauser, Boston, 2001.
[42] M.J. Wirth, D.J. Swinton, Single-molecule probing of mixed-mode adsorption at a chromatographic interface, Anal. Chem. 70 (1998) 5264–5271.
[43] M.J. Wirth, E.A. Smith, S.R. Anthony, Measurement and simulation of tailing zones of a cationic dye in analytical-scale reversed phase chromatography, J. Chromatogr. A 1034 (2004) 69–75.
[44] M.J. Wirth, D.J. Swinton, Single-molecule study of an adsorbed oligonucleotide undergoing both lateral diffusion and strong adsorption, J. Phys. Chem. B 105 (2001) 1472–1477.
[45] L. Kisley, J. Chen, A.P. Mansur, B. Shuang, K. Kourentzi, M.-V. Poongavanam, et al., Unified superresolution experiments and stochastic theory provide mechanistic insight into protein ion-exchange adsorptive separations, Proc. Natl. Acad. Sci. U.S.A. 111 (2014) 2075–2080.
[46] L. Kisley, J.X. Chen, A.P. Mansur, S. Dominguez-Medina, E. Kulla, M.K. Kang, et al., High ionic strength narrows the population of sites participating in protein ion-exchange adsorption: a single-molecule study, J. Chromatogr. A 1343 (2014) 135–142.
[47] J. Howard, Mechanics of Motor Proteins and the Cytoskeleton, Sinauer Associates, Sunderland, MA, 2001.

Please cite this article in press as: Luisa Pasti, et al., Microscopic models of liquid chromatography: From ensemble-averaged information to resolution of fundamental viewpoint at single-molecule level, Trends in Analytical Chemistry (2015), doi: 10.1016/j.trac.2015.08.007

myDesk @unife

Valentina Bosi <bsovnt@unife.it>

Fwd: Thank you for your RightsLink / Elsevier transaction

Luisa Pasti <psu@unife.it> 15 febbraio 2016 10:10
A: Valentina Bosi <bsovnt@unife.it>

---------- Forwarded message ----------
From: **Copyright Clearance Center** <rightslink@marketing.copyright.com>
Date: 2016-02-15 10:06 GMT+01:00
Subject: Thank you for your RightsLink / Elsevier transaction
To: psu@unife.it

To view this email as a web page, go here.

Do Not Reply Directly to This Email

To ensure that you continue to receive our emails,
please add rightslink@marketing.copyright.com to your address book.

RightsLink | Copyright Clearance Center

Thank You For Your Order!

Dear Mrs. Luisa Pasti,

Thank you for placing your order through Copyright Clearance Center's RightsLink service. Elsevier has partnered with RightsLink to license its content. This notice is a confirmation that your order was successful.

Your order details and publisher terms and conditions are available by clicking the link below:
http://s100.copyright.com/CustomerAdmin/PLF.jsp?ref=adc33ab9-fa15-4f96-a52c-57e8cc5be9bc

Order Details
Licensee: Luisa Pasti
License Date: Feb 15, 2016
License Number: 3810091178156
Publication: TrAC Trends in Analytical Chemistry
Title: Microscopic models of liquid chromatography: From ensemble-averaged information to resolution of fundamental viewpoint at single-molecule level

[Testo tra virgolette nascosto]

[Testo tra virgolette nascosto]

+1-855-239-3415 / Tel: +1-978-646-2777
customercare@copyright.com
http://www.copyright.com

[Testo tra virgolette nascosto]
[Testo tra virgolette nascosto]